Università degli Studi di Milano
Facoltà di Scienze Matematiche,
Fisiche e Naturali

Scuola di Dottorato in Fisica,
Astrofisica e Fisica Applicata

Ciclo XXXII

Search for supersymmetry with a compressed mass spectrum using the ATLAS detector

Supervisore: Dott. Tommaso Lari
Direttore della scuola: Prof. Matteo Paris

Tesi di Dottorato di:
Lorenzo Rossini

Anno Accademico 2018-2019

Contents

1 Introduction

At present day the Standard Model is the framework for particle physics. This model has been developed during the 20^{th} century, making accurate predictions which has been confirmed to great precision by experimental measurements, culminating with the discovery of the Higgs boson by the ATLAS [1] and CMS [2] experiments at the Large Hadron Collider (LHC) [3] in 2012 [4, 5].
Despite all of these successes, there are still open problems in the current description of the particle physics world. This has lead many to think that that the Standard Model is only an effective theory at low energy, and that a more general extension is needed.
One important aspect that is left without a satisfying answer is the origin of the Higgs boson mass. In the Standard Model the Higgs mass is a free parameter of the Lagranian that receives radiative corrections to its mass proportional to the maximum energy accessible to virtual particles: $\delta m_H^2 = k\Lambda^2$.

This means that the Higgs mass should be of the same order as the maximum energy in the theory, however its mass has been measured to be just 125 GeV, and this is a strong hint that the SM it is not valid anymore at the scale of $\mathcal{O}(1\ \text{TeV})$. Moreover, if the SM is extended as it is now to higher scales such as the Plank Scale ($\mathcal{O}(10^{16}\ \text{TeV})$), the mass also diverges. This means that the parameters in the contribution to the radiative corrections (k) must be tuned in such a way that they cancel out each other, in order to give exactly the measured value of the Higgs boson mass. This kind of behavior is called a *fine tuning*, and it is generally considered *unnatural*. Instead in a *natural* theory, parameters are allowed to be arbitrary small only if their replacement with zero increase the symmetry of the system.
An additional problem is that from cosmological and astronomical measurement, it is known that $\sim 23\%$ of the universe is made of so called *Dark Matter*, matter that is stable, neutral, and that interacts gravitationally, and maybe also through the weak force. However in the Standard Model there is no such candidate that could satisfy these criteria.
Moreover, there is no description of gravity inside this model. All these hints point to the fact that the Standard Model is just an effective description of a more general theory that lives at higher energy. Supersymmetry (SUSY) is one of the most interesting solutions and

also one of the most compelling. In SUSY it is assumed that there is a more fundamental symmetry, where for every boson (fermion) it exists a partner (called *superpartner*) with a fermionic (bosonic) nature, which means a particle with a difference of half a unit of spin. With this new rules is possible to have a new set of particles, that can help to reduce the problems of the Standard Model. As an example, the presence of these new particles can introduce new terms in the correction to the Higgs boson mass that can cancel out in a natural way the other contribution, leaving a mass that is compatible with the one measured. Also, if the lightest supersymmetric particle is stable and neutral, it could be a good candidate for the Dark Matter.
However if supersymmetric particles were just the same copy of the Standard Model particles, but with a changed spin, they would have already been observed. This means that this symmetry must be broken, allowing the SUSY particles to have larger masses than their corresponding Standard Model partner. However, for naturalness reasons, these partners cannot have masses too high, and should be around the scale of the TeV.
In many SUSY models, the lightest supersymmetric particles, called neutralino ($\tilde{\chi}^0$), is mainly a superposition of the super partner of the Higgs boson, and its mass parameter, μ is the same that drives the mass of the Higgs boson. This means that the two masses should be rather similar, and well within the reach of the LHC.
This thesis is inserted in the context of the ATLAS experiment, located at the LHC at CERN, in Geneva, Switzerland. LHC delivers proton-proton collisions at an energy in the center of mass of 13 TeV. The ATLAS experiment purpose is to investigate the nature of the Higgs boson and its proprieties, and to search for new physics outside the Standard Model, by looking for Dark Matter, supersymmetric particles, and other exotic models.
In this thesis I present two analysis searching for SUSY.The first one was done using the data recorded by ATLAS during 2015 and 2016, for a total integrated luminosity of 36.1 fb^{-1}, while the second analysis was performed with the full dataset of Run 2, the data taking period from 2015 to 2018, for a total integrated luminosity of 139 fb^{-1}.
These searches both look for the direct production of SUSY particles via electroweak interactions, with a compressed mass spectra, meaning that the particles considered all have similar masses and therefore the decay products are soft. The produced particles are the charged and

neutral superpartners of gauge and Higgs bosons, called respectively *chargino* ($\tilde{\chi}^{\pm}$) and *neutralino* ($\tilde{\chi}^{0}$), with increasing subscript indicating increasing mass (i.e. $m(\tilde{\chi}^{0}_{3}) > m(\tilde{\chi}^{0}_{2}) > m(\tilde{\chi}^{0}_{1})$), and together are called electroweakinos. The processes considered are $\tilde{\chi}^{0}_{2}\ \tilde{\chi}^{0}_{1}$, $\tilde{\chi}^{\pm}_{1}\ \tilde{\chi}^{0}_{2}$, and $\tilde{\chi}^{+}_{1}\ \tilde{\chi}^{-}_{1}$, where the decays are $\tilde{\chi}^{0}_{2} \rightarrow Z^{(\star)}\tilde{\chi}^{0}_{1}$ and $\tilde{\chi}^{\pm}_{1} \rightarrow W^{(\star)}\tilde{\chi}^{0}_{1}$, with the virtual Z boson decaying into two leptons, while the W into either two leptons or two quarks. Here the $\tilde{\chi}^{0}_{1}$ is considered stable, and a candidate for Dark Matter.
In the considered scenario, the three lightest electroweakinos ($\tilde{\chi}^{0}_{2}$,$\tilde{\chi}^{\pm}_{1}$,$\tilde{\chi}^{0}_{1}$) are considered mainly a mixture of higgsinos, the superpartners of the Higgs boson. In this case the difference in mass between them is small, of the order of few GeV, and therefore the objects, in this case leptons, coming from their decay are rather soft. This scenario is rather interesting because it is one of the most *natural* SUSY extensions. Moreover the last results on this interpretation were obtained by the LEP experiment, and is then important to be able to set new limits and probe new scenarios.
The main difficulty in these analysis is then to be able to reconstruct the soft leptons coming from the decays of the $\tilde{\chi}^{0}_{2}$. The first analysis looked for final states with 2 leptons (either an electron or muon) with p_{T} down to 4 GeV. This was the first search in ATLAS to use leptons with p_{T} lower than 7 GeV, allowing the analysis to be sensible to the scenario considered. Instead in the second analysis with the full Run 2 data set it was used a final state with 1 lepton and 1 track. This allows gaining more efficiency to leptons with a p_{T} of 2 GeV, and to push forward even more the sensitivity of the analysis at very low Δm. These analysis depend crucially from the ability of the detector to correctly reconstruct and identify very soft leptons. This requires a very precise comprehension of the detector's response and its evolution in time. One important aspect is the radiation damage on the performance of the pixel detector. This was another topic on which I have worked during my thesis and that will be presented here.
The content of this thesis is divided as follows. Chapter 2.2 presents the theory and the motivation of the Supersymmetry, and how it extends the Standard Model, in the so called Minimal Supersymmetric Standard Model. It is also presented in details the properties of the scenario considered in this thesis, and its phenomenology. The current limits on SUSY models are also presented. Chapter 3 describes briefly

the LHC accelerating complex and the most important experiments currently present at CERN. The ATLAS experiment is then described in more detail, focusing on each of its subdetectors. Chapter 4 instead focus on the Pixel Detector of ATLAS, the innermost part of the detector, and its performances during Run 2. Chapter 5 describes how the damage due to the high fluence of radiation impacts the pixel detector, and how the radiation damage has been implemented inside the simulation of the detector. The reconstruction and identification procedure of the physical objects that are used in the analysis are described in chapter 6. Efficiency for both data and simulations are presented. The details of the analysis using two leptons are presented in chapter 8, while chapter 9 shows the analysis done with 1 lepton and 1 track. Finally chapter 10 presents the conclusions.

2 Beyond The Standard Model: Supersymmetry

The Standard Model (SM) is the theoretical framework that describes the elementary particles and their interactions [6–8]. The SM is a gauge quantum field theory based on the group SU(3)× SU(2)×U(1). It has been developed during the 20$^{\text{th}}$ century and for decades has been tested and its predictions found in agreement with the experiments, up to an energy of around 1 TeV and, in some cases, with precision greater than 0.1 %. The last great success has been the discovery of the Higgs boson by the ATLAS and CMS experiments in 2012 [4, 5]. This discovery has been the highest success of the SM and a proof of internal consistency for the theory.
Despite all of these achievements the SM has still different problems unsolved. The SM does not provide any suitable candidate to the Dark Matter [9]. As we know now, the universe is composed by almost 25% of *"Dark"* matter [10], this seems to be a form of matter that is stable and neutral and that interacts gravitationaly [11] and (probably) weakly(see section 2.1.3). Similarly there is the problem of the Dark Energy, that make up almost 70 % of the universe, while it is not clear what is its nature. Other problems include the mass of the neutrinos [12], the CP violation and the asymmetry of matter anti-matter in the universe [13], the fermion mass hierarchy (why the fermions masses are spread over such a large spectrum), and many more. Moreover there is the problem that the SM doesn't include gravity among the described forces, and there is no clear indication of a unification of the other forces (section 2.1.2) [14]. All these hints point to the SM to be only an effective theory for low energies, while it breaks when extended to higher energies. It is possible to consider as a limit of validity the scale where the coupling are closer to a unification, the GUT scale ($\Lambda_{\text{GUT}} \approx 10^{16}$ GeV) or Planck ($\Lambda_{\text{Planck}} \approx 10^{19}$ GeV) scale, where the gravity effects can not be ignored anymore. However this introduces an additional problem: why these scales are so different from the electroweak scale ($\Lambda_{\text{EW}} \approx 10^{2}$ GeV) where the SM has been tested. This, called hierarchy problem (section 2.1.1)[15], affects the mass of the Higgs boson, which, without further extensions to the SM, diverges with the corrections received by the one-loop diagram contributions when considering higher and higher energy scales.

An extension is then due, and many theories have been trying to accomplish this. One of these, and perhaps the most interesting one, is the supersymmetry.

2.1 The limits of the Standard Model

In this section will be presented in more details the questions left unanswered by the SM, in particular those that can be easily solved by the Supersymmetry. A solution of these will be presented in section 2.2.

2.1.1 The Higgs mass and naturalness

The Higgs potential is introduced in the SM to explain the mass of the gauge bosons. The expected value of its mass is related to the vacuum expectation value (v) and the Higgs self coupling (λ).

$$m_H^2 = -2v^2\lambda \tag{1}$$

Where v is related to the Electro-Weak Symmetry Breaking scale, and in fact the ATLAS and CMS experiments have found the Higgs boson to have a mass of around 125 GeV, which is in agreement with the EW-scale.When adding corrections from one-loop, the mass gains terms from each particle it couples with, directly or indirectly, in particular the biggest contribution comes from the top quark, which has the highest mass and coupling with the Higgs (since, for fermions, this is proportional to the mass of the particle). These dominant corrections are coming from fermions and are,

$$\Delta m_H^2 = -\frac{|\lambda_f^2|}{8\pi^2}\Lambda_{\mathrm{UV}}^2 + ... \tag{2}$$

Where Λ_{UV} is the ultraviolet cut-off energy, the largest energy scale for which the standard model is valid.
As it can be seen, this contribution diverges quadratically with the energy scale, therefore when considering higher scales (like the Plank Scale $\Lambda_{Pl} \sim 10^{19}$ GeV) all contributions must cancel out in order to avoid that the correction exceed the physical value of the Higgs mass observed at the EW scale. This large difference in scale between the EW and the Planck is what is usually referred to as *hierarchy problem*.

In order for this cancellation to happen all the parameters must be tuned to a level around 1 part in 10^{30}. The precise choice by nature of these particular values of the theory is called *fine tuning*. The fact that these parameters have these exact values is not per-se a problem, but it is considered quite *unnatural*, and could be a hint to the presence of an underlying structure, where the new logic impose the values observed: in a *natural* theory, coupling constants are all of the same order of magnitude, and no fine tuning would be necessary [16].
It is worth noticing however that this is not a problem of internal consistency of the theory (the Standard Model): a very large fine tuning is only a problem of ***Naturalness***. Naturalness is a guiding principle that can be described as a sense of "aesthetic beauty" of the formulation of the theory, a warning signal for the presence of an underlying structure. It is possible to try to describe quantitatively naturalness by measuring how the EW-scale is sensible to variation in the fundamental parameters [17]. This is done taking the maximum of the logarithmic variations of the $M_Z(a_i)$ (the mass of the Z boson)as a function of the parameters a_i of the theory with respect of a_i, as shown in equation 3:

$$\Delta = \max \left| \frac{a_i \partial M_Z^2(a_i)}{M_Z^2 \partial a_i} \right|. \tag{3}$$

From this definition we get that a theory with $\Delta = 10(100)$ has a fine tuning no greater than 10 % (1%), and so on. It is worth noticing that the amount of fine tuning Δ can also be considered in a statistical way. It might be shown that Δ can be interpreted as the inverse of the probability that in the scenario considered appears a cancellation among terms that gives a Δ smaller or equals to the one observed. This means:

$$p - \text{value} \sim \Delta^{-1}. \tag{4}$$

Therefore for uncorrelated source of fine tuning, the probability is the product of each single term.
What can be considered enough for a natural theory is rather subjective, but nonetheless it can be an helpful guide to find new physics. Already in the past this principle has been found successful in discovering new physics, so it is fair to use it as a starting point for new theories and researches.

2.1.2 Grand Unification Theories

All the open questions of the SM hint at some more general theory that includes inside the SM itself. In many such theories the three fundamental forces of the SM appear after the breaking of some more general symmetry (for example SU(5)), this implies that at high enough energies (GUT energy, E_{GUT}) all the fundamental forces unite. If this is true then the relative coupling constants would be the same at the GUT energy. In fact all the constants receive a correction which depends on the energy considered. Extrapolating from the measurement done at the EW-scale is possible to evaluate how couplings change. In figure 1 a plot of the evolution of the interaction couplings of the SM is reported.

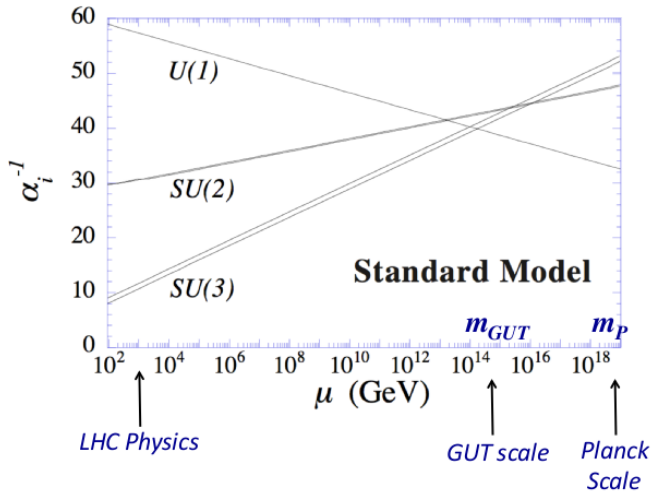

Figure 1: Evolution of the inverse of the coupling constants with the energy

As is visible, an unification of the couplings does not happen. The failure of the unification in the SM may be a strong hint that at some energy higher than the EW-scale some new physics must happen, some new theory where the three couplings evolve down to the EW-scale and match their experimental value.

2.1.3 Dark Matter

From precise cosmological measurements (from the Cosmic microwave background [10, 18]) it appears that ordinary matter accounts for only around 5% of the observable universe, while 23 % is Dark Matter. *Dark* because it is non-luminous and non-absorbing, while it is *Matter* because its cosmological state equation is the same as for the ordinary matter ($\omega = P/\rho = 0$). The other 72 % comes from Dark Energy ($\omega = P/\rho = -1$) and accounts for cosmic inflation. The evidence of Dark Matter comes also from the measurement of galaxies' rotational velocity and colliding galaxies [19].
The presence of Dark Matter is established, but it is not known what composes it. A very plausible scenario is that it is a stable particle, or at least with a lifetime longer than the age of the universe, massive and neutral [20]. In the SM there is no possible candidate to this particle, in fact the neutrinos, which are neutral stable and massive particles, they would not suffice to account for all the 25 % of Dark Matter. Neutrinos are always relativistic ($p/m >> 1$) and this would made them a candidate for the so called *hot* Dark Matter, opposed to *cold* Dark Matter, where $p/m << 1$. However hot Dark Matter is generally considered not to be a good solution (at least as the only component of Dark Matter) since it doesn't fit models of galaxies formation. Therefore an extension of the SM is needed in order to account for the Dark Matter.
Interesting candidates are the WIMPs, Weakly Interacting Massive Particles. These are interesting since they could explain the current density of Dark Matter. In fact it is possible to express the relative abundance (Ω_{DM}) in terms of the annihilation cross section (σ_{ann})[21, 22] of Dark Matter:

$$\Omega_{\mathrm{DM}} \approx \frac{6 \cdot 10^{-27} \mathrm{cm}^3\,\mathrm{s}^{-1}}{< \sigma_{ann} v >} \tag{5}$$

where $< \sigma_{ann} v >$ is the averaged cross section with the thermal velocity. Since $\Omega_{\mathrm{DM}} \approx 0.25$, it is possible to evaluate the cross section, obtaining a results similar to the one of an annihilation of a particle through Weak interaction. With a electroweak cross section it is needed a $\mathcal{O}(100)$ GeV Dark Matter candidate, and the higher the cross section, the higher the WIMP mass. Therefore, a WIMP is a very strong candidate.

2.1.4 Other Problems in the Standard Model

Besides the issues already presented, there are other problematic aspects in the SM, not necessarily connected to the Supersymmetry. Maybe the most important one is gravity. In none of the theoretical framework considered here there is a renormalisable quantum field theory of gravity. It is even worse, quantum field theory and general relativity are not compatible, since the first needs a flat space-time (CPT conservation) while from general relativity we know it is not true. At the energies of TeV, gravity is negligible since its coupling constant is many orders of magnitude smaller. But with increasing energy there is a point where gravitational contribution becomes significant, this energy is called the Planck scale ($\Lambda_{\mathrm{Pl}} \approx 10^{19}$ GeV). This energy corresponds to the mass of a particle with its Compton wavelength smaller than its Schwarzchild radius. Then, when approaching these energies, is impossible to not consider gravity, and every theory should deal with it. Different theorists have proposed many solutions, like String Theory [23] or Quantum Loop Gravity [24]. Experiments allowing to prove these theories are still out of reach for today possibilities.
Another important issue is the observed asymmetry between matter and anti matter in the universe, with the first being dominant over the second, with an observed asymmetry of

$$\eta = \frac{n_B - n_{\bar{B}}}{n_B + n_{\bar{B}}} \approx 10^{-10}. \tag{6}$$

Since in the primordial universe it is generally assumed an initial balance between matter and anti-matter, a CP-violating term is needed. In order to get the observed asymmetry it is also needed a barion number violation, and that interactions interact out of thermal equilibrium (known as Sakharov conditions). In the SM there is only one source of CP-violation, the CKM matrix, but it could not account for all the observed asymmetry. New sources of CP violation are then needed to explain this phenomenon.
Another open question is the neutrino masses. In the SM neutrinos are massless and since only left handed (right handed) neutrinos (anti neutrinos) interact, right handed (left handed) neutrinos (anti neutrinos) do not exist. Despite this, it is a well-established experimental fact that the neutrinos oscillate implying a nonzero neutrino mass and neutrino flavour mixing. Differences in masses have been measured but absolute values are still not known, even if these masses must be

smaller than 1 eV. This also implies that either the neutrino (anti neutrino) has a Dirac right handed (left handed) partner or the neutrino is a Majorana spinor. No evidence has been found yet. Either way, the Standard Model needs an extension to account for this.

2.2 Supersymmetry

Supersymmetry (SUSY) [25–31] is a theory that for every boson (fermion) in the SM associates a fermionic (bosonic) partner. The generator of these transformations is a fermionic operator Q

$$Q\,|\text{Boson}\rangle = |Fermion\rangle\,, \qquad Q\,|\text{Fermion}\rangle = |Boson\rangle\,, \tag{7}$$

$Q^\dagger$ is also a generator. Supersymmetry is a spacetime symmetry, therefore in order to have chiral fermions and parity-violating interactions the generators Q and $Q^\dagger$ must satisfy an algebra with the following form

$$\begin{aligned} \{Q, Q^\dagger\} &= P^\mu \\ \{Q, Q\} &= \{Q^\dagger, Q^\dagger\} = 0 \\ [P^\mu, Q] &= \left[P^\mu, Q^\dagger\right] = 0 \end{aligned} \tag{8}$$

where P^μ is the generator of spacetime translations. Indices are suppressed in this notation. The single particle states are the irreducible representation of the algebra, called supermultiplets. These contain both fermion and boson states, called superparteners of each other. From equation 8 it is possible to see that the mass operator P^2 commutes with both Q and $Q^\dagger$, therefore particles in the same irreducible supermultiplet have the same masses. Moreover the supersymmetry generators commute with the generators of gauge transformations, therefore superpartners have same electric charges, weak isospin and color degree of freedom. The number of fermionic and bosonic degree of freedom in a supermultiplet must be the same. This implies that supermultiplets are either formed by one Weyl fermion ($n_F = 2$) and two scalars ($n_B = 1$ each), called a *chiral* supermultiplet, or a massless spin-1 boson ($n_B = 2$ before symmetry breaking) and a massless spin-1/2 Weyl spinor ($n_F = 2$, spin-3/2 is not renormalisable), called a *gauge* supermultiplet. Eventually, spin-2 particles (Graviton-like) would have a spin-3/2 Weyl superpartner.
From these observations comes that it is not possible to complete a

supermultiplet with only SM particles, therefore, in order to have a correct supersymmetry, a totally new set of particles is needed.

2.2.1 Supersymmetry as a solution to the SM problems

One of the most important aspect that leads to consider Supersymmetry when extending the SM is the possibility to solve many of the shortcomings of the SM.

Hierarchy problem In supersymmetry for every fermion there is a scalar term. The corrections at one-loop to the Higgs mass for a scalar particle S with coupling $\lambda_S = |\lambda_f|^2$ are

$$\Delta m_H^2 = \frac{\lambda_S}{16\pi^2}\Lambda_{\mathrm{UV}}^2 + ... \tag{9}$$

where corrections going like a logarithm are not considered. Looking back at equation 2 it is possible to see that if every SM fermion has two complex scalars partners (as it has been shown before with supermultiplets), the quadratically divergent term will cancel out in a very natural way. Moreover, this cancellation persists not only for one-loop corrections but also to higher orders.
The terms that do not cancel out are

$$\Delta m_H^2 = \frac{\lambda}{16\pi^2}\left[m_f^2 \ln\left(\Lambda_{\mathrm{UV}}/m_f\right) - m_S^2 \ln\left(\Lambda_{\mathrm{UV}}/m_S\right)\right] \tag{10}$$

where λ is just to represent all the coupling constants. As we have seen in the previous section, in a supersymmetric theory, superpartners' masses are equal. Therefore there is an exact cancellation of every term. Unfortunately, this would imply that electrons and selectrons have the same masses, but a scalar electron has never been observed. For this reason supersymmetry has to be broken, causing Δm_H^2 to be nonzero. But, in order to avoid a fine tuning too unnatural, these corrections must not be much greater than the EW-scale. Using as M_{UV} the Planck scale, one obtain that in order to avoid an excessive fine tuning and still have a *natural* theory, at least the lightest supersymmetryc particles should be around 1 TeV. These define an energy scale at which the SM must be necessarily extended.
However it is important to remember that any bound based on naturalness depends on what level of fine-tuning is considered acceptable.

The before mentioned limit of 1 TeVcan be easily put at 10s of TeVby relaxing the request on fine-tuning. A more in depth discussion of what are the constraints on SUSY will be presented in sub-section 2.5

Dark Matter Supersymmetry allows having a new set of particles. As it will shown in the next section, the gauge bosons superpartners mix together to form mass eigenstates. In general it is not necessary that these states are stable, but with some request (as will be presented in sub section 2.3.2) it is possible that the lightest supersymmetric particle is stable, and in case it is neutral it will be an ideal WIMP candidate.

GUT A good hint that supersymmetry could work is the apparent unification of gauge couplings. In the equations for the running of gauge couplings, supersymmetry has more particles than SM, therefore it has different (and larger) coefficients that allows the unification. In figure 2 the evolution of the inverse of the couplings (α^{-1}) in the Minimal Supersymmetric Standard Model, MSSM, (solid lines) and SM (dashed lines) is compared. The agreement is not perfect, α_3 is smaller at intersection point, but it could be corrected by new particles near those energies.

2.3 Minimal Supersymmetric Standard Model

Supersymmetry is an attractive way to extend the SM, and the minimalistic approach is called the Minimal Supersymmetric Standard Model (MSSM) [32, 33]. Since it is not possible to construct a supersymmetric theory with only SM particles, there must be a new set of particles in order to complete the supermultiplets. It is called *minimal* since it introduces the minimal number of new particles necessary to build a supersymmetric theory.
The names for spin-0 superpartners are obtained by adding an *s* to the name, i.e. *selectron* or *stop*. The symbol of superpartners is a ˜ over the SM symbol. Standard Model fermions are part of chiral supermultiplets and since left-handed and right-handed quarks and leptons are separate two component Weyl fermions with different gauge transformation proprieties, each of them must have its own scalar partner, i.e. the (u_L, d_L) doublet corresponds to a supermultiplet $(u_L, d_L), (\tilde{u_L}, \tilde{d_L})$ while the u_R will have as superpartener $\tilde{u_R}$ (is important to note that

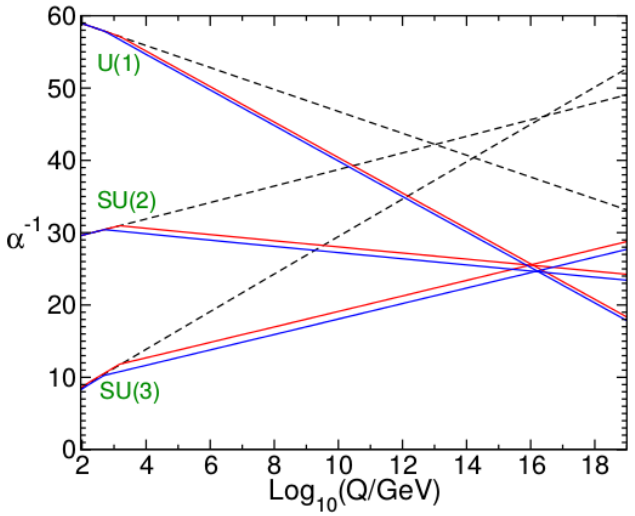

Figure 2: Running of the coupling constants (2-loop) in the MSSM (solid lines) and SM (dashed lines) with sparticle masses threshold of 500 GeV (blue line) and 1.5 TeV (red line). Figure from [32].

the $_L$ or $_R$ refers to the origin particle, not the superpartener).
Gauge bosons, on the other hand are represented in a gauge supermultiplet. Spin-1/2 superpartner names are obtained by adding an *-ino* at the end of the name, i.e. *photino* or *bino*. The electroweak gauge bosons superpartners are the bino and winos, from W^0, B^0, and $W^{\pm}$. After the electroweak symmetry breaking, the W^0 and B mixes to form the Z and γ, the corresponding gauginos are called zino ($\tilde{Z}$) and photino ($\tilde{\gamma}$). If supersymmetry was unbroken they would have the same masses of Z and γ.
An Higgs boson, since it is a spin 0 scalar, must be represented in a chiral multiplet with a spin 1/2 Weyl fermion. Actually in a supersymmetric theory there are two different Higgs multiplets. There are two reasons for why this must happens. First, with only one Higgs supermultiplets the electroweak gauge symmetry would suffer a gauge anomaly. In fact, in order to avoid those anomalies it is requested that $\mathrm{Tr}[T_3^2 Y] = \mathrm{Tr}[Y^3] = 0$, over all the left-handed Weyl fermionic degrees of freedom (where T_3 is the third componente of the weak isospin and Y the weak hypercharge, such that $Q_{\mathrm{EM}} = T_3 + Y$). This is indeed true in the SM, but in SUSY this is not true, because the Weyl fermion that partners with the Higgs in the supermultiplet must have a weak

hypercharge of either $Y = 1/2$ or $Y = -1/2$. In both cases traces will not be zero, however if there is a second multiplet with the opposite hypercharge, the contributions to the traces will cancel out.
The second reason is that in a supersymmetric theory up-type quark can receive mass only from a $Y = 1/2$ Higgs while down-type quarks receive mass from a $Y = -1/2$ Higgs, therefore two different Higgs are necessaries. These are noted as (H_u^+, H_u^0) for the u-type and (H_d^0, H_d^-) for the down-type, with the superpartners being: $(\tilde{H}_u^+, \tilde{H}_u^0)$ for the u-type and $(\tilde{H}_d^0, \tilde{H}_d^-)$ for the d-type.

In table 1 are summarised all the chiral supermultiplets, while in table 2 the gauge multiplets, classified according to their transformation properties under the Standard Model gauge group.

Names	Symbol	spin 0	spin 1/2	$SU(3)_C \times SU(2)_L \times U(1)_Y$
squark, quark	Q	$(\tilde{u_L}, \tilde{d_L})$	(u_L, d_L)	(**3**,**2**,1/6)
(×3 families)	$\bar{u}$	$\tilde{u}_R^*$	$u_R^\dagger$	($\bar{\mathbf{3}}$,**1**,-2/3)
	$\bar{d}$	$\tilde{d}_R^*$	$d_R^\dagger$	($\bar{\mathbf{3}}$,**1**,1/3)
sleptons, leptons	L	$(\tilde{\nu}, \tilde{e_L})$	(ν, e_L)	(**1**,**2**,-1/2)
(×3 families)	$\bar{e}$	$\tilde{e}_R^*$	$e_R^\dagger$	($\bar{\mathbf{1}}$,**1**,1)
Higgs, higgsino	H_u	(H_u^+, H_u^0)	$(\tilde{H_u^+}, \tilde{H_u^0})$	(**1**,**2**,1/2)
	H_d	(H_d^0, H_d^-)	$(\tilde{H_d^0}, \tilde{H_d^-})$	(**1**,**2**,-1/2)

Table 1: Summary of the chiral supermultiplets in the MSSM.

Names	spin 1/2	spin 1	$SU(3)_C \times SU(2)_L \times U(1)_Y$
gluino, gluon	$\tilde{g}$	g	(**8**,**1**,0)
wino, W	$\tilde{W^\pm}$,$\tilde{W^0}$	$W^\pm$, W^0	(**1**,**3**,0)
bino, B	$\tilde{B}$	B	(**1**,**1**,0)

Table 2: Summary of the gauge supermultiplets in the MSSM.

For each supermultiplet of leptons and quarks there are three families, that are possible to distinguish by defining an index i, for example $(\bar{e}_1, \bar{e}_2, \bar{e}_3,) = (\bar{e}, \bar{\mu}, \bar{\tau})$. The bar over the symbol is part of the name and doesn't indicate any conjugation.
It is worth noticing that the Higgs supermultiplet H_d has the same

quantum numbers as the L supermultiplet. We could, naively, suppose that the Higgs boson is actually the sneutrino and therefore having only one supermultiplet. This possibility has been investigated in the past but it would not work because of phenomenological problems with the neutrino masses and because it would alter the electroweak gauge symmetry. Therefore, all the superpartners of SM particles are totally new particles.

2.3.1 The superpotential and supersymmetric interactions

The most general Lagrangian is composed of a free term and an interaction term. The free term is composed of chiral and gauge supermultiplets, the interaction term is defined just by their gauge transformation proprieties and by a superpotential W, function of the complex scalar fields. In the MSSM framework W is

$$W_{\text{MSSM}} = \bar{u} y_u Q H_u - \bar{d} y_d Q H_d - \bar{e} y_e L H_d + \mu H_u H_d. \tag{11}$$

where the objects appearing here are chiral superfields corresponding to the chiral supermultiplets in Table 1, and y_i are the dimensionless Yukawa coupling parameters, here they are 3×3 matrices in the family space. Index over all the gauge and flavor degrees of freedom are suppressed. The μ term is the SUSY version of the Higgs mass.
The 3×3 matrices are often approximated with only the term with the top quark, bottom quark and tau lepton since they are the heaviest fermions and their coupling is much larger than the other. The interaction coming from these are represented in figure 3.

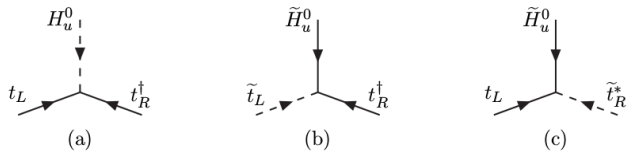

Figure 3: The top-quark Yukawa coupling (a) and its "supersymmetrizations" (b), (c), all of strength y_t

Figure 4 shows the coupling of squarks and sleptons with binos and winos. In figure 4 (b) is possible to see the decay $\tilde{q} \to \tilde{W} q'$. It is worth noticing that winos only couple to left-handed sparticles, also leptons (sleptons) and Higgs (higgsino) do not couple with gluino. A

complication arise from the fact that binos and winos are not mass eigenstates. These will be described better in section 2.3.3.

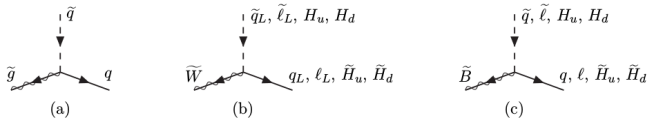

Figure 4: Couplings of the gluino, wino, and bino to MSSM (scalar, fermion) pairs

2.3.2 R-Parity

The superpotential presented in equation 11 contains only the terms that produce a phenomenology in agreement with present observations. In particular there are no terms that violate either the baryon number (B) or the total lepton number (L). One could add terms violating these numbers that are renormalisable and perfectly legit in a supersymmetry theory, for example

$$\begin{aligned} W_{\Delta \mathrm{L}=1} &= \frac{1}{2}\lambda L L \bar{e} + \lambda' L Q \bar{d} + \mu' L H_u \\ W_{\Delta \mathrm{B}=1} &= \frac{1}{2}\lambda'' \bar{u}\bar{d}\bar{d} \end{aligned} \tag{12}$$

Baryon number $+1/3$ is assigned to Q_i, while for $\bar{u}_i$ and $\bar{d}_i$ is $\mathrm{B} = -1/3$, and $\mathrm{B} = 0$ for all the other terms. The lepton numbers are $\mathrm{L} = +1$ for L_i and $\mathrm{L} = -1$ for $\bar{e}_i$. Therefore the first equation violates lepton number by one unit while the second equation violates baryon number of one unit. Such terms however are not observed and one would have to postulate the conservation of B and L "by hand", even if this is a step back from the SM, where such terms are not present and B and L are conserved. Moreover the violation of both these terms at the same time would cause disturbing problem, such as the proton decay, as shown in figure 5. This decay violates both L and B. From a simple dimensional analysis is possible to find the decay width,

$$\Gamma_{p \to e^+ + \pi^0} \propto |\lambda' \lambda|^2 \frac{m_p^5}{m_{\bar{d}}} \tag{13}$$

which for a squark mass of about 1 TeV and unit λ's gives a fraction of seconds of decay time, in obvious contrast with the experimental established lower limit of the proton decay of about 1.6×10^{36} seconds.

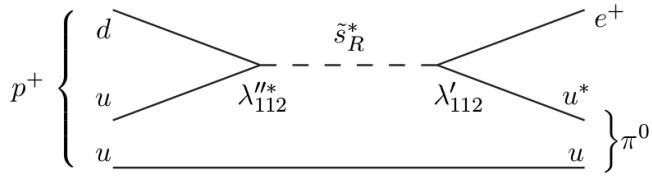

Figure 5: Squark mediated proton decay $p \to e^+ + \pi^0$

Therefore either λ's are really small or it must be postulated the B and L conservation. This second approach is rather unpleasant and seems a step back since in the SM B and L conservation is a consequence of the fact that there are no renormalisable terms that allow this. The way the MSSM deals with this problem is by introducing a new symmetry, the "R-parity". This is a multiplicatively conserved quantum number defined as:

$$P_R = (-1)^{3(\mathrm{B}-\mathrm{L})+2s} \tag{14}$$

where B and L are respectively baryon and lepton numbers and s is the spin of the particle. This number has the propriety that it is equal to $+1$ for every SM particle, while $P_R = -1$ for all the superpartners. Therefore, if R-parity is exactly conserved, the only allowed processes are the ones that conserve the P_R. This has many experimental consequences.

- The lightest supersymmetric particle (LSP) is stable. It has $P_R = -1$ and therefore can't decay in a SM particle and also can't decay in another SUSY particle. If the LSP is electrical neutral it interacts only weakly, and therefore could be the WIMP candidate for the Dark Matter.

- All the other sparticles besides the LSP must eventually decay into an odd number of LSP.

- Sparticles coming from SM particles (i.e. collider experiments) must be produced in even numbers.

Now the R-parity conservation has been *imposed* by well motivated phenomenological aspects, but from a theoretical point of view the MSSM would not suffer any inconsistency without this symmetry. It is therefore fair to ask if it should be imposed, since other discrete symmetries in the SM are broken, such as charge (C), parity (P), and time (T) violation. Fortunately, many mechanism that impose R-parity conservation in extensions of the MSSM have been proposed, for example in many GUT theories. Nonetheless there are also SUSY theories in which R-parity is violated, the so called RPV theories.

2.3.3 Supersymmetry breaking

As already said, SUSY is a broken symmetry, since otherwise we would have already observed SM selectrons with mass equal to the SM partner, and similarly for the other leptons, quarks, and gauge bosons. Therefore the theoretical model must have a Lagrangian density invariant under supersymmetry transformations, but a vacuum state that is not, allowing SUSY to be hidden at low energies, in the same way it happens with the electroweak breaking. In order to provide a solution to the hierarchy problem even in presence of supersymmetry breaking the quadratic divergent term must still vanish, this can happen if the relation between the dimensionless constants is still $\lambda_S = |\lambda_f|^2$, since the radiative correction is in the following form

$$\Delta m_H^2 = \frac{1}{2}(\lambda_S - |\lambda_f|^2)\Lambda_{UV}^2. \tag{15}$$

Therefore the MSSM Lagrangian must contain a *soft* breaking term, called $\mathcal{L}_{soft}$, that is a term that violates supersymmetry but contains only mass terms and coupling parameters with positive mass dimension, with m_{soft} the largest mass scale. It is possible to construct a soft breaking term by just introducing the following Lagrangian density

$$\begin{aligned}
\mathcal{L}_{soft}^{\text{MSSM}} = &-\frac{1}{2}\left(M_3\tilde{g}\tilde{g} + M_2\tilde{W}\tilde{W} + M_3\tilde{B}\tilde{B} + c.c\right) \\
&-\left(\tilde{\bar{u}}a_u\tilde{Q}H_u - \tilde{\bar{d}}a_d\tilde{Q}H_d - \tilde{\bar{e}}a_e\tilde{L}H_d + c.c.\right) \\
&-\tilde{Q}^\dagger m_Q^2\tilde{Q} - \tilde{L}^\dagger m_L^2\tilde{L} - \tilde{\bar{u}}m_{\bar{u}}^2\tilde{\bar{u}}^\dagger - \tilde{\bar{d}}m_{\bar{d}}^2\tilde{\bar{d}}^\dagger - \tilde{\bar{e}}m_{\bar{e}}^2\tilde{\bar{e}}^\dagger \\
&-m_{H_u}^2 H_u^* H_u - m_{H_d}^2 H_d^* H_d - (bH_uH_d + c.c.)
\end{aligned} \tag{16}$$

where M_1, M_2, and M_3 are bino, wino, and gluino mass terms. All the indices are suppressed. a_i are 3×3 matrices in the family space,

and are in a direct correspondence with the Yukawa coupling of the superpotential. $m_{\bar{e}}^2$ and the other similar terms are also 3×3 matrices in family space that can have complex entries, but must be hermitian. In the last line there are the Higgs sector mass terms that break supersymmetry. All of this parameters must be $\approx m_{soft}$. By including all of them it is found that there are 105 masses terms, phase and mixing angles in the MSSM. However many of these parameters are restricted by phenomenology. The MSSM soft SUSY breaking term is therefore obtained by assuming that all the parameters are real, besides the CKM matrix, this prevents new CP-violation sources. Moreover all the $m_{\tilde{e}}^2$ and the a_i are diagonal, in order to prevent flavour-changing neutral current processes. This is due to measured branching ratio of $\mu \to \gamma e$ and the oscillation of kaons $K^0 \leftrightarrow \bar{K}^0$. After all these requests, the MSSM is left with a total of 18 new parameters besides the usual SM gauge and Yukawa couplings, six parameters per family: left squark mass, right squark mass, left slepton mass, right slepton mass, and two mixing angles.

Following this approach supersymmetry breaking has been explicitly introduced and constraints on the parameters imposed by hand. It is possible to understand these patterns considering models in which supersymmetry is spontaneously broken in a *hidden sector* of particles that have very small couplings with the *visible sector*, composed of chiral supermultiplets of the MSSM (figure 6). SUSY breaking is communicated to the visible sector through some mediator, resulting in the MSSM soft term, that, if the mediating interactions are flavour-blind, will automatically obey the conditions that have been imposed by hand before. There are two main ideas about the origin of the mediating interaction:

- *Gravity mediated* (or *Planck-scale mediated*): in this scenario, the mediating interactions are part of a new physics arising at high energies (around Planck scale M_P) containing also gravity. If supersymmetry is broken in the hidden sector at an energy F, then the soft term will be

$$m_{soft} \approx \frac{F^2}{M_P} \tag{17}$$

  In order to have a visible sector around 1 TeV then the supersymmetry breaking energy should be $\approx 10^{10}$ GeV

- *Gauge-mediated*: The other possibility is that the mediating interactions are the ordinary SM gauge interactions. The messengers are new chiral supermultiplets with mass m_{mess}. The soft mass term is then obtained by

$$m_{soft} \approx \frac{F^2}{m_{mess}} \tag{18}$$

where F is still the energy of SUSY breaking. However, looking at this formula, if F and m_{mess} are similar, the mass of the mediator could be as low as 10^4 GeV. Having a low mass mediator also helps avoiding gravity contributions in flavour changing neutral currents.

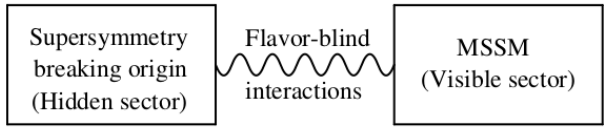

Figure 6: Schematic structure for supersymmetry breaking

2.3.4 The mass spectrum

After electroweak symmetry and supersymmetry breaking, interaction eigenstates are not necessarily also mass eigenstates. Sparticles with the same quantum numbers will mix. Here the results of the mixing of the superpartners are presented.

Electroweak symmetry breaking and Higgs sector The electroweak symmetry breaking in the MSSM is more complicated than in the SM because of the two complex $SU(2)_L$ doublets of Higgs bosons: (H_u^+, H_u^0) and (H_d^0, H_d^-). This accounts for eight real scalar degrees of freedom. After electroweak symmetry breaking three of them are the Nambu-Goldstone bosons (G^0 and $G^\pm$) and gives the longitudinal modes (and therefore masses) to the Z_0 and $W^\pm$ vector bosons. The remaining five degree of freedom mix to give five mass eigenstates with defined CP eigenvalue: two CP-even neutral scalars, h^0 and H^0, one CP-odd neutral scalar A^0, and a charge +1 scalar H^+ (plus its conjugate H^-). The lightest CP-even Higgs boson in the MSSM can be

identified as the SM Higgs boson observed by both ATLAS and CMS. The measured couplings, spin, and parity of the observed Higgs boson seems to agree with the SM prediction, this means that in a supersymmetric theory it must be $m_A >> m_Z$, implying a SM-like state, h_0, while the other bosons are around the same scale of m_A.

Neutralinos and Charginos Because of the electroweak breaking, higgsinos and gauginos mix together to give six mass eigenstates. Neutral higgsinos ($\tilde{H_u}^0$, $\tilde{H_d}^0$) and neutral gauginos ($\tilde{B}0$, $\tilde{W}^0$) mix to form mass eigenstates called neutralinos and labelled $\tilde{\chi}_i^0$ $(i = 1, 2, 3, 4)$ where the indices indicates the mass hierarchy, so that $m_{\tilde{\chi}_1^0} < m_{\tilde{\chi}_2^0} < m_{\tilde{\chi}_3^0} < m_{\tilde{\chi}_4^0}$. The charged higgsinos ($\tilde{H_u}^+$, $\tilde{H_d}^-$) and winos ($\tilde{W}^\pm$) mix and form two eigenstates called charginos and labelled $\tilde{\chi}^\pm$ with the same notation for the indices. These eigenstates are also collectively called **electroweakino**. The $\tilde{\chi}^0$ is usually assumed to be the LSP and it could be a WIMP candidate for the Dark Matter. In other models the LSP is the gravitino.
In the eigenstates basis $\psi^0 = (\tilde{B}, \tilde{W}^0, \tilde{H}_d^0, \tilde{H}_u^0)$ the neutralino mass term in the Lagrangian is

$$\mathcal{L} = -\frac{1}{2}(\psi^0)^T \boldsymbol{M}_{\tilde{\chi}^0} \psi^0 + c.c \tag{19}$$

where $\boldsymbol{M}_{\tilde{\chi}^0}$ is a matrix, of the form

$$\boldsymbol{M}_{\tilde{\chi}^0} = \begin{pmatrix} M_1 & 0 & -c_\beta s_W m_Z & s_\beta s_W m_Z \\ 0 & M_2 & c_\beta c_W m_Z & -s_\beta c_W m_Z \\ -c_\beta s_W m_Z & c_\beta c_W m_Z & 0 & -\mu \\ s_\beta s_W m_Z & -s_\beta c_W m_Z & -\mu & 0 \end{pmatrix} \tag{20}$$

where $c_\beta = \cos(\beta)$, $s_\beta = \sin(\beta)$ and $s_W = \sin(\theta_W)$. M_1 and M_2 comes from the MSSM soft Lagrangian term, μ is the supersymmetric higgsino mass term, and m_Z is the Z mass term. $\boldsymbol{M}_{\tilde{\chi}^0}$ can be diagonalised by a unitary matrix $\boldsymbol{N}$. In general the M_1, M_2, and μ can have arbitrary complex phases, but is possible to redefine them in order to have M_1 and M_2 real and positive. If μ is not real there could be CP-violating terms at low energies not observed, and electric dipole moments for electrons and neutrons. Therefore, it is usual, even if not necessary from a strict theoretical point of view, to set μ real.

Charginos have similar proprieties, in the gauge eigenstate basis $\psi^{\pm} = (\tilde{W}^+, \tilde{H}_u^+, \tilde{W}^-, \tilde{H}_d^-)$ the Lagrangian mass term is

$$\mathcal{L} = -\frac{1}{2}(\psi^{\pm})^T \boldsymbol{M}_{\tilde{\chi}^{\pm}} \psi^{\pm} + c.c \tag{21}$$

where $\boldsymbol{M}_{\tilde{\chi}^{\pm}}$ is a 2×2 block matrix of the form

$$\boldsymbol{M}_{\tilde{\chi}^{\pm}} = \begin{pmatrix} 0 & \boldsymbol{X}^T \\ \boldsymbol{X} & 0 \end{pmatrix} \tag{22}$$

with

$$\boldsymbol{X} = \begin{pmatrix} M_2 & \sqrt{2} s_\beta m_W \\ \sqrt{2} c_\beta m_W & \mu \end{pmatrix} \tag{23}$$

with the same convention on the symbol as in the $\boldsymbol{M}_{\tilde{\chi}^0}$ but with m_W as the mass of the $W^{\pm}$. Mass eigenstates are then obtained by rotating this matrix with two 2×2 unitary matrix, $\boldsymbol{U}$ and $\boldsymbol{V}$.
In general the explicit forms of the mass terms are quite complicated mixture of gauginos and higgsinos (even at tree level), but there are very interesting limits where these relations simplify. For example, if $m_Z << |\mu \pm M_1|, |\mu \pm M_2|$ and also $\mu \ll M_2 < M_1$ then the electroweak breaking effects can be seen as small perturbation, giving *bino-like* $\tilde{\chi}_1^0 \approx \tilde{B}$ and *wino-like* $\tilde{\chi}_2^0 \approx \tilde{W}^0$ neutralinos, and *higgsino-like* $\tilde{\chi}_3^0, \tilde{\chi}_4^0 \approx (H_u \pm H_d)/\sqrt{2}$. In the same limit for the charginos there are *wino-like* $\tilde{\chi}_1^{\pm} \approx \tilde{W}^{\pm}$ and *higgsino-like* $\tilde{\chi}_2^+ \approx \tilde{H}_{u,d}^{\pm}$. In the case in which $\mu \ll M_2, M_1$ the $\tilde{\chi}_2^0$,$\tilde{\chi}_1^0$, and $\tilde{\chi}_1^{\pm}$ would form a quasi degenerate triplet of higgsinos, with the other neutralinos and chargino almost purely made of bino and wino, at higher masses.

Gluinos Gluinos are described by a color octet fermion, therefore, even if R-parity is violated, it cannot mix with other MSSM particles. This is an unique feature between all of the MSSM sparticles. In many gauge mediated supersymmetry breaking models, the gluino mass parameter M_3 (see equation 16) is related to the bino and wino mass parameters M_1 and M_2 by the following formula:

$$M_3 = \frac{\alpha_s}{\alpha} \sin^2 \theta_W M_2 = \frac{3}{5} \frac{\alpha_s}{\alpha} \cos^2 \theta_W M_1 \tag{24}$$

These equations hold up to small two-loop corrections and in any energy scale. Therefore this implies that near the 1 TeV scale the following relation between the masses apply:

$$M_3 : M_2 : M_1 \approx 6 : 2 : 1 \tag{25}$$

A more precise estimates of the ratios in eq. 25 must take into account the fact that M_3 is a running parameter and has an implicit dependence on the energy scale (equation 24 hold its form). The correction terms can be rather large, since gluinos interacts strongly and can couple to all the squark-quark pairs.

Sleptons and Squarks In the most general scenario, with completely arbitrary soft terms, scalars with the same color, electric charge, and R-parity can mix with each other. Therefore the mass eigenstates of squarks and sleptons can be obtained by diagonalizing three 6×6 matrices for up-type squarks, down-type quarks and charged sleptons, and one 3×3 matrix for sneutrinos. But if the hypothesis of flavor-blind soft breaking holds, then most of these terms are null or very small. Because of the large Yukawa (y_t, y_b, y_τ) and soft (a_t, a_b, a_τ) couplings, third generation squarks and sleptons can have very different masses compared to the first two families. First and second generation sleptons and squarks end up in fourteen nearly degenerate states (seven for each family), since their Yukawa and soft couplings are negligible. This also helps the suppression of large contributions to flavor-changing processes.
The top squarks masses are a particular case, since there are several non-negligible contributions. First, as for first and second generation squark, there are the squared masses terms: $\tilde{t}_R^* \tilde{t}_R$ and $\tilde{t}_L^* \tilde{t}_L$, then there are terms proportional to the top quark mass squared, m_t^2, for both the left-handed and right-handed contribution. These last terms come from the superpotential (see equation 11) terms $y_t^2 H_u^{0*} H_u^0 \tilde{t}_{L/R}^* \tilde{t}_{L/R}$, when H^0 is replaced by its vacuum expectation value (v.e.v, v). Another terms comes from the superpotential term $-\mu^* y_t \tilde{\bar{t}} \tilde{t} H_d^{0*}$ that when the Higgs field is replaced by its vev it becomes $-\mu^* v y_t \cos\beta \tilde{t^*}_R \tilde{t}_L$. Finally there are contribution from the soft terms $a_t \tilde{\bar{t}} \tilde{Q}_3 H_u^0$, that become $a_t v \sin\beta \tilde{t}_L \tilde{t}_R^*$. In the gauge eigenstates basis then we have to diagonalise the following term

$$\mathcal{L}_{\text{stop masses}} = -\begin{pmatrix}\tilde{t^*}_L & \tilde{t^*}_R\end{pmatrix} \boldsymbol{m}^2_{\tilde{t}} \begin{pmatrix}\tilde{t^*}_L \\ \tilde{t^*}_R\end{pmatrix} \tag{26}$$

where

$$\boldsymbol{m}^2_{\tilde{t}} = \begin{pmatrix} m^2_{Q_3} + m^2_t + \Delta_{\tilde{u}_L} & v(a^*_t \sin\beta - \mu y_t \cos\beta) \\ v(a_t \sin\beta - \mu^* y_t \cos\beta) & m^2_{\tilde{u}_3} + m^2_t + \Delta_{\tilde{u}_R} \end{pmatrix} \tag{27}$$

with $\Delta_{\tilde{u}_L} = (\frac{1}{2} - \frac{2}{3}\sin^2\theta_W)\cos(2\beta)m^2_Z$ and $\Delta_{\tilde{u}_R} = (\frac{2}{3}\sin^2\theta_W)\cos(2\beta)m^2_Z$ being an *hyperfine* splitting produced by electroweak symmetry breaking. Once the matrix has been diagonalized it is possible to define the two mass eigenstates are called $\tilde{t}_1$ and $\tilde{t}_2$, such as $m_{\tilde{t}_2} > m_{\tilde{t}_1}$, by solving the following equation

$$\begin{pmatrix}\tilde{t}_1 \\ \tilde{t}_2\end{pmatrix} = \begin{pmatrix} c_{\tilde{t}} & -s_{\tilde{t}}* \\ s_{\tilde{t}} & c_{\tilde{t}} \end{pmatrix} \begin{pmatrix}\tilde{t}_\text{L} \\ \tilde{t}_\text{R}\end{pmatrix} \tag{28}$$

with $|c_{\tilde{t}}|^2 + |s_{\tilde{t}}|^2 = 1$, and if these parameters are real then $c_{\tilde{t}}$ and $s_{\tilde{t}}$ are the cosine and sine of the stop mixing. Since the off-diagonal terms in equation 27 are typically not negligible, this induce a significant mixing which would cause $c_{\tilde{t}} \sim 0$ and $s_{\tilde{t}} \sim 1$ and therefore always reduce the lighter top-squark mass eigenvalue. For this reason, the $\tilde{t}_1$ is often considered the lightest squark as it is mainly composed of $\tilde{t}_\text{R}$. For bottom squark and tau slepton a very similar analysis can be done. For these particles the mixing depend strongly on $\tan\beta$, if this quantity is smaller than 10, sbottom and stau will be almost degenerate with their first and second generation counterpart. However, even in this case, the mass of $\tilde{b}_\text{L}$ could be significantly less than the masses of $\tilde{d}_L$ and $\tilde{s}_L$. If $\tan\beta$ is quite large, because of the Yukawa and soft terms coupling being non-negligible, the mixing can be rather large, with mass eigenstates, called $\tilde{b}_1$ and $\tilde{\tau}_1$, being significantly lighter than their first and second generation counterparts.

2.4 Electroweakinos

The higgsinos mass is controlled by the μ parameter, as seen in 2.3.4, and at the same time it enters at tree-level the Higgs mass. This means that in order to have the electroweak symmetry breaking at the correct mass scale, the mass of the higgsinos must be around the same scale, and therefore within reach of LHC. It is then important

to have a closer look at how these sparticles are produced, what are their cross sections, and how they decay.

2.4.1 Production

In order to produce electroweakinos there are two different ways. The first is to produce electroweakinos through the production of heavier sparticles (stop, sbottom, or gluinos) that then decay into neutralinos and charginos. The advantage of this kind of production is that the cross section are higher (when considering squarks and neutralinos of the same mass) and that there are many sparticles that decays into electroweakinos, giving de facto a multiplying factor. However the downside is that in order to study these production mechanisms the information on the whole mass spectra of the supersymmetric sparticles is needed. Alternatively, it is possible to consider direct pair production of electroweakinos. The obvious downside is that the cross sections are much lower than the ones for, as an example, a stop. However it is then possible to study electroweakino without having to rely on the whole mass spectrum.
Figure 7 shows the possible (leading order) Feynman diagrams at an hadron collider for direct electroweak production of sparticles from quark-antiquark annihilation. It is possible to see contributions from electroweak vector bosons in the s-channel, and also t-channel squark-exchange contributions, even if these are of lesser importance in most models. Figure 8 compares direct electroweak production cross section at LHC with the gluino and squark cross section. The right side Y axis also shows the number of expected events in 300 fb^{-1}. As it is possible to see, the cross section for electroweak production are several orders of magnitude smaller.
These are calculated at the next-to-leading order, with the resummation of soft-gluon emission evaluated at NLO+NLL. The theoretical uncertainties are evaluated from differences in cross section prediction with different Parton Density Function (PDF) sets, factorisation, and renormalisation scale.

2.4.2 Decay

Assuming that R-parity is conserved, the possible decays of neutralinos and charginos are presented here. These sparticles contains in

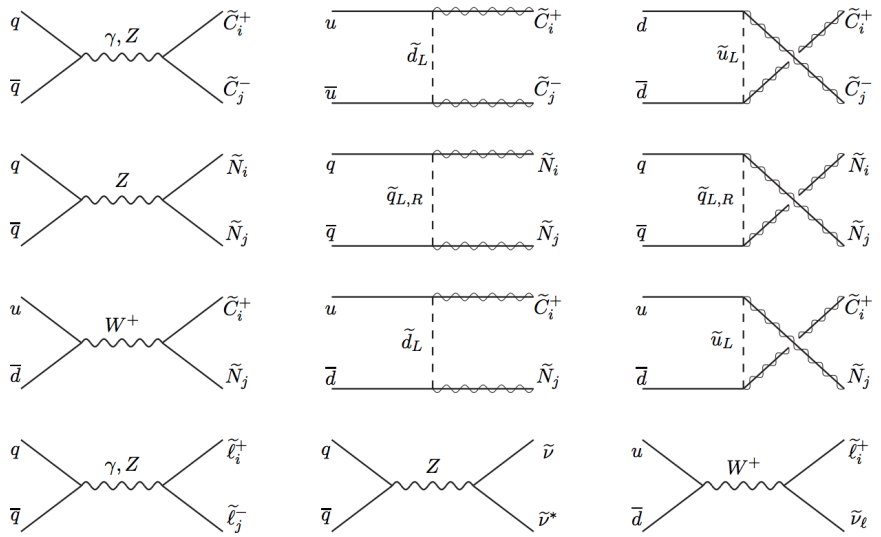

Figure 7: Feynman diagrams for electroweak production at hadron colliders from quark-antiquark annihilation.

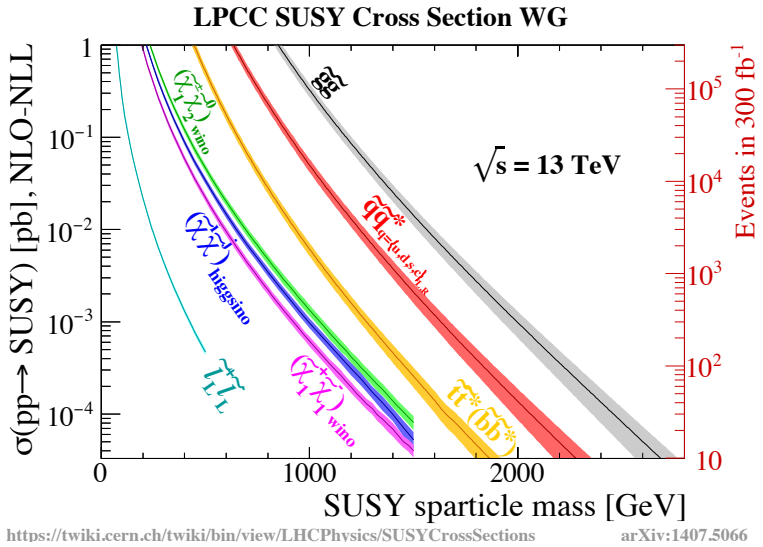

Figure 8: Cross sections for selected SUSY processes. Right side Y axis also shows the number of expected events in 300 fb^{-1}

some degree a mixture of $\tilde{B}$, $\tilde{W}^{\pm}$, and $\tilde{W}^0$, therefore the strength of the weak interaction of $\tilde{\chi}^0$ and $\tilde{\chi}^{\pm}$ to scalar and fermions is given from

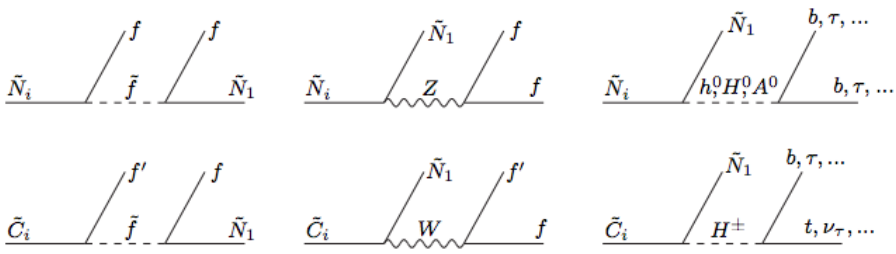

Figure 9: Allowed decays of neutralino ($\tilde{N}$) and chargino ($\tilde{C}$) in the MSSM.

the inherited coupling of the electroweak gauginos. Depending on the mass spectra of the supersymmetric sparticles, different modes of decay are viable in many final states. If the mass difference between the neutralino or chargino and the ligther electroweakinos is larger than the SM bosons, then the neutralino (chargino) will go through a two-body decay. A two body decay can also happens if the sleptons are light enough, where the electroweakinos decays into a lepton and its superpartner. Equation 29 and 30 summarize the possible two body decays in MSSM:

$$\tilde{\chi}^0{}_i \to Z\tilde{\chi}^0{}_j, \quad W\tilde{\chi}^\pm{}_j, \quad h^0\tilde{\chi}^0{}_j, \quad \ell\tilde{\ell}, \quad \nu\tilde{\nu} \tag{29}$$

$$\tilde{\chi}^\pm{}_i \to W\tilde{\chi}^0{}_j, \quad Z\tilde{\chi}^\pm{}_j, \quad h^0\tilde{\chi}^\pm{}_j, \quad \ell\tilde{\nu}, \quad \nu\tilde{\ell} \tag{30}$$

where for the mass indexes is true that $i > j$, and ℓ ($\tilde{\ell}$) is a generic lepton (slepton) with its corresponding neutrino (sneutrino) ν ($\tilde{\nu}$).
Depending on the difference in mass between the i and j electroweakino some of the decay mode might be suppressed, in this case the three-body decays are open:

$$\tilde{\chi}^0{}_i \to ff\tilde{\chi}^0{}_j, \quad \tilde{\chi}^0{}_i \to ff'\tilde{\chi}^\pm{}_j, \quad \tilde{\chi}^\pm{}_i \to ff'\tilde{\chi}^0{}_j, \quad \text{and} \quad \tilde{\chi}^\pm{}_2 \to ff\tilde{\chi}^\pm{}_1, \tag{31}$$

where f and f' are general fermions (leptons or quark) and their partner in the $SU(2)_L$ multiplet. In this case the decays actually proceed through the same gauge bosons or slepton as in the two-body decay, but here they are off-shell.
Decays with leptons in the final states, such as $\tilde{\chi}_1^\pm \to \ell^\pm\nu\tilde{\chi}_1^0$ or $\tilde{\chi}_2^0 \to \ell^+\ell^-\tilde{\chi}_1^0$, are among the most important at colliders, since they

give a very clear signature. However in some models the large mixing with staus mean that the branching ratios of neutralino and chargino in staus is dominant.

2.4.3 Compressed spectra

Most of the analysis at colliders that looks into electroweak production targets scenarios with large mass splitting between the two electroweakinos [34]. There is therefore a "blind spot" in the region where this difference is rather small. This is due not only to strategy optimization, but to the intrinsic difficulty of studying this region. However this exact blind spot correspond to the spectrum that a naturalness driven supersymmetry would generate [35, 36]. In this scenario the higgsino is light, while wino and bino are much heavier. As it will be shown here, in this scenario the difference in mass between the $\tilde{\chi}_2^0$ and $\tilde{\chi}_1^0$ is of the order of $1-50$ GeV and the main decay is through three-body decay. As already said the clearest decay is with leptons in the final state (especially at an hadron collider), however in this case these leptons have very low momentum and their identification is challenging. Nonetheless it is a very interesting scenario.
In order to have the scenario presented we consider an higgsino multiplet which is much lighter that the other electroweakinos. To have this it must be true that:

$$\mu \ll M_1, M_2, \tag{32}$$

with μ the higgsino mass parameter and M_1 and M_2 the wino and bino masses. We suppose also that all the other superpartners (gluinos, squarks, and sleptons) are much higher in mass and effectively decoupled. Once the electroweak symmetry is broken, the mixing of higgsinos, bino, and wino gives the mass eigenstates. In this scenario there is a triplet of states ($\tilde{\chi}_1^{\pm}$, $\tilde{\chi}_1^0$, $\tilde{\chi}_2^0$) with a similar mass, and mainly higgsino-like, while the $\tilde{\chi}_2^{\pm}$ and $\tilde{\chi}_3^0$ and $\tilde{\chi}_4^0$ are heavier and around the mass of M_1 and M_2. It is possible to distinguish different cases depending on the relation between the mass parameters in eq. 32.

$M_1 \gg M_2 > |\mu|$ Consider equation 20. In this case is possible to remove the heavy bino component. When $m_W \ll M_2 \mp \mu$ the splitting

between the lightest states are:

$$\left|m_{\tilde{\chi}_1^\pm}\right| - \left|m_{\tilde{\chi}_1^0}\right| \approx \frac{m_W^2\,(1 \mp s_{2\beta})}{2\,(M_2 + |\mu|)} \tag{33}$$

$$\left|m_{\tilde{\chi}_2^0}\right| - \left|m_{\tilde{\chi}_1^\pm}\right| \approx \frac{m_W^2\,(1 \pm s_{2\beta})}{2\,(M_2 - |\mu|)} \tag{34}$$

$$\left|m_{\tilde{\chi}_2^0}\right| - \left|m_{\tilde{\chi}_1^0}\right| \approx \frac{m_W^2\,(\pm|\mu| s_{2\beta} + M_2)}{(M_2^2 - |\mu|^2)} \tag{35}$$

where $s_{2\beta} = \sin(2\beta)$ and $\pm$ depends on the sign of μ. From equation 33, 34 and 35 is possible to see that the difference in mass can be easily of the order of few GeV.

$M_2 \gg M_1 > \mu$ In this new case it is instead possible to remove the heavy wino component. Depending on the sign of μ:

$$\left|m_{\tilde{\chi}_1^\pm}\right| - \left|m_{\tilde{\chi}_1^0}\right| \approx \frac{m_W^2 t_{\theta W}^2\,(1 \pm s_{2\beta})}{2\,(M_1 - |\mu|)} \tag{36}$$

$$\left|m_{\tilde{\chi}_2^0}\right| - \left|m_{\tilde{\chi}_1^\pm}\right| \approx \frac{m_W^2 t_{\theta W}^2\,(1 \mp s_{2\beta})}{2\,(M_1 + |\mu|)} \tag{37}$$

$$\left|m_{\tilde{\chi}_2^0}\right| - \left|m_{\tilde{\chi}_1^0}\right| \approx \frac{m_W^2 t_{\theta W}^2\,(\pm|\mu| s_{2\beta} + M_1)}{(M_1^2 - |\mu|^2)} \tag{38}$$

where $t_{\theta W} = \tan(\theta_W) \approx 0.5$. In this case the mass splitting is smaller because the mixing of a (heavy) bino and the Higgsino is smaller than the mixing between (heavy) wino and Higgsino, as in the previous case.

Another interesting case happens when the $\tilde{\chi}_1^0$ is a pure higgsino, and so M_1 and M_2 are completely. decoupled. In this case the difference in mass between $\tilde{\chi}_2^0$ and $\tilde{\chi}_1^0$ vanish, but the one between $\tilde{\chi}_1^\pm$ and $\tilde{\chi}_1^0$ still remains due to radiative corrections [37]. However here the phase space of the decay can be so restricted that the sparticles will not decay promptly but will have an half life ($c\tau$) determined from almost only the mass splitting. Considering only the decay of the $\tilde{\chi}_1^\pm$

in quarks ($\tilde{\chi}_1^{\pm} \to \pi\tilde{\chi}_1^0$), it is possible to obtain:

$$c\tau[\text{mm}] \approx 7 \times \left[\left(\frac{\Delta m\left(\tilde{\chi}_1^{\pm}, \tilde{\chi}_1^0\right)}{340 \ \ \text{MeV}} \right) \sqrt{1 - \frac{m_\pi^2}{\Delta m\left(\tilde{\chi}_1^{\pm}, \tilde{\chi}_1^0\right)^2}} \right]^{-1} . \quad (39)$$

Ranges of the traveled space can varies from few mm to several cm, corresponding to lifetimes of the order of fraction of ns. In this case the mass splitting is a function of the mass, and from 255 MeVfor $\mu = 100$ GeV it increase to 355 MeVfor asymptotically higher masses [38].

2.4.4 Lepton Invariant Mass Distribution

As presented before, in case of compressed mass spectra, the three-body decay is favorite, and the decay ${\tilde{\chi}^0}_i \to \ell\ell{\tilde{\chi}^0}_j$ is the most important because of the clear signature. In addition, the branching ratio into leptons and decay distributions are heavily affected by the underlying parameters of the supersymmetry model. Therefore an in depth studies of these distribution can bring many information on the supersymmetric parameters of the theory. In particular one important distribution is the invariant mass of the two leptons from the decay of the ${\tilde{\chi}^0}_i$.

It is possible to evaluate the invariant mass distribution analytically [39, 40]. In order to do so let's consider the decay ${\tilde{\chi}^0}_B \to f\bar{f}{\tilde{\chi}^0}_A$ for a general fermion f, and consider also negligible the left-right mixing of $\tilde{f}$, and the mass of f. The squared amplitude $|M|^2$ (spin averaged), considering the two channels: Z^0 and $\tilde{f}_{L,R}$ is

$$\begin{aligned} |M|^2 =& 2\left(A_{LL}^2 + A_{RR}^2\right)(1-y)\left(y - r_{\tilde{\chi}_B}^2\right) \\ &+ 2\left(A_{LR}^2 + A_{RL}^2\right)(1-x)\left(x - r_{\tilde{\chi}_B}^2\right) \\ &- 4\left(A_{LL}A_{RL} + A_{RR}A_{LR}\right) r_{\tilde{\chi}_B} z \end{aligned} \quad (40)$$

with the $A_{LL,RL,RR,LR}$ being substitutes for:

$$A_{LL} = \frac{1}{2} g_Z^2 \frac{z^{\tilde{\chi}^0}_{BA} z^f_L}{z - r_Z^2} - \sum_X \frac{1}{2} g_2^2 \frac{a^f_{AX} a^f_{BX}}{y - r^2_{\tilde{f}X}} \tag{41}$$

$$A_{RL} = - A_{LL}(y \leftrightarrow x) \tag{42}$$

$$A_{LR} = \frac{1}{2} g_Z^2 \frac{z^{\tilde{\chi}^0}_{BA} z^f_R}{z - r_Z^2} + \sum_X \frac{1}{2} g_2^2 \frac{b^f_{AX} b^f_{BX}}{x - r^2_{\tilde{f}X}} \tag{43}$$

$$A_{RR} = - A_{LR}(y \leftrightarrow x) \tag{44}$$

where $z^f_L = T_{3fL} - Q_f s^2_W$, $z^f_R = -Q_f s^2_W$ with $s^2_W = \sin\theta^2_W$ are the coupling constant of the Z to the left-right fermions involved. The $\tilde{\chi}^0$ couples to the Z in the form of $N_{B3}N_{A3} - N_{B4}N_{A4}$, with $B(A)$ indicating the parent(daughter) particle and 3(4) the higgsino component. Instead x, y, z parametrize the decay phase space and are defined as:

$$x = (\bar{p} + q)^2 / m^2_{\tilde{\chi}^0{}_A}, \quad y = (\bar{p} + \bar{q})^2 / m^2_{\tilde{\chi}^0{}_A}, \quad z = (q + \bar{q})^2 / m^2_{\tilde{\chi}^0{}_A} \tag{45}$$

with the relation between them: $x + y + z = 1 + m_{\tilde{\chi}^0{}^2_B} / m_{\tilde{\chi}^0{}^2_A}$. It is also helpful to add the following ratios between masses

$$r_{\tilde{\chi}^0{}_B} = m_{\tilde{\chi}^0{}_B} / m_{\tilde{\chi}^0{}_A}, \quad r_Z = m_Z / m_{\tilde{\chi}^0{}_A}, \quad r_{\tilde{f}_X} = m_{\tilde{f}_X} / m_{\tilde{\chi}^0{}_A}. \tag{46}$$

Then the partial decay width is given by

$$\frac{d\Gamma}{dxdy}(\tilde{\chi}^0{}_A \to \tilde{\chi}^0{}_B \bar{f} f) = \frac{N_C}{256\pi^3} m_{\tilde{\chi}^0{}_A} |M|^2(x, y, z) \tag{47}$$

with N_C the number of color of f. This might seem a complicated formula, but it has interesting features. An important one is that the ratio $r_{\tilde{\chi}^0{}_B} = m_{\tilde{\chi}^0{}_B} / m_{\tilde{\chi}^0{}_A}$ enters the final results and it depends on the relative sign in the mass parameter between the two neutralinos. This will end up giving different results for different scenarios. The presence of a negative mass parameter doesn't mean tachyons, the actual mass is the absolute value, but the relative sign does matter. This sign comes from the requirement of having neutralinos with real mixing angles in the matrices.

In order to get from equation 47 the invariant mass distribution, and since z is the ratio of the squared masses, we must integrate over all possible y. Changing base of eq. 47 in $m = |q + \bar{q}|$ we get

$$\frac{\mathrm{d}\Gamma}{2m\mathrm{d}m} \propto \frac{\sqrt{m^4 - m^2(m^2_{\tilde{\chi}^0_1} + m^2_{\tilde{\chi}^0{}_A}) + (m^2_{\tilde{\chi}^0{}_A} - m^2_{\tilde{\chi}^0_1})^2}}{(m^2 - m_Z^2)^2} + \\ \left[-2m^4 + m^2(m^2_{\tilde{\chi}^0_1} \pm 6 m_{\tilde{\chi}^0_1} m_{\tilde{\chi}^0{}_A} + m^2_{\tilde{\chi}^0{}_A}) + \right. \\ \left. + (m^2_{\tilde{\chi}^0_1} - m^2_{\tilde{\chi}^0{}_A})^2\right] \tag{48}$$

where the $\pm$ depends on the relative sign of the mass parameters of the neutralinos. Figure 10 shows the analytic function (dashed lines) compared with simulations (solid lines) for different assumption on the mass sign: $m_{\tilde{\chi}^0_2} \times m_{\tilde{\chi}^0_1}$ is negative for Higgsino ($\tilde{H}$, blue) while it can be both positive and negative for the Wino-Bino case ($\tilde{W}/\tilde{B}$, red), meaning $\tilde{\chi}^0_2$ is Wino and $\tilde{\chi}^0_1$ is bino, depending on the relative sign of the mass eigenstates of M_1 and M_2. The plot shows the case with positive sign for the Wino-Bino. One interesting feature that can be learned from this plot is that the distribution has a clear cut off at the value of the difference in mass between the two neutralinos. Moreover, if the signal is discovered, the shape of the observed distribution will help in define what is the right composition of the neutralinos.

2.5 Constraints on SUSY

The experimental world of SUSY is vast and different. Researches include direct production of sparticles, like at collider experiments, or indirect detection, like with the recoil of nucleon in experiments like Dark Side [41]. Supersymmetry at the moment of writing this thesis has not yet been found. Nonetheless constraints have been put on the mass and parameters that supersymmetry have that come from different experimental observations.

2.5.1 Constraints from naturalness

One of the reasons to introduce SUSY is to give a "natural" solution to the fine-tuning problem that the SM has. It comes from this that any SUSY scenario must have a low fine tuning, otherwise it would fail for the same reason it was introduced in the first place. From this it is then possible to put limits on the sparticles masses, by computing the fine tuning and requiring this to be small [17, 42].

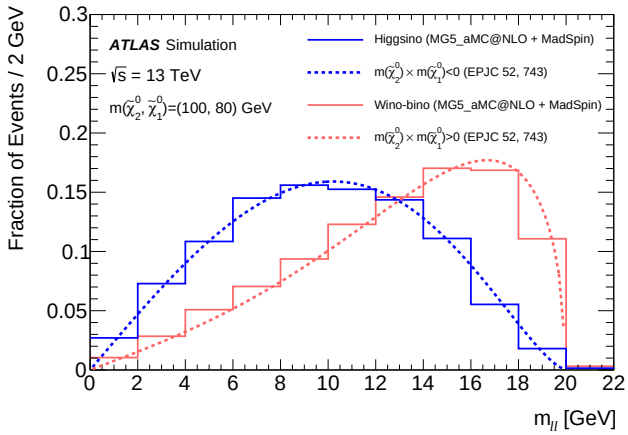

Figure 10: Dilepton invariant mass ($m_{\ell\ell}$) for two different assumptions of the signed mass of the neutralinos. The results from simulation (solid) are compared with the analytic calculation of the expected lineshape (dashed), where the product of the signed mass eigenvalues ($m_{\tilde{\chi}_2^0} \times m_{\tilde{\chi}_1^0}$) is negative for Higgsino ($\tilde{H}$) and positive for Wino-Bino ($\tilde{W}/\tilde{B}$) scenarios.

An equation for fine tuning was presented in eq. 3. However one important caveat that must be considered is that the derivation in eq. 3 should be done with respect of the initial parameters of the theory, evaluated at high energy scales (Λ_{GUT} as an example), instead of the physical masses at the low energies, such as the electroweak scale. The list of parameters depends on how the theory is build. For example, if the gaugino's masses are independent parameters, while the scalar masses have a common source, the initial parameters will be: $\tan\beta$, μ, M_1, M_2, M_3, $m_{\tilde{t}}$.
A large contribution to the fine tuning comes from the request of having the correct electroweak scale, expressed as the vacuum expectation value of the Higgs, v, which, at tree level is given by:

$$-\frac{1}{8}(g^2+g'^2)v^2 = -\frac{M_Z^2}{2} = \mu^2 - \frac{m_{H_d}^2 - m_{H_u}^2\tan^2\beta}{\tan^2\beta - 1.} \tag{49}$$

However, $\tan\beta$ is required to be large in order to get the correct Higgs mass. This means that it is possible to write:

$$-\frac{1}{8}(g^2+g'^2)v^2 = -\frac{M_Z^2}{2} = \mu^2 + m_{H_u}^2 \tag{50}$$

where the two last terms on the right have opposite signs while their value might be larger than M_Z, and eventually cause additional fine tuning. The terms on the right are evaluated at the low energies (LE), and therefore in order to calculate the fine tuning it is necessary to rewrite eq. 50 in terms of the initial parameters of the theory, so having m_{H_d} being a superposition of M_1, M_2, M_3, while μ is the same, but evaluated at the high energy (HE).

$$m^2_{H_u}(LE) = c_1 M_1^2 + c_2 M_2^2 + c_3 M_3^2 + c_2 c_3 M_2 M_3 + ... c_q m^2_{Q_3} + \quad (51)$$

$$\mu(LE) = c_\mu \mu \quad (52)$$

The coefficients come from the solution of the renormalization group equation (RGE) between the two scales, and they depend on the LE, HE, and also what are the fundamental parameters of choice. If it is then applied equation 3 and asked that

$$|\Delta_{a_i}| < \Delta^{max} \quad (53)$$

it is possible to obtain limits on the main parameters of the theory, and then, with some approximation, converting it in limits on physical parameters.

Applying then equation 3 and asking that $\Delta < 100$ it is possible to obtain a limit on the μ parameter and the Higgsinos mass in the form of:

$$\mu < (\sqrt{\Delta})\frac{M_{h^0}}{2} \sim 630 \ \text{GeV} \quad (54)$$

where the Higgs mass has been used for the electroweak scale instead of the Z[1]. This means a rather light Higgsinos, below 630 GeV. This result is rather stable, since the μ parameter runs proportional to itself. It is also worth noticing that limits go as $\sqrt{\Delta}$. Another limit is that the gluino must have a mass such as $m_{\tilde{g}} < 1.5$ TeV (for $\Delta < 100$). However this limit is dependent on the scale of the considered high energy, and can be relaxed to $m_{\tilde{g}} < 2.7$ TeV for lower energy. In a similar way there is a limit for the the stop at $m_{\tilde{t}} < 1300$ GeV for HE of $\sim \Lambda_{GUT}$, while it can be relaxed to $m_{\tilde{t}} < 3100$ GeV for HE $\sim 10^4$ GeV. Wino masses have also similar limits with $m_{\tilde{W}} < 1.3$ TeV, while Bino

[1] A more precise calculation requires that the Higgs mass to be used instead of the Z mass. A more precise description can be found in [42]

limits on the masses are over the reach of LHC with $m_{\tilde{B}} < 3.3$ TeV. Table 3 summaries limits on the sparticle's masses with three different assumptions on the HE.
In the MSSM there are also other sources of fine tuning behind the electroweak scale: as an example there is the observed Higgs mass, and the large $\tan\beta$ (A more in-depth discussion is in reference [42]). Therefore the final value of the fine tuning will be the product of all the different terms, for this reason even a small contribution can lead to large total fine tuning if there are many sources

Sparticle	HE $= 2 \times 10^{16}$ GeV	HE $= 10^{10}$ GeV	HE $= 10^{4}$ GeV
$\tilde{g}$	1440	1890	5860
$\tilde{t}$	1320	1590	3190
$\tilde{W}$	1303	1550	3435
$\tilde{B}$	3368	4237	10565
$\tilde{H}$	627	627	627

Table 3: Upper bounds for sparticle's masses for different value of the HE in the MSSM. Table from reference [42].

2.5.2 The Higgs Boson

One of the most important constraint on supersymmetry comes directly from the observation of the Higgs boson. In fact it is possible to see that at tree level the Higgs mass is:

$$m_{h^0} < m_Z |\cos(2\beta)|. \tag{55}$$

where β is one of the two mixing angles. However, if this were true LEP would have found the lightest MSSM Higgs. In fact h^0 receive large loop correction from stop and top that can lead to m_{h^0} to exceed LEP limits. When adding additional 2 loop contribution it is possible to obtain the following result for the Higgs mass

$$m_h^2 \approx m_Z^2 \cos^2 2\beta + \frac{3m_t^4}{2\pi^2 v^2}\left\{\ln\frac{M_S^2}{m_t^2} + \frac{X_t^2}{M_S^2}\left(1 - \frac{X_t^2}{12M_S^2}\right) + \right. \tag{56}$$

$$+\frac{1}{16\pi^2}\left(\frac{3m_t^2}{v^2} - 32\pi\alpha_s\right)\cdot \tag{57}$$

$$\left.\cdot\left[\frac{2X_t^2}{M_S^2}\left(1 - \frac{X_t^2}{12M_S^2}\right)\ln\frac{M_S^2}{m_t^2} + \left(\ln\frac{M_s}{m_t^2}\right)^2\right]\right\} \tag{58}$$

where $v \approx 246$ GeV, $M_S = \sqrt{m_{\tilde{t}_1} m_{\tilde{t}_2}}$, $X_t = A_t - \mu \cot\beta$ parameterizes the stop left-right mixing, and $\alpha_s \approx 0.12$. From this equation is possible to see that the Higgs mass can receive large contribution in two different way: first case is from large stop mixing (X_t), the second case is from very large stops masses ($M_S \gg m_t$). From the equation is possible also to notice that in order to have the correct Higgs mass, the $\cos 2\beta$ must be close to 1, and this imply that $\tan\beta > 10 - 20$.
Numerical results are shown in figure 11 in cases where the predicted Higgs mass is 123 GeV $< m_h <$ 127 GeV. Experimental constraint are much smaller (125.18 ± 0.16 GeV), but when considering the MSSM, theory uncertainty are of the order of ~ 2 GeV. It is possible to see that for small mixing, the stop mass must be as high as 4 TeVin order to give the observed Higgs mass. This result, combined with the lack of observation of stop at LHC seems to indicate that the stop might have TeVscale masses. However it is also interesting to notice the spread of the points: for some values of the parameter space it is possible to have the right Higgs mass with $\tilde{t}_1$ with a mass as low as 200 GeV.
In the case of MSSM this means that $\tan\beta$ must be large, with a stop with a mass of $\sim$ TeV for large mixing, or even larger $\tan\beta$ or stop masses for small mixing. However this is true only in MSSM, and in particular it does not hold in the Next-to-Minimal Supersymmetric Standard Model (NMSSM) [33].

An interesting case, called *decoupling limit*, is when $m_{A^0} >> m_Z$. In this case it could be shown that the loop corrections get saturated, causing A^0, H^0, and $H^\pm$ to be much heavier and nearly degenerate in a isospin doublet decoupled from experiment energies and h^0 has the same coupling to quarks and leptons as the SM Higgs bosons.

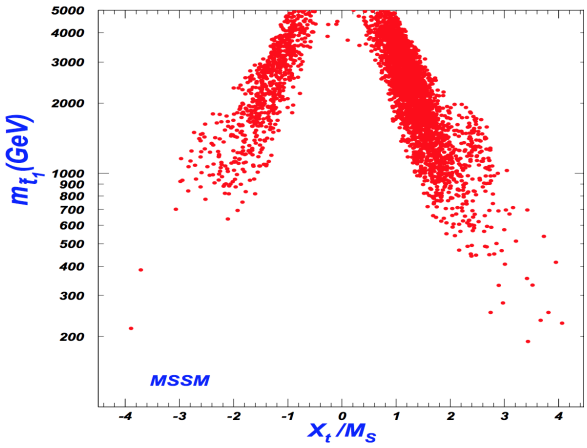

Figure 11: Values of top squark mass that give 123 GeV $< m_h <$ 127 GeV in viable MSSM models [17] as a function of the left-right stop mixing. Figure from [17].

2.5.3 Flavor CP violation

Low energy flavor and CP violation gives some of the most stringent limits on supersymmetry. Sfermions masses arising from supersymmetry breaking violates both CP and flavor, due to off-diagonal elements that mediate flavor mixing and CP in the mass matrix m^2_{ij} of down-type squarks $(\tilde{d}_L, \tilde{s}_L, \tilde{b}_L)$. Constrains then arise from asking that supersymmetric box contributions to the mass splitting of mesons and that the branching ratio of $l_i \to l_j \gamma$ don't exceed the observed value. These are expressed by the following limits

$$\left[\frac{12 \text{ TeV}}{m_{\tilde{q}}}\right]^2 \left|\text{Re}\left(\frac{m^2_{\tilde{d}\tilde{s}}}{m^2_{\tilde{q}}}\right)^2\right| \lesssim \frac{\Delta m_K}{3.49 \times 10^{-12} \text{ MeV}} \tag{59}$$

$$\left[\frac{2.4 \text{ TeV}}{m_{\tilde{l}}}\right]^2 \left|\text{Re}\left(\frac{m^2_{\tilde{e}\tilde{\mu}}}{m^2_{\tilde{l}}}\right)^2\right| \lesssim \frac{B(\mu \to e\gamma)}{2.4 \times 10^{-12}} \tag{60}$$

For order $\mathcal{O}(1)$ flavor violation these requirement implies that first and second generation sfermions must have masses of the order of 10 TeV. Third generation squarks instead satisfy these results for sub-TeV masses.

Another constraint comes from the Electric Dipole Moments (EDM) of electrons and neutron. These are generated by penguin diagrams that involves Higgsinos and sfermions in the loop, and are dominated by the mixing between Higgsino and Wino, and can be dangerous because in the EDM (d_f) computation, given by:

$$d_f \sim e\frac{g_2^2}{64\pi^2} m_f \frac{|\mu M_2|}{m_{\tilde{f}}^4} \tan\beta \sin\theta_{CP} \tag{61}$$

enter the $\tan\beta$ where it can lead to very large CP-violating phase. Here $m_{\tilde{f}}$ is the mass of the heaviest sfermions in the loop. In order then to suppress this phase it is necessary that the phase in the masses of the gauginos and the μ parameters must be somehow correlated. The limits obtained can be written as:

$$\left(\frac{2.5\,TeV}{m_{\tilde{l}}}\right)^2 \frac{|\mu M_2|}{m_{\tilde{l}}} \frac{\tan\beta}{10} \frac{\sin\theta_{CP}}{0.1} \lesssim \frac{d_e}{1.05\times 10^{-27} e\,\mathrm{cm}}. \tag{62}$$

This constraints, for an order of $\mathcal{O}(0.1)$ in the discrepancy, the first generation superpartners to be greater than TeV.

2.5.4 Experimental constraints from LHC: SUSY searches

LHC, at this time, provides proton-proton collisions at an energy of $\sqrt{s} = 13$ TeV, allowing the experiments to search for direct production of sparticles.
The ATLAS and CMS SUSY groups search sparticles in a wide range of scenarios that include many of the supersymmetric models presented in the previous sections. These scenarios include all the production mechanism presented: strong production of squark and gluinos, with a particular emphasis on third generation squarks [43–45], and electroweak production [46–48] . There are also scenarios where R-parity is violated [49] and scenarios with long-lived particles [50]. Searches are also divided in different final states (i.e. 0, 1, or 2 leptons). In figure 12 the mass reach of the limits from the results for run 2 are reported. Searches are divided by channel studied, and the boxes group together the one for (from top to bottom): inclusive squark and gluinos production, dedicated third generation squark production in gluon decay or direct production, electroweak searches, RPV, and long lived particles.

Most of the models considered are the so called Simplified Models [51], which focus on a specific final state, considering the decay branching ratio of sparticles to be 100 %. This is a strong simplification since it's likely that there are multiple competing decay modes for each sparticle, but it still helps to set benchmark points. Possible reinterpretations combining different channels are possible. In figure 13 a summary of the excluded masses for different SUSY particles by ATLAS in collision at $\sqrt{s} = 8$ TeV is shown. In this plot a scan of all the relevant MSSM parameters has been done, and for all the possibles combinations the masses and the branching ratios have been calculated and it has been checked if the model pass all the searches done by ATLAS. For each particle (vertical bars) the fraction of excluded models with that mass are reported. It is worth noticing that for sparticles with color charge, most of the lower masses are excluded for almost all the models, while for charginos and neutralinos there is still a significant fraction of models not excluded.

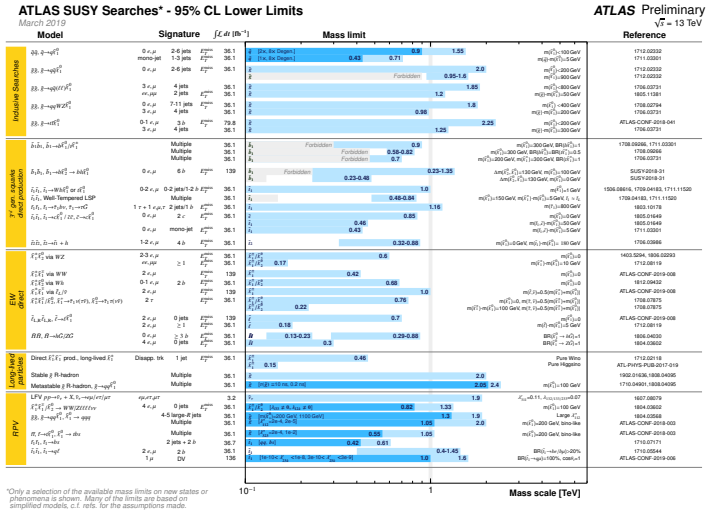

Figure 12: Mass reach of ATLAS searches for Supersymmetry. Only a representative selection of the available results is shown. Plot from ref. [52].

The searches of interest for this thesis are those for the electroweak production. Limits are usually established in defined slices of the parameters space, by fixing one parameter at the time. For the higgsino production, before the analysis the will be presented in this thesis, the

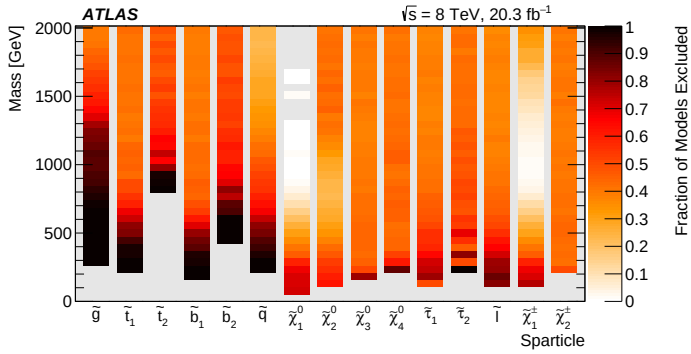

Figure 13: Each vertical bar is a 1D projection of the fraction of model points excluded, with colour coding representing the fraction of model points excluded for each sparticle. Plot from ref. [53].

latest results come from the LEP experiment, and they are summarized in figure 14. Here it is shown the expected (dashed lines) and observed (light blue area) exclusion contour as a function of the mass of the $\tilde{\chi}_1^{\pm}$ and the difference in mass between $\tilde{\chi}_1^{\pm}$ and $\tilde{\chi}_1^0$, assuming a mass of $\tilde{\nu} > 500$ GeV. This figure is composed of different analysis, from the four experiments of LEP (ALEPH, DELPHI, L3, OPAL) [54–64]. The region with $\Delta m > 3$ GeV is covered by analysis in which the $\tilde{\chi}_1^{\pm}$ decays via a W^* into leptons or jets. The region with $\Delta m < 3$ GeV and $\Delta m > 200$ MeV is instead covered by a mono-photon analysis, where there is a photon from Initial State Radiation. Finally the region with $\Delta m < 200$ MeV is covered by analysis with disappearing tracks, displaced vertices or heavy stable charged particles.

Limits at the LHC instead are presented in figure 15 for ATLAS searches, considering the direct production of $\tilde{\chi}_1^+$,$\tilde{\chi}_1^-$ and $\tilde{\chi}_1^{\pm}$,$\tilde{\chi}_2^0$ with SM-boson or $\tilde{\ell}$ mediated decay, as a function of $\tilde{\chi}_1^{\pm}$,$\tilde{\chi}_2^0$ and $\tilde{\chi}_1^0$. In this scenario the production cross section is for pure wino, and the mass of the $\tilde{\chi}_2^0$ is considered the same as $\tilde{\chi}_1^{\pm}$. It is important to notice that this is a different scenario as figure 14. It is worth remembering that the analysis presented in the plot are not redundant, they are not excluding the same region multiple times. The analysis use Simplified Models, as already explained, and therefore the branching ratio in each fixed to 100 % for the considered channel. More realistic limits will have to take into account the branching ratios and therefore weakening

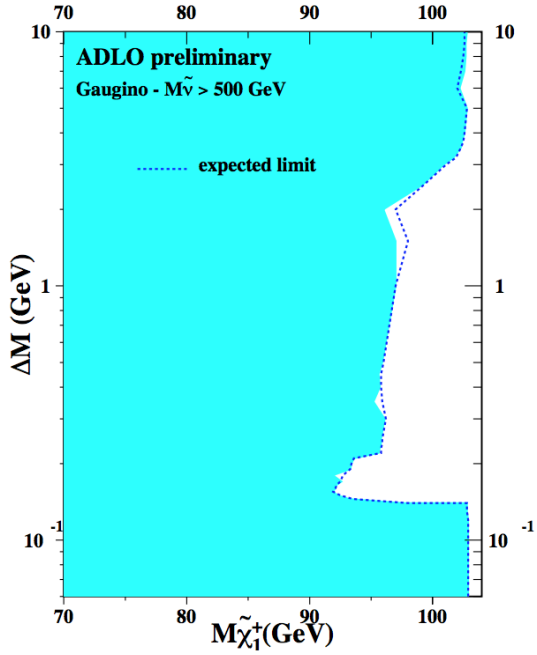

Figure 14: Summary of the LEP searches for higgsino pair production of $\tilde{\chi}_1^{\pm}$ at a center of mass energy of 208 GeV. Expected (dashed) and obtained (full line) mass limits, based on the Likelihood Ratio multichannel method, as function of DM for $m(\tilde{\nu}) = 500$ GeV. From ref. [54]

all the limits. Other interesting limits come from figure 16. Here the $\tilde{\chi}_1^0$ is considered a pure higgsino, causing, as shown before, the $\tilde{\chi}_2^0$, $\tilde{\chi}^{\pm}$, and $\tilde{\chi}_1^0$ to be mass degenerate. Moreover in this model the $\tilde{\chi}_1^0$ is supposed to decay into a SM Higgs boson and a gravitino ($\tilde{G}$). The limits are shown as a function of the triplet mass and the branching ratio of $\tilde{\chi}_1^0$ into $h\tilde{G}$

A different approach has been developed [65] to visualize the results without the assumption that all sparticles decay with a 100 % branching ratio (BR). In this case, for a scenario with three sparticle decay modes the results are shown on a triangular plot, where at the vertices there are the cases with 100 % BR while all the other points are combinations such that $BR_1 + BR_2 + BR_3 = 1$. In figure 17 is reported an example with a reinterpretation of a CMS research of gluino decay in the three channel $t\bar{t}\tilde{\chi}_1^0$, $b\bar{b}\tilde{\chi}_1^0$, and $q\bar{q}\tilde{\chi}_1^0$. In the coloured scale

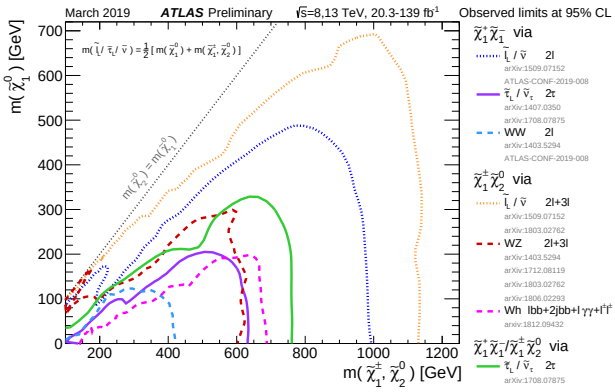

Figure 15: Exclusion limits at 95% CL are shown in the $\tilde{\chi}_1^0$-($\tilde{\chi}_1^{\pm}$,$\tilde{\chi}_2^0$)mass plane for $\tilde{\chi}_1^+$ $\tilde{\chi}_1^-$ and $\tilde{\chi}_1^{\pm}$ $\tilde{\chi}_2^0$ production with either SM-boson-mediated or $\tilde{\ell}$-mediated decays. The production cross-section is for pure wino $\tilde{\chi}_1^+$ $\tilde{\chi}_1^-$ and $\tilde{\chi}_1^{\pm}$ $\tilde{\chi}_2^0$. Each individual exclusion contour represents a union of the excluded regions of one or more analyses. From ref [52]

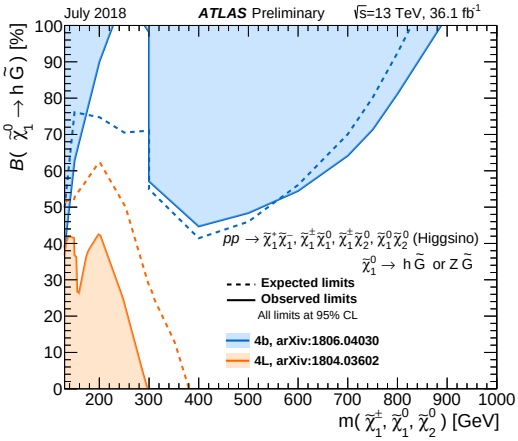

Figure 16: The 95% CL exclusion limits on a general gauge mediation model from $\sqrt{s} = 13$ TeV data. The model assumes a pure Higgsino NLSP that promptly decays to either Z gravitino or Higgs gravitino. The limits are displayed as a function of the mass of the nearly mass-degenerate Higgsino triplet and the branching fraction of lightest Higgsino to Higgs gravitino. From ref. [52].

are represented the 95 % C.L. exclusions for the gluino mass. This approach could be important since in some models the mixed states could give very different results from the Simplified Models.

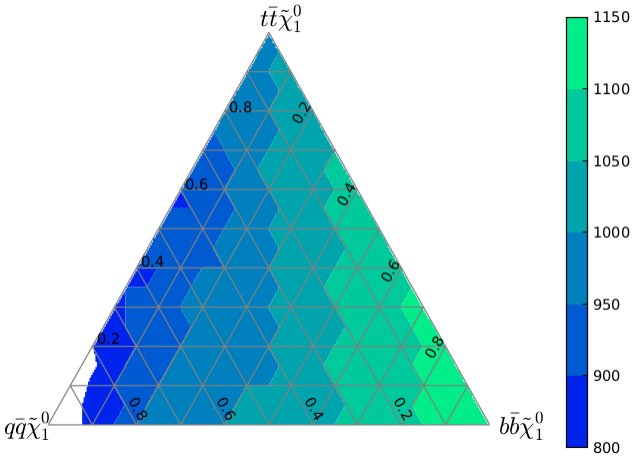

Figure 17: Each point in the above triangle has a unique combination of the three branching fractions and the vertices represent the simplified models with 100% branching fractions into one of the three final states. The bottom left corner is empty since the results are weak and the limits would have been off scale. From ref. [65].

3 LHC and the ATLAS Detector

The data used in the analysis presented in this thesis are taken from $\sqrt{s} = 13$ TeV proton-proton collisions produced by the LHC at CERN from 2015 to 2018, the so called Run 2, and recorded by the ATLAS detector. In section 3.1 I will give an overview of the experimental setup of the LHC, its accelerating facilities and the experiments which are sited there. In the following section (3.2) I will present in more detail the ATLAS detector.

3.1 The Large Hadron Collider

The idea of a proton-proton collider arose in the late '80s, while the first project was approved in 1994. The Large Hadron Collider (LHC) is placed in the 27 km tunnel previously built for LEP at CERN, and its energy reaches 13 TeV in the center of mass, making this machine the most powerful accelerator in the world by at least one order of magnitude. This allows experimental physicists to investigate new energy never reached before. At the scale of the TeV we can study the fundamental process that controls the electroweak symmetry breaking and search for new physics beyond the Standard Model: this includes the study of the Higgs boson and the search for Supersymmetric particles.

The choice of a proton-proton collider instead of an electron-positron one is motivated by the power of discovery of this machine. In fact, with a machine like LHC we can reach a much higher energy than the one achievable from machine with electrons. This is due to fact that any charged particle radiates photons when accelerated. The energy loss of a particle in a circular motion, known as synchrotron radiation, depends on its mass m as the following formula:

$$\frac{dE}{dt} \propto \frac{E^4}{m^4 R} \tag{63}$$

where E is the energy of the particle and R the radius of the orbit of the particle. As we can see, this implies that for fixed radius and fixed energy, as we would have at a collider, electrons loose $(m_p/m_e)^4 \approx 10^{12}$ times more energy than a proton. This sets a limit to the energy of accelerating electrons to around 100 GeV. To compensate this we would have to build a much bigger ring for the electrons, causing the price

of the project to increase. Nonetheless, there are, at the current time, projects involving circular electron-positron accelerators: CEPC [66, 67](in China) and FCC-ee (at CERN) [68]. They both will have a circumference of around 100 km, and a cost significant higher than LEP or LHC. Another approach that is under study is the idea of a linear accelerator using electrons, as the projects CLIC [69] (at CERN) and ILC [70–73] (in Japan) are studying. They both require technology that were developed after the LHC was built. This is why it was never an option when LHC was being designed. These projects still need a great length, for CLIC in the initial configuration proposal it is 11 km long with an energy of 380 GeV, while ILC could reach an energy of 250 GeV, and could be expanded to 50 km in order to reach 3000 GeV. Another drawback is the fact that in a linear accelerator bunches can cross just one time and therefore the luminosity would be smaller. Using protons solves these problems but brings in new ones that are absent in an electron collider. This is due to the fact that protons have a complex structure (they are not elementary particles).

Interesting collisions between protons can be of two different kinds: *soft* or *hard*. *Soft* collisions are the results of protons interacting as a whole, with low momentum transfer ($\approx$ 500 MeV) and large cross section. *Hard* collision happens when the constituents of the protons, gluons and quarks, interact with each other. In this kind of events we can produce new particles.

In hard collision events the partonic center of mass energy it is unknown, since quarks and gluons carry an arbitrary fraction of the proton momentum. For this reason, making kinematic calculations is more difficult.

Moreover, the important events for physics are the ones from *hard* collisions, but these have cross sections orders of magnitude smaller than *soft* collisions. For this reason an high luminosity collider is needed. The rate of events at LHC is given by the product of the cross section σ and the luminosity $\mathcal{L}$.

The instantaneous luminosity is defined by the equation 64, expressed in terms of occurrence of a given process, dN/dt, and its cross section:

$$\mathcal{L} = \frac{1}{\sigma}\frac{dN}{dt} \tag{64}$$

This quantity is measured in inverse centimeters per second ($\mathrm{cm}^{-1}\mathrm{s}^{-1}$). It can also be expressed in terms of the product of the number of

particle in both bunches (n_1 and n_2) and the frequency f of bunch crossing over the crossing area $A = 4\pi\sigma_x\sigma_y$, as in equation 65. In this way it is independent of the process considered.

$$\mathcal{L} = \frac{f n_1 n_2}{4\pi\sigma_x\sigma_y} \tag{65}$$

Integrating over the period of *working* time of the machine we get the total number of events recorded, defined as *integrated luminosity*:

$$\mathcal{L}_{int} = \int \mathcal{L} dt \tag{66}$$

The final design of LHC predicted bunches containing $\approx 10^{11}$ protons colliding at an energy of 7 TeV for each beam, resulting in an energy in the center of mass of 14 TeV, with a bunch crossing every 25 ns (4 GHz of frequency). The project goal of LHC is an instantaneous luminosity of $\mathcal{L} = 10^{34}\text{cm}^{-2}\ \text{s}^{-1}$, with an average of 23 inelastic scatterings per bunch crossing, with almost 1000 new particles produced. LHC started colliding the first beams in 2009, used for tests and calibration. In March 2010 LHC reached the proton-proton collision energy of 7 TeV, starting a period of data-taking that lasted till 2011. During 2012 LHC reached an energy at center of mass of 8 TeV with a peak instantaneous luminosity of $8\times10^{33}\text{cm}^{-2}\text{s}^{-1}$. Together these periods are referred as *run* 1, and they amount to a total of 25 fb^{-1}data taken, for both the ATLAS and the CMS experiments. After a shutdown during 2013 and 2014 for technical improvements, LHC started again to operate in 2015, reaching an energy in the center of mass of 13 TeV and a peak luminosity of $5\ \times10^{33}\ \text{cm}^{-2}\text{s}^{-1}$ with a separation of bunches of 25 ns. LHC delivered 4.2 fb^{-1}in 2015, and ATLAS recorded a total of 3.9 fb^{-1}. From 2016 to 2018 LHC has steadily continued to deliver collisions at the same energy in the center of mass, delivering 38.5 fb^{-1}in 2016, 50.24 fb^{-1}in 2017, and 63.35 fb^{-1}in 2018. The luminosity recorded by ATLAS is instead: 35.56 fb^{-1}in 2016, 46.89 fb^{-1}in 2017, and 60.64 fb^{-1}in 2018, for a total in Run 2 of 146.9 fb^{-1}. The dataset used in the thesis are a smaller sub-sample where are removed events where there might have been problem in the detector compromising the data quality. This sample consists of 139 fb^{-1}.
Between 2019 and 2021 LHC will be shut down to allow for additional improvement and maintenance of the acceleration facilities and the detectors. In 2021 the run 3 will start, and LHC will deliver protons

with an energy in the center of mass of 14 TeV.
Figure 18 shows the average number of interactions per bunch crossing for each year of the run 2, for proton-proton data with 13 TeV.

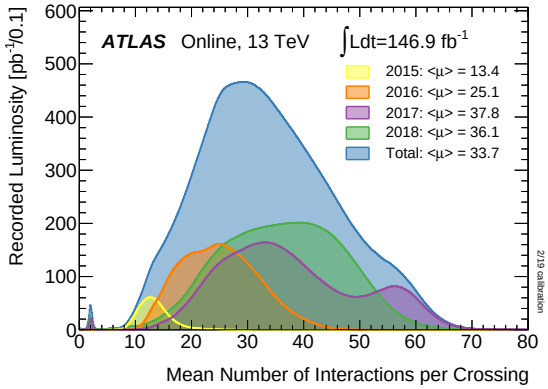

Figure 18: Luminosity weighted distribution of the mean number of interactions per bunch crossing divided per year for the run 2 collision data with energy in the center of mass of 13 TeV.

A brief summary of the data taking periods at LHC, from both Run 1 and Run 2 for pp collisions, is reported in figure 19. In figure 19 is reported the cumulative integrated luminosity taken by the ATLAS experiment as a function of time. In figure 20 is reported the instantaneous peak luminosity as a function of time, as measured by the ATLAS experiment during 2018 data taking period.
Together with proton-proton collisions, LHC also delivers collisions with lead ions, in order to study the propriety of gluon-quark plasma. Table 5 shows the summary of heavy ions data taking periods.

3.1.1 The accelerator complex

Before entering the ring of 27 km that compose the LHC, protons (or lead ions) are accelerated in different steps by a complex system of other machines. The accelerating chain (together with the experiments) is shown in figure 21. The first step is to produce protons, which is done by ionizing a hydrogen source. These protons are then accelerated up to 50 MeV by a linear accelerator: LINAC 2. Then they enter a circular machine: Proton Synchrotron Booster (PSB) where

Year	Energy [TeV]	Peak Luminosity [10^{33}cm^{-2}s^{-1}]	Integrated Luminosity [fb^{-1}]	Bunch separation [ns]
2010	7	0.207	0.048	50
2011	7	3.65	5.55	50
2012	8	7.73	23.115	50
2013	2.76	0.148	0.0047	25
2015	13	5.02	4.193	25
2015	5	0.379	0.028	25
2016	13	13.8	38.5	25
2017	13	20.9	50.24	25
2017	5	1.34	0.28	25
2018	13	21.0	63.35	25

Table 4: Summary of LHC performance for pp collisions

Year	Energy [TeV*Z]	Type Collision	Peak Luminosity [10^{26}cm^{-2}s^{-1}]	Integrated Luminosity [nb^{-1}]	Bunch separation [ns]
2010	7	PbPb	0.304	0.0096	50
2011	7	PbPb	5.12	0.165	50
2013	8	p-Pb	1120.	30.962	50
2015	13	PbPb	28.8	0.570	25
2016	13	p-Pb	6220.	65.5	25
2016	13	Pb-p	8620.	117.8	25
2018	13	PbPb	61.7	1.8	25

Table 5: Summary of LHC performance for PbPb and p-Pb collisions

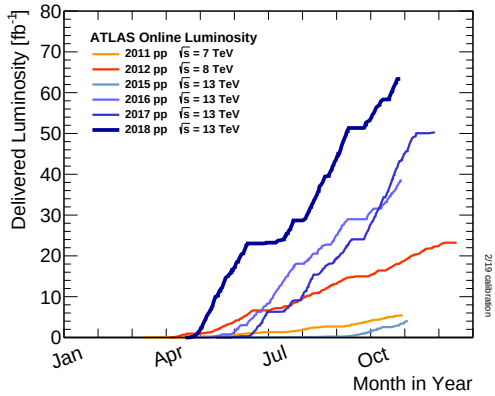

Figure 19: Cumulative integrated luminosity as a function of time.

they are brought to an energy of 1.4 GeV, so that they can safely enter the Proton Synchrotron (PS). This is the first accelerator built

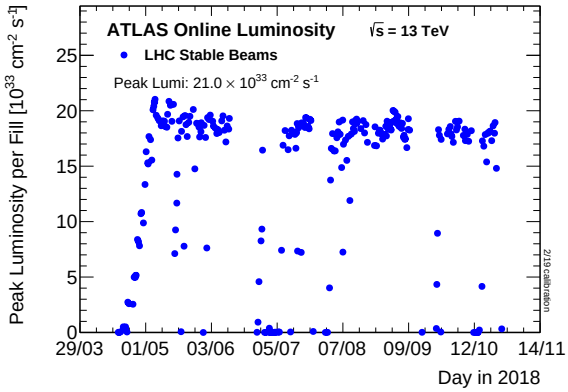

Figure 20: Peak Luminosity measured by ATLAS detector as a function of time.

at CERN in 1959 and it is still used to accelerate protons from 1.4 GeV to 26 GeV. The next step is passing protons to the Super Proton Synchrotron (SPS), the machine used in the '80s to discover the W boson by the UA1 and UA2 collaborations, where protons are accelerated to 450 GeV. Once they have reached this energy, the protons are ready to be injected into the LHC.
For lead ions the chain of machine is slightly different. They are accelerated first by the LINAC 3 (a linear accelerator) and then by the Low Energy Ion Ring (LEIR). At this point they enter the PS and then the chain of process is the same as for the protons: SPS and then LHC.

3.1.2 The experiments at LHC

The main experiments at LHC are ALICE [74], ATLAS, CMS [2] and LHCb [75]. They are located in correspondence of the interaction points of the ring. There are also three additional experiments: TOTEM [76], LHCf [77] and MoEDAL [78]. These are focused on forward emitted particles, and therefore are situated along the beam, in proximity of the collisions points. All the experiments have similar features: they all have to have a very high speed of response, due too the high rate of collisions. For the same reason they must have a trigger system able to select only interesting events. It is also important to have a good spatial segmentation, in order to determine the posi-

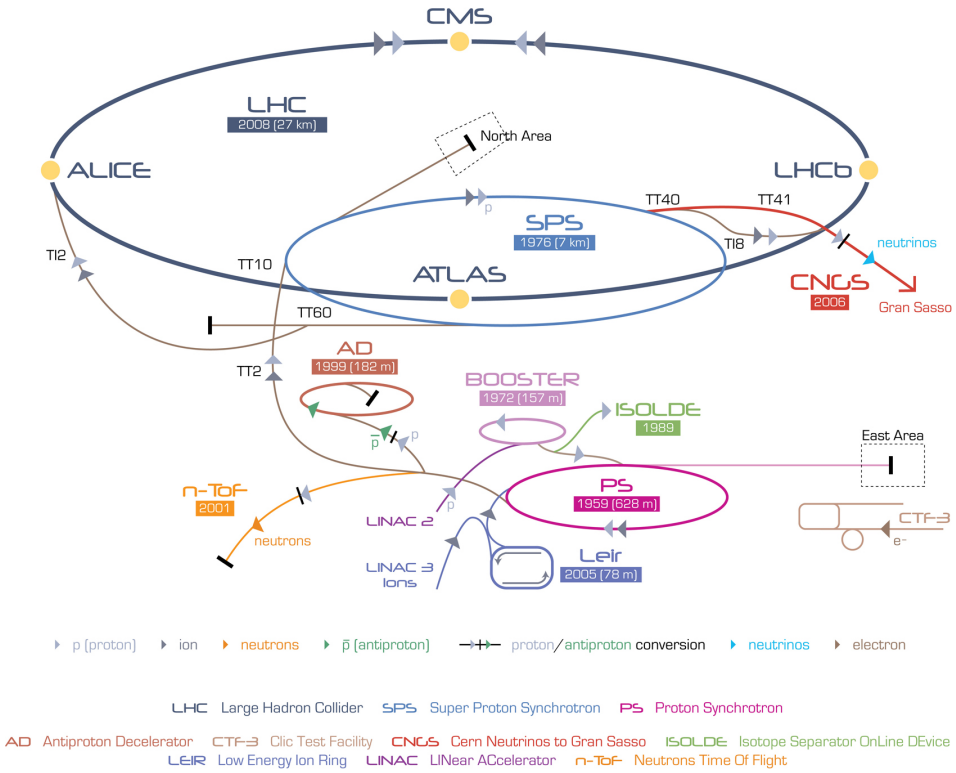

Figure 21: Chain of accelerating facilities at CERN and most important experiments

tion of tracks and energy deposits. Moreover, every detector must be able to distinguish the signatures of the different particles.
However the experiments have different purposes.

ATLAS (A Toroidal LHC ApparatuS) and **CMS** (Compact Muon Solenoid) are two of the biggest detector located at the LHC. They are both built for the search of the Higgs boson and to investigate new physics beyond the Standard Model. Even if they use different technologies, their performances are similar, and the agreement between their results is a fundamental cross check of the validity of their results.

LHCb is dedicated to the study of the violation of CP, the symmetry between matter and anti-matter, by targeting the decay of states containing b and c quarks. Its design is quite different from the other detectors, since it is not symmetrical along the

interaction point. This is to enhance the detection of b quarks. Moreover at LHCb rare decays of hadrons, such as $B_s^0 \to \mu^+\mu^-$, suppressed at leading order, but still possible are studied.

ALICE (A Large Ion Collider Experiment) is a detector designed to detect the products of heavy ions collisions. Its goal is to study quark-gluon plasma, that is the nature of strongly interacting matter at extreme energy densities. ALICE also studies proton-proton collisions both as a comparison to the Pb-Pb collisions and to do research in areas where it is competitive with the other experiments

TOTEM (TOTal cross section, Elastic scattering and diffraction dissociation Measurement at the LHC) is used to monitor the LHC luminosity and make precise measurements in the forward region, where most of the other experiments can't operate.

LHCf (Large Hadron Collider forward) uses forward particles from the LHC as a source. This is useful to calibrate models for the showering of high-energy cosmic rays in the atmosphere. LHCf is placed at 140 m from the interaction point, the same place where is positioned the experiment ATLAS

MoEDAL has started taking data just in 2015, and it is the newest of all this. Its main purpose is to search for magnetic monopoles. It is placed at the same interaction point of LHCb.

3.2 The ATLAS experiment

The ATLAS detector is one of the four main experiments at LHC. It is located at interaction Point 1 (see figure 21) in a cavern almost 100 m underground. It has a cylindrical symmetry along the beam axis, with a length of 44 m and a diameter of 25 m. It weights almost 7000 tons. It was first proposed in 1994, but the construction didn't start until 2003, and it took until 2007 to be finished. It began operative in 2008 by looking at cosmic ray events, and since 2009 it records events from proton-proton and heavy ions collisions with a rate up to 400 Hz during run 1. In run 2 ATLAS reached a rate of recorded events of 1000 Hz.
ATLAS is a general purpose detector, that means its aim is to reconstruct the nature and energy of all the particles generated in the

collisions of protons (or ions) in a bunch crossing. In order to do so it must have some specific characteristics: first of all, it must be hermetic, this means that the detector must cover as much as possible of the solid angle around the interaction point so that the possibility of particles escaping through a non-instrumented zone is minimal. To be able to identify all the particles, using only one detector is not a feasible way. For this reason ATLAS (and most of the modern detectors) is divided in different sub-detectors, each of them with a specific purpose. Moreover the detector must be fast in response to the very high rate of events that occur. The rate of collisions is 40 MHz and it must be lowered to 1 kHz; in order to do so it is necessary to have a fast system of triggers (section 3.2.7). This constraint is due to available computational resource for the storage, reconstruction, and analysis of data.
In figure 22 we can see a schematics of the ATLAS detector. In the innermost part, just around the interaction point, we have the Inner Detector (section 3.2.2), used for tracking particles, filled by a solenoidal magnetic field. The Inner Detector is divided in a barrel region in the middle and two end caps. Over this there is the Calorimeter system (section 3.2.3), for the identification of hadronic and electromagnetic showering, and after that the Muon Spectrometer (section 3.2.4), built for the identification of muons. Also these parts are divided in a barrel region and two end-caps. A dedicated magnetic system is present for the Muon Spectrometer (section 3.2.5). The last part is the Forward Detector which covers the most forward part near to the beam (3.2.6).

3.2.1 Coordinate System

Before analysing the detector and its features it is useful to briefly describe the coordinate system that is used in ATLAS. In fact, ATLAS does not use a cartesian coordinate system (x,y,z) but, due to its cylindrical symmetry, use a right-handed coordinate system (ϕ,η,z). The origin of the system is located at the center of the detector, the interaction point, and the z axis is along the beam line. The azimuthal angle ϕ is defined by measuring around the z axis perpendicularly to the beam. Instead of the polar angle θ it is used the *pseudorapidity*, which can be related to θ by

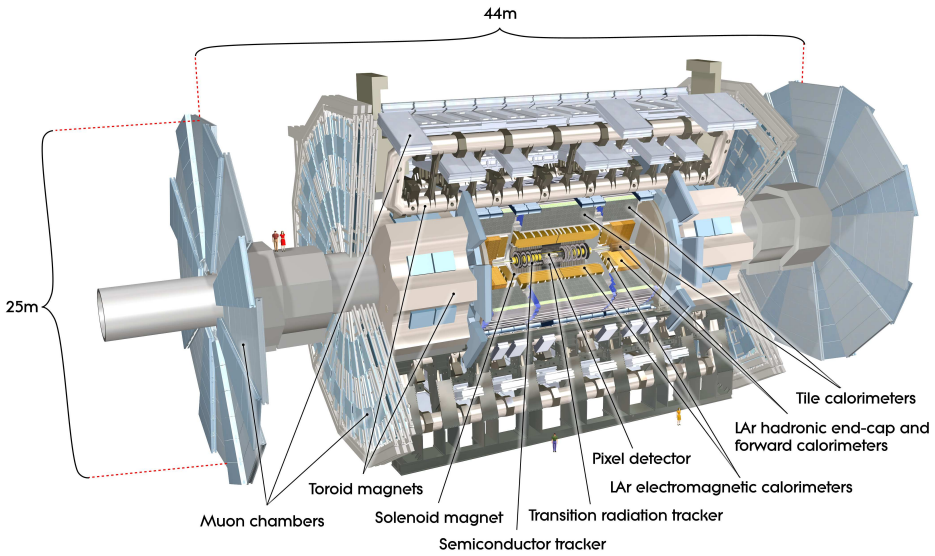

Figure 22: Cut-away view of the ATLAS detector

$$\eta = -\ln \tan \frac{\theta}{2}. \tag{67}$$

Pseudorapidity is the limit for massless particles of the quantity *rapidity* (y), described by:

$$y = \frac{1}{2} \ln \left(\frac{E + p_z}{E - p_z} \right). \tag{68}$$

Those quantities, rapidity and pseudorapidity, are very useful in colliders because of their Lorentz transformation propriety. In fact, under a Lorentz boost β along the z-axis, y transform by adding a constant in the following way:

$$y' = y + \operatorname{arctanh}(\beta). \tag{69}$$

This mean that rapidity differences, and therefore the spectrum of high energy particles dN/dy, is invariant for boost along the z axis, and this is helpful since in hadronic colliders we do not know the rest frame of parton collisions. For these reasons it is preferred η to the polar angle θ.
An important set of variables are the transverse one: momentum and

energy. Those are defined as the momentum (or energy) perpendicular to the beam axis (z axis). It can be defined as:

$$p_T = \sqrt{p_x^2 + p_y^2} \tag{70}$$

3.2.2 Inner Detector

The Inner Detector (ID) [79] system (figure 23) is the innermost part of the ATLAS detector. It is used for the reconstruction of the tracks and the interaction vertices of charged particles. Vertices can be both primary, from proton-proton collisions, and secondary, from long lived hadrons decays, such as hadrons containing b quarks. For this purpose, the ID must have high spatial resolution and granularity, to discriminate all the tracks, and an high resistance to radiation, since it is the closest system to the beam. It consists of a silicon pixel detector, a silicon microstrip detector (SCT) and the straw tubes of the transition radiation tracker (TRT). Its coverage is in the region $|\eta| < 2.5$ and it is surrounded by a solenoid magnet that generates a 2T field. Between run 1 and run 2 the ID has been upgraded and now before the pixel detector there is a new layer of pixel: the insertable B-layer (IBL). All of these components are described in this section. The pixel detector will be analyzed in more details in the next chapter.

Pixel Detector The ATLAS [1] pixel detector [80] is the innermost part of the Inner Detector. It consists of four barrel layers and three disk layers per end cap (six in total). The barrel layers are composed of n^+-in-n planar oxygenated silicon detectors, and n^+-in-p 3D silicon detectors. The innermost layer, the Insertable B-Layer (IBL)[81], is located at just 3.3 cm from the beam axis and is made of pixel of 50 $\times$ 250 μm^2 in size, which are just 200 μm thick, while in the region with high $|z|$ of the IBL there are n^+-in-p 3D pixel of 50 $\times$ 250 μm^2 in size that are instead 230 μm thick. The other layers are respectively at 5.05 cm (B-Layer), 8.85 cm (Layer1), and 12.255 cm (Layer2) from the beam axis and made of pixel of 50 $\times$ 400 μm^2 in size and 250 μm thick. They cover a range in pseudorapidity of $|\eta| < 2.5$. The end caps (which close the barrel) are made of the same sensors as B-Layer/Layer 1 /Layer 2 and have three disk each and have 288 modules. The total number of readout channels is 86×10^6.
IBL was installed in ATLAS in May 2014 before the start of LHC Run

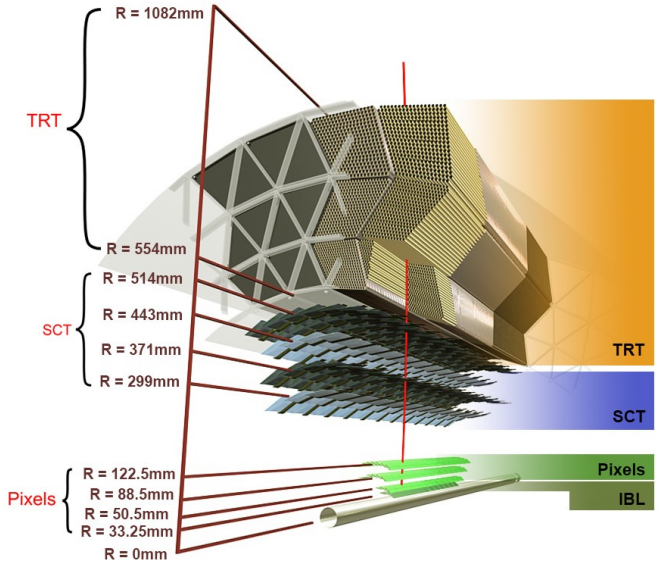

Figure 23: Cut-away view of Inner Detector

2, while the other three layers have been there since the beginning of Run 1. The motivation for this new layer arose from the high luminosity expected in run 2 and beyond that would cause a much higher pileup and a greater number of tracks, and therefore it becomes difficult to correctly assign the vertices to the right tracks.
A bias voltage of 150 to 600 V is required to completely deplete the semi-conductor. Current is constantly monitored and pixel calibrated. A signal is registered if it is over a certain threshold. When a particle deposits enough charge in a pixel to be over the threshold the front-end electronics stores the Time-over-Threshold (ToT), i.e. the time the signal from the pre-amplifier is over the threshold. This has a nearly linear dependence to the charge released in the pixel and therefore to the energy deposited by the particle. ToT is also useful for measuring the dE/dx of the particles.

Semi-Conductor Tracker The next layer of detector is the Semi-Conductor Tracker (SCT) [82]. It is composed by a central barrel and two end-caps. The barrel is divided in four cilynders of radii from 299 mm to 514 mm that cover a range of $|\eta|$ <1.1 -1.4 for a length of 1492 mm. The end-caps disks are composed of 9 plates covering

the remaining range $|\eta| < 2.5$ with a radius of 56 cm. The SCT, as the pixel detector, is made of silicon sensors, but with larger strips in order to cover a bigger area. In the barrel they all are 285 μm thick single sided p-on-n semi-conductor, with a dimension of 64.0 $\times$ 63.6 mm and 80 μm strip pitch, while in the end-caps they have different geometry to maximise the coverage and the pitch change between 56.9 to 90.4 μm. The SCT covers 61 m^2 of silicon detectors with 6.3 million readout channels. SCT had a mean hit efficiency between 98 % and 98.5 % during 2018 data taking in the active part of the detector, while around 1.5 % of the subdetector is inactive. The precision on the azimuthal direction is of 17 μm and 580 μm along the z direction.

Transition Radiation Tracker The Transition Radiation Tracker (TRT) [83] covers the last part of the ID. It is a straw-tube tracker with a diameter of 4 mm, made of Kapton and carbon fibres, filled with a mixture of Xenon, Argon, CO_2, and oxygen. In the middle of each tube there is a gold-plated tungsten wire of 31 μ diameter. The TRT is composed of 52 544 of these tubes, each 1.5 m in length parallel to the beam axis. They cover a pseudorapidity range of $|\eta| < 1.$ with a radius from 0.5 m to 1.1 m. The remaining range of pseudorapidity, $1 < |\eta| < 2.$, and 0.8 m $< |z| <$ 2.7 m, is covered by the end-caps straws. These are perpendicular to the beam axis and are 0.4 m long. Each side of the end-caps contains 122 880 straws.
The edge of the wall is kept at -1.5 kV while the wire is at ground. In this way every tube behaves as a proportional counter. The space between straws is filled with polymer fibers and foils, respectively in the barrel and in the end-caps, to enable high energy particles to emit radiation. This effect depends on the relativistic factor $\gamma = E/m$, so for electrons is stronger. This is helpful in the identification process. The TRT is complementary to the other silicon-based part of the ID, but its information is only on the R-ϕ plane and the resolution is about 120 μm. However the number of straws that a particle has to travel is 35, therefore even if the resolution on the single hit is low, the combination of all the hits gives a resolution on the momentum that is compatible with the one from the other silicon detector.

3.2.3 Calorimeter

The next layer in the ATLAS detector is the calorimeter system (figure 24). Its purpose is the measure of the energy of photons, electrons and hadrons. In a calorimeter a particle must deposit all of its energy before the end of the detector to be correctly measured. Electromagnetic and hadronic showering are the results of the interaction of electron/photon or hadrons in matter. These particles produce a cascade of other secondary particles less and less energetic. The sum of all this deposit is used to reconstruct the original particle energy. However the response of electron and photons in matter compared to hadrons is different. For this reason two different calorimeters to address these two different kinds of particles are needed.
The ATLAS calorimeter is divided in three different parts: electromagnetic calorimenter (ECAL), just after the Solenoid, followed by the hadronic calorimeter (HCAL) and near the beam the Forward Calorimeter (FCAL). The first two are also divided in end-caps and barrel (EC-B). They all are sampling calorimeters without compensation (which is done offline) for the hadronic signal ($e/h > 1$). The sampling is done using materials with high density where particles release most of their energy. The measure is done by sampling periodically the shape of the shower. This helps better containing the particles inside the detector but as a drawback the energy resolution is lower. The segmentation of the calorimeters also allows the implementation of a position measurement.
Together they cover the range of $|\eta| < 4.9$. It is important to have a large η coverage because it helps reducing the momentum taken away by particles too forward to be detected, that would degrade the measurement of the transverse missing momentum.

Electromagnetic Calorimeter The Electromagnetic Calorimeter (ECAL) [84] is composed of four sampling calorimeters, all using liquid Argon (LAr) as an active medium and lead as passive material. The detectors are housed inside cryostats filled with LAr and kept at around 88 K. The ECAL has an *accordion* geometry (figure 25). With this feature is possible to cover all the solid angle without an instrumentation gap. Moreover it allows a fast and azimuthally uniform response.
The barrel (EMB) covers a range in pseudorapidity of $|\eta| < 1.475$,

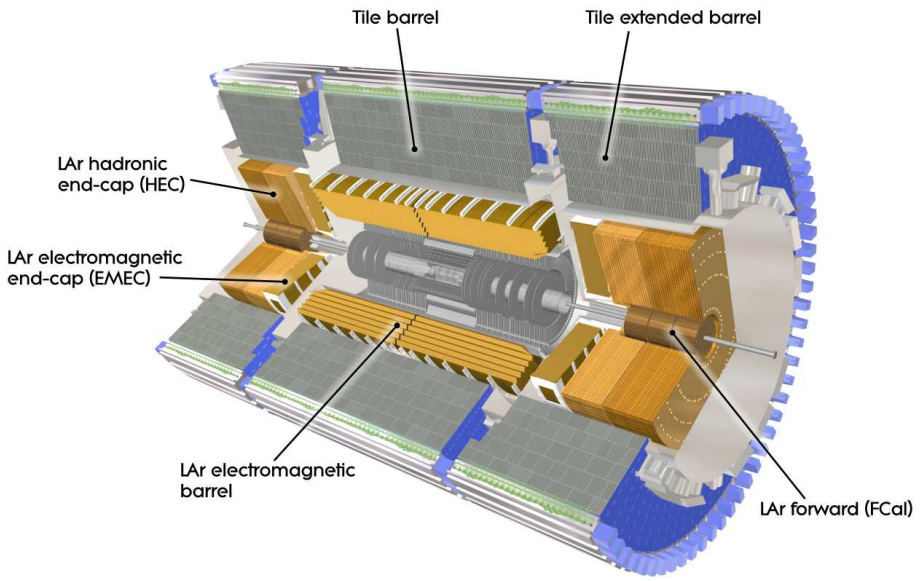

Figure 24: Cut-away view of the Calorimeter

while the end-caps (EMEC) the remaining range of $1.375 < |\eta| < 3.2$. It has two wheels, an inner and an outer one.
The ECAL has length of 24 X_0, electromagnetic radiation length. ECAL is segmented in three parts (front, middle and back) of increasing cell size and different radiation length (respectively 2, 20, 2); this help to efficiently discriminate between prompt photons and photons coming from π^0. Furthermore in front of the first strip (in the region $|\eta| < 1.8$) is located a presampler, an instrumented argon layer that provides information on the energy lost before the ECAL. In fact, photons and electrons lose a part of their energy in passing through the ID and the solenoid, since those are, obviously, matter. Hadronic particles do not suffer much of this effect since an hadronic interaction length is longer then the space between the interaction point and the calorimeters.
The energy resolution is given by:

$$\frac{\sigma}{E} = \frac{10\%}{E} \bigoplus 0.7\% \tag{71}$$

where E is expressed in GeV, and $\bigoplus$ is the quadratic sum.

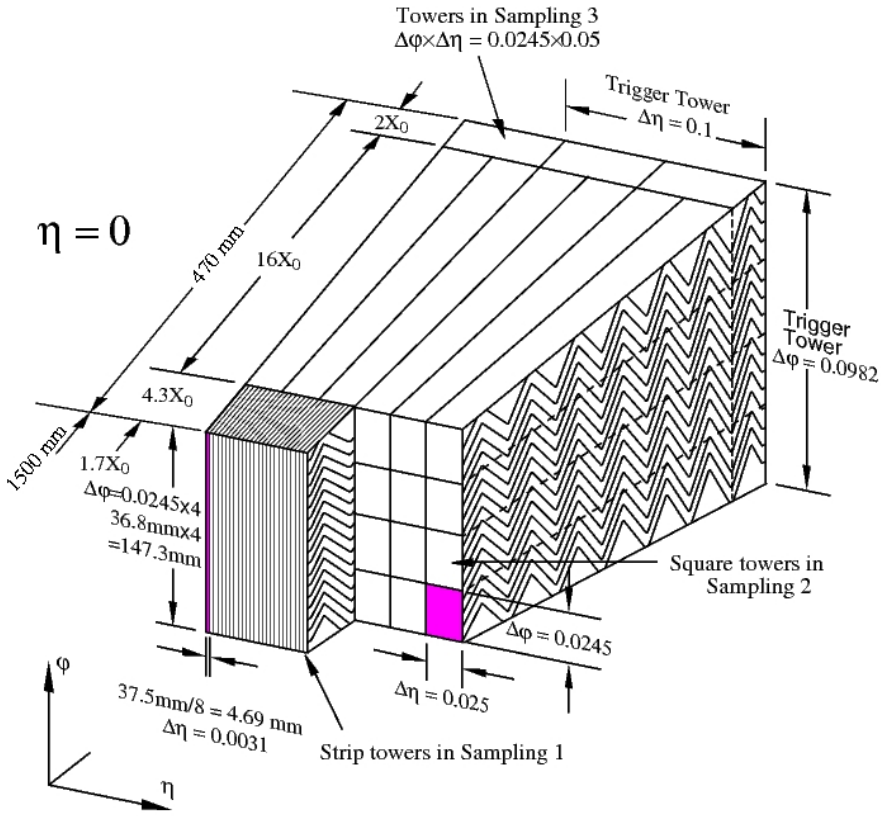

Figure 25: View of the accordion geometry of the ECAL

Hadronic Calorimeter The Hadronic Calorimeter (HCAL) is divided in a central part in the barrel, called *Tile Calorimeter* (TileCal) [85], and two end caps, called HEC. The two parts have different composition, but are both sampling calorimeters.
The TileCal as sampling material uses scintilators while for absorber uses steel. The TileCal is composed of three sections: a long barrel (LB) in the range $|\eta|$ <1.0 and two extended barrels (EB) in the range 0.8< $|\eta|$ <1.7. Between the two there is a gap filled with scintillator to help recover energy otherwise lost in this transition region.
The HEC consists of two wheels divided in two longitudinal segments perpendicular to the beam covering the pseudorapidity range $1.5 < |\eta| < 3.2$. The wheels are made of copper as the passive material, and LAr as active medium, due to the high radiation resistance requested in this area.

The energy resolution for the TileCal is

$$\frac{\sigma}{E} = \frac{50\%}{E} \bigoplus 3\% \tag{72}$$

Forward Calorimeter The Forward Calorimeter (FCal) covers the part the closest to the beam pipe, in the pseudorapidity range $3.1 < |\eta| < 4.9$. It measures both electromagnetic and hadronic particles. The geometry of the FCal is a cylindrical one, with three different modules. It is segmented using LAr as active medium while copper and tungsten are used as absorber. This choice is due to the high dose of radiation in this region, in fact the LAr can be easily replaced so that it doesn't lose in performance. The FCal has a poor performance in particle reconstruction but is fundamental for the missing transverse energy and the reconstruction of very forward jets. In fact the energy resolution for the FCal is

$$\frac{\sigma}{E} = \frac{100\%}{E} \bigoplus 3.1\% \tag{73}$$

3.2.4 Muon spectrometers

The Muon Spectrometer (MS) (figure 26) [86, 87] is the outermost part of the ATLAS detector. This is due to the fact that muons lose energy almost always through ionization, meaning that they loose very little energy interacting in matter. Therefore they can travel all the detector without being stopped. Powerful magnetic fields are then needed to bend the trajectories and measure the momentum. The MS has also an important function as a trigger. Therefore it has to be fast and with high granularity.
The MS consists of one barrel that covers the pseudorapidity range $|\eta| < 1.05$ and two end-caps that cover the range $1.05 < |\eta| < 2.7$. In the barrel region tracks are measured by three layers with a cylindrical geometry, while the end-caps are wheels perpendicular to the beam. The momentum measurement in the barrel region is done by the Monitored Drift Tubes (MDT), while in the the region at large pseudorapidity the measurement is done by the Cathode Strip Chambers (CSC, multiwire proportional chambers with cathodes segmented into strips). This is done by measuring with high precision the coordinates of the curvature of the particles bended by the magnetic systems. Since $p = 0.3BR$, where B is the magnetic field expressed in

Tesla, R the curvature in meters, and p the momentum of the particle in GeV, measuring R and knowing exactly B is possible to obtain p. The MDT measure the ϕ coordinate while the CSC the R one. They give a spacial resolution of 80 and 60 μm respectively for the MDT and CSC.
The trigger system is done by the Resistive Plate Chambers (RPC) in the barrel and by the Thin Gap Chambers (TGC) in the end-caps. Together they cover a pseudorapidity range $|\eta| < 2.4$.
During the shutdown before run 2, the MS has been upgraded (actually its original design) by adding some more chambers in the transition region between barrel and end-caps ($1.0 < |\eta| < 1.4$). Moreover other RPC and MDT chambers has been installed with tubes with smaller radius, in order to cope with the new higher rates.
The bending provided is of about 2.5 Tm in the barrel and 6 Tm in the end-caps. This is provided by a system of three large superconducting air-core toroidal magnets. In the barrel, in the pseudorapidity range $|\eta| < 1.4$ by the large barrel toroid, while for $1.6 < |\eta| < 2.7$ by the end-caps toroids. The region in between ($1.4 < |\eta| < 1.6$) is deflected by a combination of the barrel and end-cap.

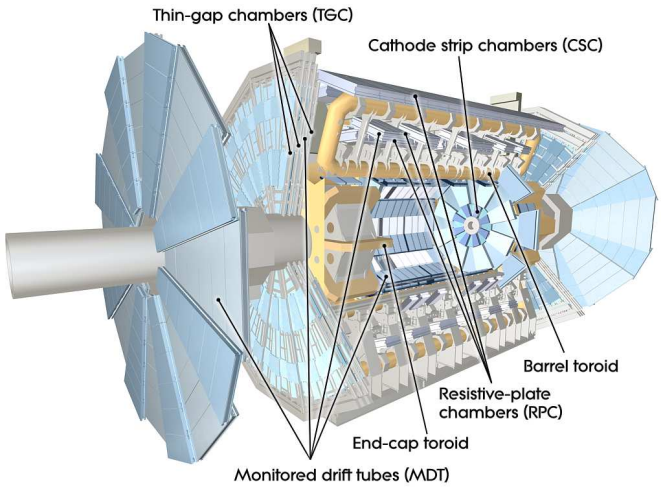

Figure 26: Cut-away view of the Muon Spectrometer

3.2.5 The magnet system

The ATLAS magnetic system (figure 27) [88–90] is composed of four different large superconducting magnets. The magnetic system is 22 m in diameter and 26 m in length. The magnets are divided in one thin solenoid around the ID, and three large toroids, one in the barrel and two end-caps, arranged around the calorimeters. They provide bending power for the Muon Spectrometer.

The **solenoid** is aligned to the beam axis and provides a 2 T magnetic field, it is as thin as possible (0.66 X_0) to minimise the impact on the ECAL energy resolution. It is made of a single layer coil, wound with a high-strength Al stabilised NbTi conductor. The inner and outer diameter of the solenoid are respectively 2.46 m and 2.56 m. Its length is 5.8 m. The flux of the magnetic field is returned by the steel of the ECAL.

The **toroids** produce a magnetic field of 0.5 and 1 T respectively for the barrel and end-caps region sustained by a 25 kA current. Every toroid in the barrel has its own and separated cryostat, while in the end-cap they all have common cryogenic system. The toroids are made of a mixture of copper, niobium, aluminium and titanium.

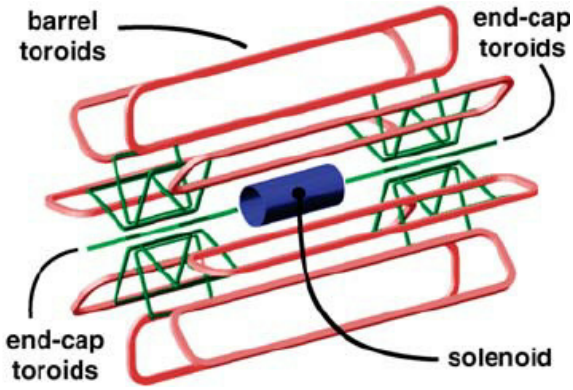

Figure 27: Cut-away view of the Muon Spectrometer

3.2.6 Forward detectors

There another four smaller detectors in the forward region that help with the measurement of the luminosity. At 17 m from the interaction point (in both directions) there is LUCID (LUminosity measurement using Cerenkov Integrating Detector) a detector designed to detect the proton-proton scattering in the forward region ($5.6 < |\eta| < 6.0$). It is the main online relative-luminosity monitor for ATLAS. Located at 140 m, there is the ZDC (Zero-Degree Calorimeter). It's made of layers of alternating tungsten plates and quartz rods. It covers a range of pseudorapidity of $|\eta| > 8.2$. It's helpful for heavy-ions alignment. The third detector is AFP (ATLAS Forward Proton) that is used to identify protons that emerge intact from the proton-proton collisions. It is composed of tracking and timing silicon detectors 2 mm from the beam at 210 m from the ATLAS interaction point. Last, at 240 m lies the ALFA (Absolute Luminosity For ATLAS) detector. It is made of scintillating fibre trackers as close to beam as 1 mm.

3.2.7 Trigger and data acquisition

Collisions happens at every bunch crossing with a frequency of 40 MHz. On average at each crossing there are 50 collisions, as shown also in figure 18, and at a instantaneous luminosity of $\approx 2 \times 10^{34}$ cm^{-2}s^{-1}. This large amount of data (almost 1.5 PBs^{-1}) can not be processed or stored. Therefore triggers are necessaries, that reduce this rate to approximately 1000 Hz, almost a factor 10^5. The ATLAS trigger are designed to decide what events are worth keeping for the analysis in the shortest time possible.
This is implemented by the Trigger and Data Acquisition (collectively TDAQ) systems [91, 92] and the Detector Control System (DCS). These are divided in sub-system associated to the various sub-detectors. During run 1 the trigger had a system composed of three different levels more and more selective: Level 1 (L1), Level 2 (L2) and Event Filter. The first was hardware-based while the other two were software based in the High Level Trigger (HLT). Due to the higher luminosity in run 2, the triggers have been upgraded. In the new trigger system for the run 2 L2 and Event Filter have been merged into a single HLT. The L1 is composed of different subtrigger: L1 calorimeter (L1Calo), L1 muon (L1Muon), Central Trigger Processors (CTP) and the new L1 topological trigger modules (L1Topo). This new part of the trigger

calculate event topological quantities between L1 objects within the L1 latency time ($\approx 2\mu$s) and use those to perform selections. For example it is possible to compute invariant masses or angular distances between objects. Another improvement is that now L1 can sustain a bandwidth of 100 kHz and HLT up to 1 kHz. In figure 28 is reported a scheme of the trigger flow.

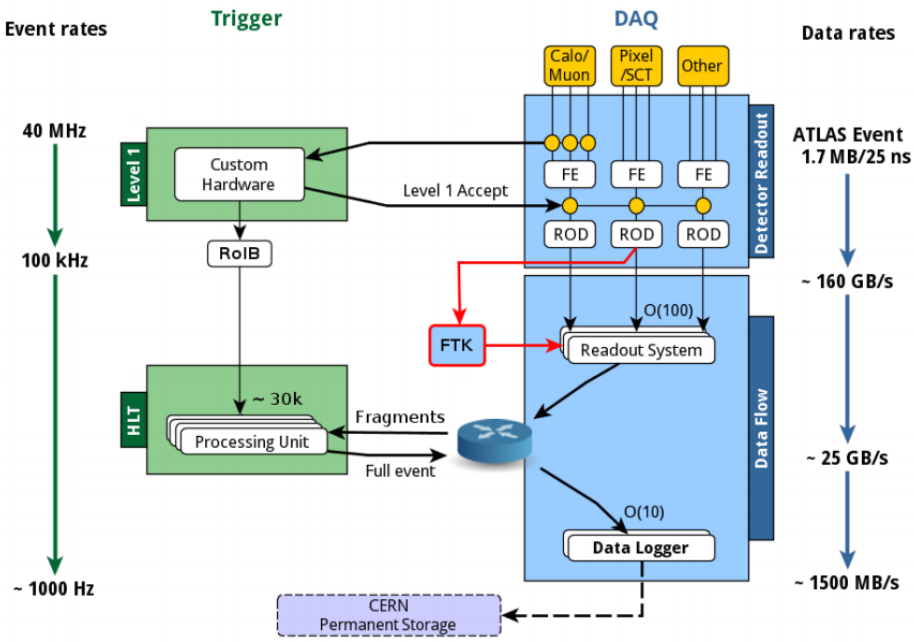

Figure 28: ATLAS TDAQ System in Run 2

L1 uses informations from just a part of the detector with reduced granularity. L1 takes a decision, using information from the calorimeters and the muon spectrometer to identify high p_T muons, electron/photons, jets, τs decaying into hadrons and missing energy, in less than 2.5 μs . L1 reduces the rate to 100 kHz.
When an event passes L1 a signal is sent back to the rest of the detector causing the data associated with the event to be read out for all components of the detector. In order to reduce the quantity of transferred data Regions-of-interest (RoI) are constructed, these are regions of the detector where the L1 trigger has identified possible object.

HLT uses fast algorithms to access RoIs to read informations such as coordinates, energy and type of signature to reduce once again the rate of events. The HLT output is 1000 Hz with a processing time of 0.2 s on average. Events passing also the HLT are permanently moved to the CERN's storage.
During all the data taking period it is active the Detector Control System (DCS) that monitors every aspect of the ATLAS detector, from the value of magnetic fields to the humidity and temperature. It also checks for abnormal behaviour and permits to operate safely all the hardware.

4 The ATLAS Pixel Detector

As already introduced in 3.2.2, the ATLAS Pixel detector is the innermost layer of the ID. In the following section the geometry and layout of the detector will be described. The sensor technology, the electronics that reads the signal, and the mechanics that hold the modules will also be described. Finally the calibration used and the performance of the pixel during Run 2 will be introduced.

4.1 General Layout

The Pixel Detector [93] is made of four barrels layer and three disk layers per end cap (six in total). With the addition of the IBL [94] the first layer is now at 33.5 mm from the beam axis, where the beam pipe has been reduced inner radius size of 23.5 mm, in order to accommodate the new layer of pixels. Its coverage goes up to $|\eta|< 2.5$, while it covers the full azimuthal angle (ϕ). The nominal pixel size is 50μm in ϕ direction and 250μm in z direction for the IBL, with a depth of 200 μm for the planar sensors and 230 μm for the 3D, instead for the other layers (B-Layer, Layer 1 and Layer 2) the size is 50 μm in ϕ direction and 400 μm in z direction, with a depth of 250μm. The base element of the detector are pixel modules, composed of the silicon sensor itself, the front-end electronics, and the flex-hybrids with control circuits. There are 46,080 pixel electronic channels in a pixel module and 43,000 in a IBL module. Pixel modules are connected with FE-I3 front-end chip for the read out, while the IBL modules use a FE-I4B, that allows also for a larger active area. The pixel system is then composed in sub-elements called staves (in the barrel) and sectors in the disks that contains pixel modules, the mechanics and cooling system. Staves and sectors are then mounted together on supporting structure to form the barrel and the disks. The barrel modules are mounted on the staves overlapping in z in order to avoid any gap in particle detection, at least for particles with $p_{\mathrm{T}} > 1$ GeV, and facing the beam pipe. Additionally the IBL modules are tilted by 14° in the azimuthal direction, as shown in figure 30, while the other pixel layer by 10° , achieving overlap in the active area, and also helping in compensate for the Lorentz angle drift of the charges inside the detector. The IBL staves are composed each of the two types of sensors: 12 modules with planar sensors in the middle and 4 with 3D

sensors at each end of the staves, as shown in figure 31. Barrel and endcap disk are mounted on a carbon-fiber support. Services, such as electronics, optics, and cooling, are connected within service panels from patch panels (Patch Panel 0-PP0) at the ends of the supporting spaceframe to the end of the Pixel Support Tube. Services connections are made at the end of the Pixel Support Tube at Patch Panel 1 (PP1), while connections of external services are at additional patch panels (PP2, PP2, and PP4), situated outside the ID.

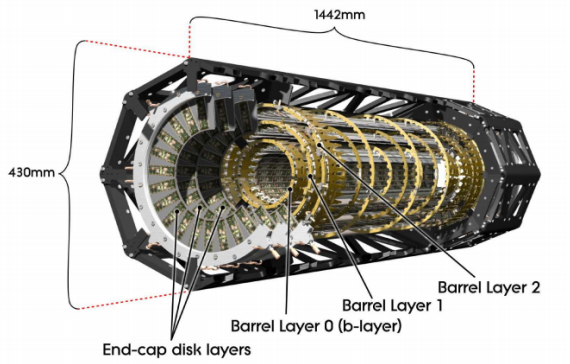

Figure 29: Schematic view of the pixel detector consisting of barrel and end cap. The IBL is not shown

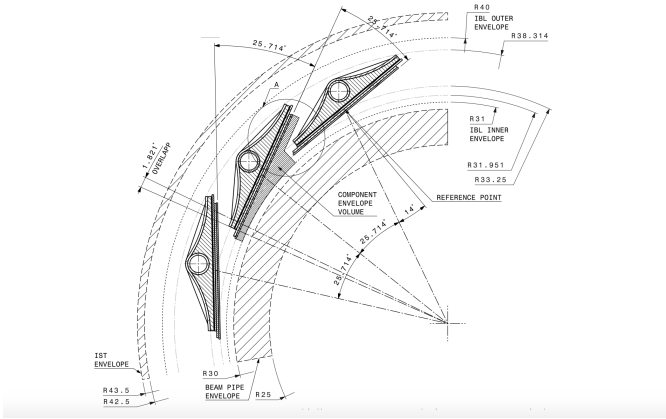

Figure 30: $r - \phi$ section of the IBL barrel showing the staves, how they are inclined and overlap. Also showing the beam pipe and the services

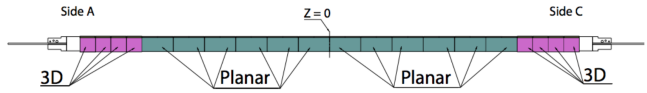

Figure 31: Layout of the IBL: schematics of a stave containing both IBL planar modules and 3D modules.

The main parameters of the Pixel Detector are summarized in table 6, 7 (barrel) and 8, 9 (disk). An important aspect that has been considered during the production of the pixel detector is the material budget: the amount of material that compose the detector. In fact this must be optimized in order to reduce multiple scattering of incoming particles and optimize tracking and vertex performances. For the IBL the radiation length averaged over is 1.88% χ_0 for tracks perpendicular to the beam axis originating in $z = 0$, while for the other pixel layer it is 30% more. IBL small radiation length was achieved with new technology, including: staves with lower 974 density; CO_2 evaporative cooling instead of C_3F_8, allowing for a more efficient cooling in terms of mass and pipe size; new modules with lower mass; and using aluminum conductors for the electrical power services.

Layer Name	Mean Radius [mm]	Number of Staves	Number of Modules	Number of Channels
IBL	33.5	14	20 (12 planar+8 3D)	43,000
B-Layer	50.5	22	13	46,080
Layer 1	33.5	38	13	46,080
Layer 2	33.5	52	13	46,080

Table 6: Basic parameters for barrel pixel detector layers.

4.2 Sensors

Sensors are the sensitive part of the Pixel Detector, and work as a solid-state ionization chamber for charged particles. Sensors must have high geometry precision and granularity. Another important requirement is a high charge collection efficiency, while at the same time

Layer Name	Active Area [m^2]	Pixel Size [μm]	Sensor Thickness [μm]	Pixel array (columns rows)
IBL	0.15	50×250	200/230 (p/3D)	336×80
B-Layer	0.28	50×400	250	160×18
Layer 1	0.49	50×400	250	160×18
Layer 2	0.67	50×400	250	160×18

Table 7: Basic parameters for barrel pixel detector layers.

Layer Name	Mean z [mm]	Number of Sectors	Number of Modules	Number of Channels
B-Layer	495	8	6	46,080
Layer 1	580	8	6	46,080
Layer 2	650	8	6	46,080

Table 8: Basic parameters for disk pixel detector layers.

Layer Name	Active Area [m^2]	Pixel Size [μm]	Sensor Thickness [μm]	Pixel array (columns rows)
B-Layer	0.0475	50×400	250	160×18
Layer 1	0.0475	50×400	250	160×18
Layer 2	0.0475	50×400	250	160×18

Table 9: Basic parameters for disk pixel detector layers.

being resistant to high dose of radiation damage from ionizing and non-ionizing particles. The requirements are met with a careful design of the structure of the sensor and the bulk material. In the ATLAS pixel detector there are two different technologies implemented: planar and 3D.

Planar Sensors The Pixel sensors are arrays of bipolar diodes placed on a high resistivity n-type bulk close to the intrinsic charge concentration, they are n+-in-n sensors. This is obtained by implanting on each

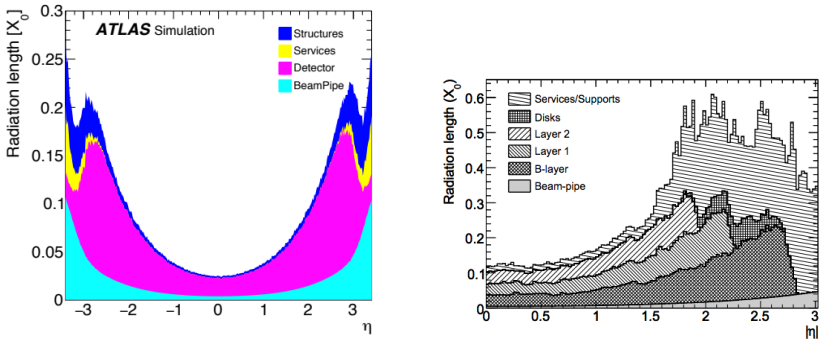

(a) (b)

Figure 32: Radiation length of the IBL (a) and pixel detector (b) versus pseudorapidity showing the contribution from the different layers, beam pipe, and services. (a) from ref. [94] and (b) from ref. [80].

side of the wafer high positive (p^+) and negative (n^+) dose regions. Due to concentration gradient electrons and holes from the n and p type side are recombined, forming a small depletion region. This is expanded with a reverse bias applied on the sensor. The voltage at which point the sensor is fully depleted in the bulk it is called Depletion Voltage. This is proportional to the doping concentration and depends also on the thickness of the bulk, and its resistivity. Charges and holes produced by the ionization of charged particles passing through the sensor are then free to reach the electrodes and can be detected by the electronics. Figure 33 shows the depletion region for sensors with n and p type bulk.

Planar IBL sensors are 200 μm thick n-bulk, while for the other pixel layers the sensors are 256 ± 3 μm thick. In both cases the n^+ implants are on the read-out side and the p-n junction on the back side . The n-side is made in order to match the FE-I4B [95] read out electronics, for IBL, while FE-I3 [96] for the other layers. Guard-rings are positioned on the p-side: 13 in the IBL and 16 on the other pixel layers. The module's edges are kept at ground in order to avoid discharge in the air, and because of this the sensors at the edges are not depleted. Inactive edge has also been reduce from 1100 μm to 200 μm between the outermost pixels and IBL. Pitch size in IBL is 250 μm by 50 μm, while in the two central columns of the double-chip sensor they are

extended to 450 instead of 250 μm in order to cover the gap between the two adjacent FE-I4B chip. A schematics of the layout is in figure 34.

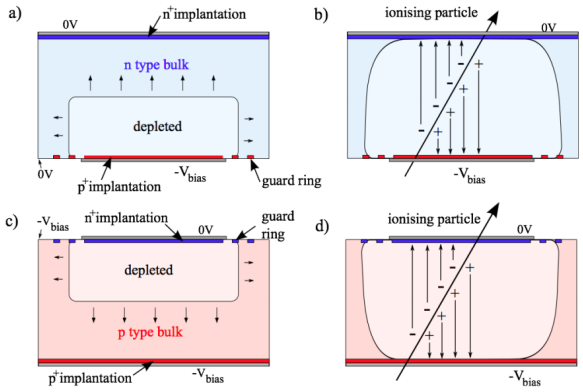

Figure 33: Schematics of a n (top) and p (bottom) type bulk sensor showing the growth of the depletion region.

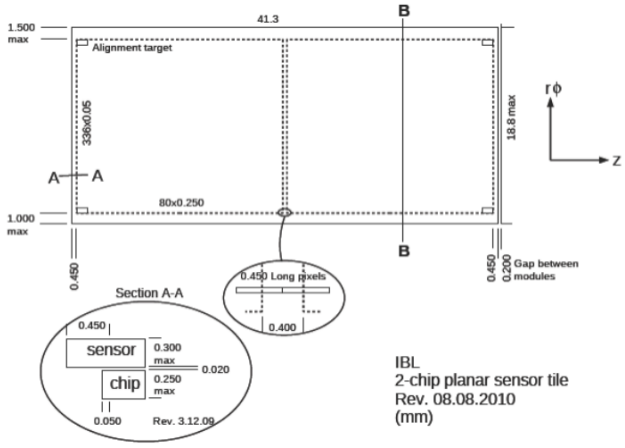

Figure 34: IBL double-chip planar sensor tile.

In the other layers it is similar, and we have a nominal pitch of 400 μm and 50 μm against long pixels with a pitch of 600 μm and 50 μm. All the read-out channel in a tile are connected to a common structure for the bias voltage via a punch-through connection that provides DC-coupled bias to each channel. This allows to bring the bias voltage to

the sensors without individual connection, but still having isolation between pixels.

3D Sensors In order to sustain the high dose of radiation that the pixel has and will receive, new technologies have been developed. 3D sensors [97] have been developed to sustain these problems, and also to keep low power consumption even after irradiation.
3D sensors are silicon sensors with electrodes that are columns that penetrate the bulk, reducing the drifting path while keeping the same signal size. This means that the electric field is parallel to the surface instead of perpendicular. Each column is $\sim 12\,\mu$m wide and closer to each other, dramatically reducing the depletion voltage (it can be as low as 20 V) and charge collection distance, reducing the probability of charge trapping. The low depletion voltage also implies low leakage current, therefore requiring less cooling. Signal size is still determined by the thickness of the sensor, meaning signal with similar amplitudes than the planar sensors. However signal is much faster.
The 3D sensor in the IBL were produced with a double-sided technology [citation needed]. In a p-bulk sensor columns of electrodes were implanted on both sides. Sensor bias is applied on the back side (p^+), as in planar sensors. Figure 35 shows the schematics of 3D sensors as built by the two main manufacturers. Each pixel has two readout (n^+) columns with an inter-electrode spacing between n^+ and p^+ columns of 67 μm. Figure 36 shows the electric field in a 3D pixel grid.

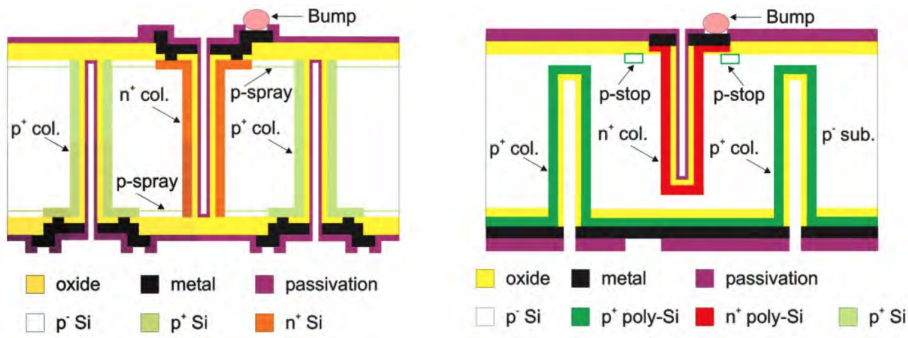

Figure 35: IBL 3D sensors schematics from the two main manufacturers: FBK (a) and CNM (b).From ref. [94].

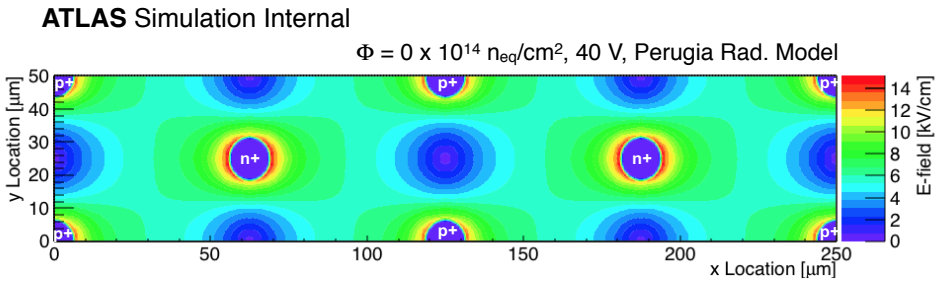

Figure 36: Electric field in a IBL 3D sensors. From ref [98].

4.3 Electronics

A schematics of the electronics in the Pixel layers is shown in figure 37. For each module there are 16 front-end chips, FE-I3, arranged in two rows of 8 chip each. IBL instead uses FE-I4B. The read-out of the chip is done by the Module Control Chip (MCC), and data are transferred between chips and MCC thorough Low Voltage Differential Signaling (LVDS) serial links. Modules are then connected with optical fiber links (opto-links) to the Read-out Drivers (RODs) of the off-detector. Power supply is provided from a single DC supply over long cables, requiring low-voltage regulators boards.

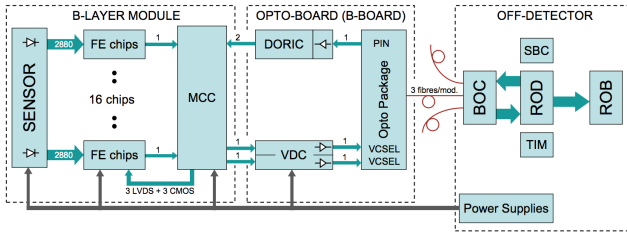

Figure 37: Pixel Electronics schematics.

Front-End Chip In the ATLAS detector there are two types of Front End: FE-I4B for the IBL modules and FE-I3 for the other layers. FE-I3 readout chip contains 2880 pixel cells of 50×400 μm^2 arranged in a 18 matrix, while FE-I4B contains 26,880 pixel cells of 50×250 μm^2 ordered in a 336×80 matrix. Each cell contains an analog block where the signal is amplified. The digital readout save a timestamp at the leading edge (LE) and at trailing edge (TE) and

sent it to the buffers and uses the difference to evaluate the Time-over-Threshold (ToT). This is proportional to the signal charge and can therefore be used to estimate amplitude.
Information can be stored in the chip for latency up to 255 LHC clock cycles of 25 ns, and it is saved if a trigger is supplied within this time. FE-I3 chips have a read out in 8 bit, giving ToT signals from 0 to 255, while FE-I4B have 4 bit readout, giving a range in ToT from 0 to 15.

Module Control Chip (MCC) The MCC works on three different aspects: first of all they load parameters and configurations into the Front-End chips, they also distribute timing signal, L1 triggers, and resets, and finally they read out the FE chip. MCC must be set up at the beginning of each run of data taking, and during when a L1 trigger command arrives to the MCC, a trigger is sent to the FE, as long as there are less than 16 events stored, otherwise the event it is not saved. Information is sent back with also the number of missed events in order to keep the synchronization.

Optical communication Opto-link make possible communication between the modules of the detector and the off-detector electronics. This is made with optical fiber, and were designed in order to have electrical decoupling and to minimize the material budget. The two main components are the opto-boards, mounted on the module side, and the Back of Crate Card (BCC), on the off-detector side. Signal transmission from the modules to the opto-boards is made with LVDS electrical connections. Read out bandwidth depends on the LHC instantaneous luminosity, on the L1 trigger, and the distance from the interaction point. Electrical-to-optical conversion happens on the opto-board. The bandwidth of the opto-link has been improved during run 2 in order to keep up with the increase in luminosity.

Data Acquisition System In the ATLAS detector the Data Acquisition System (DAQ) has a part for each sub system, called Read Out Drivers (ROD), and a part common to the whole detector, called Read Out System (ROS). The Pixel ROD is a 9U-VME module and its purpose is to transfer the data from the electronics on the detector to the ROS system. ROD modules are put in crates, 9 of these crates are present and each one can contain 16 ROD for a total of 14 RODs modules for the IBL (one crate), 44 modules (three crates) for B-Layer, 38

modules for Layer-1, 28 modules for Layer-2 (together in four crate), and 24 modules (two crates) for the disk. In the crates is also present the interface with the trigger system. Data are routed directly from the ROD to the ROS with optical links. Commands, trigger, and clock are transmitted with one down link, while event readout goes through another one (or two) up-link. Read-out is done with "data-push", meaning that when buffers are full there is no mechanism to stop transmission (busy). This means also that each component of the chain (from FE to ROD) always transmit at maximum rate. Each step also monitors the number of events received and the triggers sent, if these are different by a certain amount, triggers are blocked and empty events are generated.

4.4 Calibration

ToT is the final output of the sensors, however this must be converted in charge. In order to do so it is necessary to calibrate the pixels. In order to do so there are different step: first it must be calibrated the time walk (assign the event to the correct bunch crossing), threshold, and finally the ToT-to-charge conversion.

Time Walk Hits are digitized by the pixel modules with respect to the master clock, which is also synchronized to the LHC clock. Hits are saved only if they happens within one clock cycle, meaning in a time interval of 25 ns. It can happen that small signal charges when passing through the amplifier cross the discriminator threshold with a time delay with respect of the signal reference that might be a large signal. This small signal charge will then be assigned to the wrong bunch crossing. This effect is the time walk. To estimate the time walk it is therefore needed to measure the difference in time between when the signal charge arrives at the input of the amplifier and the time when amplifier output crosses the discriminator threshold. This is measured by injecting a known charge directly from the FE chip with an adjustable delay, that allows to change globally the injection time with respect to the chip master clock. In this way it is possible to decrease the time difference between the charge injection and the digitization window. A scan of the delay is performed and the hit detection probability is measured. The t_0 time is defined as the time

for a 50% hit detection probability plus a safety margin of 5 ns. A small t_0 means that the time between the charge injection and the digitization time window is larger. Figure 38 (a) shows the hit detection probability for on pixel as a function of the delay time for a fixed charge of 10 ke^-. Figure 38 (b) instead show the distribution of t_0 for all the pixel array as a function of injected charge. Time walk is visible for small charges, where t_0 is small, meaning that there is a large difference in time. Therefore small charge hit will be out of time. In order to recover them, in the pixel FE-I3 all hits below a certain ToT value are duplicated in the previous bunch crossing. Instead in the FE-I4B hits with a ToT of 1 or 2 are duplicated in the previous bunch crossing only if they are near-by a larger hit (ToT$>$ 3). This is because small charge hit are usually due to charge sharing.

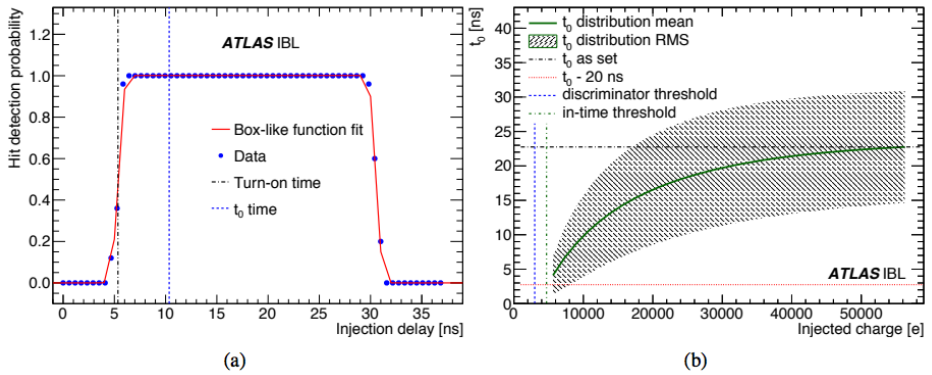

Figure 38: (a) Single pixel hit detection probability for one pixel during t_0 scan with injected charge of 10 ke^-. (b) distribution of the measured t_0 as a function of the injected charge for an entire chip. Solid line is the average of all measurement and shaded area is the RMS of the t_0 obtained. From ref. [94].

Threshold Signal charge is saved when it pass a module threshold. This threshold has to be measured and it is done by injecting a known charge in the FE and measuring where there is a 50 % hit efficiency, both at global and pixel level. Figure 39 shows the measured threshold (left) and equivalent noise charge (ENC, right) for each pixel in the IBL detector, after tuning the threshold to 2500 electrons at the end of 2016. Tuning of the threshold has been done constantly during Run 2

operations. In fact, due to radiation damage effects on the electronics, the actual threshold drift away from the nominal value. This is possible to be seen in figure 40, where it is shown the measured threshold over all the pixels in IBL as a function of integrated luminosity and the corresponding radiation sustained (total ionizing dose TID). Regular re-tuning helps to recover the reduction in the threshold.

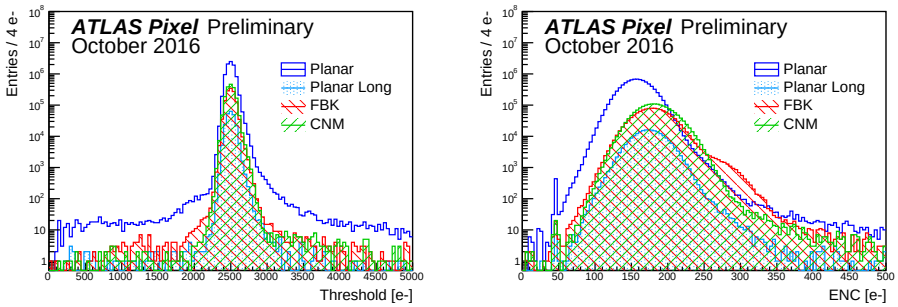

Figure 39: Measured threshold and equivalent noise charge (ENC) for pixel in the IBL detector, divided per sensor type, after tuning at the end of 2016 with a threshold of 2500 electrons. From ref. [99].

ToT Tuning and Calibration The Time over Threshold is the final output of the digitizer. It is a integer number from 0 to 15 (for IBL) and from 0 to 255 (on the other pixels). ToT must be first tuned at some value in order to have a coherent response between all the pixels, then it must be calibrated to give the same results for all the signal charges above the threshold. Calibration is done using a fit function. Threshold tuning is also repeated after the ToT one because the latter changes the threshold.
Tuning is done by injecting a know charge and asking that the output is a given value of ToT. For the three outermost pixel it is injected a 20k e^- charge and it is set 30 ToT. Tuning is done in three steps: first it is used an algorithm to tune the average ToT for each Front End; then it is used another algorithm that tunes the ToT at pixel level, while keeping the same average ToT per FE, this allows to reduce the RMS of all the responses; finally any badly tuned FE is identified and the tuning procedure repeated. This allows to have a response from all the pixels that it is the same within a sigma of $\sim 2\%$.

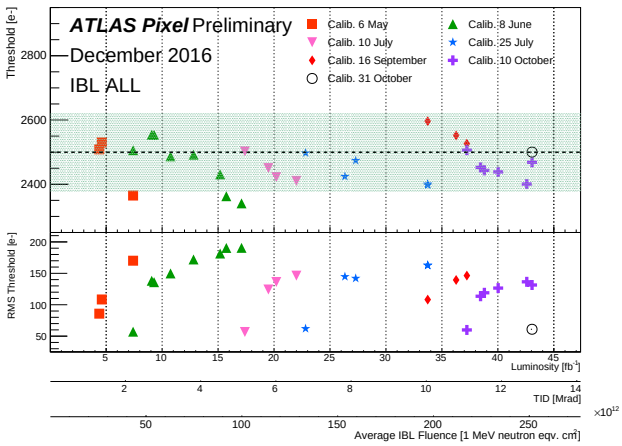

Figure 40: The evolution of the mean and RMS of the measured threshold over all pixels in the IBL detector as a function of the integrated luminosity, the corresponding total ionizing dose (TID) and the average IBL fluence in 2016, as measured in calibration scans. The threshold was tuned to 2500 electrons. Radiation effects caused the measured threshold to drift downward with integrated luminosity, but short period of regular re-tuning brought the mean threshold back to the tuning point. Each color / symbol series corresponds to a single tuning of the detector. The shade indicates ±5% of the tuning point. From ref. [99].

After tuning the response is the same for all the pixels, but only for the value of the injected charge. However the response to the charge of the sensor is not linear and therefore it is not know what ToT correspond to what charge. The response is almost linear around the tuning point, but it is more quadratic at low ToT and reaches a plateau at high ToT. Calibration is done at module level. In order to have a map of the values it is used a fit function, and the ToT is the obtained from the formula:

$$ToT = a_0 \frac{a_1 + Q}{a_2 + Q} \tag{74}$$

Where Q is the charge, and a_0, a_1, and a_2 are the fit parameters. The fit is done starting injecting charge and divide the pixel by the response in ToT, as shown in figure 41 (a). The mean of each peak is then reported and an error is assigned as the width of the distribution. These values are then graphed as shown in figure 41 (b) and used to

fit the function and obtain the parameters a_0, a_1, and a_2.

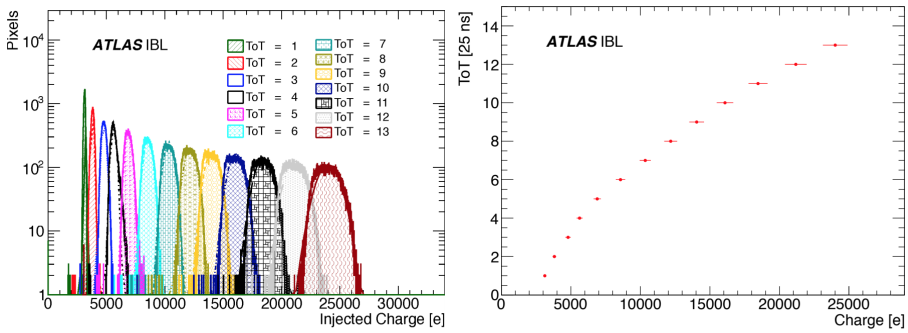

Figure 41: (a) Number of pixels with a certain Time-over-Threshold (ToT) given a certain charge injected. (b) Charge to ToT calibration curve, obtain from the mean and width of plot in (a). From ref. [94].

Calibration has been changed many times during the Run 2 in order to recover effects due to the radiation damage. In addition the mean value of the tuning point for the ToT shifts also because of the effects of the radiation, in the same way as for the threshold, and needs to be adjusted. Figure 42 shows the evolution of the mean ToT over all pixels as a function of time during the tuning scans.

Table 10 summarize the threshold and ToT tuning of the pixel detectors during Run 2 operations.

4.5 Cooling

An important aspect to consider to reduce the effects of radiation damage, in particular the increase in leakage current, is the cooling system. Silicon detector should be kept at low temperature (from few degree to 10s of degree Celsius below the zero). IBL cooling is based on CO_2, while the other pixels is based on C_3F_8. The cooling is a two-phased liquid-vapor mixture that goes from USA15 service cavern to the detector and back. The cooling plant in the cavern condensate the returning liquid and send it back to the detector. A schematic is shown in figure 43. When the CO_2 evaporates when heat is applied, depending on the pressure. By controlling the pressure in USA15 is possible to set control the cooling, that can go from 15 °C to −40 °C. During the Run 2 operation the cooling has been changed to recover

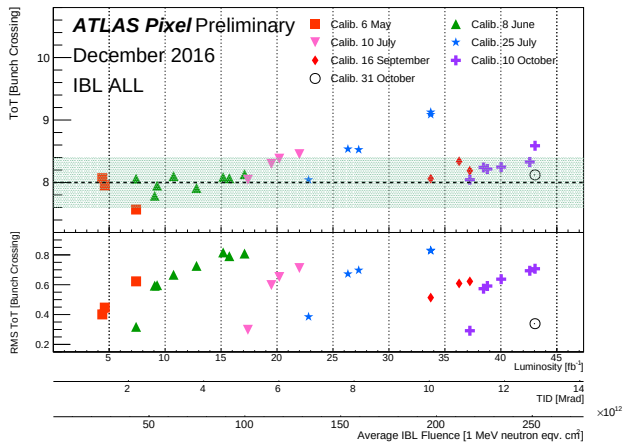

Figure 42: The evolution of the mean and RMS of the measured Time-over-Threshold (ToT) over all pixels in the IBL detector as a function of the integrated luminosity, the corresponding total ionizing dose (TID) and the average IBL fluence in 2016, as measured in calibration scans. The ToT was tuned to 8 bunch crossings (1 BC = 25 ns) for 16k electrons. Radiation effects caused the measured ToT to drift upward with integrated luminosity, but short period of regular re-tuning brought the mean ToT back to the tuning point. Each color / symbol series corresponds to a single tuning of the detector. The shade indicates ±5% of the tuning point. From ref. [99].

effects of radiation damage. However too low temperature can be problematic for the mechanics due to the thermal dilation between the cold (during operation) and warm (during shutdown) detector. Table 10 also shows the temperature of the sensors during Run 2.

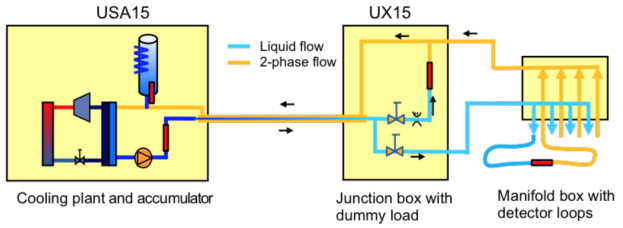

Figure 43: Cooling schematics for the IBL.

Sensor	IBL planar	IBL 3D	B-Layer	Layer 1	Layer 2	Disks
			2018			
Tuning point [ToT]	10	10	18	30	30	30
Analogue Threshold [e]	2000	2000	4300 /5000	3500	3500	3500
Digital Threshold [ToT]	0	0	3	5	5	5
Temperature [° C] -20	-20	-20	-20	-20	-20	
			2017			
Tuning point [ToT]	8	8	18	30	30	30
Analogue Threshold [e]	2550	2550	5000	3500	3500	4500
Digital Threshold [ToT]	0	0	5	5	5	8
Temperature [° C] -20	-20	-20	-20	-20	-20	
			2016			
Tuning point [ToT]	8	8	18	30	30	30
Analogue Threshold [e]	2550	2550	5000	3500	3500	3500
Digital Threshold [ToT]	0	0	5	5	5	5
Temperature [° C] 15	15	-10	-10	-10	-13	
			2015			
Tuning point [ToT]	10	10	30	30	30	30
Analogue Threshold [e]	2550	2550	3500	3500	3500	3500
Digital Threshold [ToT]	0	0	3	3	3	3
Temperature [° C] -3	-3	-2	-2	-2	-7	

Table 10: Basic parameters for disk pixel detector layers. Temperatures are an average over the whole period and over all sensors.

4.6 Clusterization

Neighboring pixels in a given sensor are grouped together with a signal above the detection threshold. A spatial position is assigned to them, and the resulting object is called a *hit* or cluster and its position is called *space-point*.
A connected component analysis (CCA) [100] is used for pixel clustering. Two pixels are considered neighbors if they share at least a corner, this means that each pixel has 8 neighbors. A group of connected pixels is called cluster. In order to refine the position of where the charged particle crosses the module, the information from the charge collected in each pixel is used. An interpolation is done between the first and last rows and columns of the cluster, weighted for the charge of each pixel. The position of the crossing of the particle is then defined

as:

$$x_{\text{cluster}} = x_{\text{centre}} + \Delta_x(\phi, N_{\text{row}}) \cdot \left[\Omega_x - \frac{1}{2}\right] \tag{75}$$

$$y_{\text{cluster}} = y_{\text{centre}} + \Delta_y(\theta, N_{\text{col}}) \cdot \left[\Omega_y - \frac{1}{2}\right] \tag{76}$$

where Ω_i is given by

$$\Omega_{x/y} = \frac{q_{\text{last row/col}}}{q_{\text{first row/col}} + q_{\text{last row/col}}} \tag{77}$$

and q is the charge collected in a given row or column of pixels. The parameter $\Delta_{x/y}$ is a function of the projected incident angle with respect to the sensor surface.
In the case of dense environment, as shown in figure 44, there is an high probability of close-by tracks entering the same pixels cluster. An additional algorithm then try to correctly split the clusters, in order to resolve the nearby tracks. This is done with a neural network (NN) algorithm [101, 102] that estimates the true local x and y positions for each particle in a given cluster. The process is used also for single particle cluster, in order to improve the resolution. Figure 45 shows the distance between the cluster position and the track associated to it, the so called *residual*, for cluster with a 3 pixel width where it was applied only the CCA algorithm (dashed) and where it was also used the NN (solid).

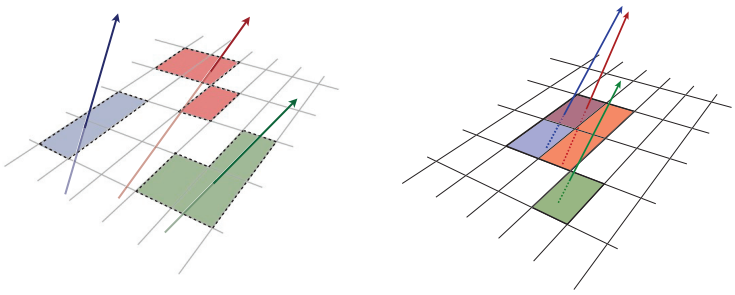

(a) (b)

Figure 44: Schematics of (a) tracks enough far away to have separate clusters, and (b) tracks close-by, with sharing pixels.

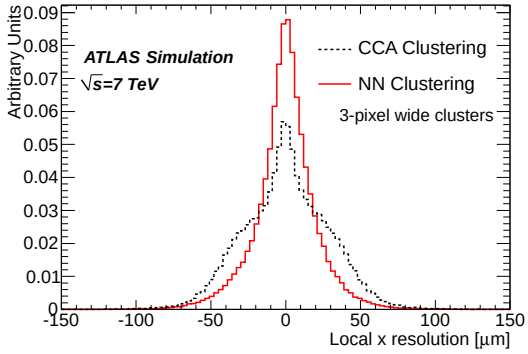

Figure 45: The cluster residual in the local x direction for clusters with a width of three pixels in the x-direction reconstructed with the CCA clustering algorithm (dashed line) and the NN clustering algorithm (solid line). From ref. [102].

5 Radiation Damage Effects on the ATLAS Pixel Detector

As the detector component closest to the interaction point, the ATLAS Pixel detector has been exposed to a significant amount of radiation over its lifetime. Radiation creates defects in the sensors and, over time, reduce their efficiency, causing a degradation of the performance of the whole detector to reconstruct physical quantities. Current ATLAS Simulations don't account for this kind of effects, therefore causing a bias in all the results. Therefore in order to reduce the discrepancy it is important to have a set of simulations that take into account the radiation damage. This is done in the simulation by implementing a new *digitizer* [98], the step in the simulation where the conversion of energy deposit (from Geant4) into digital signals happens. In the digitizer the charge converted is reduced to account for the loss of efficiency.
In section 5.1 I will illustrate how radiation damage degrade silicon detectors and what are the consequences on the performance of a detector. In section 5.2 I will present the current status at the end of Run 2 of the ATLAS pixel detector and its level of damage sustained. The description of the digitizer and how it was implemented is described in section 5.3, while its predictions are compared to data in section 5.4.
During my PhD my main task was the implementation of the digitizer in the standalone software Allpix and in the ATLAS common software. Also I produced most of the validation plot with data from Run 2.

5.1 Radiation Damage

Radiation passing through the detector damages the sensors. These effects are caused by the appearance of defects in either the bulk structure, where crystal atoms are displaced, or the surface [103]. Surface defects imply an increase of the interface oxide region charge, which saturates after $\sim$ kGy (the ionizing dose). The macroscopic effects due to damage in the bulk are increase in leakage current, change in the depletion voltage and charge trapping. A brief description of the nature of the effects due to bulk damage will be presented here.

5.1.1 Microscopic Nature of Radiation Damage

Initial concentration of defects are first introduced in the crystal of the silicon sensors depending on the purity of initial wafer. These defects introduce localized energy levels that can, if within the forbidden band gap, change the electrical characteristic of the bulk. If a particle with an high enough energy (around $\mathcal{O}(10)$keV) [104] crosses the detector, it is possible that it will collide with an atom of the lattice, and if there is enough energy, it will remove it from its position, leaving an empty space called *vacancy*, while the atom will end on a position non in the lattice, called *interstitial* defect. This pair of displaced atom-hole is called a *Frenkel Pair*. If the atom itself has enough energy it might release energy by ionization first, and then by nuclear collisions, generating more defects. The primary of these collisions is called *Primary Knock on Atom* (PKA). If many Frenkel pairs are grouped together they can build clusters[105].
Different particles interact in different ways with the lattice of the sensor: charged particles tend to scatter via electromagnetic interaction with the atoms, while neutrons interact directly with the nuclei. In order to compare the damage from different types of particles with different energies, radiation damage is scaled to the *Non-ionizing Energy Loss* (NIEL), which is the component that causes the damages to the lattice. In semiconductor *ionizing* damage is generally fully recovered. Particles can lose energy with both non-ionizing and ionizing processes, in different ratio depending on the type of radiation involved. NIEL then summarizes the energy deposited from only the processes that cause non reversible damage on the lattice of the sensor, using as reference 1 MeVneutrons. In this way a fluence ϕ_{phys} from an arbitrary particles is equivalent to the fluence ϕ_{eq} of a 1 MeVneutron. The conversion factor k (called also *hardness factor*) between ϕ_{phys} and ϕ_{eq} must then be calculated for each specific particle and energy, and are provided as look up table [106]. Figure 46 shows the displacement damage function $D(E)$, normalized to 95 MeV mb, which correspond to the $D(E)$ value for 1 MeV neutron, because of this the ordinate axis actually represent the damage equivalent to 1 MeV neutrons.
Silicon interstitial, vacancy, and primary defects are able to move inside the crystal (they are not stable), and if they meet inside the crystal it is possible that this will lead to the creation of a cluster defect, or it is also possible that secondary point defects will be formed. This

process of traveling and combination is called *defects annealing*. This can cause energy levels in the band gaps, and can have an impact on the space charge in the depletion zone. The mobility of the defects is strongly dependent on the temperature, and therefore the changes in the detector will have a complex annealing behavior due to the many possible secondary defects.

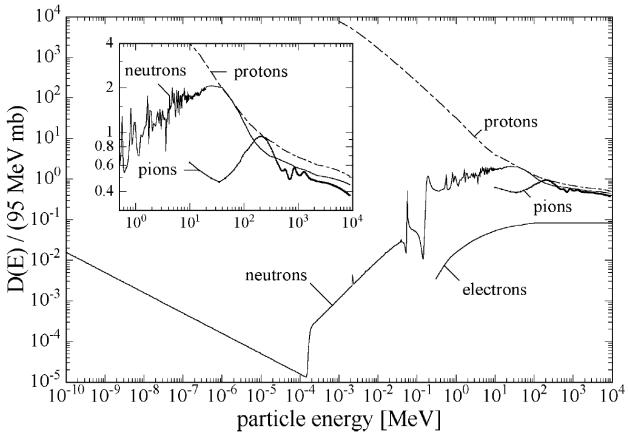

Figure 46: Displacement Damage function ($D(E)$) normalized to 95 MeV mb, for neutrons, protons, pions, and electrons. Because of the normalization to 95 MeV mb the ordinate axis represents the damage equivalent to 1 MeV neutrons. The insert is a zoom. From ref [104].

5.1.2 Leakage Current

The presence of energy levels in the band gap caused by defects in the crystal helps generating additional electron-hole pairs within the depleted region of the sensor. This leads to a decrease of the generation life time τ_g and an increase of the volume generation current I_{vol} proportional to the fluence ϕ:

$$\frac{1}{\tau_g} = \frac{1}{\tau_{g,\phi=0}} + k_\tau \phi \tag{78}$$

$$\frac{I_{\text{vol}}}{V} = \frac{I_{\text{vol},\phi=0}}{V} + \alpha \cdot \phi \tag{79}$$

with V being the volume, defined as junction area times detector thickness. Instead k_τ is the *life time related damage rate* and α the *current related damage rate*. Increase of leakage current is a problem because it increase the noise; moreover it heats up the sensor, and therefore it needs a cooling system to avoid a thermal runaway.
The two constants can also be related between them by the relation: $\alpha = en_i k_\tau$, where n_i is *intrinsic carrier concentration*. Also, it is possible to reformulate as $\alpha = \Delta I_{\text{vol}}/\phi \cdot V$.
It is important to note that α is independent of the initial resistivity of the silicon and the production method of the sensor.
Figure 47 shows that with time, after irradiation, the leakage current will anneal. It is also possible to see that it is strongly dependent on the temperature [107]. For long annealing times or high annealing temperature it is possible to parametrize the evolution of α with a function such as:

$$\alpha(t) = \alpha_i \cdot \exp\left(-\frac{t}{\tau_i}\right) + \alpha_0 - \beta \cdot \ln\left(\frac{t}{t_0}\right) \tag{80}$$

with t_0 an arbitrary time (e.g. set at 1 min), and τ_i hides the dependence on the temperature in the following way:

$$\frac{1}{\tau_i} = k_{0,i} \cdot \exp\left(-\frac{E_i}{kT_a}\right). \tag{81}$$

where E_i is a parameter set to $E_i = (1.11 \pm 0.05)$ eV. It is also worth noticing that T_a is evaluated at the temperature at which the sensor was annealed, and not the current one.

5.1.3 Effective doping concentration

A sensor is considered fully depleted when there are virtually no free carriers in the bulk, and there is an electric field that collects the charge created by ionizing particles passing trough it. The bias voltage necessary to have inside the sensor a fully depleted region is called depletion voltage, V_{depl}.
For biases below the depletion voltage, charges are recombined inside the non depleted region and can't reach the electrode. This means that in this case only the depleted part of the sensor is sensible; if this is on the side of the electrode, the sensor works but as if it was thinner. This means that there are two different behaviors: before and after

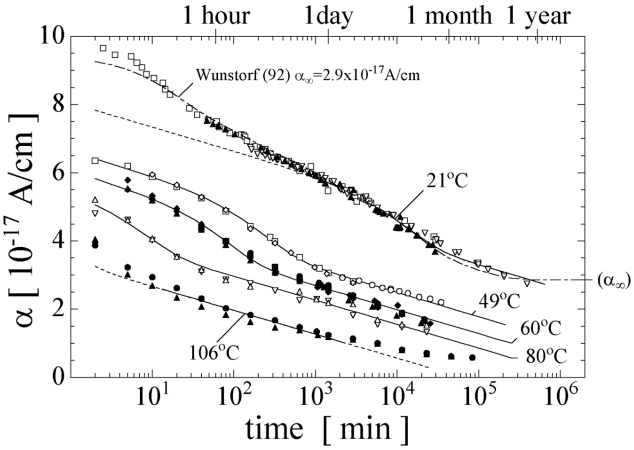

Figure 47: Rate of increase of the leakage current α as a function of the annealing time. From ref [104]. Top and bottom axis both represent time, bottom one in minute, while the top one shows the same time but in hours/days/months/years.

the depletion voltage.
The depletion voltage is also related to the *net doping* or *effective doping* N_{eff}, which is the difference of all donor like states and all acceptor like states, via the following formula:

$$|N_{eff}| = \frac{2\epsilon_0 \epsilon_{Si} V_{depl}}{ed^2} \tag{82}$$

where d is the depth of the sensor. N_{eff} can be both negative or positive, depending on whether acceptors or donors are dominating. In general, defects caused by irradiation are responsible for a change in the N_{eff}. This is due to the removal or formation of acceptor or donor, caused by the formation of either defects cluster containing acceptor or donor, or cluster assuming positive/negative charge states in the space-charge region. When irradiated, a n-doped material will decrease its N_{eff}up until a certain fluence, depending on the initial concentration, where the material becomes intrinsic. The material then with increasing the dose increase the absolute value of N_{eff}, dominated by acceptor like defects with a negative space charge, showing the behaviors of a p-type material [108]. This change in nature is called *type inversion*. Figure 48 shows the evolution of the depletion voltage for a 300 μm thick silicon sensor as a function of the fluence. This

cause the shift of the p^+ side of the sensor to the n^+ side.

Due to the mobility of the defects, the N_{eff}changes after irradiation. An empirical description of this behavior is given by the so called *Hamburg Model*:

$$N_{eff} = N_{eff,\phi=0} - (N_C(\phi) + N_a(\phi, T_a, t) + N_Y(\phi, T_a, t)) . \tag{83}$$

Where N_C describes the *stable damage* that don't depends on annealing time or temperature. This term has a dependency on the fluence such as:

$$N_C(\phi) = N_{C,\phi=0} \left(e^{-e\phi}\right) + g_e\phi. \tag{84}$$

The second term N_a describes the short-term or *beneficial* annealing and is parametrized as

$$N_a(\phi) = \phi \sum_i g_{a,i} e^{-t/\tau_{a,i}(T_a)} \sim \phi g_a e^{-t/\tau_a(T_a)}. \tag{85}$$

The last term, N_Y instead describes the *reverse annealing* which describes the increase of the full depletion voltage after few weeks at room temperature. It can be parametrized in the following way:

$$N_Y = g_Y\phi \left(1 - \frac{1}{1 + t/\tau_Y}\right) \tag{86}$$

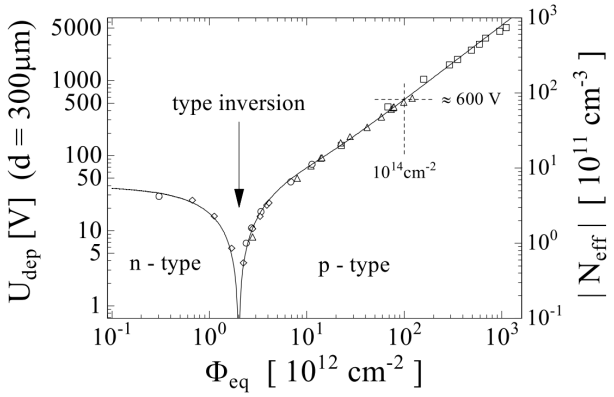

Figure 48: Evolution of the depletion voltage for a 300 μm thick silicon sensor as a function of the fluence. From [104].

5.1.4 Electric field in irradiated sensors

The electric field inside a silicon detector is a straight line as shown in figure 56. However after irradiation the profile can change. Under reverse bias drifting carriers fill some of the defects. In an n-on-n detector electrons drift toward the n^+ side while holes toward the p^+ one. This means that there is an higher changes of having negatively charged defects close to the n^+ side and positively charged defects close to the p^+ electrode. This cause an unbalance in the charge distribution causing more complicated electric field profile. The typical profile is the *double peak* [109]. An example of a double peak electric field is shown in figure 56. An important consequence of this is that at very high fluence the depletion voltage does not make any more sense. In fact here due to the double peak feature, the electric field has a not null value everywhere also at very low biases. However it is difficult to obtain a signal from the regions with a low electric field because of the trapping, causing these region to be basically non sensible.

5.1.5 Trapping

Another important effect of radiation damage is the creation inside the sensor of trapping centers. Crystalline defects introduce localized energy levels in the bulk with high capture cross section. A charge carrier trapped inside one of these levels has a re-emission time that is far larger than the charge collection time needed for a tracking detector, and therefore its signal is lost, reducing the total amplitude of the signal.
An important parameter is the *trapping time*, τ_i, that describes the (inverse of the) probability of a charge to be trapped:

$$\frac{1}{\tau_t(\phi)} = \frac{1}{\tau_{t,\phi=0}} + \gamma\phi \tag{87}$$

where γ is a coefficient that has been measured and it is $0.41 \times 10^{-6}\text{cm}^2\text{s}^{-1}$ for electrons and $0.60 \times 10^{-6}\text{cm}^2\text{s}^{-1}$ for holes. Smaller values of the trapping time for the electrons than the holes means also that holes are more likely to be trapped. This is why, in general, sensors that collects electrons instead of holes are more used in applications. These values however have a dependence on the annealing time, as found in ref [110]. Figure 49 shows the trapping constant as a function of the annealing time for two different sensors using neutrons

for irradiation and showing results for both electrons (empty marker) and holes (full marker).

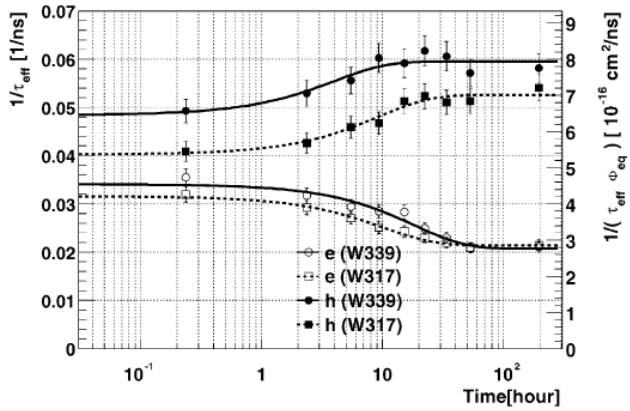

Figure 49: Evolution of the depletion voltage for a 300 μm thick silicon sensor as a function of the fluence. From [110].

5.2 ATLAS Pixel Detector Conditions

As it has been shown in the previous section, radiation induced defects change the characteristic of the sensors, in particular the voltage needed to fully deplete the sensor. Predictions of the radiation fluence that will impact the detector are then important for the performance of the detector itself.

The estimate of the fluence depends on two different key aspects: first is the modeling of the secondary particles produced in the collisions, and second, their interactions with the detector. In ATLAS this estimation is done using a combination of different simulations. Pythia 8 [111, 112] generates inelastic proton-proton scattering using the MSTW2008LO parton distribution with the tuned set of parameters A2 [113]. The produced particles are then propagated through the detector using the particle transport software FLUKA [114, 115]. Particles are transported down to an energy of 30 keVfor photons, thermal energy for neutrons, and 100 keVfor everything else.

It is very important to model correctly the geometry of the Inner Detector because of secondary particles generated in the high energy hadronic interactions in the detector. Figure 50 (a) shows the estimated 1 MeV neutron-equivalente fluence per fb^{-1}, while figure 50 (b)

shows the same information but as a function of time, divided for the 4 layers of the pixel detectors. The most important contribution comes from charged pions coming directly from the proton-proton collision. As it possible to see, there is a z dependence that can be as high as 10%. From figure 50 (b) instead is possible to notice how, even if the IBL was installed after the other pixel layers, it has received more fluence, due to its close proximity to the interaction point.

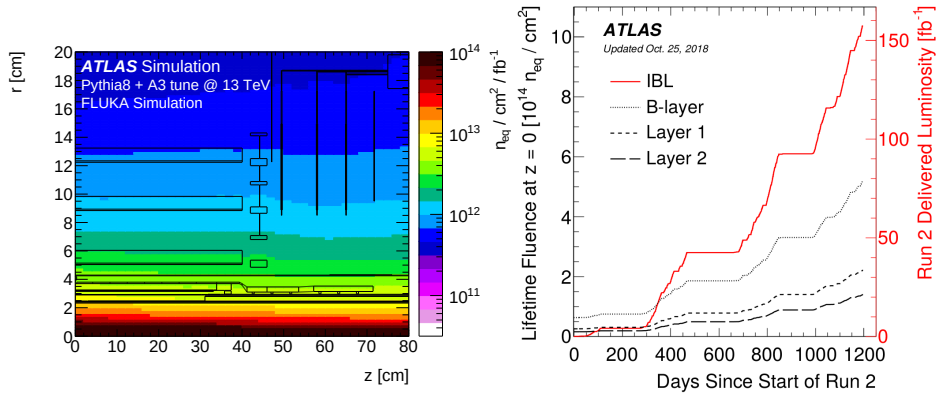

(a) (b)

Figure 50: (a) Simulated 1 MeVn_{eq} fluence prediction in the Pixel detector as a function of r and z position using FLUKA for 1 fb^{-1}. The position of the detector elements are overlaid on the figure. (b) Predictions for the lifetime fluence experienced by the four layers of the current ATLAS pixel detector as a function of time since the start of Run 2 (June 3, 2015) at $z \sim 0$ up to the end of 2017. For the IBL, the lifetime fluence is only due to Run 2 and for the other layers, the fluence includes all of Run 1. The IBL curve represents both the fluence on the IBL (left axis) as well as the delivered integrated luminosity in Run 2 (right axis). (a) from ref. [116], (b) from ref. [117].

5.2.1 Luminosity to fluence validation

Fluence is also an important input for the simulation. In order to compare simulation and data it is needed to know the correct fluence corresponding to the luminosity of the data sample. A conversion

factor from Luminosity to fluence is then needed, and in order to do that FLUKA is used again, but to validate the prediction and to estimate the systematic effects fluence is converted into leakage current. In fact the leakage current can be predicted using 80 knowing the fluence and the temperature, using a value of $E_i = (1.30 \pm 0.14)$ eV.

Properties were predicted (and measured) in time intervals of 10 minutes during the whole Run 2, and in each time period predictions were fitted to the data, divided per group of modules. This is because different modules have different distances from the interaction point along the beam axis. Predictions were also scaled to a reference temperature of 20 °C. Leakage current measurements are done with two different subsystems: the high voltage patch panel subsystem (HVPP4) and the multi-module power supply subsystem. The HVPP4 monitors the current using a Current Monitoring Board system, at the pixel level from the Iseg high voltage power supplies, while the multi-module power supply system uses a mix of custom components and commercially available components for high and low voltage for the readout electronics and sensor bias.

Figure 51 shows the measured and predicted leakage current for the IBL detector. Here each module group is 8 cm long, on both sides of the detector. M1, M2, and M3 cover the the ranges from -24 to 24 cm, while M4 cover from 24 to 32 cm (on both sides) and contains only 3D sensors. The conversion factors were obtained from the results in the grey dashed area. Figure 52 shows the extracted conversion factors as a function of z. Results are normalized to the $\phi(z = 0)$ of data. Data fitted to the Hamburg model are shown as the arrows. A 10% uncertainty is assigned, accounting for the difference between the leakage current at the operational bias voltage and the current at the full depletion voltage. This is important because after irradiation the leakage current increases with increasing bias voltage, while in the Hamburg [104] model it is assumed to be constant. Data and predictions deviate by about 1.5 σ at $z = 0$ and even more at higher z. There are also different setups compared, but none of them can correctly predict the z dependence. Another source of uncertainty comes from the silicon hardness factors [106], that enters both the Geant4 [118] and the FLUKA simulations. In the rest of the chapter most of the results are for $z = 0$, and therefore this value of the conversion factor is used, assigning an error of 15 % to account for the discrepancy shown in

figure 52.

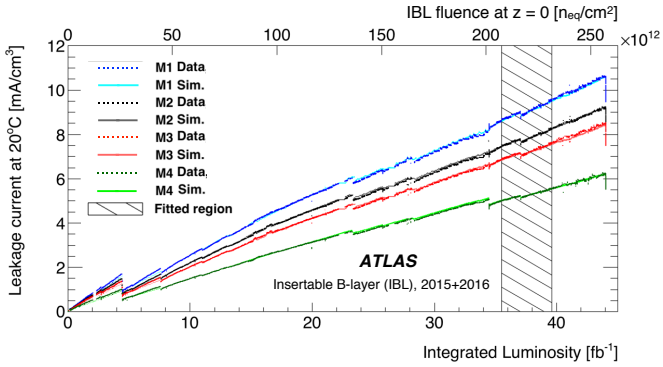

Figure 51: Evolution of the leakage current in the IBL during 2015 and 2016 data taking (dashed lines) and predictions of the leakage current according to **??** (solid lines) for 4 different modules group. Grey dashed area correspond to were simulations are fitted to the data to obtain the fluence - luminosity conversion factors. Predictions were scaled to a reference temperature of 20 °C. From ref. [98].

5.2.2 Annealing and depletion voltage

Another important aspect of the detector that must be kept under control is the annealing and the depletion voltage of the sensors. From equation 82 and 83 it is possible to predict the evolution of the depletion voltage with fluence. In order to measure this there are two different methods. The first one consists of using cross-talk of adjacent pixels, since pixels are only isolated when fully depleted. However this is true only before type inversion, after that point pixels are isolated even before full depletion. A bias voltage scan is then used in this case. The operating voltage of the sensor is raised in steps and at each value the collected charge is measured. As already said, at high fluences the depletion voltage lose its meaning. It is however used as an operational parameter to indicate the bias voltage needed to recover most of the charge. This is done by fitting with two curves, a straight line and squared function that parametrize the two different behaviors, to the mean collected charge as a function of the bias voltage. The depletion voltage is then defined as the operating voltage where the two curves cross. Figure 65 shows the fraction of collected charge as a function

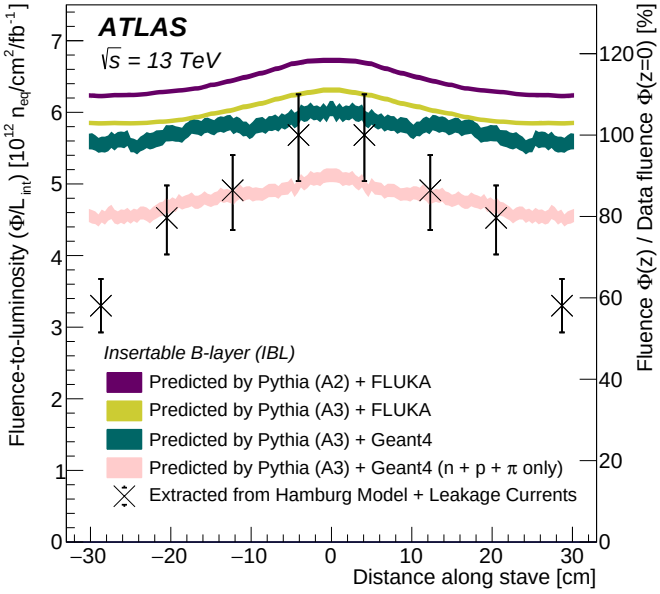

Figure 52: The fluence-to-luminosity conversion factors (extracted from leakage current fits) as a function of z, compared with the Pythia+FLUKA and Pythia+Geant4 predictions. From ref. [98].

of the bias voltage for both data and simulation. Figure 53 shows the evolution of the depletion voltage as a function of the days of operation of the LHC during 2015 and 2016 for IBL (a) and B-Layer (b). The points are data collected with both the cross talk and the voltage scan. Prediction are from equation 83. Uncertainty contain variation of the initial parameter of the equation and an additional 20% in the initial doping concentration.

5.3 Digitizer Model

A description of the effect of radiation damage on the detector response and performances is needed in order to correctly predict the behavior of the detector, decide the operation conditions (like electronics threshold, temperature and bias voltage) that minimize the impact on the performances, and also have a good description of physical quantities.

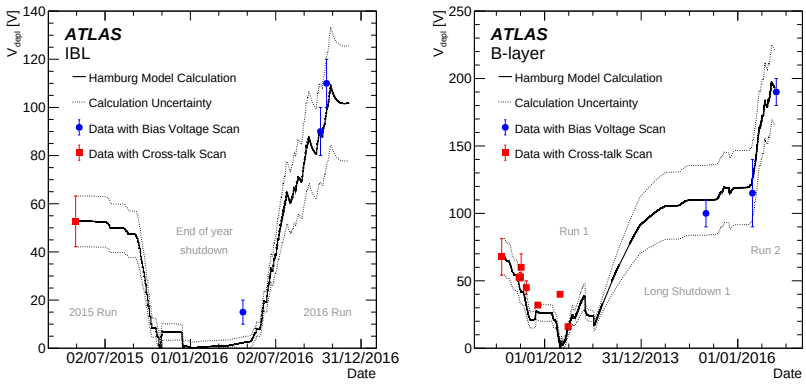

(a) (b)

Figure 53: Calculated depletion voltage of (a) IBL and (b) B-layer according to the Hamburg model as a function of time from the date of their installation until the end of 2016. Circular points indicate measurements of the depletion voltage using the bias voltage scan method while square points display earlier measurements using cross-talk scans.From ref. [98].

5.3.1 Overview

The implementation of these effects is done in the *digitization* step, where the energy deposits of charged particles are converted to digital signals sent from the front ends to the detector readout system. Energy deposits are obtained from Geant4, a software that evaluates the trajectories of particles inside the detector and their interaction with the material, and whose output is a list of energy deposits and their position in the sensible material, called *hits*. The results presented in this chapter uses two different setups for the digitization step. The first one uses a standalone software based on Allpix [119], that takes Geant4 inputs and transform them into digital signals. The second setup uses the ATLAS common software framework Athena. The Allpix based software describes the response of a single pixel module to the arrival of a single particle, while the Athena software describes the whole ATLAS detector. The first software was developed in order to have a quick tool to test the features of the digitizer without having to describe the whole ATLAS geometry. Once the results were proven to be stable, it was migrated inside the Athena software, in order to com-

pare with more precision with the data from Run 2, and to integrate the effects of radiation damage in the official Monte Carlo production of the experiment. However, in both cases the structure of the main algorithm to evaluate the effects of the radiation damage is the same, while there are some differences on how some maps and geometry setting are initialized. In this chapter it will be described mainly how the digitizer is initialized in Allpix, unless otherwise stated.

Figure 54 describes a schematics of how the digitizer works. The software is initialized by loading the geometry of the pixel module such as: thickness, pitch, number of rows and columns, and tilt with respect to the beam, that are sent to Geant4 for generating the main block and the energy hits. Then all the constant values in the digitizer are also set, such as: fluence, trapping time for electrons and holes, temperature, and B field strength. Still in the initialization, Ramo potential maps and Electric field maps corresponding to the correct bias voltage and fluence are loaded and stored in root histograms, ready to be used as look up table. These maps are obtained from separate simulation with the TCAD (Technology Computer Aided Design) tool, containing the radiation damage effects. Secondary maps are built from all the inputs and the maps, such as: Lorentz angle values, and final position maps.

The digitizer reads the ionization energy deposits of the hits created by Geant4, and converts them into electrons-holes pairs. The energy needed for a particle to create a pair of electron and hole is ~ 3.6 eV. Electrons and holes are then drifted towards the opposite electrodes using the information from the lookup tables. In order to speed up the software, charges are grouped together in groups of ~ 10, however this is a settable parameter. Results were obtained in Allpix with this value of the parameter. For each charge then the probability of being trapped is evaluated, and charge carriers are considered trapped if the time needed to reach the electrode is larger than a random trapping time τ exponentially distributed as $1/k\phi$, where ϕ is the fluence and k the trapping constant. In case the charge carrier is trapped, it is necessary to evaluate how much charge is induced in the neighboring pixel. This is done with *Ramo* maps, as it will be explained in section 5.3.6.

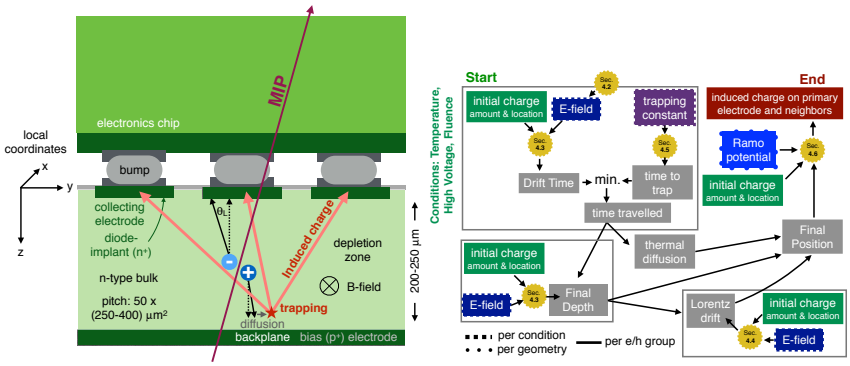

(a) (b)

Figure 54: (a) schematics of the planar digitizer. (b) work flow of the digitizer. From ref. [98].

5.3.2 Electric Field Simulation with TCAD Tool

In the presence of a constant doping inside the bulk, as in the case of unirradiated sensors, the electric field is linear. The Hamburg [104] model predicts the change in time and temperature of the effective doping concentration (N_{eff}), but not the change in concentration within the sensor, that is responsible for the non trivial shape of the electric field. The electric field shape is instead simulated with software based on TCAD, which is a type of automation for electronic design that models the fabrication and operation of semiconductor devices. The commercial TCAD products used were Silvaco Atlas (for planar modules) [120, 121] and Synopsys (for 3D) [122, 123]. Inside these tools it is also present the modeling of diffusion and ion implantation, and it is possible to see the effects on the electrical devices base due to the doping profiles. Another important aspect of TCAD, that it is also why this technology was chosen, is the possibility of model the radiation damage effects. This is done by adding trap centers to the energy band gap, that influence the density of space charge, that is positioned between the valence band (E_V) and conduction band (E_C). Since there are two technologies in the pixel sensors (n-on-n for the planar and p-on-n for the 3D), two sets of simulations are used, base on two different radiation damage models. Figure 55 shows the positions and name convention for the energy bands and the acceptor and donor traps.

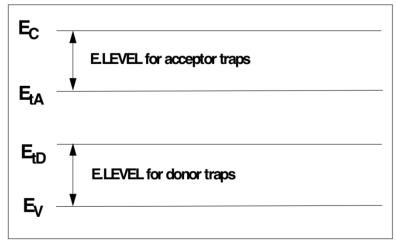

Figure 55: Energy band and trapping levels for acceptor and donor.

The radiation damage model used for planar sensors was proposed in [124] by Chiochia et al, which has been found to give a better modeling than the alternative Petasecca model [125]. The Chiochia model uses a double trap, with one acceptor and one donor trapping center, with energy level at $E_C - 0.525$ eV and $E_V + 0.48$ eV for the conduction and valence band energy level respectively. This model was first developed for CMS sensors, that are also n-in-n pixel modules, as the planar ones in the ATLAS pixel detector. Simulations are performed for only one quarter of the pixel sensors, because it is possible to take advantage of the symmetry of the pixel geometry. The z direction is defined as the direction of the depth of the sensor, while x and y correspond to the ϕ and η direction. Temperature in the simulations is set to $T = -10°\text{C}$ and an effective doping concentration of $1.6 \times 10^{12}/\text{cm}^3$ with steps of 1μm in each direction. Table 11 shows the values of the main parameters used in the TCAD simulation for the planar modules, where $N_{A/D}$ is the acceptor/donor defects concentration and $\sigma_{e/h}^{A/D}$ are the electrons/holes capture cross section for acceptor and donor defects. The density of traps increase with fluence, so for each trap it is associated an introduction rate, $g_{int}^{A/D}$ in table 11 , defined as $g_{int}^{A/D} = N_{A/D}/\phi$.

Fluence $[10^{14} n_{eq}/\text{cm}^2]$	N_A $[10^{-15}\text{cm}^{-3}]$	N_D $10^{-15}\text{cm}^{-3}]$	$\sigma_e^{A/D}$ $[10^{-15}\text{cm}^{-3}]$	σ_h^A $[10^{15}\text{cm}^2]$	σ_h^D $[10^{15}\text{cm}^2]$	g_{int}^A $[\text{cm}^{-1}]$	g_{int}^D $[\text{cm}^{-1}]$
1	0.36	0.5	6.60	1.65	6.60	3.6	5
2	0.68	1	6.60	1.65	6.60	3.4	5
5	1.4	3.4	6.60	1.65	1.65	2.8	6.8

Table 11: Basic parameters of the Chiochia model used in the TCAD simulation for planar sensors. From [124].

Radiation damage effects in the 3D sensors instead are implemented with the Perugia model [126] using the Synopsys TCAD package. In this model there are instead three trap levels: two acceptor and one donor trap with energies as: $E_C - 0.42$ eV, $E_C - 0.46$ eV, and $E_V + 0.36$ eV. The parameters of the model used for 3D sensors are reported in table 12.

Type	Energy [eV]	g_{int} [cm^{-1}]	σ_e [10^{-15} cm^2]	σ_h [10^{-14} cm^2]
Acceptor	$E_c - 0.42$	1.613	1	1
Acceptor	$E_c - 0.46$	0.9	3	3
Donor	$E_v + 0.36$	0.9	$3.23{\cdot}10^2$	3.23

Table 12: Basic parameters of the Perugia model used in the TCAD simulation for 3D sensors. From [126]

For planar sensors the electric field profile is rather independent of the x and y position. Figure 56 shows the z dependency of the electric field for different fluence and bias voltages. From the figure it is possible to see that for low fluences the electric field is almost linear (as one would expect), but then after type inversion the field is almost all shifted on the other side. After even more fluence it appears a minimum in the center and the electric field has a typical "U"-shaped profile. In the low electric field region the charges move slowly and are more likely to be trapped on small distances, therefore the charge in this region is not collected in an efficient way. However the electric field is not zero, at high enough fluence, and therefore the meaning of depletion depth is not valid anymore.

Effective modeling of annealing effects in TCAD simulations An important difference between the Hamburg model prediction and the TCAD simulation is that Hamburg model consider a constant space-charge density as a function of depth, while in the TCAD model this is not a trivial description, as shown in figure 57. It is then non obvious how to implement annealing effects into the description of the TCAD electric field. In order to emulate the annealing effects in the sensor predicted by the Hamburg model into the TCAD simulation, the mean space charge density (normalized by electric charge) is set to the same value obtained by the Hamburg model

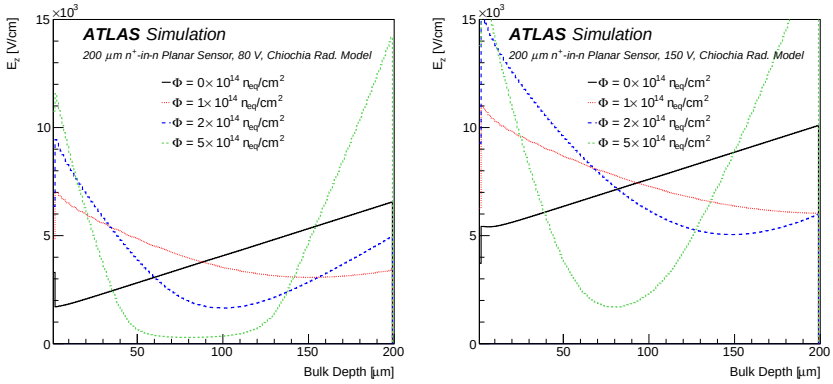

(a) (b)

Figure 56: Simulation of the electric field profile for ATLAS planar pixel modules along the z axis. From ref. [98].

$$\langle \rho/e \rangle_{\mathrm{TCAD}} = (N_{eff})_{\mathrm{Hamburg}}. \tag{88}$$

Figure shows the difference in electric field between three cases: one is the TCAD simulation without the assumption of equation 88, one is the simulation where the N_{eff}in the TCAD was constant, and the last one is the TCAD simulation with 88, called in the plot *TCAD with effective annealing*. The difference between the nominal and the effective annealing is smaller than the uncertainty of the model (descried below), so no additional systematic effects are considered.

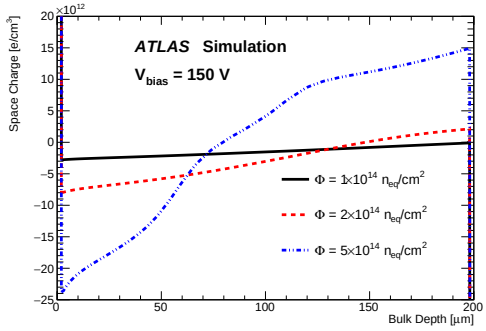

Figure 57: Simulation of the space charge density profile for ATLAS planar pixel modules along the z axis. From ref. [98].

Electric Field Systematics Systematic uncertainties needs to be assigned to the electric field prediction. These are obtained by comparing the nominal results with the prediction obtained by varying the parameter of the Chiochia model. Capture cross sections ($\sigma_{e/h}$) and introduction rate (g_{int}) are varied by a $\pm 10\%$ of their nominal value, while the trap energy level E_t (defined as the difference between the trap energy and the relevant state) is varied of $\pm 10\%$ of the thermal energy $V_{th} = k_B T$, which correspond to $\sim 0.4\%$ of the actual energy level. Figure 58 shows the electric field profile for planar modules of the IBL with a bias voltage of 80 V and a fluence of $\phi = 1 \times 10^{14} n_{eq}/\text{cm}^2$ for both the nominal value and all the systematic variations concerning the acceptor. The variations in the model parameters cause a variation of the peaks in the electric field between 15% and 30 %. In all cases there is one point where the curves crosses, and this is due to the fact that the overall normalization is the same (80 V in this case). All the variations that instead use the donors go in the opposite direction.

5.3.3 Time-to-electrode, position-at-trap

Another important input in the digitizer is the time needed by the charge carriers to reach the electrodes, and what is the final position. In fact, due to trapping, if the time is too long, the electron/hole will be trapped, and the final position will define were the charge ends, and thus the charge induced on each pixel cell. A map is computed with the final position as a function of both the initial position and time of drift, and is used in each loop of the digitizer. The maps are computed once per geometry and conditions (fluence, bias voltage, and temperature). Electrons and holes drift towards the opposite electrodes with a mobility μ that depends on the nature of the charge carrier, the electric field and also the temperature [127], following the equation from Jacoboni-Canali [128]

$$\begin{aligned} \mu_e(T) =& 1533.7\text{cm}^2/(V \cdot s) \times T_n^{-2.42} \\ \mu_h(T) =& 463.9\text{cm}^2/(V \cdot s) \times T_n^{-2.20}. \end{aligned} \tag{89}$$

Drift velocity is then given by $\vec{v}(E) \sim r\mu(E)\vec{E}$, where r is the Hall scattering factor. From this the estimated time for collecting the charge is given by

$$t_{\text{collection}}(\vec{x}_{\text{initial}}) = \int_C \frac{ds}{r\mu(E)E} \tag{90}$$

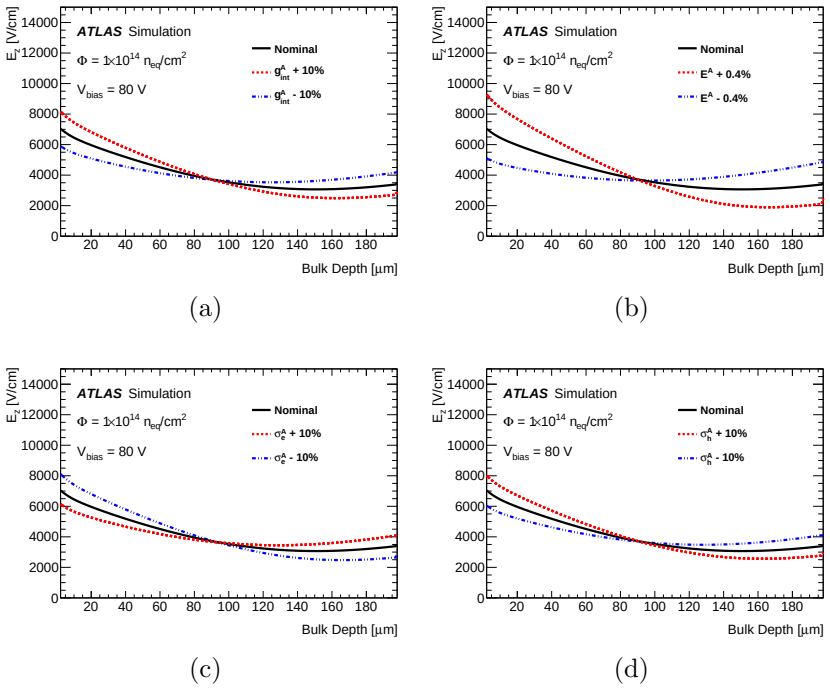

Figure 58: Electric field profiles along the z axis of ATLAS IBL planar modules, using the Chiochia model parameter for 80 V and a fluence of $\phi = 1 \times 10^{14} n_{eq}/\text{cm}^2$. Together with the nominal values are also shown the results obtained with variations of the parameter of the model, only for acceptors. From ref. [98].

Where C is the path from the initial to the final position. The integration is done in the z direction, since the field is nearly independent of x and y. Figure 59 shows the time to reach the electrode for both electrons and holes, for different fluences, for a IBL planar sensor with a bias voltage of 80 V. Holes drift toward the 200 μm side, while electrons toward the zero side. From the figure it is possible to see that the times go from few ns to tens of ns.
Electrons are collected in few ns, except for very high fluences, were the electric field is quite low in the central part of the sensor; in this case most of the charges are trapped before reaching the electrodes. Holes instead are slower. Signal formation is still, in general, faster than the LHC clock of 25 ns, but could be a problem for very high fluences. However most of the signal comes from the region the closest

to the electrodes, were the time to reach the electrodes is fast, due to the effect of the Ramo potential, as it will be explained in 5.3.6.
For trapped charge carriers it is important to know the position of the trapping, in order to be able to evaluate the induced charge. As previously explained, a charge carrier is trapped if its time to reach the electrode is larger than a random number distributed as an exponential function with mean value the trapping time. Therefore it is possible to evaluate the final position as:

$$\vec{x}_{\text{trap}} = \int_0^{t_{\text{trap}}} r\mu(E)\vec{E}dt. \tag{91}$$

where t_{trap} is the random time of trapping of the charge carrier considered.

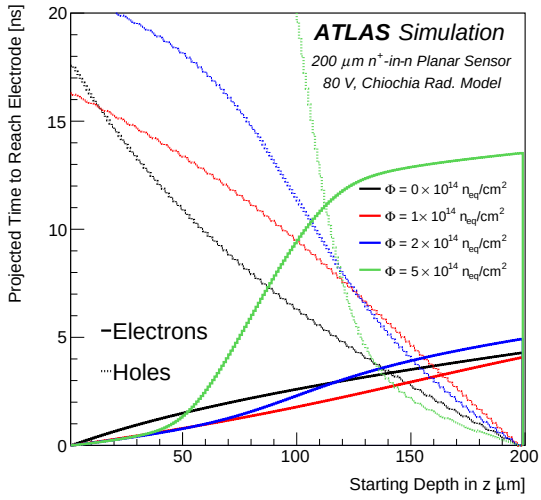

Figure 59: Time to reach the electrodes as a function of the initial position of the charge carrier. Electrons goes toward the zero side, while holes toward the 200 μm one. From ref. [98].

5.3.4 Lorentz angle

Charge carriers in the silicon sensors drift due to the electric field towards the electrodes. The presence of a magnetic field deviates the path of the charge carriers from straight lines. The Lorentz angle (θ_L)

is defined as the angle between the drift direction and the electric field, and this causes that the minimum of the cluster size is obtained for particles entering the sensor with an incident angle equals to the Lorentz Angle. In a given point inside the bulk of the sensor the Lorentz Angle is given by

$$\theta_L = rB\mu(E(z)) \tag{92}$$

where μ is the mobility. The mobility depends on the electric field, in particular it diminishes for very high field, and therefore this means that the Lorentz Angle depends itself on the electric field. This also means that the total effects, as the incident angle corresponding to the minimum cluster size, depends not only on the average electric field (which is the bias voltage divided by the depth of the sensor), but also on the profile of the electric field which is modified by the radiation damage. It is possible to write the Lorentz angle with following formula:

$$\tan\theta_L(z_i, z_f) = \frac{rB}{|z_f - z_i|}\int_{z_i}^{z_f} \mu(E(z))dz. \tag{93}$$

where $z_{i/f}$ is the initial/final position of the charge carrier.
In the digitizer code the Lorentz angle maps are saved at the beginning for each geometry and condition setup (fluence, bias voltage, and temperature). The final position of the charge carrier when adding together the drift and the Lorentz angle is then given by:

$$\begin{aligned} x_f &= x_i + |z_f - z_i| \cdot \tan\theta_L + d_x \\ y_f &= y_i + d_y \end{aligned} \tag{94}$$

where the y direction is the direction perpendicular to the magnetic field, while the x is parallel to it. $d_{x/y}$ instead is the thermal diffusion in the x and y direction, and it is given by:

$$d = \epsilon \cdot d_0 \sqrt{\frac{|z_f - z_i| \cdot \cot\theta}{0.3}} \tag{95}$$

with d_0 a diffusion constant and ϵ a random number. The Lorentz angle for electrons is larger than for holes because of the larger mobility. Figure 60 (a) shows the tangent of the Lorentz angle as function of the initial position in a planar module with a bias voltage of 80 V for different fluences. Instead figure 60 (b) shows the same plot but as a function of both the initial and final position, for a fluence of $2 \times 10^{14} n_{eq}/\mathrm{cm}^2$

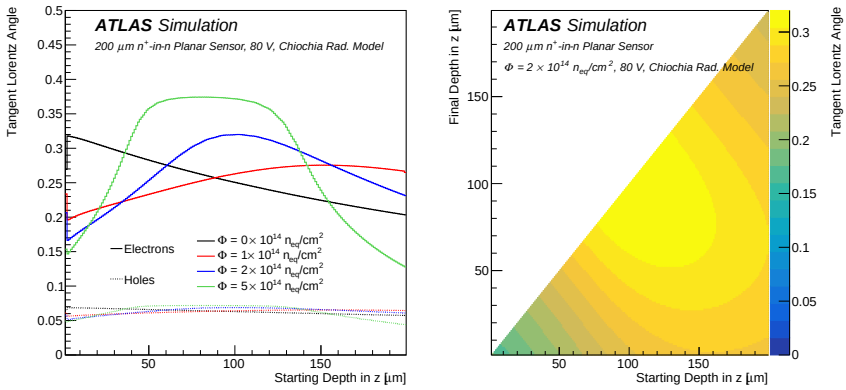

(a) (b)

Figure 60: Tangent of the Lorentz angle as a function of the starting position in z of the charge carrier (a) or as a function of both the initial and final position (b) in an ATLAS IBL planar module, with a bias voltage of 80 V. From ref. [98].

5.3.5 Charge Trapping

As already stated, the charge carriers are considered trapped if their time to reach the electrodes is larger than a random time distributed as an exponential with mean value $1/\phi\beta$, where β is the trapping constant.

This constant is a set at the beginning of the digitizer, and it is taken from literature. From different measurement β has been found to depend on the type of irradiation, the temperature, and the annealing history, and also if the charge carrier it is an electron or an hole. In the digitizer an average of different measurement mainly from references [needed1], [needed2] it is used. Values are reported in table 13 for the different values of β, together with the method of irradiation, the level of annealing and type of irradiation. Measurement were obtained with different techniques: for reference [129] and [110] a transient current technique (TCT) was used, while for reference [80] [130] results from test beam were used . Measurements were also performed at different temperatures, between $-10°$C and $10°$C, and a significant dependence of β on temperature was found. Therefore all the results were scaled to $0°$C in order to be comparable. Both results with TCT find a β increasing with annealing for electrons while decreasing for holes.

In the digitizer the values used were:

$$\begin{aligned}\beta_e &= (4.5 \pm 1.5) \times 10^{-16}\text{cm}^2/\text{ns} \\ \beta_h &= (6.5 \pm 1.5) \times 10^{-16}\text{cm}^2/\text{ns}\end{aligned} \tag{96}$$

These values were chosen in order to be representative of the conditions of the ATLAS Pixel detector during Run 2. The uncertainty instead were set to cover differences between all the reference used.

Irradiation	Annealing	β_e (10^{-16}cm^2/ns)	β_h (10^{-16}cm^2/ns)	Reference	Method
Neutrons	minimum V_{depl}	4.0 ± 0.1	5.7 ± 0.2	[110]	TCT
Pions	minimum V_{depl}	5.5 ± 0.2	7.3 ± 0.2	[110]	TCT
Protons	minimum V_{depl}	5.13 ± 0.16	5.04 ± 0.18	[129]	TCT
Neutrons	$>$ 50 hours at 60°C	2.6 ± 0.1	7.0 ± 0.2	[110]	TCT
Protons	$>$ 10 hours at 60°C	3.2 ± 0.1	5.2 ± 0.3	[129]	TCT
Protons	minimum V_{depl}	4.0 ± 1.4	-	[80, 130]	Test-beam
Protons	25h at 60°C	2.2 ± 0.4	-	[80, 130]	Test-beam

Table 13: Measurements of the trapping constant β are summarized, normalized to a temperature of 0°C. Some measurements are reported after annealing to the minimum in the full depletion voltage V_{depl} (reached in about 80 minutes at 60°C) while others correspond to the asymptotic values observed after long annealing times.

5.3.6 Ramo potential and induced charge

Drifting charges inside the bulk of the sensors towards the electrodes induce a signal that is then read by the electronics. This signal can be analytically calculated, by using the Shockley-Ramo theorem [131]. The theorem states that the instantaneous current i induced on an electrode by a moving charge q is given by:

$$i(t) = q\vec{v} \cdot \vec{E}_w(\vec{r}) \tag{97}$$

where $\vec{v}$ is the instantaneous velocity of the charge. Instead E_w is the electric field generated at the position r by q on the electrode considered, and removing all other charges and electrodes. E_w is called *weighting field* or *Ramo field*. Integrating equation 97 over time it is obtained:

$$Q_{\text{induced}} = -q[\phi_{\text{w}}(\vec{x}_{\text{f}}) - \phi_{\text{w}}(\vec{x}_{\text{i}})], \tag{98}$$

where ϕ_w is the ramo potential $\vec{E}_w = \nabla\phi_w$. The Ramo potential depends only on the geometry of the electrodes, and therefore it is

possible to be evaluated in advance. In presence of a pair of electrons-holes formed in the position x_i that drifts towards their respective electrodes and they both arrive to the end, the induced charge is q, the charge of the electrons. However if one of the charge carrier is trapped, the charge is not zero, but can be evaluated using 98, and it is always smaller than the charge q.
In the digitizer the Ramo maps are loaded in the initialization process, and are used in each loop whenever a charge is trapped to estimate the induced charge in all the pixels in a 3×3 matrix around the closest pixel to the trapping position. These maps are evaluated with TCAD in order to solve the Poisson equation. For planar sensors there is a small x and y dependence, while the main changes are in the z direction. However x and y directions are important to evaluate the charge induced on the neighboring pixels. Figure 61 shows the Ramo potential of a quarter of an IBL planar sensor. The white dashed lines indicates the edge of the electrode. It is then possible to see that indeed the potential is not zero outside the pixel area.
The Ramo potential for 3D sensors is slightly more complex, due to not only the 3D geometry, but also to the fact that the two n^+ columns are connected, and so they must be kept at ground together when doing the calculation, and this requires a relatively large simulation area. Figure 62 shows the Ramo potential map for a 3D sensor

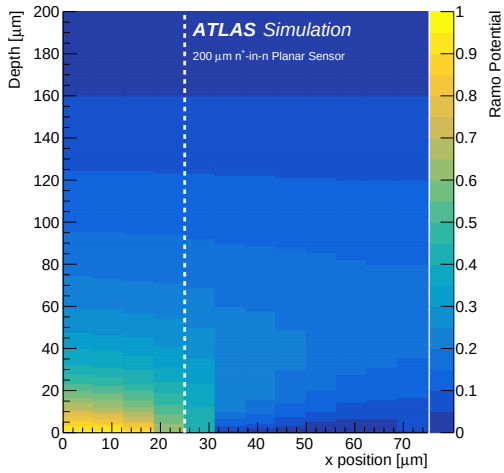

Figure 61: Ramo potential maps of a quarter of a ATLAS IBL planar module in the $z - x$ plane. From ref. [98].

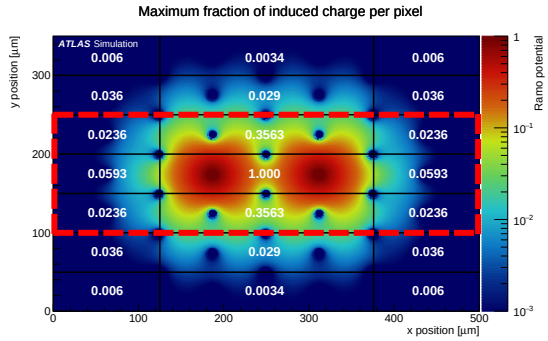

Figure 62: Ramo potential maps of a ATLAS IBL 3D module. Numbers indicate the maxium induced charged (normalized to one). Blue holes are the p^+ columns. The red dashed lines illustrates which pixel are put in the simulations. From ref. [98].

5.4 Model Validation on data

The digitizer presented in the previous section was tested by comparing its prediction with data taken by the ATLAS detector during the Run 2. In order to study the correct modeling of the radiation damage effects some key observables were chosen. In particular the Charge Collection Efficiency and the Lorentz Angle. Simulations were obtained using the Allpix software. Data were taken from different period during the Run 2, from 2015 to 2018. Events passing di-muon or di-jet trigger were considered. Charged-particle tracks are reconstructed from hits in the pixel detector, silicon strip detector, and transition radiation tracker. Clusters on the innermost pixel layer associated with tracks are considered for further analysis.

5.4.1 Charge Collection Efficiency

The collected charge is one of the most important parameters to monitor, and is also directly affected by radiation damage. Some analysis for new physics uses directly the information on the collected charge in the pixel cluster, therefore it is an important parameter to monitor. Moreover a decrease in collected charge means also a decrease in the cluster size, since the pixels with low charge can end up below threshold. Also, it is possible that due to the reduction of collected charges whole clusters might disappear, therefore reducing the efficiency of the tracking performance. It is then clear why an accurate

description of this phenomenon is essential.
Charge deposited in the pixel cluster is well described by a Landau distribution [132], and from this is possible to define a Charge Collection Efficiency (CCE) as the ratio of the Most Probable Value (MPV) of the Landau distribution of the sensor at one fluence and the MPV from an unirradiated sensor in over-depletion. Figure 64 shows the cluster ToT (the sum of the ToT of each pixel that compose the cluster) distribution for two simulation points: $1 \times 10^{14} n_{eq}/\text{cm}^2$ and $2 \times 10^{14} n_{eq}/\text{cm}^2$ both at 80 V. The geometry setup in Allpix is such that the position of the module with respect to where the particles are fired is the same as for central IBL planar modules, that cover the region with $|\eta| < 0.2$, with respect to particles coming from $z = 0$. In this way it is possible to compare data from Run 2 collisions and simulations.
Figure 63 shows the CCE for IBL planar modules with $|\eta| < 0.2$ as a function of luminosity (bottom axis) and fluence (top axis). Data are selected in $Z \rightarrow \mu\mu$ events with track with $3.5 < p_{\text{T}} < 150$ GeV, $0 < \phi$ on surface < 0.5 , $|\theta$ on surface $| < 0.2$. No clusters with pixels with ToT$= 1$ or > 14 are used. Results are obtained from ToT. The reference run for data (unirradiated) is the 279169, at the beginning of 2015.
As expected the CCE decreases with luminosity, and therefore fluence. At the end of 2016 (around 30 fb^{-1}) the IBL detector was under-depleted, and the CCE was quickly decreasing. Increasing the bias voltage from 80 V to 150 V then was needed to recover this trend. From mid 2017 to beginning of 2018 the bias voltage was increased again to 350 V, and in 2018 increased again to 400 V.
Error bands on the y axis on the simulations account for all the systematic variations presented in section 5.3.2, and also variation (of 1 σ) of the trapping constants. Table 14 summarizes all the systematic uncertainties used and their impact on the total one. These uncertainties depend on the fluence, and can vary from 2 % to up to 20 %. This is due to the fact that when under-depleted the description of the electric field is less precise. On the x axis there is a 15 % uncertainty from the fluence-to-luminosity conversion. Data have instead an uncertainty that accounts for the shift in ToT (described in section 4.4) along the y axis, and a 2% uncertainty on the x due to the luminosity measurement uncertainty. Data and simulation are in agreement within the uncertainty, even if the last data points seems to be systematically lower than the prediction.

Bias voltage [V]	80	80	80	150	150	150
Fluence [$10^{14} n_{eq}/\mathrm{cm}^2$]	1	2	5	1	2	5
Luminosity fb^{-1}	16.6	33.3	83.3	16.6	33.3	83.3
Variation	Impact [%]	Impact [%]	Impact [%]	Impact [%]	Impact [%]	Impact [%]
Energy acceptor +10%	0.4	2.2	0.7	0.2	1.6	1.5
Energy donor +10%	0.5		4.5	0.2	0.3	5.7
Energy acceptor −10%		1.7	3.8	0.1	0.3	1.6
Energy donor −10%	0.5	0.1	2.9	0.1	0.9	
g_{int} acceptor +10%	0.4	0.3	3.8	0.1	0.9	1.3
g_{int} donor +10%	0.2	1.0	4.2	0.1	0.4	5.7
g_{int} acceptor −10%	0.3	1.7	14.0	0.1	0.3	1.5
g_{int} donor −10%	0.03	0.4	6.8	0.1	0.7	6.9
σ_e acceptor +10%	0.3	1.4	0.9	0.06	0.4	2.3
σ_e donor +10%	0.2	1.0	1.8	0.01	0.4	0.6
σ_e acceptor −10%	0.4	0.3	1.9	0.1	0.8	4.7
σ_e donor −10%	0.1	0.6	0.1	0.1	0.6	5.5
σ_h acceptor +10%	0.3	1.5	1.3	0.1	0.8	2.6
σ_h donor +10%	0.3	0.1	1.4	0.1	0.6	5.0
σ_h acceptor −10%	0.3	2.0	1.0	0.1	0.3	2.2
σ_h donor −10%	0.3	0.5	0.8	0.01	0.3	0.8
electron trapping constant +33%	2.3	1.1	1.1	1.3	2.5	1.0
hole trapping constant +23%	0.5	2.4	11.8	1.2	2.1	6.0
electron trapping constant −33%	1.1	2.0	5.1	0.5	0.1	6.1
hole trapping constant −23%	2.2	2.5	0.4	0.6	0.2	2.9
Total Uncertainty	3.4	5.1	21.3	1.9	4.2	15.6

Table 14: List of systematic uncertainties considered in the simulation and their relative impact on the predicted charge collection efficiency. Blank spaces correspond to uncertainties that are below 0.005. The total uncertainty is the sum in quadrature of the maximum of the up and down variations.

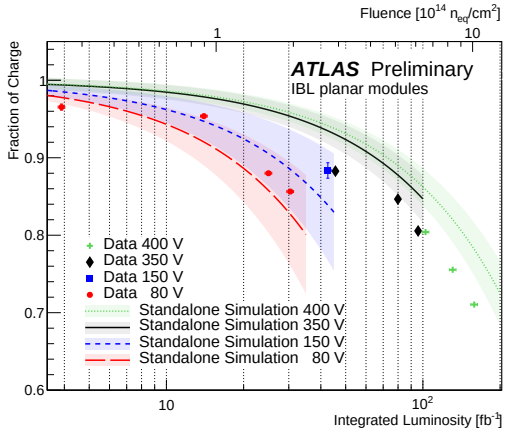

Figure 63: Charge Collection Efficiency as a function of the integrated Luminosity (bottom axis) and fluence (top axis) for IBL modules with $|\eta| < 0.2$. For the simulation, the vertical bars include radiation damage parameter variations and the horizontal errors bars reflect uncertainty in the lumi-to-fluence conversion. From ref. [133].

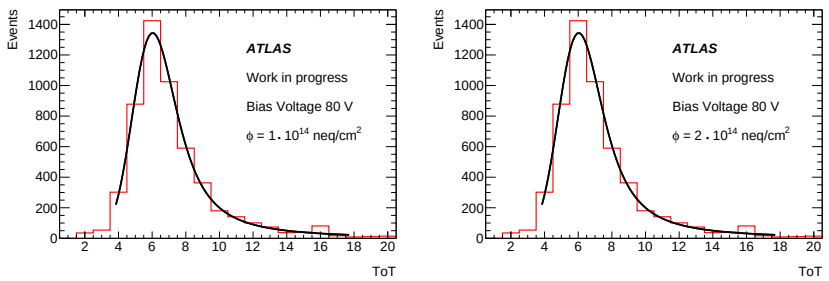

Figure 64: Distribution of the IBL pixels cluster ToT for (a) fluence of $1 \times 10^{14} n_{eq}/\text{cm}^2$ and (b) $2 \times 10^{14} n_{eq}/\text{cm}^2$, both with a bias voltage of 80 V. Distribution are fitted with a Landau curve.

It is also possible to evaluate the charge collection efficiency as a function of the bias voltage applied, instead of as a function of the luminosity.This is possible because the bias voltage was varied in special runs, called *Voltage Scan*, during the data taking. In the whole run 2, eight different voltage scans were taken, one at the beginning and one at the end of each year. This was done to monitor the depletion voltage of the sensors. Figure 65 shows the fraction of collected charge

Sample	Fluence [$10^{14} n_{eq}/\mathrm{cm}^2$]	Luminosity [fb^{-1}]	Depletion Voltage [V]
Data	5.5		240 ± 4
Data	8.7		278 ± 4
Simulation	5.5		250 ± 4
Simulation	8.7		268 ± 4

Table 15: Depletion voltage obtained from fit on data and simulation.

as a function of the bias voltage in IBL planar modules for two data runs, one at the end of 2017 and one at the end of 2018, compared with the corresponding simulations, obtained also with Allpix. Simulations agree with data at high bias voltage, while they are higher than data at low bias voltages. It is also possible to see a change in the slope of the curves with the increase of the bias voltage, as it was already explained in section 5.1.3. This can be then used to estimate the "full bias voltage" as explained before as the point were the charge is efficiently collected. The obtained Depletion Voltage are reported in table 15. Still it is important to notice that at very high fluence the concept of Depletion Voltage is not relevant anymore, since the model provides a non zero electric field everywhere. However it is possible to define the Depletion Voltage as the point where the electric field is high enough to efficiently collect most of the charge from the whole sensor. Discrepancy at low bias voltage doesn't compromise the ability to emulate the behavior of the detector during Run 2, since the operational bias voltage was always at levels higher than full depletion.

5.4.2 Lorentz Angle

The Lorentz angle is determined by performing a fit to the transverse cluster size F as function of the incidence angle of the associated track using the following functional form:

$$F(\alpha) = [a \times |\tan\alpha - \tan\theta_{\mathrm{L}}| + b/\sqrt{\cos\alpha}] \otimes G(\alpha|\mu = 0, \sigma),$$

where α is the incidence angle with respect to the normal direction of the sensor in the plane perpendicular to the magnetic field. θ_{L} is the fitted Lorentz angle, G is a Gaussian probability distribution evaluated at α with mean 0 and standard deviation σ, and a and b are two additional fit parameters related to the depletion depth and the minimum

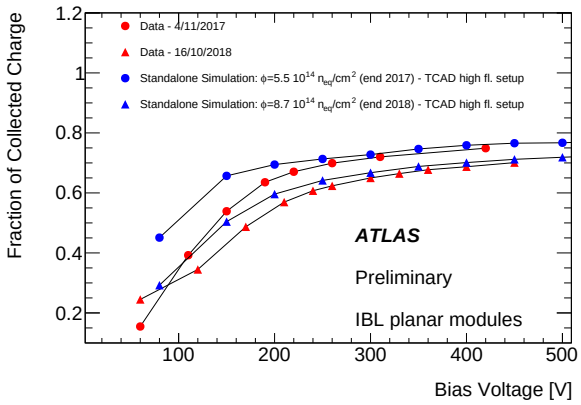

Figure 65: Charge Collection Efficiency as a function of the Bias voltage applied to IBL modules. From ref. [133].

cluster size, respectively. An example input to the fit is shown in Figure 66(a). Cluster size depends on many effects that are not included inside the simulations, however the position of the minimum should still correspond to the Lorentz Angle. For example, the geometry used for this simulation is simplified and the extreme incidence angles are likely more impacted in the actual geometry. The simulation in Figure 66(a) matches the low incidence angles well, but this is not seen for all fluences; it could be due in part to the uncertainty in the fluence.

The fitted Lorentz angle as a function of integrated luminosity is shown in Figure 66(b). Due to the degradation in the electric field, the mobility and thus the Lorentz angle increase with fluence. This is not true for the Petasecca model, which does not predict regions of low electric field. Charge trapping does not play a significant role in the Lorentz angle prediction. The overall normalisation of the simulation prediction is highly sensitive to the radiation damage model parameters, but the increasing trend is robust. An overall offset (not shown) is consistent with previous studies and appears even without radiation damage (zero fluence) [134], which is why only the difference in the angle is presented.

Figure 67(a) shows the evolution of the Lorentz angle during the whole run 2. Each fit is done for data with the same conditions (temperature and bias voltage). Only data are presented. Differences in Lorentz Angle are due to changes in Bias Voltage and temperature.

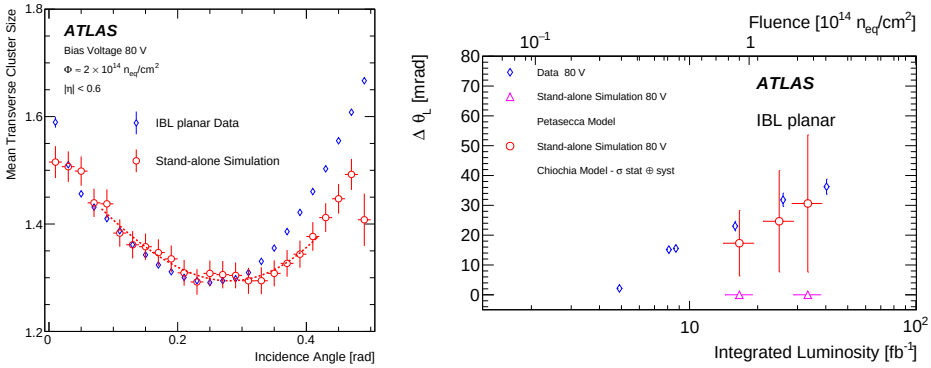

(a) (b)

Figure 66: (a) The mean transverse cluster size versus transverse incidence angle near the end of the 2016 run ($\sim 2 \times 10^{14}$ n_{eq}/cm^2) with a bias voltage of 80 V. (b) The change in the Lorentz angle (θ_{L}) from the unirradiated case as a function of the integrated luminosity in 2015-2016. Two TCAD radiation damage models are considered, Chiochia and Petasecca. Chiochia model points have both statistical and systematic uncertainties, while Petasecca only the statistical uncertainties. From ref. [98].

Figure 67(b) instead shows the evolution of the Lorentz angle during 2017 compared with the prediction from the Allpix simulations. Here the simulation points are fitted with a straight line, where the offset is fixed so that it matches the one from the data. A more parametrization of the mobility will resolve this offset, as shown in ref [134], but it is not yet implemented in these simulations. Error bands account for all the systematic variations. For each one a linear fit is done ($x \cdot m + q$), and it is assigned as the final error the sigma of the distribution of the m values. The increase is well described.

5.4.3 Data MC comparison with ATLAS Athena Common Software

Previous results were implemented using the Allpix software. As already stated, Allpix is a good approximation and can be used for quick checks and to evaluate systematic effects. However in order to have a good representation of the effects due to the complex geometry of ATLAS, the full simulation is needed. For this reason the digit-

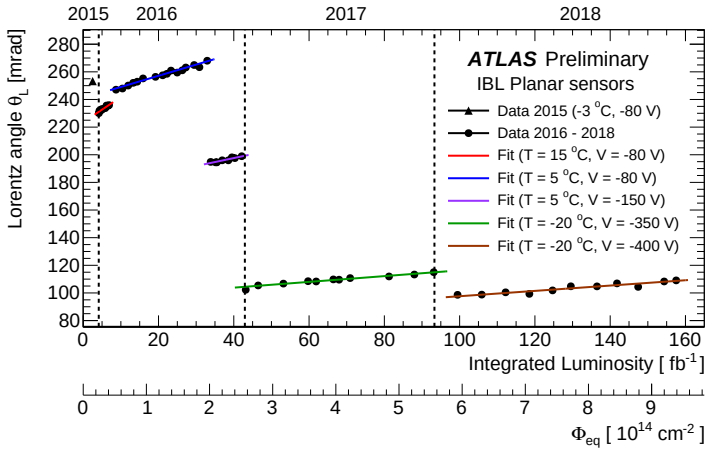

(a)

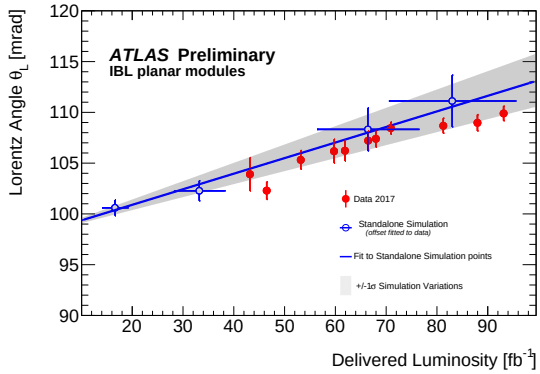

(b)

Figure 67: The evolution of the Lorentz angle (θ_L) (a) during the full Run 2, just with data, and (b) during 2017 compared with simulations from Allpix using the Chiochia model. From ref. [135].

izer presented here was also implemented inside the common software Athena. The main algorithm is the same as in the Allpix software, but maps and geometry are loaded in a different way, mainly because Athena needs to load all the modules from all the layers at the same time.

Figure 68 shows the results obtained with the Athena simulations, for all the Layers of the pixel detector. The 7 points are reported for all the layers in table 16. They correspond to (0) all sensors unirridated, (1) start of Run 2 with zero fluence on the insertable B-layer (IBL),

Benchmark Point	0	1	2	3	4	5	6
				IBL			
Fluence	0	0	1	2	2	5	8.7
Bias Voltage	80	80	80	80	150	350	400
				B-Layer			
Fluence	0	0.7	1.2	1.7	1.7	3.1	4.6
Bias Voltage	150	150	150	150	350	350	400
				Layer 1			
Fluence	0	0.3	0.5	0.7	0.7	1.3	2.1
Bias Voltage	150	150	150	150	250	250	250
				Layer 2			
Fluence	0	0.2	0.3	0.4	0.4	0.8	1.3
Bias Voltage	150	150	150	150	150	150	150

Table 16: Depletion voltages and Fluences used in the different benchmark points for the simulations in figure 68.

(2) half of 2016 ($\sim 15\text{fb}^{-1}$) (3) near end of 2016 data taking period ($\sim 36\text{fb}^{-1}$) (4) same point as the previous one, but with bias voltages increase (5) end of 2017, and (6) end of 2018. Prediction with the full simulation are compatible with the Allpix results.
The code at the moment is in validation phase, and optimization of the required CPU. The current plan is to use it in the official production of the MC samples for the Run 3 analysis.

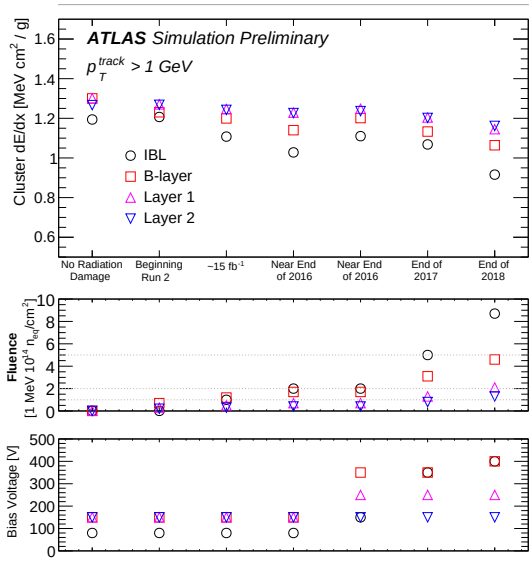

Figure 68: dE/dx for different benchmark point and for each Pixel Layer. Bias voltages and fluence used in each benchmark are reported in the bottom panel. From ref. [136].

6 Object reconstruction

The raw events provided by the data acquisition system are basically a list of detector elements identifiers, with information on the signal registered by each such as energy or time. These events are subject to a procedure called object reconstruction, which is a first level of analysis which processes the raw information to produce a higher level information: a list of charged particle trajectories (tracks), jets, electron, photons, muons, hadronically decaying τs, along with information such as their trajectory and energy. These are the objects which are the input to the subsequent physics analyses. The event-level missing transverse energy is also provided. During object reconstruction, refined momentum and energy calibration is also applied. The identification of the nature of an object (such as electron or jet) is never unambiguous: tighter selections leads to smaller misidentification rates but lower efficiency, and the optimal choices are analysis-dependent. For this reason the object reconstruction often provides candidates with a quality score, and the same detector signature can be often reconstructed as different objects (for example, all electron candidates are also jet candidates). Each analysis will select objects with the desired quality level, and remove overlaps. In this chapter the reconstruction of the objects relevant for the analysis presented in this thesis will be described: jets (section 6.2), b-jets (section 6.3), electrons (section 6.4), muons (section 6.5), and missing transverse energy (section 6.6). Charged particle trajectories (tracks) are described first (section 6.1), as well as the reconstruction of the proton-proton interaction vertices, which is also used in the analysis

6.1 Tracks and primary vertex

6.1.1 Track Reconstruction

The tracks of charged particles with $p_T > 0.5$ GeV and $|\eta| < 2.5$ are reconstructed in the ID in a many step process [137]. The first step in the track reconstruction is the clusterization of the raw measurement of the pixel and SCT detector. Pixel clusterization has been described in section 4.6. SCT strips are clustered also with a CCA algorithm, and a 3D measurement is obtained only if the signal from the modules on the two sides of each tracking layer are used. The second step is the *Iterative combinatorial track finding*. Here tracks seeds are

formed from three space points, starting from SCT-only seeds, then Pixel-only, and finally mixed seeds, in order of purity. Purity is then improved with additional requirement on d_0 and p_{T}, and by requiring an additional space point to be compatible with the track extrapolation from the seed. Then a Kalman filter [138] is used to build tracks candidates including additional space points in the remaining layers. The next step is the *ambiguity solver*, where tracks are scored according to the likely of being a good candidate using information such as the number of clusters associated to it, the number of holes, and the χ^2 of the track fit. Tracks are then processed in decreasing order of track score, favoring tracks with higher scores, and the ambiguity solver then deals with clusters assigned to multiple tracks, asking that clusters are not shared by more than two tracks and that there are no more than two shared cluster in the same track, and other quality requirements. The last step is the extension to the TRT, where tracks in the silicon detector are used as input to search for matching measurements in the TRT. The silicon-only track is not modified by this process and the association with the TRT hits are only extensions. The first step is to perform a fit between the TRT hits and the silicon tracks and then, as for the silicon hits, try to match onwards. Finally a fit is performed again to try to improve the momentum resolution. Sometimes it might happen that a candidate track in the TRT doesn't match to any tracks in the SCT. This can happen when ambiguous hits shadow the tracks or when tracks come from a secondary vertex with few hits in the silicon. In this case the algorithm will start a second sequence starting from the TRT and moving inside towards the silicon. There is another difference in the two sequences, that the track finding algorithm in the TRT does not start from a space-point since the drift tubes provides only an information on the $r - \phi$ plane in the barrel and $r - z$ plane in the end-caps.

6.1.2 Tracking Efficiency

Two different sets of criteria (working points) [139] are used in ATLAS to select tracks to be used in physics analysis:

Loose

- $p_{\mathrm{T}} > 500$ MeV

- $|\eta| < 2.5$
- $N_{Si} \geq 7$: At least 7 hits in the silicon detectors (Pixel and SCT, including dead sensors)
- $N_{mod}^{sh} \leq 1$: Less than or equal to 1 Pixel/SCT hits assigned to multiple tracks
- $N_{si}^{hole} \leq 2$: Less than or equal to 2 Pixel/SCT hits missing
- $N_{pix}^{hole} \leq 1$: Less than or equal to 1 Pixel hits missing

Tight Primary (in addition to the Loose selection requirements)

- $N_{Si} \geq 9$ (if $|\eta| < 1.65$): At least 9 hits in the silicon detectors (if $|\eta| < 1.65$)
- $N_{Si} \geq 11$ (if $|\eta| > 1.65$): At least 11 hits in the silicon detectors (if $|\eta| > 1.65$)
- $N_{IBL} + N_{B-Layer} > 0$: At least 1 hit in either one of the two innermost layers (the IBL or the B-Layer
- $N_{pix}^{hole} = 0$: No Pixel hits missing

A shared hit is a hit that it is used by more than one tracks, while a missing hit (hole) is defined as intersections of reconstructed tracks trajectory with a sensitive detector element that do not result in a hit. A sensitive module is a module that is not dead, or an inactive area such as edges of the silicon sensors. A pixel module is considered shared if it has one or more shared hits, while for SCT a shared module has at least two shared hits.
Tracking efficiency is evaluated from simulation, using truth information of the particles at hit level. The first step consist of assign to each cluster the truth particle with the high energy deposit in the MC. Depending on which sub detector the cluster is in, it is assigned a different weight: 10 for Pixels, 5 for SCT, and 1 for TRT and from this is then defined a matching probability P_{match}:

$$P_{\text{match}} = \frac{10 \cdot N_{\text{pixel}}^{\text{common}} + 5 \cdot N_{\text{SCT}}^{\text{common}} + 1 \cdot N_{\text{TRT}}^{\text{common}}}{10 \cdot N_{\text{pixel}}^{\text{track}} + 5 \cdot N_{\text{SCT}}^{\text{track}} + 1 \cdot N_{\text{TRT}}^{\text{track}}} \tag{99}$$

where N^{common} is the number of hits that are common to both the track and the truth, while N^{track} is the number of hits associated to

the track. A track is defined matched if $P_{\text{match}} > 0.5$, and it is called a *primary* track. It is then defined the tracking efficiency $\epsilon(p_{\text{T}}, \eta)$ as a function of p_{T} and η as:

$$\epsilon(p_{\text{T}}, \eta) = \frac{N_{\text{rec}}^{\text{matched}}(p_{\text{T}}, \eta)}{N_{\text{gen}}(p_{\text{T}}, \eta)} \tag{100}$$

where $N_{\text{rec}}^{\text{matched}}$ is the number of tracks truth matched, and N_{gen} the number of total tracks. Figure 69 shows the track efficiency as a function of both p_{T} and η for the two WP presented before.

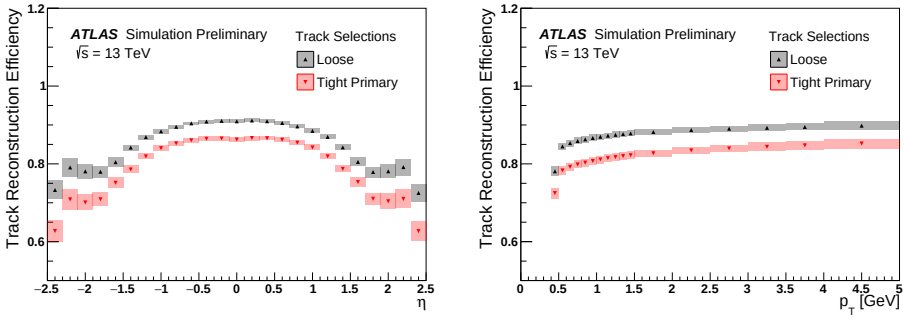

(a) (b)

Figure 69: Track efficiency as a function of p_{T} and η for the the Loose and Tight Primary working point. From ref. [139].

Fake tracks are reconstructed tracks that don't match to any charged particle traveling in the detector. Combinatorial effects, that grow with pile-up, increase the fake rate. An estimate is given by the deviation from the linear fit of the number of tracks as a function of the mean number of inelastic interactions per bunch crossing, $\langle\mu\rangle_{\text{bunch}}$. Figure 70 shows the average number of charged particle tracks that pass a preselection of $p_{\text{T}} > 1$ GeV and $|\eta| < 2.5$ reconstructed per event as a function of $\langle\mu\rangle_{\text{bunch}}$, for the Loose and Tight Primary track selections. The solid lines show a linear fit to the data in the region $9 < \langle\mu\rangle_{\text{bunch}} < 16$, and extended to higher $\langle\mu\rangle_{\text{bunch}}$. From this figures it is possible to see that with the Tight Primary the tracking efficiency is lower (84%, for $|\eta| < 1.0$) than with the Loose working point (90 %, for $|\eta| < 1.0$), but the fake rate is almost zero.

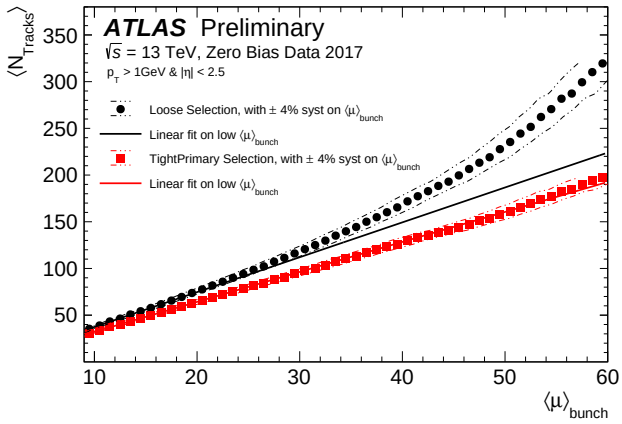

Figure 70: Average number of charged particle tracks that pass a preselection of $p_{\mathrm{T}} > 1$ GeV and $|\eta| < 2.5$ reconstructed per event in the ATLAS Inner Detector as a function of $\langle\mu\rangle_{\mathrm{bunch}}$, for the Loose and TightPrimary track selections. The solid lines show a linear fit to the data in the region $9 < \langle\mu\rangle_{\mathrm{bunch}} < 16$, and extended to higher $\langle\mu\rangle_{\mathrm{bunch}}$. From ref. [140].

6.1.3 Vertex Reconstruction

A *vertex* is defined as a point from where two or more tracks starts, with no other hits behind [141, 142]. There are three kinds of vertices: first there is the so called *primary vertex*, and it is the origin of objects originated from the hard scattering processes and it is the defined as the vertex with the tracks with the highest p_T. Then there are those from a particle with a relatively long half life decaying in charged particles, called *secondary vertices*. There are also vertices from proton-proton pile-up collisions.

The first kind are important since the interesting objects for physics, those with an high-p_{T}, will be associated with one single collision, and therefore only the tracks coming from this vertex are considered. Other tracks coming from other proton-proton vertices will not be considered in the construction of the $E_{\mathrm{T}}^{\mathrm{miss}}$, and also muons or electrons not coming from the primary one will be discarded. Displaced vertices are also important because they hint to a possible presence of B or D hadrons, or τ, and can be used to identify b-jets, c-jets, and $t\tau$s. Vertices are identified starting from the reconstructed tracks. A *finding-*

through-fitting approach is used. The reconstruction starts by selecting tracks likely to originate from the same area, they are then fitted together with only one vertex candidate. Outliers tracks are removed and refitted using them as a seed for an additional vertex. The fit is redone and the process repeated.
Another approach is the *fitting-after-finding*. Here the vertices are formed searching for cluster of tracks in the longitudinal projection. These clusters are then fitted and the outlier rejected and never used in any other cluster. The maximal number of vertex is then decided at the seeding stage.
In a single collision different vertices are identified since on average per bunch crossing there are 13 interactions in the 2015 data, 25 in the 2016, 37 in 2017, and 36 in 2018, for a total average of 33.

6.1.4 Vertexing Efficiency

Vertex efficiency is estimated from data by taking the ratio between the events with a reconstructed vertex and events with at least two reconstructed tracks passing the Tight Primary working point [143]. The results is show in figure 71 from low$-\mu$ runs in the beginning of 2015, as a function of the number of tracks. At higher pileup, efficiency is instead computed by comparing the average interactions per bunch crossing, with the number of reconstructed vertices, as shown in figure 72, for two fills in 2018 with different average μ.

6.2 Jets

Coloured particles arising from the hard scattering (gluons and quarks) can not stay in a free state, therefore they create other particles in order to have colourless state [145]. Initial partons involved in the hard scattering may radiate further gluons, which then may split into further quark anti-quark pairs, and so on until partons are confined in colourless state, i.e. hadrons. This process is called hadronization. This happens in a time of the order of $\Lambda_{\mathrm{QCD}}^{-1}$, which for the time scale considered in the colliders, is almost instantaneous, and therefore happens inside the beam pipe, in the collision point. The produced particles (typically K, π, neutrons, and very few protons) will then reach the detector and consequently interact in the matter, creating a

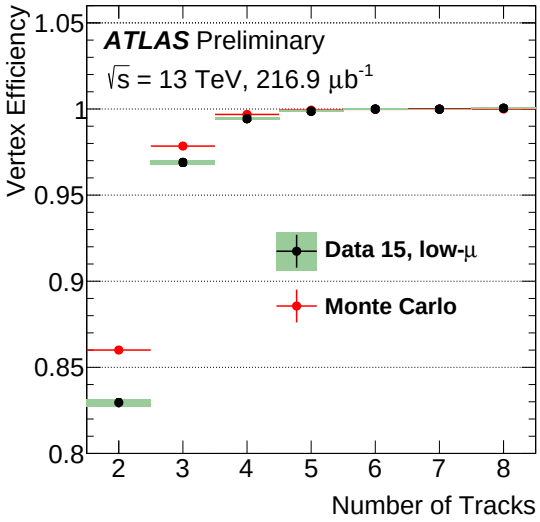

Figure 71: Efficiency of vertex reconstruction as a function of the number of tracks in the low$-\mu$ data in 2015. From ref. [143].

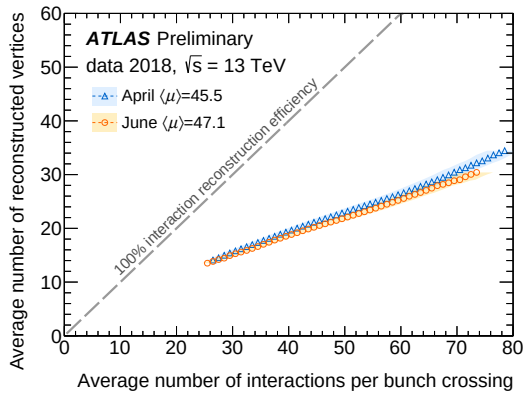

Figure 72: The number of vertices reconstructed as a function of the average number of interactions per bunch crossing, in two fills with different average μ taken at different points in 2018. From ref. [144].

chain reaction, called a *shower*, which generates many other particles. Moreover π^0 generates photons couples that generate more compact electromagnetic showers inside the hadronic one.
For initial quark and gluons with a momentum of 10-20 GeV, this QCD radiation, and then the resulting hadrons, is usually at close

angles with respect of the direction of the initial parton, therefore the concept of *jet* is commonly used, a *pseudo-particle* formed by the vector sum of all the particles generated by the hadronization process inside a given cone. This is useful since it can give an indication of the properties of the initial parton, which otherwise would be unknown.
These hadronic particles deposit most of their energy in the calorimeters system, and it is possible to see the jet as a *local maximum* of deposited energy. Clustering together the inputs from the cells it is possible to construct the jets and try to point to the original coloured particle [146, 147] . A sketch of this is presented in figure 73. Thanks to the high granularity it is possible to discriminate jets from adjacent jets and soft isolated particles. Moreover with the high granularity it is possible to separate and calibrate in different ways the energy deposits due to the electromagnetic shower and the deposits from the hadronic shower.
The first step in the reconstruction of a jet is to cluster together energy deposits in the calorimeter and sum together their energy. The TopoCluster algorithm is used for this purpose. This process starts with a seed cell and then adds the neighboring cells if the energy in that cell is over a certain threshold. This algorithm is divided in two separate steps: cluster maker and cluster splitter.
Initially all the cells with a signal-to-noise ratio over a certain (very high) threshold t_{seed} are identified. The noise here is the RMS of the electronics noise, while the signal is the cell energy. These cells are the seed around which to build the cluster, called now *proto-cluster*. Now all the neighboring cells are considered and if their signal-to-noise ratio is above a t_{neighbor} threshold, the cell is added to the proto-cluster. If a cell is adjacent to more than one proto-cluster, these proto-clusters are merged together. This process is repeated until all the cells are in a proto-cluster or below threshold. Clusters are selected according to the transverse energy, E_T. In general, this variable is defined by $E_T = E \cos\theta$, where θ is the polar angle relative to the center of the detector and E the energy of the particle, and for massless particles the E_T is the same as the transverse momentum p_{T}. If a cluster has a E_T less than a certain threshold it's removed. This is useful to remove pure noise proto-cluster.
The next step is to further separate the cluster, using an algorithm called *cluster splitter*. The first step is to find a set of local maximum cells satisfying:

- $E > 500$ MeV
- Energy greater of any adjacent cell
- At least 4 neighboring cells with energy over threshold.

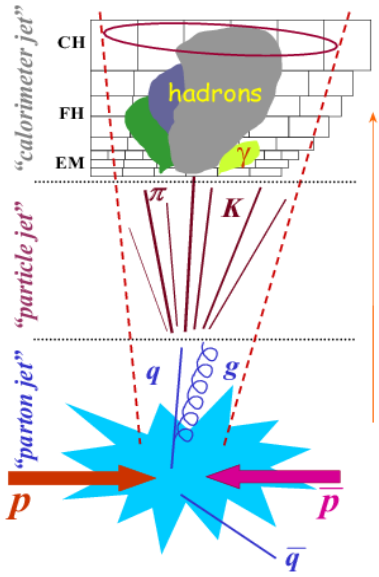

Figure 73: Scheme of jet reconstruction levels

Clusters are now again grown, but starting from these maximum and using only the cells in the proto-clusters. Moreover there is no merging. Cells shared by multiple proto-clusters are added to the two most energetic proto-clusters with a weight $w_{1,2}$ defined by:

$$w_1 = \frac{E_1}{E_1 + rE_2}, \qquad w_2 = 1 - w_1, \qquad r = \exp(d_1 - d_2), \tag{101}$$

where $E_{1,2}$ are the energies of the proto-cluster and $d_{1,2}$ is the distance between the cell and the proto-cluster center.
The next step is to cluster the proto-cluster in jets, in ATLAS this is done by the anti-k_T jet clustering algorithm [148]. The algorithm works by first defining a distance d_{ij} between the objects i and j,

and the distance d_{iB} between the object i and the beam (B). These quantities are built in the following way:

$$\begin{aligned} d_{ij} &= \min(k_{ti}^{2p}, k_{tj}^{2p}) \frac{\Delta_{ij}^2}{R^2} \\ d_{iB} &= k_{ti}^{2p} \end{aligned} \tag{102}$$

where $\Delta_{ij}^2 = (y_i - y_j)^2 + (\phi_i - \phi_j)^2$ and ϕ_i, y_i, and k_{ti} are respectively the azimuth, rapidity, and transverse momentum of the particle i. R is the radius parameter (set to $R = 0.4$), while p is a parameter that governs the relative power of the energy versus geometrical scales (Δ_{ij}^2). p can be 0,1 or -1. In the last case we have the anti-k_t algorithm. The algorithm then works by identifying the smallest of the distances and if is a d_{ij} adding together the objects i and j, that means: $k^{\text{new}} = k_i + k_j$; while if it is d_{iB} then i is defined a jet and removed from the list. The process is then repeated until no more objects are left.
The choice of the parameter $p = -1$ instead of the other option is driven by the fact that, even if more complex than other algorithm, it is more stable and will converge better. Moreover this algorithm is less sensible to soft particles. In others algorithms, such as SISCone, soft particles tend to destabilise the process of convergence, while in the anti-k_T soft term do not modify the shape of the jet, while hard particles do. This is due to the fact that for equally separated particles, the d_{ij} for an hard particle i and a soft particle j is smaller than the d_{ij} between two soft terms, therefore the algorithm clusters together the soft and the hard particles before. This avoids the situation where a lot of soft term cluster together and change the shape of the jet. The different behaviours of the algorithms are illustrated in figure 74.

6.2.1 Jet Energy Calibration

Jets are built by clustering energy deposit in the calorimeter. This energy is measured at the electromagnetic scale (EM-scale), which is the signal scale that electromagnetic showers deposit in the calorimeter. This means that for hadrons the energy measurement is underestimated by $15 - 55$ %, because hadronic and electromagnetic particles interact differently in material and the ATLAS calorimeter does not compensate for this effect. Variable electromagnetic content, and energy losses in the dead material lead to a worst resolution on the jet energy measurement in comparison to particles interacting only

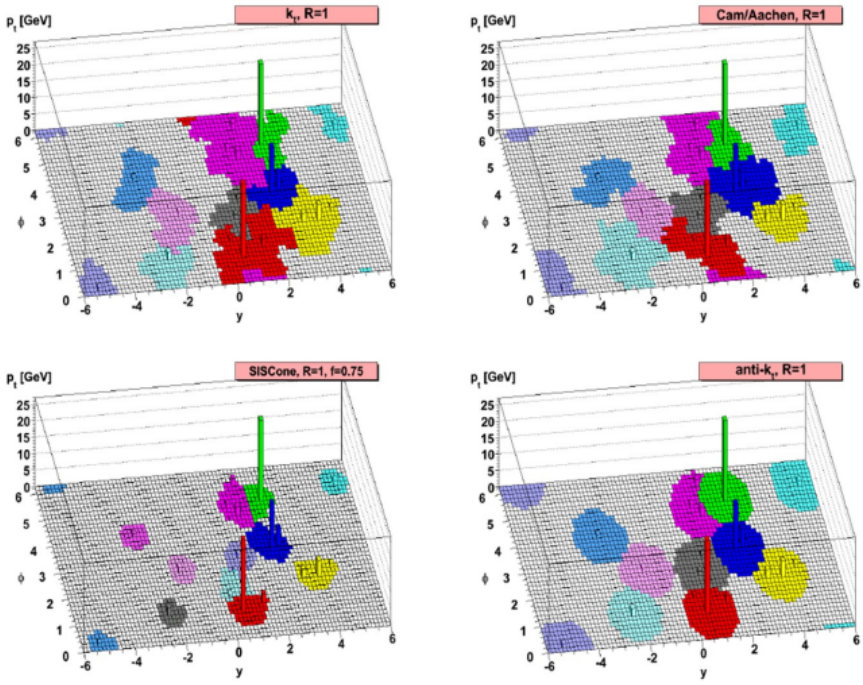

Figure 74: A simulated event at parton level with different soft terms, clustered with four different algorithms

electromagnetically (electrons and photons). For this reason a jet calibration is needed, to correct the bias in the reconstructed energy and reduce as much as possible the spread in the response. The calibration corrections are obtained by trying to unify the response of the jets by applying corrections obtained from Monte Carlo simulation and data driven methods [149]. This process define the *jet energy scale* (JES). Figure 75 shows a schematics of the different steps used in the calibration, that are explained here:

Origin correction The first step is to change the origin direction of the four-momentum of the jets, so that it will point to the hard-scatter primary vertex, rather than the center of the detector. The jet energy is kept constant. This step improves the resolution in η.

Pile-up correction Two other steps are used to reduce the effects of in-time and out-of-time pile-up [150, 151]. In the first

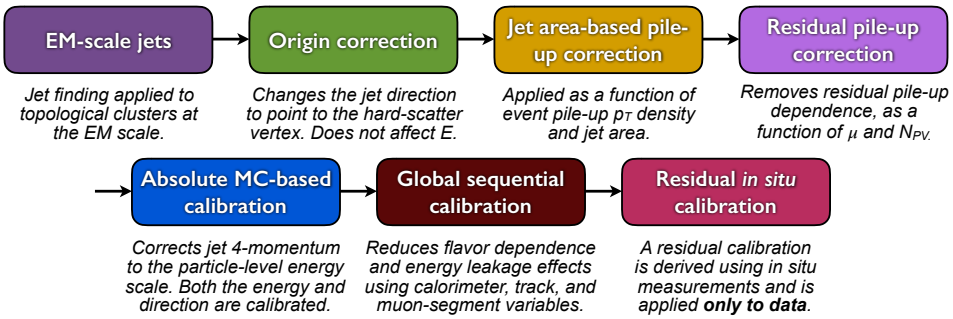

Figure 75: Schematics of the algorithms used for the Jet Energy Calibration

part of the procedure (*jet area-based pile-up correction*) the average pile-up contribution in each event is removed from the p_{T} of each jet, according to an area-based method. The pile-up contribution is obtained from the p_{T} density of jets (ρ) in the $\eta - \phi$ plane. The density of each jet is defined as p_{T}/A. The second part of the procedure take care instead of the residual p_{T} dependence on N_{PV} and μ (*Residual pile-up correction*). These dependence are found to be linear and independent of one another and coefficients are fitted. After these corrections the p_{T} is:

$$p_{\mathrm{T}}^{\mathrm{corr}} = p_{\mathrm{T}}^{\mathrm{reco}} - \rho \times A - \alpha \times (N_{PV} - 1) - \beta \times \mu. \tag{103}$$

Absolute calibration The absolute jet energy scale (JES) and η calibration corrects the reconstructed jet four-momentum to the particle-level energy scale and accounts for biases in the jet η reconstruction, caused by the transition between different parts of the calorimeter. The correction is derived from MC, matching jets to truth particles within $\Delta R = 0.3$, and using only isolated jets (no further jets of $p_{\mathrm{T}} > 7$ GeV within $\Delta R = 0.6$). The response is then defined as E^{reco}/E^{truth} and binned in η.

Global sequential calibration This calibration scheme is based on the jet structure to try to compensate for the energy fluctuation [149]. This method uses the topology of the jet (number of tracks in the jets, or muons segments) and its energy deposit to characterize the energy fluctuations. For each observable used,

the four momentum is corrected, as a function of p_{T}^{truth} and η, but with an overall constant in order to leave unchanged the average energy of the jets at each step.

In-situ calibration The last step of the calibration accounts for differences in the response between the data and the MC, due to imperfect description in the simulations: from detector material, to hard scatter, and pile-up. This is done by balancing the p_{T} of the jet against well known objects. Central jets ($|\eta|< 0.8$) use Z/γ+jets events, where the jets are balanced against the Z boson or the γ. Multijet events are instead used for high p_{T} central jets (300 GeV $< p_{\mathrm{T}} <$ 2000 GeV), where the high p_{T} jets are balanced against well-known central low p_{T} ones. Dijet events are instead used for forward jets ($0.8 < |\eta|< 4.5$), where the jets are balanced against the central jets. Figure 76 shows the ratio of the response for jet of the EM+JES calibration for nominal MC and data.

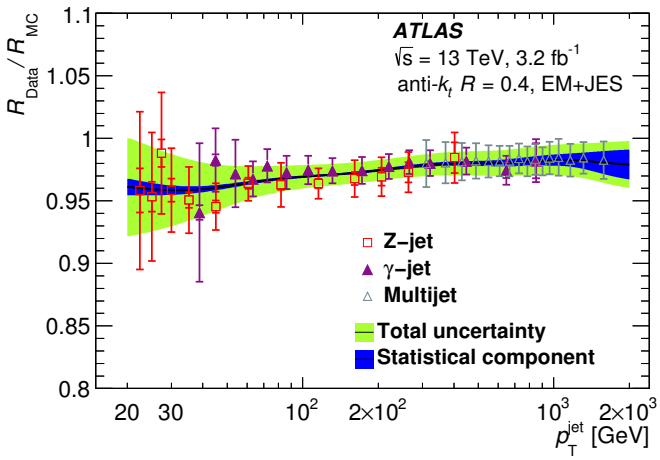

Figure 76: Ratio of the EM+JES jet response in data to that in the nominal MC event generator as a function of jet p_{T} for Z-jet, $\gamma-$jet, and multijet in situ calibrations. The final derived correction (black line) and its statistical (dark blue) and total (light green) uncertainty bands are also shown. From ref [149]

6.2.2 Jet Calibration Systematic Uncertainties

The calibration procedure brings with it a set of uncertainties that are propagated from the individual calibration to the final jet [149]. In total are present 80 JES systematic uncertainties: 67 comes from Z/γ+jets in situ calibration, and accounts for topology assumption, MC simulation and statistic, and propagated electrons/muons/photon energy scale. The other 13 systematic uncertainties come from pile-up (4), η-intercalibration in the region with $2.0 < |\eta| < 2.6$ region (3), and difference in response of light-quark, b-quark, and gluon initiated jets (3). Another uncertainty comes from the Global Sequential Calibration (GSC) punch-through correction. For jets outside the in-situ methods (with a $p_{\mathrm{T}} > 2$ TeV) an additional uncertainty is applied. For fast simulation a AFII modeling uncertainty is also considered for non closure in the JES calibration. Figure 77 shows the total uncertainty as a function of p_{T} and η. However most of the physics analysis

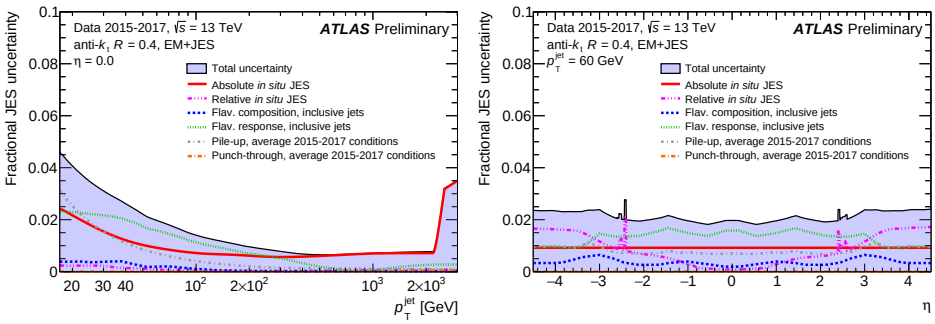

(a) (b)

Figure 77: Fractional jet energy scale systematic uncertainty components for $R = 0.4$ anti-kt jets for: (a) $\eta = 0.2$ as a function of p_{T}, (b) $p_{\mathrm{T}} = 60$ GeV as a function of η, reconstructed from electromagnetic-scale topo-clusters. The total uncertainty (all components summed in quadrature) is shown as a filled region topped by a solid black line. From ref. [152].

don't need to evaluate and propagate each one of the systematics and their correlation by themselves. Moreover, most of the information is unnecessary for some analysis. Therefore in order to simplify a reduced set of nuisance parameters (NPs) is produced that try to preserve as precisely as possible the correlation across p_{T} and η.

The first step is to reduce the in-situ uncertainty: from the 67, the five most relevant are kept separate, while the others are combined in a single parameter. Then these remaining 19 NPs (6 from the in-situ plus 13) are combined into four reduced NPs. This reduction of course reduces the correlations between most of the uncertainties, but the loss of information is indeed small for most of the analysis. In case an analysis needs more information a more extended set of NPs is provided.

6.2.3 Jet Energy Resolution

After the jet energy scale calibration, it is also measured the energy resolution (JER). This can be parametrized as

$$\frac{\sigma(p_{\mathrm{T}})}{p_{\mathrm{T}}} = \frac{N}{p_{\mathrm{T}}} \oplus \frac{S}{\sqrt{p_{\mathrm{T}}}} \oplus C \tag{104}$$

Where N is a *noise* term that contains effects from pileup and electronic noise, that enters at very low p_{T}. S is the statistical Poisson fluctuations due to the sampling nature of the calorimeter. The last term, C, is due to the passive material inside the detector. JER is measured in data and MC by balancing the jet p_{T} with dijet events, Z+jets and γ+jets in a similar way as for the JES. Again, this procedure gives a results with ~ 100 uncertainties, that should be propagated to the analysis, and as for the JES they are combined together in NPs, two sets are possible: 7 NPs and 12 NPs, depending on the needs of the single analysis. The uncertainties are also constrained with respect to the inputs by the use of a fit function that constrain N, S, and C. Figure 78 (a) shows the Jet Energy Resolution as a function of p_{T} for 2017 data and MC, while figure 78 (b) shows its relative uncertainty, divided by type.

6.2.4 Jet Vertex Tagger

Pile-up can be a problem not only because it can bias the energy of the jets, but also because it can lead to the reconstruction of jets that are actually not originating from the hard scattering interaction. Most of the pile-up jets however can be removed using the Jet-Vertex-Fraction (JVF) [154–156]. This variable is the ratio between the scalar

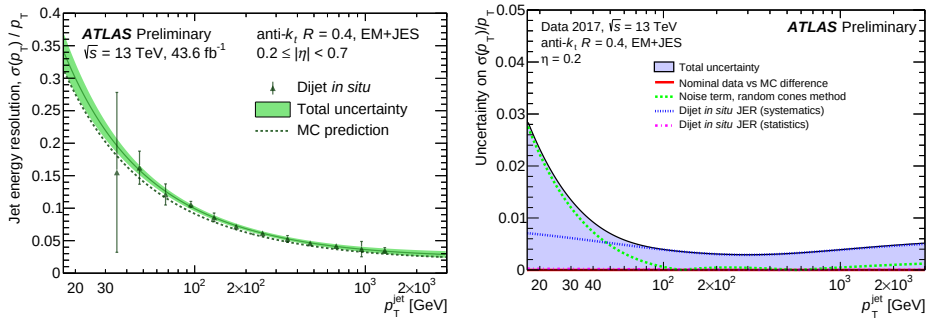

(a) (b)

Figure 78: (a) The relative jet energy resolution $\sigma(p_{\mathrm{T}})/p_{\mathrm{T}}$ and (b) the uncertainty on the relative jet energy resolution, as a function of p_{T} for anti-kt jets with a radius parameter of $R = 0.4$ and inputs of EM-scale topoclusters calibrated with the EM+JES scheme followed by a residual in situ calibration and using the 2017 dataset. From ref. [153].

sum of the tracks p_{T} associated to the jet and to the vertex, and the scalar sum of the p_{T} of all the tracks:

$$\mathrm{JVF} = \frac{\sum_k p_{\mathrm{T}}^{trk_k}(\mathrm{PV}_0)}{\sum_l p_{\mathrm{T}}^{trk_l}(\mathrm{PV}_0 + \sum_{n\geq 1}\sum_l p_{\mathrm{T}}^{trk_l}(\mathrm{PV}_n)} \tag{105}$$

where PV_0 is the hard scatter vertex, while PV_j are the primary vertices of pile-up events. JVF is bound between 0 and 1, but -1 is assigned to jets with no associated tracks. With increasing pile-up, however, this variable is less efficient due to a dependence in the scalar sum of p_{T} on the number of vertexes. For this reason is introduced an additional variable called corrJVF, defined as:

$$\mathrm{corrJVF} = \frac{\sum_k p_{\mathrm{T}}^{trk_k}(\mathrm{PV}_0}{\sum_l p_{\mathrm{T}}^{trk_l}(\mathrm{PV}_0 + \frac{\sum_{n\geq 1}\sum_l p_{\mathrm{T}}^{trk_l}(\mathrm{PV}_n)}{(k\cdot n_{trk}^{\mathrm{PU}})}} \tag{106}$$

where n_{trk}^{PU} is the number of tracks per event and $k = 0.01$, and should be the slope of $\langle p_{\mathrm{T}}^{\mathrm{PU}} \rangle$. Another important variable used to discriminate hard scattering events and pile-up ones is $R_{p_{\mathrm{T}}}$, defined as the ratio between the scalar sum of the tracks p_{T} associated to the PV_0 and

the p_{T} of the jet:

$$R_{p_{\mathrm{T}}} = \frac{\sum_k p_{\mathrm{T}}^{trk_k}(\mathrm{PV}_0)}{p_{\mathrm{T}}^{jet}} \tag{107}$$

Figure 79 (a) and (b) shows the distribution of corrJVF and $R_{p_{\mathrm{T}}}$. These two variables are then combined in a 2-dimensional likelihood, based on a k-nearest neighbor (kNN) algorithm, into a single tagger, called Jet Vertex Tagger. Figure 79 (c) shows the JVT distribution for hard scattering and pile-up jets, while figure 80 shows the JVT selection efficiency for the JVT>0.59 as a function of the jet p_{T}.

6.3 b-tagging

Identification of b-quark jets, called b-tagging, is a vital aspect of the ATLAS experiment. This is made possible because of the special features of the hadrons containing b-quark. In fact these hadrons have relatively long lifetimes ($\approx 10^{-12}$ s) that because of the high energy involved can travel long distances ($\approx$1 mm) before decaying, therefore leaving a secondary vertex in the ID. There are different algorithms exploiting this feature, returning three variables helpful to discriminate between b-quark jets and light-quark (u, d, s) jets [159]. All these algorithms use charged particles tracks associated with jets and ask them to pass different quality selections. These algorithms differentiate themselves by using complementary informations: impact parameter, secondary vertex, and decay chain.

IP3D The IP3D algorithm uses the impact parameter (both longitudinal and transverse) significance of the tracks of the jet. The impact parameter, d_0, is the point of closest approach of the track to the primary vertex. d_0 is positive if it is in front and negative if it is behind. The significance of the impact parameter is the ratio between the impact parameter and its error: $d_0/\sigma(d_0)$ for the transverse and $z_0/\sigma(z_0)$ for the longitudinal one. Probability density functions for the impact parameter are used to define ratios for the b and light jet hypothesis and combined together in a log likelihood ratio discriminant (LLR). LLR can be constructed with different sets of PDF for different track categories. During run 2 these categories have been refined.

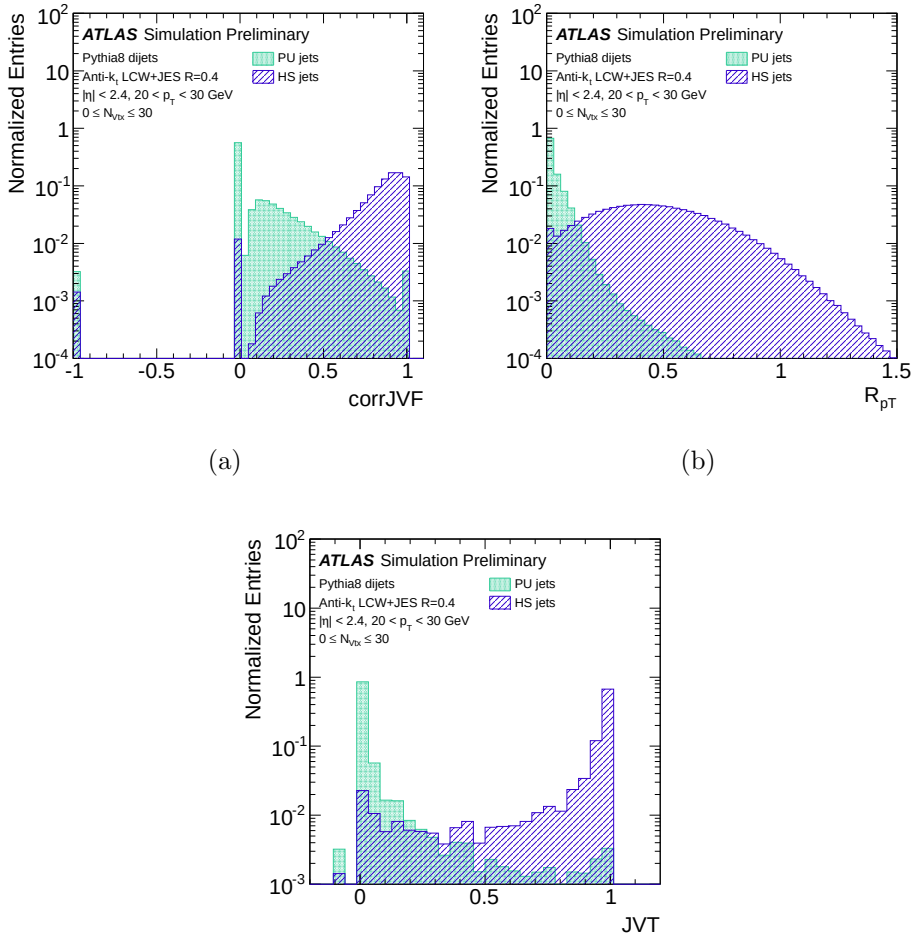

(a) (b)

(c)

Figure 79: Distribution of (a) corrJVF , (b) $R_{p_{\mathrm{T}}}$, and (c) JVT for pileup and hard-scatter jets with $20 < p_{\mathrm{T}} < 30$ GeV. From [157].

SV1 The secondary vertex (SV1) algorithm try to reconstruct the displaced secondary vertex within the jet. The first step is to reconstruct two-track vertices. Tracks that are compatible with long lived particles (K_S or Λ) are rejected. Also photon conversions or hadronic interactions with the detector material are rejected. The discriminant is constructed with the decay length significance: $L/\sigma(L)$.

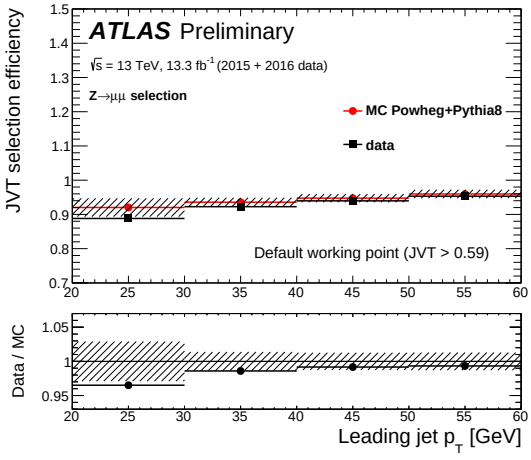

(a)

Figure 80: The hard-scatter jet selection efficiency, in Powheg+Pythia8 MC and in 2015+2016 data, of a JVT> 0.59 cut on a jet balanced against a Z boson decaying to muons. From ref. [158].

JetFitter The JetFitter algorithm use the topological structure of b and c hadrons to reconstruct the whole chain decay PV$\rightarrow$ $b \rightarrow c$ decay. The algorithm try to find a common line between the primary vertex and the bottom and charm vertices, as well as their position on the line, approximating the b-hadron flight path. The discrimination between b-, c- and light jets is based on a neutral network using similar variables.

From this algorithm we gain different variables that are combined and used in multivariate analysis using a boosted decision tree (BDT) to discriminate b-jets from light and c-jets. The algorithm used is called MV2c10, and it is the output of the BDT trained with 5 million $t\bar{t}$ events assigning b-jets as signal and light and c-jets as background. The jets considered in the algorithm have a $p_T > 20$ GeV and $|\eta| < 2.5$. The MVc10 output is illustrated in figure 81.

Working points are defined by a single cut on the output and are chosen to represent a particular b-jet efficiency in a $t\bar{t}$ sample. In table 17 are reported the benchmark value for different efficiency, the c-jets, τ - jet, and light jets rejection rates (absolute value). Figure **??** shows

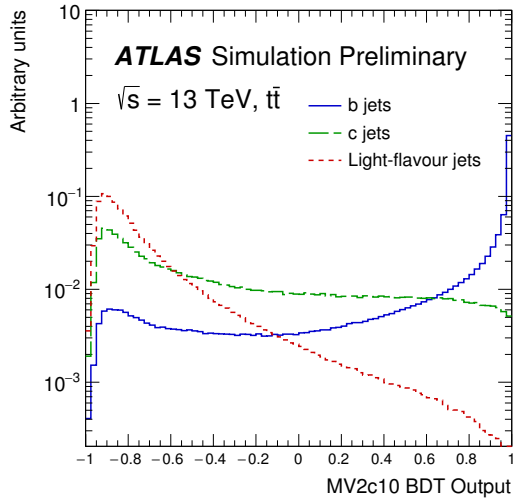

Figure 81: MV2c10 algorithm output for b-jets (dashed blue), c-jets (solid green)and light-jets (dotted red) in $t\bar{t}$ events. From ref. [160].

the b-tag efficiency for a 77% working point as a function of the p_T of the jet, for the same sample of $t\bar{t}$.

Cut Value	b-jet Efficiency [%]	c-jet rejection	τ - jet rejection	Light-jet rejection
0.9349	60	34	1538	184
0.8244	70	12	381	55
0.6459	77	6	134	22
0.1758	85	3.1	33	8.2

Table 17: Operating points for the MV2c10 b-tagging algorithm, including benchmark numbers for the efficiency and rejections rates.

The insertion of the IBL helped not only to sustain the higher particle rate of run 2, but also provide new inputs for the b-tagging algorithm. Moreover the new MV2c10 algorithm is a substantial improvement of the one used in during run 1, called MV1, that used a neural network instead of a BDT. The new approach significantly improves the performance but also it simplifies the algorithm. In Figure 83 the light jet and c-jet rejections are reported as a function of the b-tagging efficiency for different configurations of the b-tag algorithm: MV2c20 (2015 and 2016 configuration), MV2c10, MV2c00. The differ-

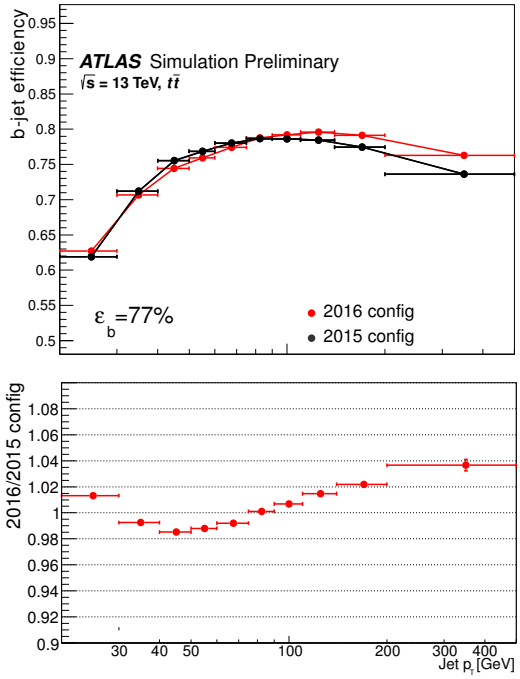

Figure 82: b-tagging efficiency for the Mv2c10 algorithm at the 77% working point as a function of jet p_T for the 2015 (black) and 2016 (red) configuration. From ref. [161].

ences between these configurations consist in the percentage of c-jets in the training samples. For MV2c20 is 15%, for MV2c10 is 7%, and for MV2c00 there are no c-jets. The configuration used in the analysis is the 2016 of the MV2c10 one.

6.3.1 b-tagging efficiency

The b-tagging efficiency can differ between data and MC, and Scale Factors are needed to correct the simulations [160, 162]. It is then important to measure correctly this quantity. The efficiency, ϵ_b, is measured in a sample almost pure of $t\bar{t}$ due to its high b-jet purity, due to the almost 100 % BR of $t \to Wb$. Additional non b-jets events are reduced by asking that both the W from the top decay goes into leptons. Two methods are then used to estimate ϵ_b: a *tag-and-probe* method and a *combinatorial likelihood* method. In the first method,

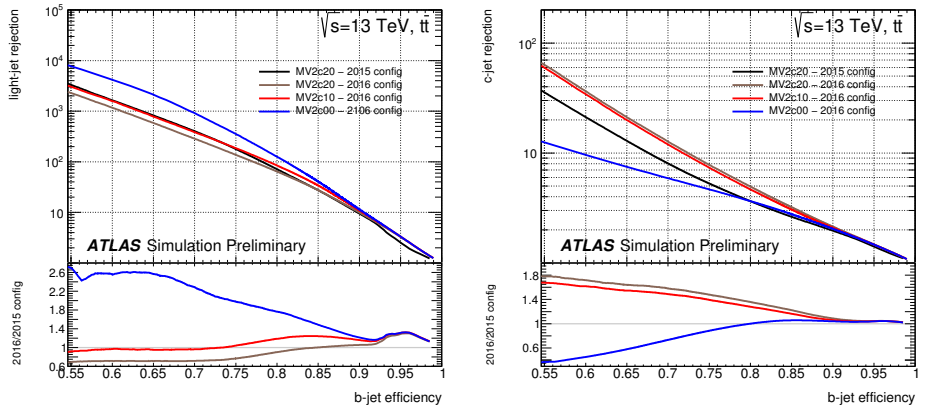

(a) (b)

Figure 83: Light (left) and c-jet (right) rejection versus b-jet efficiency using different b-tag algorithm. From ref. [161].

the efficiency is measured on the *probe* b-jet, meaning the second jet, if the first one is a b-tagged jet at 85 % OP (which is called *tag*). The b-tagging efficiency is measured as

$$\epsilon_b = \frac{f_{\text{tagged}} - (1 - f_b)\epsilon_j}{f_b} \tag{108}$$

where f_{tagged} is the fraction of tagged b-jets in data, while f_b is the fraction of b-jets in $t\bar{t}$ events. ϵ_j instead is the efficiency of non-btagged jets.

In the second method instead the events are divided in many categories depending on the flavor of the two leptons, the number of jets, and the number of b-tagged jets. Normalization of MC is obtained by fitting the simulations to data. From all this selection a likelihood is built that is then maximised. This approach has the advantage of preserving better the correlations and giving then a much more precise measurement. Different sources of uncertainty are considered in the method, including MC modeling, MC normalization and experimental effects. Figure 84 shows the ratio of data and simulation efficiency for both the Likelihood method and the Tag and Probe method.

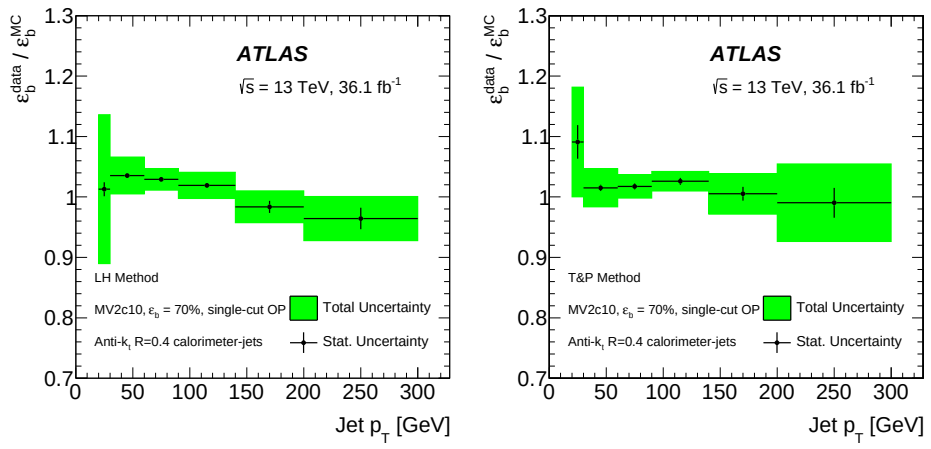

(a) (b)

Figure 84: Data-to-simulation scale factors as a function of the jet p_{T} using (a) the Likelihood method and (b) the Tag and Probe method. Both the statistical uncertainties (error bars) and total uncertainties (shaded region) are shown. From ref [162]

6.4 Electrons

6.4.1 Reconstruction

The electron reconstruction procedure is based on clusters in the electromagnetic calorimeter that are matched with a reconstructed track inside the Inner Detector [163]. The algorithm used is built to allow for an optimal reconstruction of the momentum and energy of the electrons in all the pseudorapidity range and for any luminosity.

The EM-calorimenter is divided into a grid in the $\eta \times \phi$ directions in 200×256 elements (called towers) corresponding to the granularity of the second layer of the EM-calorimeter. Energy in the first, second, and third layer of this detector are then summed together to get the energy of the tower. Clusters are then seeded starting from towers with energies above 2.5 GeV and see if there is a match with one or more tracks. Reconstructed tracks are matched to seed clusters by extrapolating their last hit to the calorimeter layer and if their $\eta - \phi$ position is in a certain window around the cluster position then the track is considered matched. If tracks do not contain silicon hits, the matching is restricted to the ϕ coordinate since the η accuracy in the

TRT is limited. It is also possible that multiple tracks match the same cluster, in this case the track with the smallest $\Delta R = \sqrt{\Delta\phi^2 + \Delta\eta^2}$ is considered matched. Tracks with silicon hits have priority over one without silicon hits, since it is more likely for the one without hits to come from photon conversion. Track matching is also affected by Bremsstrahlung losses, resulting in an asymmetric $\Delta\phi$ distribution. This can be mitigated by extrapolating the track from the perigee and uses the cluster energy for the electron momentum.
The electron trajectory is computed from the track information, while the energy is a weighted average of the track momentum and the energy deposit in the calorimeter. The η and ϕ coordinates are taken from the tracks, unless there are no silicon hits, in this case the ϕ position is taken from the TRT and the η position by cluster pointing. Figure 85(a) shows the reconstruction efficiency for simulated electrons as a function of the truth p_{T} for each of the step of the formation of the electron candidate.

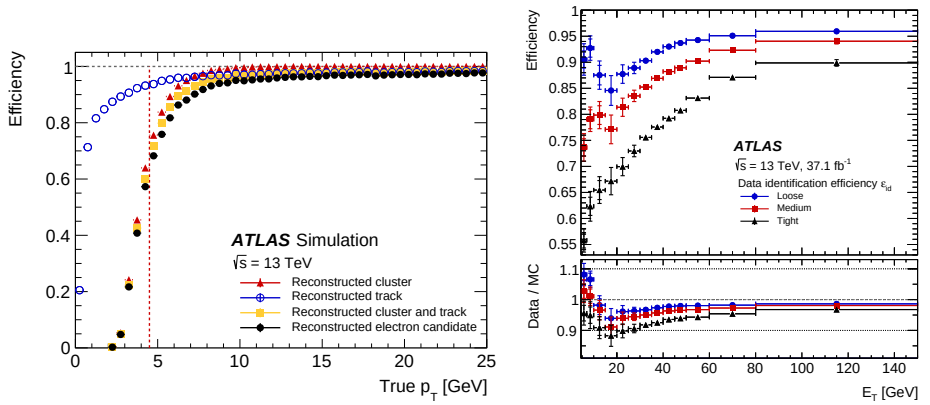

(a) (b)

Figure 85: (a)The total reconstruction efficiency for simulated electrons in a single-electron sample is shown as a function of the true (generator) transverse momentum p_{T} for each step of the electron-candidate formation. (b) The reconstruction and identification efficiency as a function of the E_T for MC and data (2016) for three different working points. From ref. [163]

6.4.2 Identification

Electrons are identified by different sets of criteria. This definition relies on a Likelihood based discriminant, whose inputs are variables with high discriminating power between isolated electrons and jets signatures. These variables includes: information from the tracker and the matching, information from the electromagnetic calorimeter, and hadronic leakage. The combination of all these variables are put together in a Likelihood $L_{s/b}$, for both signal (s) and background (b). The discriminant is $d_L = \frac{L_s}{L_s+L_b}$ and to each electron candidate is given a value. The likelihood distribution was built with two different method, depending on the time period, since the ATLAS reconstruction software changed release. Analysis started before 2017 and that used only 2015 and 2016 data used the so called Release 20.7 (R20.7), while the newer analysis using the whole Run 2 dataset used Release 21 (R21). In R20.7 the likelihood discriminant is build from data, using for signal $Z \to ee$ events and $J/\Psi \to ee$ events (for low E_T events), while dijet samples for the background [163]. Instead in R21 the pdfs of the likelihoods are derived from MC samples, of J/Ψ and $Z \to ee$ for the signal, and samples with one electron reconstructed [164].
Different working points are obtained, using the same variables, but with different values of the discriminant: *Loose*, *Medium*, *Tight*, with increasing threshold values, and are chosen in order to have efficiency for electrons with $E_T > 40$ GeV of 93%, 88%, and 80% respectively. This means that they are inclusive, and one the subset of the other. All of these working points have fixed requirement on tracking criteria, they all require at least two hits in the pixel detector, and at least 7 hits in pixel and SCT detector combined. Medium and Tight requires also that one of the pixel hits must be in the IBL, helping reducing backgrounds from photon conversions. Figure 85(b) shows the combined reconstruction and identification of electrons for both data and MC, using $Z \to ee$ and $J\Psi \to ee$ events, in order to cover both high and low p_{T} of the electrons. It is important to notice that the electron reconstruction algorithm is able to go as down as 4.5 GeV, this was a huge improvement with respect to Run 1, where it was 7.5 GeV, and it was crucial in allowing sensitivity to the analysis presented in this thesis. It is also important to notice that even if electrons are identified only for $p_{\mathrm{T}} > 4.5$ GeV, they can be reconstructed even for lower p_{T}, even if with low efficiency.

6.4.3 Calibration

As for the jets, electrons energy needs to be calibrated to deal with effects such as energy losses in passive materials, EM shower leakages and fluctuations in the deposited energy [165]. These corrections are evaluated by comparing Data and Monte Carlo on a very well know Standard Model process, i.e. $Z \to e^+e^+$, $W \to e\nu$, and $J/\Psi \to e^+e-$. The correct parameters are obtained after a global fit on the invariant mass of the e^+e^- couple. Any residual miscalibration is then corrected by the scale factor defined by:

$$\alpha = \frac{E_{\text{measured}} - E_{\text{truth}}}{E_{\text{truth}}} \tag{109}$$

where E_{measured} is the energy measured by the calorimeters after the MC-based correction, and E_{truth} is the truth energy of the electrons.

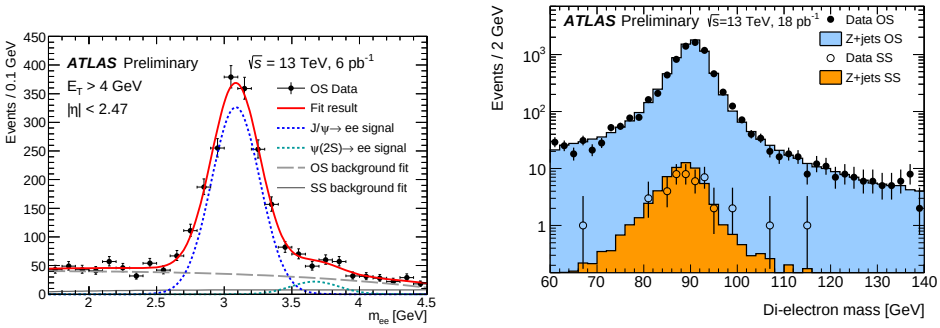

(a) (b)

Figure 86: Invariant mass of the e^+e^- couple for the J/ψ and the Z for both same sign and opposite sign electrons. From ref. [166].

6.4.4 Isolation

Prompt electrons are usually further away (isolated) from other objects than electrons coming from hadrons decays. To then reduce backgrounds coming from these events, an *isolation* cut is applied to the electrons [164]. Different criteria are defined, with different levels of efficiency in rejecting the background. Which one to use is an analysis dependent task. The isolation working points uses variables from the tracking and from the calorimeter.

Calorimetric isolation variables are build by summing the transverse energy of positive energy deposit clusters whose barycentre falls within a cone centered around the selected electron. Then the energy of the electron itself is removed, and other corrections are done to account for pile-up. This variable is called E_T^{coneXX} where XX depends on the size of the cone. For tracking isolation variable the method is similar: the p_{T} of the tracks inside a cone of given size around the candidate electrons are summed together. In order to compensate for very busy environment at high p_{T} the cone is of variable size:

$$\Delta R = \min\left(\frac{k_T}{p_{\text{T}}}, R_{\text{max}}\right). \tag{110}$$

Different Working Points (WP) are defined using a combination of the calorimetric and tracking isolation variables. The WP are obtained by asking either a fixed value of efficiency or with fixed cut on the isolation variables. *Gradient* WP is built by asking that the efficiency is 90% at $p_{\text{T}} = 25$ GeV and 99% at $p_{\text{T}} = 60$ GeV, and uniform in η. Instead the other WP have fixed cuts. *FCHighPtCaloOnly* instead doesn't use tracking information, this is done in order to reduce the contribution of fake leptons and very high p_{T} from multijet processes. Table 18 shows the definition of each WP, instead figure 87 shows the efficiency for the Gradient WP as a function of p_{T} and η for both data and MC.

Working Point	Calorimetric Isolation	Track Isolation
Gradient	$\epsilon = 0.1143 \times p_{\text{T}} + 92.14\%$ (with E_T^{cone20})	$\epsilon = 0.1143 \times p_{\text{T}} + 92.14\%$ (with $p_{\text{T}}^{\text{varcone20}}$)
FCHighPtCaloOnly	$E_T^{\text{cone20}} < \max(0.015 \times p_{\text{T}}, 3.5 \text{ GeV})$	-
FCLoose	$E_T^{\text{cone20}}/p_{\text{T}} < 0.20$	$p_{\text{T}}^{\text{varcone20}}/p_{\text{T}} < 0.15$
FCTight	$E_T^{\text{cone20}}/p_{\text{T}} < 0.06$	$p_{\text{T}}^{\text{varcone20}}/p_{\text{T}} < 0.06$

Table 18: Operating points for the electron isolation and their cuts on the Calorimetric and Track isolation variables.

6.5 Muons

6.5.1 Reconstruction

The muon reconstruction is done independently by both MS and ID, then the information from the different sub detectors is combined

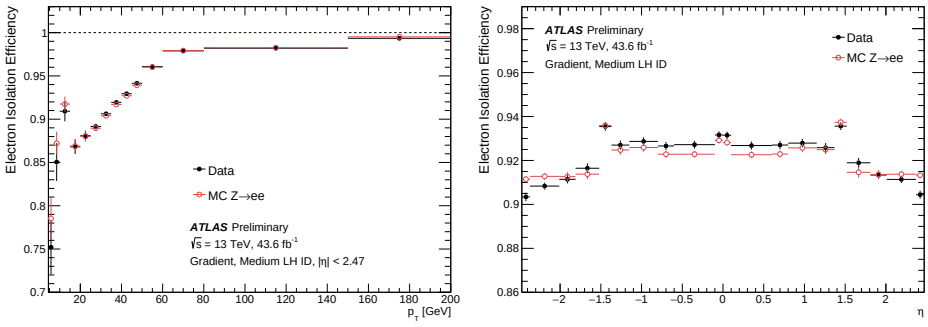

(a) (b)

Figure 87: Isolation efficiency for the Gradient WP as a function of (a) p_{T} and (b) η, from $Z \to ee$ events in both data and MC. Using Medium WP for ID. From ref. [167].

[168]. Reconstruction in the ID is the same as for any other particle. The reconstruction in the MS starts with the search in the muon chamber of hit patterns forming segments in the bending plane of the detector. Muon track candidates are built from a fit with segments from different layers. The algorithm used starts from a track-seed in the middle layers and then select other track using criteria such as hit multiplicity and fit quality. Hits associated to a track are fitted and the track candidates are accepted if the χ^2 of the fit satisfies the selection criteria. Outlier hits in the χ^2 are removed.
The next step in the reconstruction is the match between the ID and the MS informations. Four muon *type* are defined according to the subdetectors involved:

Combined (CB) Tracks are reconstructed independently in the ID and MS, and a global fit is done. Hits may be removed or added to have a better fit. Muons reconstruction follow an outside-in approach, starting from the MS and searching a match in the ID, while inside-out approaches are used as complementary.

Segment-tagged (ST) ID tracks are extrapolated to the MS and at least one track segment in the first layer MDT or CSC chamber is searched. This is helpful for low p_T muons or for muons that exit the MS acceptance.

Calorimeter-tagged (CT) A track in the ID is associated with an energy deposit in the calorimeter that is compatible with a minimum ionizing particle. This type of muon has a low purity but is helpful in those part of the MS detector less instrumented, where are positioned the cabling and services of the calorimeter and ID. CT identification criteria are optimised for a range $15 < p_{\mathrm{T}} < 100$ GeV.

Extrapolated (ME) Muons trajectories are reconstructed based only on the MS track and loose criteria on the compatibility with the interaction point. Energy loss in the in the calorimeter is estimated. Tracks are required to have at least two layer of MS chambers in the barrel and at least three in the forward region. This type of muons are helpful to recover muon outside the ID acceptance, in the pseudorapidity range $2.5 < |\eta| < 2.7$.

Overlaps between different types are resolved giving different priority. For muons sharing the same ID tracks, preference is given to the CB category, then ST and finally CT. ME overlaps are resolved by selecting tracks with better fit quality.

6.5.2 Identification

Muon identification is done by applying quality requirements. This suppresses background from pions or kaons decays. Several variables are studied using a $t\bar{t}$ sample that have high discriminating power.

Some of these variables are:

- q/p significance: difference between the ratio of the charge and momentum of muons candidates in the ID and the MS divided by the sum in quadrature of the corresponding uncertainties.
- ρ': difference between the transverse momentum measured in the ID and MS over the combined p_T.
- normalised χ^2 of the combined track

Then five different identification categories are defined with different sets of requirement. This correspond to five different working point, with different background rejection rate and identification efficiency.

Medium muons This is the default selection, it minimise the systematic uncertainties. Only CB and ME tracks are used. The CB muons are required to have at least three hits in at least two MDT layers, unless in $|\eta| < 0.1$ where also tracks with up to one MDT hole are allowed. The ME are used in the $2.5 < |\eta| < 2.7$. Requirement on ID and MS momentum compatibility are added to suppress hadrons misidentified.

Loose muons This criteria is designed to maximise the reconstruction efficiency. All type of muons are used. CB and ME *Medium muons* are included, CT and ST are restricted to the $|\eta| < 0.1$ region. This type of criteria is optimised to provide good quality muon track, specifically for Higgs searches in the four lepton channel.

Tight muons This set of cuts is chosen to increase the purity of muons at the cost of efficiency. Only CB *Medium muons* with hits in at least two stations of the MS are selected. Cuts on the χ^2 and the p_T are also applied.

High p_T muons This working point aims to maximise the p_T resolution for tracks with high transverse momentum (over 100 GeV). CB *Medium muons* with at least three hits in three MS stations are selected. Tracks in specific regions of the MS (where there are discontinuity) are vetoed. This procedure reduces the efficiency by almost 20 % but improves the p_T resolution by almost 30 % for muons up to 1.5 TeV. This criteria is helpful for searches for high-mass Z' and W'.

Low p_T muons This working point is used to reconstruct events with very low momentum: down to 4 GeVin the 2015-2016 data taking period, and then down to 3 GeV(with the change in software) [169]. For the LowPt WP only CB tracks are used, and at least one MS station, for $|\eta| < 1.3$, while at least two MS station for $1.3 < |\eta| < 1.55$. Medium WP is required for $|\eta| > 1.55$. Additional variables are used to discriminate prompt and fakes muons. Compared with the other WP, LowPt allows for higher efficiency in the barrel, at the expense of higher fake rate.

6.5.3 Efficiency measurement

A measurement of the muon reconstruction efficiency in the region $|\eta| < 2.5$ is obtained with a tag-and-probe method. This method is similar to the one used for the electrons, it selects a pure sample of $J/\Psi \rightarrow \mu\mu$ and $Z \rightarrow \mu\mu$ events (figure 88). Data and Monte Carlo comparisons are done and the difference is used to compute scale factors for compensating energy losses in the materials or distortions in the magnetic fields not optimally simulated. Figure 89 shows the efficiency for the LowPt WP compared to the Medium WP as a function of p_{T} and η for $t\bar{t}$ simulation, while figure 90 shows the efficiency as a function of p_{T} in bin of η for both simulation and data, (a) for LowPt WP and (b) for Medium.

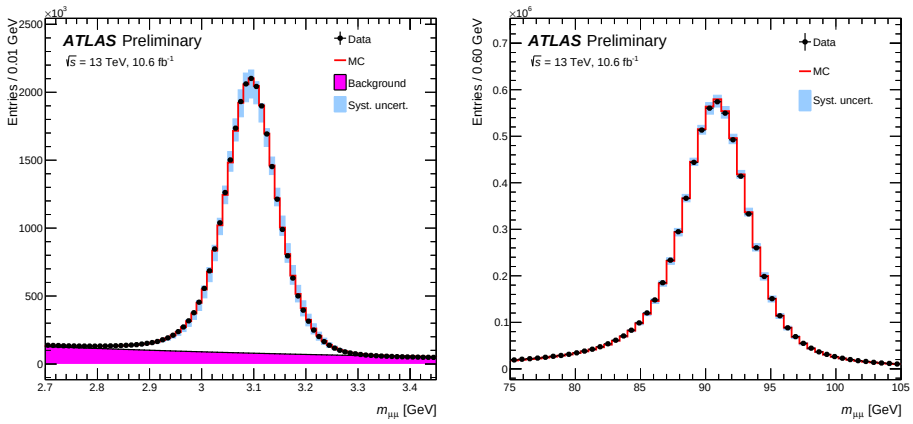

Figure 88: Invariant mass of the $\mu^+\mu^-$ couple for the J/ψ and the Z. From ref. [170].

6.5.4 Isolation

Similar to the electrons, different isolation working point are defined in order to reduce the contribution of non prompt muons. Between 2015 and 2016 data taking there were 7 different WP, while with the start of 2017 and through the whole year and in 2018 9 new WP were implemented instead of the previous 7. In the same way as for electrons, they use tracking and calorimetric isolation variables based on $p_T^{\mathrm{varconeXX}}$ and E_T^{cone20}. The WPs used in the analysis were: *FixedCutTightTrackOnly*, for the analysis using 2015 and 2016 data, and

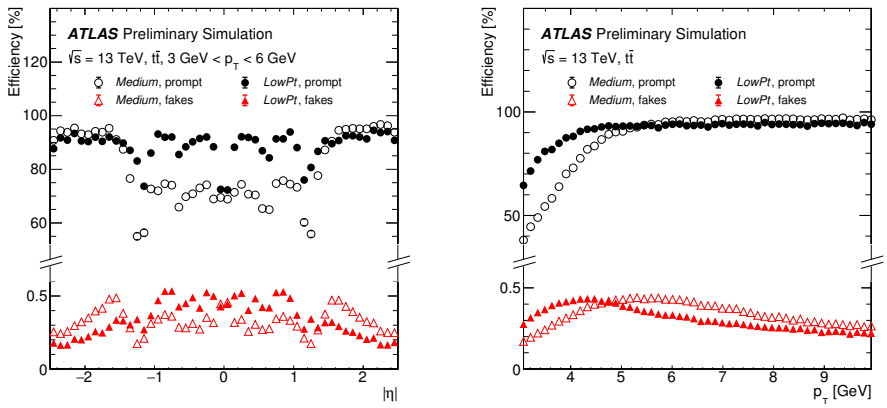

(a) (b)

Figure 89: Identification efficiency for the Medium WP and LowPt WP as a function of (a) η and (b) p_{T}, from $t\bar{t}$ MC events. From ref. [169].

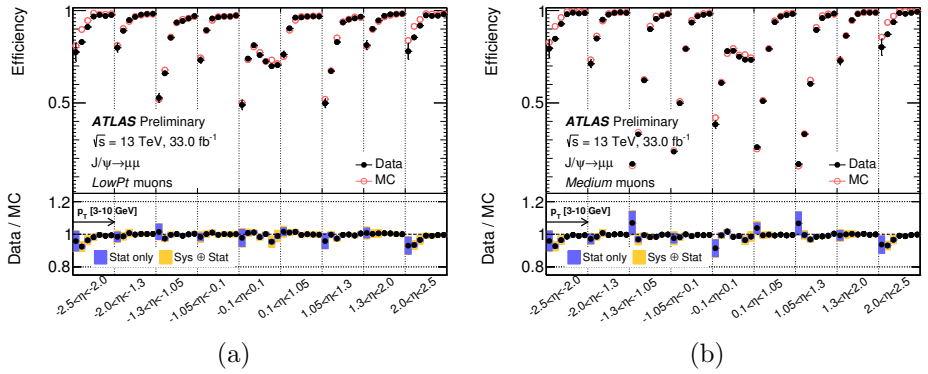

(a) (b)

Figure 90: Identification efficiency for the LowPt WP (a) and Medium WP (b) as a function of p_{T} in bins of η, for both MC and data. From ref. [169].

FCTightTrackOnly for the full Run 2 results. These two WP uses only the tracking information, the first ask for $p_{\mathrm{T}}^{\mathrm{varcone30}} < 0.06 \times p_{\mathrm{T}}^{\mu}$, while the second ask for $p_{T,\mathrm{TightTTVA}}^{\mathrm{varcone30}} < 0.06 \times p_{\mathrm{T}}^{\mu}$ where $p_{T,\mathrm{TightTTVA}}^{\mathrm{varcone30}}$ is a variation of $p_{\mathrm{T}}^{\mathrm{varcone30}}$ that takes into account also the position of the Primary Vertex. Figure 91 shows the isolation efficiency for the

FixedCutTightTrackOnly WP as a function of p_{T}. The bottom panel shows also the ratio Data/MC and the statistical and systematic uncertainties. Differences between MC and Data are used to compute Scale Factors for the simulations.

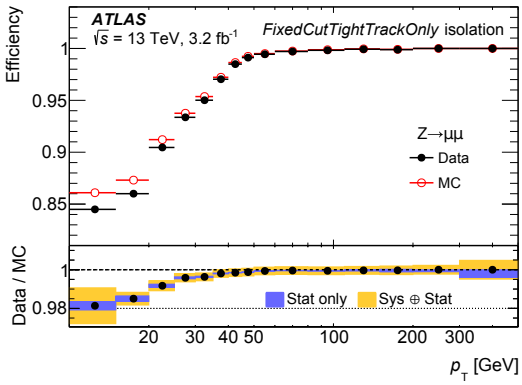

Figure 91: Isolation efficiency for FixedCutTightTrackOnly WP for data and MC, using $Z \to ee$ events, as a function of p_{T}. From ref. [168].

6.6 Missing Trasverse Energy

In proton-proton colliders the fraction of energy the partons have in the collision is unknown, therefore we do not know the initial energy and cannot use the conservation of the momentum. But considering only the transverse plane it is still possible, since in this plane the sum of the initial momentum is zero. This quantity accounts for all the particles that are invisible to the detector, mainly neutrinos or particles beyond the Standard Model, such as neutralinos. We can then define the missing transverse energy ($E_{\mathrm{T}}^{\mathrm{miss}}$) as

$$E_{\mathrm{T}}^{\mathrm{miss}} = \sqrt{(E_x^{miss})^2 + (E_y^{miss})^2} \tag{111}$$

where $E_{x(y)}^{miss} = -\sum E_{x(y)}$, and $E_{x(y)}$ is the energy deposited in the detector. Contribution for the $E_{\mathrm{T}}^{\mathrm{miss}}$ comes from the calorimeters, the muon spectrometers, and also the ID. $E_{\mathrm{T}}^{\mathrm{miss}}$ reconstruction uses calorimeter cells calibrated for the different object reconstructed (electrons, photons, hadronically decaying τ-leptons, jets and muons) and

tracks ($|\eta| < 2.5$) and cells in the calorimeter ($|\eta| > 2.5$) with no object attached [171, 172]. The $E_{\mathrm{T}}^{\mathrm{miss}}$ is then calculated as

$$E_{x(y)}^{\mathrm{miss}} = E_{x(y)}^{\mathrm{miss},e} + E_{x(y)}^{\mathrm{miss},\gamma} + E_{x(y)}^{\mathrm{miss},\tau} + E_{x(y)}^{\mathrm{miss,jets}} + E_{x(y)}^{\mathrm{miss,softjets}} + E_{x(y)}^{\mathrm{miss,calo}\mu} + E_{x(y)}^{\mathrm{miss},tracks} + E_{x(y)}^{\mathrm{miss},softcalo} + E_{x(y)}^{\mathrm{miss},\mu} \tag{112}$$

Where every term is the negative sum of all the object in that category. The sum of this terms is done in the pseudorapidity range $|\eta| < 4.9$. The azimuthal coordinate is evaluated as

$$\phi^{\mathrm{miss}} = \arctan(E_y^{\mathrm{miss}}/E_x^{\mathrm{miss}}) \tag{113}$$

$E_{x(y)}^{\mathrm{miss},softcalo}$ is the sum of the terms in the calorimeter that don't match any object, and $E_{x(y)}^{\mathrm{miss,calo}\mu}$ the energy due to muons in the calorimeters. The $E_{x(y)}^{\mathrm{miss},tracks}$ term contains the tracks from the ID, which are helpful since they are less dependent on the pileup, because is possible to identify and use only the one coming from the primary vertex. Moreover tracks are also added to the calculation to compensate low p_{T} particles

Reducing noise contamination is crucial, for this purpose the cells considered are only the one belonging to the topological clusters. An overlap removal request between calorimeter cluster with high-p_T and tracks is requested to avoid double counting. Tracks with more than 40% of uncertainty on the p_T are removed. Furthermore, for the $E_{x(y)}^{\mathrm{miss},CellOut}$ term, tracks with $p_T > 500$ MeV and passing selection criteria on the number of hits and on χ^2 are also used. $E_{\mathrm{T}}^{\mathrm{miss}}$ using the soft track is called: TST $E_{\mathrm{T}}^{\mathrm{miss}}$.

Three different working points are provided in order to satisfy the needs of the many analysis. The *Loose* WP uses all the jets with $p_{\mathrm{T}} > 20$ GeV that pass the JVT cut for $|\eta| < 2.4$ and $p_{\mathrm{T}} < 60$ GeV. A new working point was introduced: the *Tight* $E_{\mathrm{T}}^{\mathrm{miss}}$, this WP was developed in order to reduce the dependence on the pileup of $E_{\mathrm{T}}^{\mathrm{miss}}$, and it is calculated without the use of forward jets with $|\eta| > 2.4$ and $20 < p_{\mathrm{T}} < 30$ GeV. This helps remove pileup jets, at the expense of a lower energy resolution of the $E_{\mathrm{T}}^{\mathrm{miss}}$. Moreover at low pileup the resolution is worse. Another WP introduced is the *Forward JVT*

(fVJT) WP, and it is used to reduce the tails in $E_{\mathrm{T}}^{\mathrm{miss}}$. This WP keep the jet p_{T} requirement but doesn't include forward jets with $|\eta|> 2.5$ and $20 < p_{\mathrm{T}} < 50$ GeV.

Performance studies of events with no real $E_{\mathrm{T}}^{\mathrm{miss}}$ are done by looking at $Z \to \mu\mu$ events while for events with real $E_{\mathrm{T}}^{\mathrm{miss}}$, $W \to l\nu$ is studied. The value of the resolution on the TST $E_{\mathrm{T}}^{\mathrm{miss}}$ is estimated by comparing MC and data in $Z \to \mu\mu$ events, where no real $E_{\mathrm{T}}^{\mathrm{miss}}$ is expected. The resolution is evaluated as the root-mean square of the combined E_x^{miss} and E_x^{miss}.

An important quantity used to parametrize and understand the $E_{\mathrm{T}}^{\mathrm{miss}}$ resolution is the $\sum E_T$, defined as the sum of all the transverse energy

$$\sum E_T = \sum_{i=1}^{N_{cell}} E_i \sin\theta_i \tag{114}$$

where E_i is the energy of calorimeter cells associated with topocluster in $|\eta| < 4.9$, and θ_i the respective polar angle. In figure 92 is plotted the resolution as a function of the $\langle\mu\rangle$, and the number of vertices for Loose and Tight WP.

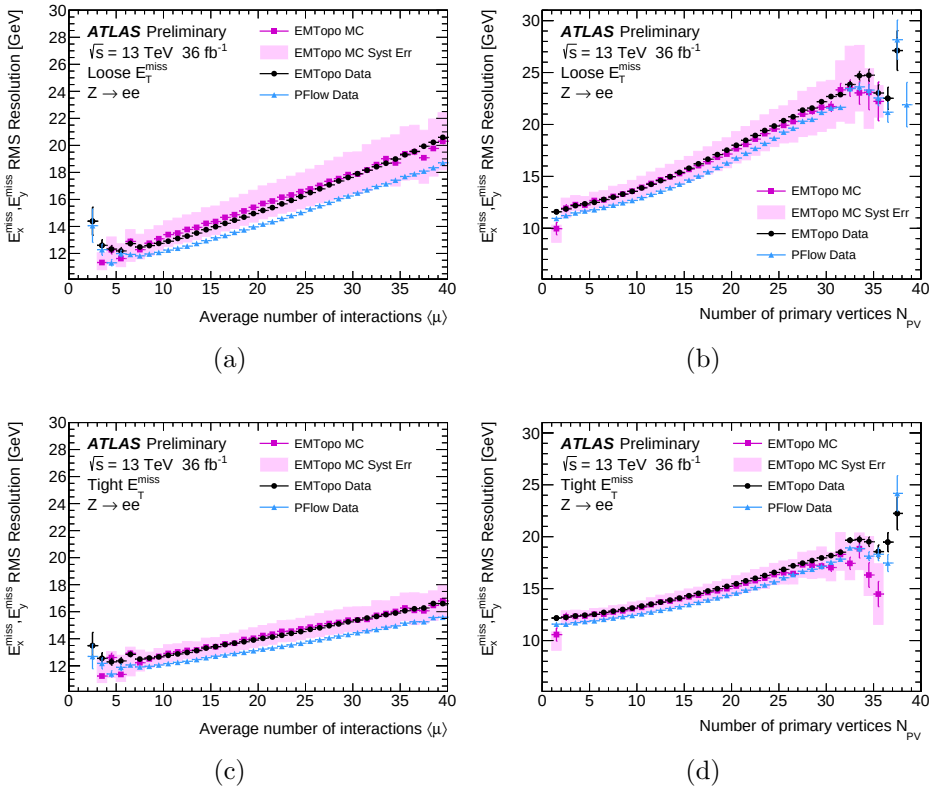

Figure 92: The RMS obtained from the combined distributions of EMTopo E_x^{miss} and E_y^{miss} using the Loose $E_{\text{T}}^{\text{miss}}$ (top) and Tight $E_{\text{T}}^{\text{miss}}$ (bottom) operating point for data and MC simulation in $Z \rightarrow ee$ events as a function of (a)/(c) $\langle\mu\rangle$ and (b)/(d) NPV. From ref. [172].

7 Overall Strategy

7.1 Statistical significance and Signal Region definition

In a search for new physics, generally, there is an *hypothesis testing*, which is a statistical procedure to confirm or reject a specific model, in this case the discovery or exclusion of new physics beyond the Standard Model [173]. Two alternative hypothesis are formulated: the null hypothesis, $\mathcal{H}_b$, that assumes only the presence of the SM background (b), and the alternative hypothesis, $\mathcal{H}_{b+s}$, that assumes the presence of both the SM background (b) and the new (s) physics signal. The two hypothesis can also be parametrized as a function of μ_{sig}, the signal strength. This is a normalization factor that for $\mu_{\text{sig}} = 1$ refers to the signal hypothesis, while for $\mu_{\text{sig}} = 0$ refers to the background only hypothesis.
It is possible to define a *test statistic* t: a real value, function of all the collected data. The Probability Density Function (PDF) of this test statistic is different depending on the choice of hypothesis considered true: null or the alternative. A $p-$value is then defined, which quantifies the compatibility of the observed data with one of the hypothesis. For each hypothesis (called test hypothesis) and for a given value of the test statistic t_{obs}, a $p-$value is computed, as the probability of observing a test statistic greater than the one observed:

$$p_{s/b} = \int_{t_{\text{obs}}}^{\infty} f(t|\mathcal{H}_{s/b})dt. \tag{115}$$

When the $p-$value is lower than a certain threshold, the test hypothesis is excluded. This threshold is generally arbitrary, but in High Energy Physics it is usually set to $p-\text{value} = 0.05$, corresponding to the exclusion at 95% Confidence Level (CL). Instead, in order to declare a "discovery" the threshold is different: for an *evidence* the $p-$value required is 1.3×10^{-3}, while for a *discovery* it is set to 2.9×10^{-7}.
Another parameter that is generally used, instead of the $p-$value, is the significance Z [174], defined as the standard deviations of a standard Gaussian needed to have an upper tail integral equal to the $p-$value

$$Z = \Phi^{-1}(1-p) \tag{116}$$

	$p-$value	Z
Exclusion	0.05	1.64
Evidence	1.3×10^{-3}	3
Discovery	2.9×10^{-7}	5

Table 19: $p-$value and significance threshold for exclusion, evidence, and discovery of new physics.

where Φ is the cumulative of the standard Gaussian. Table 19 summarizes the $p-$value and their respective significance for exclusion, evidence, and discovery.

The analysis strategy is then based on using *Signal Regions* (SR), phase space region that are enriched of signal with respect of the background. Using signal samples as benchmark, the SR is the region where the statistical significance Z is maximized. These regions are defined by a series of kinematic cuts on the main objects used in the analysis: p_{T} of the leptons, p_{T} of the jets, number of jets, $E_{\mathrm{T}}^{\mathrm{miss}}$, and so on, or combination of these.The values of these cuts are decided by comparing how the significance Z changes with varying cuts.

In the analysis presented here the Z is computed using BINOMIALEXPZ in ROOSTATS [175], and it is maximized by varying together the variables used. This is done since many of the variables are correlated. In the computation, the error on the background is considered the same in each bin, and in the analysis presented here it was fixed at 30 %. This was done since the SR optimization was done before the estimate of the background uncertainty was implemented. Therefore it was used a simplified, but conservative, approach to use as an estimate. After the estimate of the systematic uncertainty was done, the optimization was checked again, but results were similar and were not changed. Moreover, it is required to have enough statistic in the SR in order not to be biased toward region with zero or almost zero background, that might be just a statistical fluctuation in the MC of the background. All the variables used in the analysis and their cuts are described in 8.2.
Many signal models are tested, with different mass splitting, and kinematics. For this reason with only one signal region it is not possible

to enhance the sensitivity of all the signals, therefore multiple signal regions are built. In the analysis presented here two different types of signal region are defined:

- **Inclusive**: These regions are defined in order to maximize the discovery potential of the analysis to SUSY signals. Here the observable in each region is the number of observed events, the test statistic, while the hypothesis tested is the background only one. This is called a **discovery fit**, which provides an upper limit on the cross section of these signals and the $p-$value with respect of the SM hypothesis. These regions are not orthogonal between them, but overlap with each other, for this reason they are called *inclusive*.

- **Exclusive**: These regions are optimized to maximize the exclusion power of the analysis. This is achieved by splitting the inclusive regions in smaller regions, called *bins*, and are used to test the signal + background hypothesis (S+B), as it will be explained in 7.3. This is called shape fit. These regions are all orthogonal between each other, in order to be combined in the shape fit.

7.2 Control Region and Validation Region

SR initially are *blinded*: it is not allowed to look at data inside these regions, unless the background is well understood and constrained. This is done in order to avoid any biases in the definition of the SR and the test statistic that might come from a first observation of the data before the background estimation strategy is optimized.
The standard model background that enters the SR are estimated either from MC samples or from data driven techniques. It is possible to take these MC samples at face value, or it is possible to improve the prediction by using special regions where to constrain the background and therefore having a better prediction. This is done in *Control Regions* (CR): phase space regions, close to the SR but with a negligible expected rate of signal events, where the backgrounds are checked and normalized against the observed data. Generally, for each main background a specific control region is defined, by inverting one or more kinematic cuts that are applied in the SR. This allows also to have non overlapping CR and SR. Normalization factors are then extrapolated

to the SR. There are several advantages to use a CR. First it allows eliminating any mismodeling in the normalization of the MC, since they are fitted to the observed data. The second advantage is that when evaluating systematic uncertainties in the SR, these depends only on the changes in the ratio of the expected background yields in SR and CR.
The normalization obtained in the CR is also checked by extrapolating the results in *Validation Regions*. These are kinematic regions that are closer to the SR than the CRs, but have still a small expected signal contamination. Only after the modeling of the background is checked against data in the VRs it is possible to look at data inside the SR, this procedure is called *unblinding*. Figure 93 shows a schematics of how are defined the Signal, Control, and Validation Region, in a 2D plane of two arbitrary variables.

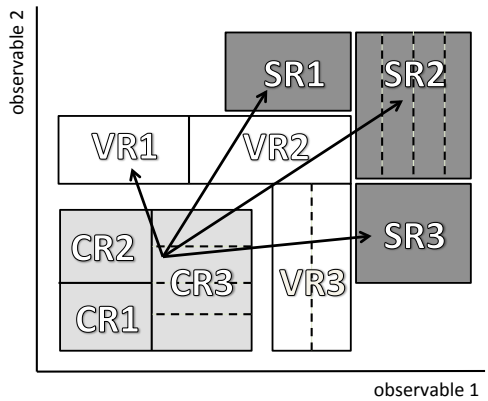

Figure 93: Schematic view of how SRs, CRs, and VRs are defined as a function of two arbitrary variables. Figure from ref [176]

7.3 Likelihood fit and CL_s method

The results obtained by the analysis must be interpreted with some statistical tool, in order to have a quantitative value to be able to decide if an eventual excess can be interpreted as discovery, or if a certain model is excluded.

In this analysis this interpretation is done with a likelihood function, that has as input the MC yields and the observed data in the CR and SR, and an additional term for the systematic uncertainties. The likelihood function is defined as:

$$\begin{aligned} L(\mathbf{n}, \boldsymbol{\theta}^0 | \mu_{sig}, \mathbf{b}, \boldsymbol{\theta}) &= P_{\text{SR}} \times P_{\text{CR}} \times C_{\text{syst}} \\ &= P(n_S | \lambda_S(\mu_{\text{sig}}, \mathbf{b}, \boldsymbol{\theta})) \times \\ &\times \prod_{i \in \text{CR}} P(n_i | \lambda_i(\mu_{\text{sig}}, \mu_{\text{NF}}, \mathbf{b}, \boldsymbol{\theta})) \times C_{\text{syst}}(\boldsymbol{\theta}^0, \boldsymbol{\theta}) \end{aligned} \tag{117}$$

Where $P_{\text{SR/CR}}$ are the Poisson distribution associated to the SR and CR with an observed number of events n_s and n_i respectively, with expected values $\lambda_{s/i}$, that depends on the background prediction $\boldsymbol{b}$, the nuisance parameters $\boldsymbol{\theta}$, the normalization factor μ_{NF}, and the signal strength μ_{sig}.
Systematic uncertainties are described with a Gaussian distribution C_{syst}, with central value $\boldsymbol{\theta}^0$. If the systematic uncertainties are uncorrelated, the probability distribution for all the systematic sources is:

$$C_{\text{syst}}(\boldsymbol{\theta}^0, \boldsymbol{\theta}) = \prod_{j \in S} G(\theta_j^0 - \theta_j) \tag{118}$$

with S being the set of all the systematic uncertainties considered. However in the fit used in the analysis the systematic errors enter with a correlation between the different nuisance parameters.
From this likelihood is then possible to compute a test statistic to probe the hypothesis [177]. For a fixed signal strength the test statistic q is defined as:

$$q_{\mu_{\text{sig}}} = -2 \log \left(\frac{L(\mu_{\text{sig}}, \hat{\hat{\boldsymbol{\theta}}})}{L(\hat{\mu}_{\text{sig}}, \hat{\boldsymbol{\theta}})} \right) \tag{119}$$

where $\hat{\hat{\boldsymbol{\theta}}}$ is the value that maximizes the likelihood for the specif μ_{sig}. The distribution of this test statistic is then defined as $f(q_{\mu_{\text{sig}}} | \mu_{\text{sig}}, \boldsymbol{\theta})$, and can be obtained with *pseudo-experiments* (called *toys*), randomizing the number of observed events. However this is rather time and resource consuming, and in case of large statistic the distribution is know to be a χ^2 distribution. In this case f is assumed to be a χ^2 and

this regime is called *asymptotic regime*.
With this function, is then possible to evaluate the $p-$value using equation 115, and test the signal hypothesis and set limits to 95 % CL.
In case that there is no significant excess in the data above the SM prediction, it is still possible to set limits looking at the CL of all the signal points. However, in cases where the distributions of the test statistic are close together for $\mathcal{H}_b$ and $\mathcal{H}_{s+b}$, a small underfluctuation in the data could exclude the signal hypothesis, even if it is close to the null hypothesis. This might happen with signals with very small cross section. It is then possible to define a modified version of the CL, called CL_s [178–180] that takes into account this effect. The CL_s is then defined as:

$$CL_s = \frac{CL_{s+b}}{CL_b} = \frac{p_{\mu_{\text{sig}}}}{1 - p_b} \tag{120}$$

where here p_b is the $p-$value for the $\mathcal{H}_b$ hypothesis. With this definition, the signal hypothesis is excluded at 95% CL if $CL_s < 0.05$.

8 Higgsino 2 Leptons Analysis

The analysis work done for this thesis is described in this chapter and chapter 9. The search presented here looks for the electroweak production of supersymmetric particles, the electroweakinos $\tilde{\chi}_2^0$,$\tilde{\chi}_1^0$,$\tilde{\chi}_1^\pm$, in final states with 2 leptons, either muons or electrons, in the final state [181]. These two leptons come from the decay of the $\tilde{\chi}_2^0$ into a virtual Z boson and a $\tilde{\chi}_1^0$. The model considered assumes that the electroweakinos are predominantly higgsino. As already explained, this implies that the difference in mass between them is between 1 and 10s of GeV, with very soft decay products.
Analysis in ATLAS have instead mainly looked at high momentum leptons, leaving the regions with soft leptons uncovered. An important step for this analysis was the introduction of the WP for isolation and ID at low momentum, that lowered the threshold from around 10 GeV to 4.5 GeV for electrons and 3 GeV for muons.

The analysis triggers on $E_{\mathrm{T}}^{\mathrm{miss}}$ and in order to do so the SUSY system need to be boosted. This happens if there is an energetic initial state radiation (ISR) jet, so that the $\tilde{\chi}_2^0$,$\tilde{\chi}_1^0$, and $\tilde{\chi}_1^\pm$ can recoil against it and receive enough energy. This request implicitly select events with high p_{T} on the $\tilde{\chi}_2^0$, therefore even its decay product will be boosted. This is important because it means that the soft lepton will also be close-by.
This analysis was done with the 2015 and 2016 dataset, and selected events with 2 opposite sign, same flavor, leptons in the final state. Instead the analysis described in chapter 9 used the whole Run 2 dataset and the events selected had 1 lepton and 1 track with opposite sign in the final state.
In the 2015 and 2016 analysis I have worked on the optimization of the signal region and of control and validation regions. I have also studied and helped to produce the low p_{T} MC samples missing and studied the QCD contribution, and finally I have helped in the statistical interpretation.

8.1 Data and Simulation samples

8.1.1 Data samples

The analysis presented here uses the data recorded by the ATLAS detector at the LHC during 2015 and 2016, at a center of mass of $\sqrt{s} = 13$ TeV. The pp collisions delivered from the LHC were 4.193 fb^{-1}in 2015 and 38.5 fb^{-1}in 2016, for a total of 42.693 fb^{-1}. Of all these events, however, not all are recorded by ATLAS, due to the efficiency of data acquisition, and problems that can happens during data taking operations.
Also, not all the recorded data are *good for physics*: some data are used just for calibration, monitoring, or special physics runs. If all the sub-detectors are recording data normally, with low levels of noise and regular rates, the runs are collected in lists of runs, called Good Runs List (GRL), that are then used by the analysis. The Luminosity after selecting only events from the GRL is 3.2 $\text{fb}^{-1}$for 2015 and 32.9 $\text{fb}^{-1}$for 2016, for a total 36.1 fb^{-1}.

These cuts contain request on the Liquid Argon system and SCT. If a LAr or Tile module has a flag associated to noise bursts or temporary trip in the high voltage, lumi-blocks are removed. Also lumi-blocks with SCT modules that were in busy and then recovered are removed. Additional cleaning cuts are then applied in order to remove events not satisfying the minimal requirements. If no primary vertices are present, events are removed. Events with jets coming from non collisional background (*beam-induced background*) are also removed. Finally events with cosmic events or cavern background are removed. These object are identified because they don't point to any primary vertex. These cuts have 100% efficiency on signal events.
Data used in the analysis were collected using the unprescaled inclusive $E_{\text{T}}^{\text{miss}}$ trigger. Different triggers, reported in table 20, were used depending on the data period with different online $E_{\text{T}}^{\text{miss}}$ cuts. The increase in the online cut was done in order to reduce the high rate due to the increase in pileup.

8.1.2 Signal samples

Signal kinematics and the optimization of the analysis is done using Monte Carlo samples. The analysis search for final states with two

Period	Lowest online $E_{\mathrm{T}}^{\mathrm{miss}}$ threshold [GeV]
2015	70
04/2016–06/2016	90
06/2016–07/2016	100
07/2016–10/2016	110

Table 20: Lowest unprescaled inclusive $E_{\mathrm{T}}^{\mathrm{miss}}$ trigger chains in 13 TeV running.

leptons. These MCs are built in the *simplified models* framework. The MSSM, in fact, has still too many free parameters, that may influence signal decay. In order to have a simplified approach and to be able to compare results with other teams, signals are generated considering only few particles, and enabling only the relevant decay. Figure 94 shows the full decay chain of the process considered. Here the $\tilde{\chi}_1^0$ is considered the LSP and stable. Two different models are considered: Higgsino and Wino / Bino production. Signal samples are produced in similar ways, with simulation setup nearly identical, but with some important different assumptions, as it is described also in section 2.4. For both models in the generation of the MC MadGraph [182] version 5.2.4.2 is used to produce the events. For the Higgsino model it is produced $pp \to \tilde{\chi}_2^0\tilde{\chi}_1^0$, $\tilde{\chi}_1^\pm\tilde{\chi}_1^\pm$, $\tilde{\chi}_2^0\tilde{\chi}_1^-$, $\tilde{\chi}_2^0\tilde{\chi}_1^+$ ($\tilde{\chi}_2^0\tilde{\chi}_1^-$ and $\tilde{\chi}_2^0\tilde{\chi}_1^+$ are produced separately), while in the Wino / Bino case there the same processes, except that there is no $\tilde{\chi}_2^0\ \tilde{\chi}_1^0$, since it is forbidden. In both cases the showering is obtained using Pythia 8 [183]. In both cases $\tilde{\chi}_1^0\ \tilde{\chi}_1^\pm$ is not produced since the analysis looks for final states with two leptons, and this process will only produce one prompt lepton.
Processes are calculated at leading order, with up to 2 additional parton emission in the final state (with $p_{\mathrm{T}} > 10$ GeV) in the matrix element. In the analysis presented here the $\tilde{\chi}_1^\pm$ is made to decay into a $\tilde{\chi}_1^0$ and a virtual W boson that then decays into ff' (with f being a SM fermion), while the $\tilde{\chi}_2^0$ is made to decay (with a 100% Branching Ratio) into a $\tilde{\chi}_1^0$ and a virtual Z ($\tilde{\chi}_2^0 \to \tilde{\chi}_1^0 Z^{(\star)}$), which is then made to decay into two leptons ($\ell = e, \mu, \tau$). However in the Higgsino model the Branching Ratio of the $Z^{(\star)}$ is not fixed to the one of the on shell boson $Z \to \ell\ell$, but it is left free to change with decreasing mass of the off-shell boson, since as it reaches zero, some decay modes

are suppressed, like $Z \to b\bar{b}$ below 10 GeV or $Z \to \tau\tau$ and $Z \to c\bar{c}$ below 3 GeV. Figure 95 shows the $Z^{(\star)}$ Branching Ratio obtained from MadGraph for the Higgsino model. However the ones used in the analysis are from `SUSYHIT` [184]. These values are similar to the ones from MadGraph but also take into account the mass of the charm quark.
In the same way this happens to the W, where below 1.7 GeV it is suppressed $W \to cs$ and $W \to \tau\nu$, which is around where also $Z \to cc$ is closed, since in this model the mass of the chargino is set halfway between the mass of the $\tilde{\chi}_2^0$ and $\tilde{\chi}_1^0$, with $m(\tilde{\chi}_1^{\pm}) - m(\tilde{\chi}_1^0) = (m(\tilde{\chi}_2^0) - m(\tilde{\chi}_1^0))/2$.
The Branching Ratio in leptonic final states of the decays in the Higgsino model are then obtained with the software `SUSYHIT`, version 1.5a [184], that takes into account the finite masses of the b-quark and the τ. Decays non relevant to the analysis are ignored. For the Higgsino samples the Branching Ratios depends only on the mass splitting between $\tilde{\chi}_2^0$ and $\tilde{\chi}_1^0$, and not the $\tilde{\chi}_1^0$ absolute mass, while for the Wino / Bino samples it is the same for all the samples, in order to be consistent with all the other analysis in ATLAS.

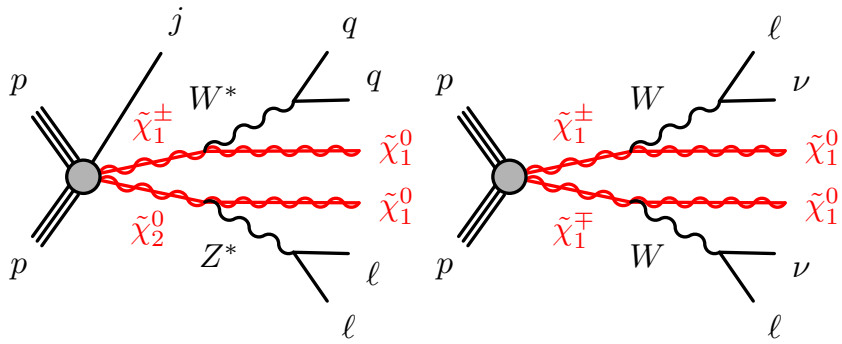

Figure 94: Diagram of the production of (a) $pp \to \tilde{\chi}_2^0\tilde{\chi}_1^{\pm}$ decaying in $lljj\tilde{\chi}^0\tilde{\chi}^0 q\bar{q}$ and (b) $pp \to \tilde{\chi}_1^+\tilde{\chi}_1^-$ decaying in $l\nu l\nu jj\tilde{\chi}^0\tilde{\chi}^0$.

These decays are done using the MadSpin [185] software, that enable to take into account the spin correlations and conserve the matrix element information. Using this software is crucial, since it preserve the shape of the invariant mass of the two leptons coming from the

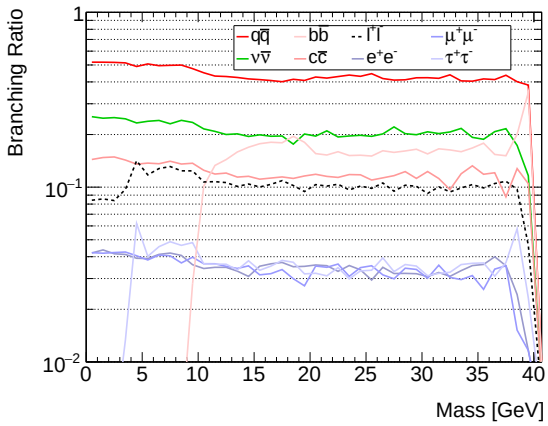

Figure 95: Z^* Branching Ratio evaluated with `MadGraph` for the Higgsino signal samples. The mass of the charm quark is not present in this `MadGraph` model and therefore there is a reduction of the total $Z^* \to \ell\ell$ branching ratio below 3 GeV.

virtual Z, as shown in section 2.4.4. This information is essential to correctly optimize the analysis and to be able to characterize the eventual observed signal. In fact the one key difference between the Higgsino and Wino / Bino model is the shape of the invariant mass of the leptons from the $Z^{(\star)}$, as already explained in section 2.4. It is therefore important to preserve this feature.
The merging scheme used is CKKW-L, with a 15 GeV scale [186]. The PDF used in the production is the NNPDF 2.3 LO [187].
Even if the production is done at LO, the cross sections and their uncertainty are evaluated with Resummino version 1.0.7 at NLO+NLL [188, 189]. Uncertainties are evaluated by varying the pdf set with CTEQ66 and MSTW, and other pdf sets, following the recommendation of ref. [190]. Cross sections are obtained for each signal MC generated. Figure 96 shows the cross section for electroweakino pair production in proton–proton collisions at $\sqrt{s} = 13$ TeV, as a function of the mass of the produced system.

8.1.3 Background samples

The main background events rates are obtained from MC simulations. These samples go through the full simulation of the detector. Table 21 summarize all the samples used, and their generator.

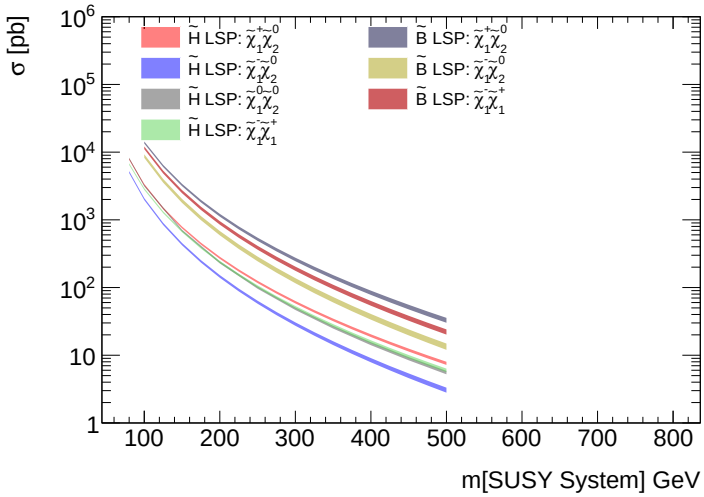

Figure 96: Cross-sections for electroweakino $\tilde{\chi}$ pair-production for proton–proton collisions at $\sqrt{s} = 13$ TeV from the public LHC SUSY Cross-sections Working Group and Refs. [188, 189, 191]. Displayed are total cross sections for the processes labelled, according to the nature of the produced electroweakino being wino $\tilde{W}$ or Higgsino $\tilde{H}$.

Top Quark Production of events with at least a top quark are between the most important background in the analysis. $t\bar{t}$ and single top (t-channel, s-channel, and Wt) events are both simulated using the software POWHEG [192], and with PYTHIA 6 [112] for the showering. Instead tZ samples use MADGRAPH 5 for the matrix element, while still using PYTHIA 6 for the showering. Minor and rare top processes, like ttV, $t\bar{t}WW$, or ttt, are also produced with MADGRAPH 5, but use PYTHIA 8 for the showering, with the NNPDF23LO pdf set.

Multiboson The software SHERPA [193–196]is used to generate MC of diboson events (WW,WZ, ZZ) and tribosons with multilepton final states. The PDF set used is NNPDF30NNLO, where available, otherwise the CT10 [197]. Samples are divided by the final state type: 1, 2, 3, or 4 leptons final states. Samples with a Z/W boson plus an energetic photon γ are obtained still with SHERPA but with CT10 PDF set.

V+Jets MC samples of Z or W bosons decaying leptonically in association with additional jets are described by SHERPA with the NNPDF30NNLO PDF set. Matrix elements is evaluated with up to four additional partons at LO. The showering is done following the ME+PS NLO prescriptions [198]. Samples are divided in sub samples with different values of $\max(H_{\mathrm{T}} p_{\mathrm{T}}(V))$ (the maximum between the sum of all the jet activity (H_{T}) and the p_{T} of the vector boson (p_{T}^{V}).

Higgs Higgs production via gluon-gluon fusion or vector boson fusion decaying fully leptonically are obtained with POWHEG and PYTHIA 8 for parton showering and hadronization. The NLOCTEQ6L1 PDF set is used. Instead single Higgs boson in association with W or Z bosons are obtained with only PYTHIA 8 using NNPDF23LO PDF set.

8.1.4 Low p_{T} samples extension

Due to rapidly increasing cross section at low lepton p_{T} and $m_{\ell\ell}$, same samples have kinematic cut at generation level to avoid this scenario, and to avoid to have to generate an excessive amount of events, that would imply long generation time and resource consumption. In the diboson samples it is required: $p_{\mathrm{T}}^{\mathrm{leptons}} > 5$ GeV and $m_{\ell\ell} > 4$ GeV (only for events with more than 2 leptons in the final states). This however is a problem, since the phase space of the signal is exactly in this uncovered region. In order to have a reliable prediction of this phase space, additional samples were produced, that require: $p_{\mathrm{T}}^{\mathrm{leptons}} > 2$ GeV and $2 * m_{\ell} < m_{\ell\ell} < 10$ GeV. Similarly in V+jets samples for on-shell Z+jets it is required $m_{\ell\ell} > 40$ GeV, for "low mass" Z+jets it is required 10 GeV $< m_{\ell\ell} <$ 40 GeV and $p_{\mathrm{T}} > 5$ GeV, while for even lower mass Z+jets it is required $2 \cdot m(\ell) < m_{\ell\ell} < 40$ GeV and $p_{\mathrm{T}} > 2$ GeV, and are produced only for $\max(H_{\mathrm{T}} p_{\mathrm{T}}(V)) > 280$ GeV. Figure 98 shows the new extension samples compared with the previous one. Samples are normalized to the their nominal cross section and to 40 fb^{-1}.

Short Name	Process	Generators	PDF
Z+jets	$Z \to \mu\mu$ ($m_{\ell\ell} > 40$ GeV) $Z \to ee$ ($m_{\ell\ell} > 40$ GeV) $Z \to \tau\tau$ ($m_{\ell\ell} > 40$ GeV) $Z \to \nu\nu$ ($m_{\ell\ell} > 40$ GeV) $Z \to \mu\mu$ ($10 < m_{\ell\ell} < 40$ GeV) $Z \to ee$ ($10 < m_{\ell\ell} < 40$ GeV) $Z \to \tau\tau$ ($10 < m_{\ell\ell} < 40$ GeV) $Z \to \mu\mu$ ($m_{\ell\ell} < 10$ GeV) $Z \to ee$ ($m_{\ell\ell} < 10$ GeV) $Z \to \tau\tau$ ($m_{\ell\ell} < 10$ GeV)	Sherpa 2.2.1	NNPDF30NNLO
W+jets	$W \to \mu\nu$ $W \to e\nu$ $W \to \tau\nu$	Sherpa 2.2.1	NNPDF30NNLO
$Z\gamma$	$(Z \to ee) + \gamma$ ($p_{\mathrm{T}}^{\gamma} > 10$ GeV) $(Z \to \mu\mu) + \gamma$ ($p_{\mathrm{T}}^{\gamma} > 10$ GeV) $(Z \to \nu\nu) + \gamma$ ($p_{\mathrm{T}}^{\gamma} > 35$ GeV)	Sherpa	CT10
$W\gamma$	$(W \to e\nu) + \gamma$ ($p_{\mathrm{T}}^{\gamma} > 10$ GeV) $(W \to \mu\nu) + \gamma$ ($p_{\mathrm{T}}^{\gamma} > 10$ GeV) $(W \to \tau\nu) + \gamma$ ($p_{\mathrm{T}}^{\gamma} > 10$ GeV)	Sherpa	CT10
Diboson	$qq\nu\nu$ (ZZ, WZ)	Sherpa 2.2.1	NNPDF30NNLO
	$\nu\nu\nu\nu$	Sherpa 2.2.1	NNPDF30NNLO
	$\ell\nu qq$	Sherpa 2.2.1	NNPDF30NNLO
	$\ell\nu qq$	Sherpa 2.2.1	NNPDF30NNLO
	$\ell\nu\nu\nu$	Sherpa 2.2.1	NNPDF30NNLO
	$\ell\ell qq$ (ZZ, WZ)	Sherpa 2.2.1	NNPDF30NNLO
	$\ell\ell\nu\nu$	Sherpa 2.2.1,2	NNPDF30NNLO
	$\ell\ell\nu\nu gg$	Sherpa	CT10
	$\ell\ell\ell\nu$	Sherpa 2.2.1,2	NNPDF30NNLO
	$\ell\ell\ell\nu jj$	Sherpa	CT10
	$\ell\ell\ell\ell$	Sherpa 2.2.1,2	NNPDF30NNLO
	$\ell\ell\ell\ell jj$	Sherpa	CT10
	$\ell\ell\ell\ell gg$	Sherpa	CT10
Triboson	$6\ell 0\nu$ $5\ell 1\nu$ $4\ell 2\nu$ $3\ell 3\nu$	Sherpa 2.2.1	NNPDF30NNLO
Higgs	$h \to WW \to \ell\nu\ell\nu$ (ggF, VBF)	Powheg+Pythia 8	NLOCTEQ6L1
	$h \to \tau\tau$ (ggF, VBF)	Powheg+Pythia 8	NLOCTEQ6L1
	$h \to \mu\mu$ (ggF, VBF)	Powheg+Pythia 8	NLOCTEQ6L1
	$h \to ee$ (ggF, VBF)	Powheg+Pythia 8	NLOCTEQ6L1
	Wh, Zh	Pythia 8	NNPDF23LO
Single top	t (t-channel)	Powheg+Pythia 6	NLO CT10
	t (s-channel, $\geq 1\ell$)	Powheg+Pythia 6	NLO CT10
	tW (2ℓ)	Powheg+Pythia 6	NLO CT10
	tZ ($\geq 1\ell$)	MadGraph + Pythia	NLO CT10
	tWZ	aMC@NLO + Pythia	NLO CT10
ttbar	$t\bar{t}$ (2ℓ) (Nominal) $t\bar{t}$ ($\geq 1\ell$) (Not used)	Powheg+Pythia 6	NLO CT10
ttV	$t\bar{t}W$	MadGraph + Pythia 8	NNPDF23LO
	$t\bar{t}(Z \to \nu\nu)$	MadGraph + Pythia 8	NNPDF23LO
	$t\bar{t}(Z \to ee)$	MadGraph + Pythia 8	NNPDF23LO
	$t\bar{t}(Z \to \mu\mu)$	MadGraph + Pythia 8	NNPDF23LO
	$t\bar{t}(Z \to \tau\tau)$	MadGraph + Pythia 8	NNPDF23LO
	$t\bar{t}Z$ (low $m_{\ell\ell}$)	aMC@NLO + Pythia 8	NNPDF23LO
	$t\bar{t}\gamma$	MadGraph + Pythia 8	NNPDF23LO
Rare top	3 top 4 top $t\bar{t}WW$	MadGraph + Pythia 8	NNPDF23LO

Table 21: Summary of Standard Model background Monte Carlo samples considered.

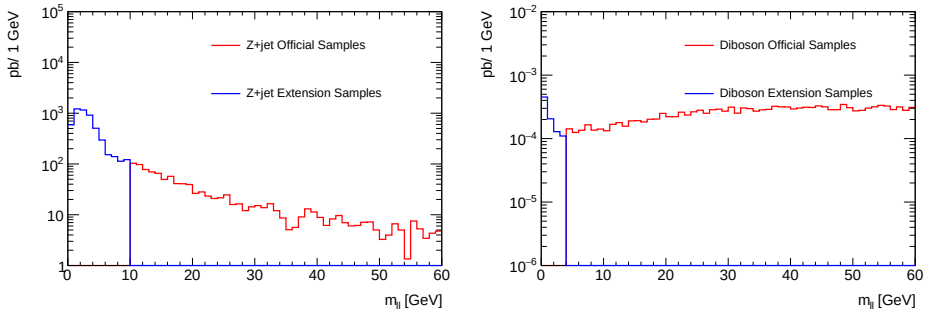

(a) (b)

Figure 97: Official samples and new extension samples to cover low $m_{\ell\ell}$ and low p_{T} region. (a) Z+jets samples, (b) Diboson samples.

8.2 Event Selection and Signal Regions

8.2.1 Object Definition

The reconstruction, identification and calibration of the objects used in the analysis was presented in chapter 6. The working point used were instead optimized in order to reduce the background while keeping an high signal efficiency. The definition of the objects used in the analysis is presented here.
For muons and electrons, two different levels of selection are defined: *baseline* and *signal*. The second is a sub set of the first, with more stringent requirement on isolation and quality. Baseline objects are the ones that enter the definition of the $E_{\mathrm{T}}^{\mathrm{miss}}$. All the requirements are reported in table 22.

Electrons Baseline electrons have to satisfy the *VeryLooseLLH* identification WP. In addition they must have $p_{\mathrm{T}} > 4.5$ GeV, and must satisfy requirement on the longitudinal impact parameter with $|z_0 \sin\theta| <$ 0.5 mm. Signal electrons must pass all the baseline selection, and in addition must satisfy the *GradientLoose* isolation WP, and *Tight* WP for identification. They also must have $|\eta| < 2.47$ and an impact parameter significance smaller than 5: $|d_0/\sigma(d_0)| < 5$. Also, electrons reconstructed from photon conversion algorithm are removed.

Property	Signal	Baseline
Electrons		
Kinematic	$p_{\mathrm{T}} > 4.5$ GeV, $\lvert\eta\rvert < 2.47$	$p_{\mathrm{T}} > 4.5$ GeV
Identification	TightLLH	VeryLooseLLH
Isolation	GradientLoose	–
Impact parameter	$\lvert d_0/\sigma(d_0)\rvert < 5$, $\lvert z_0 \sin\theta\rvert < 0.5$ mm	$\lvert z_0 \sin\theta\rvert < 0.5$ mm
Other requirements	Not from conversion	Not from conversion
Muons		
Kinematic	$p_{\mathrm{T}} > 4$ GeV, $\lvert\eta\rvert < 2.5$	$p_{\mathrm{T}} > 4$ GeV
Identification	Medium	Medium
Isolation	FixedCutTightTrackOnly	–
Impact parameter	$\lvert d_0/\sigma(d_0)\rvert < 3$ & $\lvert z_0 \sin\theta\rvert < 0.5$ mm	$\lvert z_0 \sin\theta\rvert < 0.5$ mm
Jets		
Kinematic	$p_{\mathrm{T}} > 30$ GeV, $\lvert\eta\rvert < 2.8$	$p_{\mathrm{T}} > 20$ GeV, $\lvert\eta\rvert < 4.5$
Clustering	Anti-k_t $R = 0.4$ EMTopo	Anti-k_t $R = 0.4$ EMTopo
Pileup mitigation	–	JVT Medium for $p_{\mathrm{T}} < 60$ GeV, $\lvert\eta\rvert < 2.4$
b-tagging	$p_{\mathrm{T}} > 20$ GeV,	$\lvert\eta\rvert < 2.5$, MV2c10 FixedCutBeff 85%

Table 22: Summary of object definitions.

Muons Baseline muons use the *Medium* WP for the identification, and it is asked $p_{\mathrm{T}} > 4$ GeV and $|\eta| < 2.5$, with tracks satisfying $|z_0 \sin\theta| < 0.5$ mm on the longitudinal impact parameter. Signal muons have to satisfy the baseline selection and pass the *FixedCutTightTrackOnly* isolation WP, while also passing $|d_0/\sigma(d_0)| < 3$.

Jets Baseline jets are required to have $p_{\mathrm{T}} > 20$ GeV and $|\eta| < 4.5$. Signal jets instead must be in a smaller η region with $|\eta| < 2.8$. For jets with $p_{\mathrm{T}} < 60$ GeV and $|\eta| < 2.4$ the JVT *medium* WP is applied to reduce pileup contribution. Baseline jets coming from b-hadrons and in $|\eta| < 2.5$ are identified with the MV2c10 algorithm, with a 85% efficiency WP.

8.2.2 Overlap Removal

During the object reconstruction and selection, overlaps can occur, where an object is identified in more than one category. These ambiguities must be solved, and an algorithm is used to solve them. Objects in different categories are one by one compared in a specific order.

- First it is checked if a b-tagged jets and an electron are within a cone of $\Delta R < 0.2$, in this case the electron is removed, since it is more likely to come from a b-hadron decay. Instead if the jet is not b-tagged, the jet itself is removed, since it is likely a jet coming from the shower induced by the electron.

- Jets and muons are then compared. If the they are within a cone of $\Delta R < 0.4$ from each other, the jet is removed if the muon carries more than 70 % of the jet energy. The jet is then likely to come from the muon bremsstrahlung.

- Electrons and muons that are within a cone of $\Delta R < 0.4$ to the remaining jets are removed. These objects are probably coming from semi leptonic b-/c-hadron decay

- Finally electrons with the same track in the ID as a muon are removed.

8.2.3 Isolation for nearby Leptons

As already mentioned, the SUSY system selected is boosted, due to the need of triggering on $E_{\mathrm{T}}^{\mathrm{miss}}$. In fact the $E_{\mathrm{T}}^{\mathrm{miss}}$ request implies a selection on the p_{T} of the $\tilde{\chi}_1^0$, which is similar to p_{T} of the produced particles, leading to a boost proportional to $m(\tilde{\chi}_2^0)/E_{\mathrm{T}}^{\mathrm{miss}}$. The actual boost depends not only on the trasverse component, but on the whole momentum, which is divided between the two particles.
Due to this aspect the leptons from the $Z^{(\star)}$ decay are also boosted, and therefore close-by. Isolation requirements select leptons that don't have tracks in a near-by cone, and therefore remove leptons coming from the $Z^{(\star)}$. In order to avoid a loss in efficiency, a correction to the nominal isolation working point was done, using the tool NearbyLepIsoCorrection [199]. This tool allows the re-computing of the isolation variables, if two baseline leptons that fails the isolation criteria lie within the isolation cone of each other. In this case the tracks of the nearby lepton are removed from the track isolation sum. If the lepton considered is an electron the topocluster E_T is also removed from the calorimeter isolation sum. Isolation criteria are then checked again with the corrected variables. Figure 98 (a) show the effects of the corrected isolation on data samples triggered with $E_{\mathrm{T}}^{\mathrm{miss}}$,

making possible to increase the number of events at low $m_{\ell\ell}$. Figure 98 (b) instead shows the increase of efficiency for a signal sample with $\Delta m(\tilde{\chi}_2^0, \tilde{\chi}_1^0) = 3$ GeV, going from 22 % to up to 80 %.

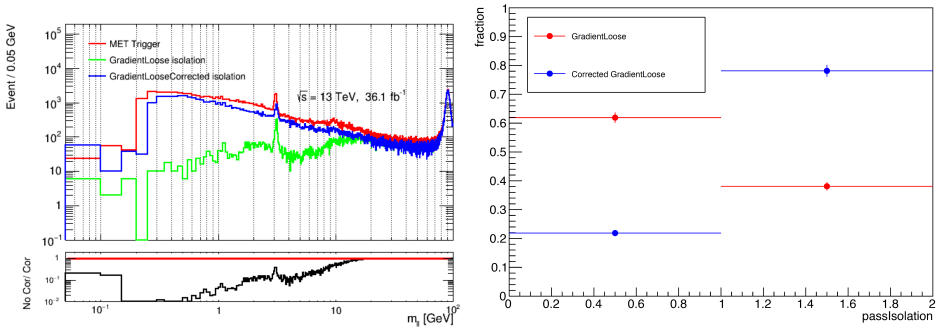

(a) (b)

Figure 98: (a) $m_{\ell\ell}$ spectrum for data passing the inclusive $E_{\mathrm{T}}^{\mathrm{miss}}$ trigger and with $\left|\Delta\phi(j_1, \mathbf{p}_{\mathrm{T}}^{\mathrm{miss}})\right| < 1.5$ (to avoid signal contamination). The red line shows events with two baseline leptons without any requirement on isolation, the green line shows events with two baseline leptons passing the GradientLoose isolation WP, and the blue line instead shows events with two baseline events passing GradientLoose isolation WP corrected with the NearbyLepIsoCorrection tool. (b) shows the fraction of events with two baseline leptons passing the GradientLoose isolation WP, while blue dots for the corrected GradientLoose isolation WP, for a signal samples with $\Delta m(\tilde{\chi}_2^0, \tilde{\chi}_1^0) = 3$ GeV.

8.2.4 Discriminating Variables

In order to discriminate between signal and background, different variables are used, that help separate the two contributions. Here the description of the ones used in the analysis is reported. Table 23 summarizes all the cuts applied to the SR.

- $E_{\mathrm{T}}^{\mathrm{miss}}$
  The $E_{\mathrm{T}}^{\mathrm{miss}}$ is used to trigger events. For the signal the contribution to the missing energy comes mostly from the two $\tilde{\chi}_1^0$ in the final state if they have been boosted enough by the ISR jet, due to the compressed phase space of the decay. Contributions

from neutrinos in the $\tilde{\chi}_1^{\pm} \to \tilde{\chi}_1^0 \nu\ell$ instead is negligible due to the small Δm between $\tilde{\chi}_1^{\pm}$ and $\tilde{\chi}_1^0$.
The trigger efficiency plateau is reached for 200 GeV. The contribution to the background from instrumental $E_{\mathrm{T}}^{\mathrm{miss}}$, like jet mismeasurement, is relevant at low $E_{\mathrm{T}}^{\mathrm{miss}}$. Therefore it is required that events have $E_{\mathrm{T}}^{\mathrm{miss}} > 200$ GeV.
In the full Run 2 analysis (presented in section 9) the events with $E_{\mathrm{T}}^{\mathrm{miss}} < 200$ GeV were partially recovered with a SR targeting specifically the region with $100 < E_{\mathrm{T}}^{\mathrm{miss}} < 200$ GeV, where it was also performed a study on the efficiency of the trigger in both data and MC.

- $\left|\Delta\phi(j_1, \mathbf{p}_{\mathrm{T}}^{\mathrm{miss}})\right|$
  $E_{\mathrm{T}}^{\mathrm{miss}}$ from a mismeasured jet tends to align with the jet itself. Therefore an angular requirement is made in order to further suppress this kind of background, mainly coming from QCD and Z+jets

- $\min\left|\Delta\phi(\text{all jets}, \mathbf{p}_{\mathrm{T}}^{\mathrm{miss}})\right|$
  This variable is similar as $\left|\Delta\phi(j_1, \mathbf{p}_{\mathrm{T}}^{\mathrm{miss}})\right|$but considering the closest jet in $\Delta\phi$.

- p_{T}^{jet}
  As already stated, the signal needs an ISR jet in order to boost the system to allows $E_{\mathrm{T}}^{\mathrm{miss}}$ triggers. For this reason it is required a jet with $p_{\mathrm{T}^{\mathrm{jet1}}} > 100$ GeV.

- **Number of *b*-tagged jets $N_{\text{b-jets}}$**
  One of the main backgrounds in a two lepton and $E_{\mathrm{T}}^{\mathrm{miss}}$ final state comes from $t\bar{t}$, where there are also present b-tagged jets. Instead the signal doesn't have b-jets. In order then to suppress this background it is required that no b-jets are in the final state. The choice of the the b-tagging algorithm at 85% efficiency WP was done in order to improve the background rejection while keeping an high signal efficiency. With this cut the background is reduced by almost 80 %, while between 75 % and 85% of the signal (depending on the signal point) pass this cut.

- **Leptons flavor and charge**
  In signal events the two leptons comes from the $Z^{(\star)}$, and therefore are opposite sign and with the same flavor (SFOS): $e^{\pm}e^{\mp}$ or $\mu^{\pm}\mu^{\mp}$. Leptons form multibosons or top instead can also have different flavor leptons (coming from different W decays), or not even opposite sign. For this reason it is asked that the lepton are SFOS, so to further reduce the background with almost no loss in signal.

- $\Delta R_{\ell\ell}$
  The distance between the two leptons is defined as

$$\Delta R_{\ell\ell} = \sqrt{(\eta_{\ell_1} - \eta_{\ell_2})^2 + (\phi_{\ell_1} - \phi_{\ell_2})^2}. \tag{121}$$

  The more the SUSY system is boosted, the more the two leptons are closed together. High $E_{\mathrm{T}}^{\mathrm{miss}}$ cuts (as applied in the analysis) select exactly this type of regions. Leptons from prompt backgrounds instead are not necessarily coming from boosted events, therefore their $\Delta R_{\ell\ell}$ distribution is more flat. However $m_{\ell\ell}$ and $\Delta R_{\ell\ell}$ are correlated between them, in fact selecting two close by lepton means that their invariant mass will be also small. For this reason it is required a cut of $\Delta R_{\ell\ell} < 2.0$. Instead non prompt backgrounds can be very close by, and since $m_{\ell\ell}$ and $\Delta R_{\ell\ell}$ are correlated they can easily enter the SR, for this reason a lower cut is also applied: $\Delta R_{\ell\ell} > 0.05$.

- $m_{\ell\ell}$
  The invariant mass of the two leptons is one of the key variables of the analysis. It is used both to reduce the background and to exploit the signal shape. Events with on-shell Z bosons and $ZZ \to \ell\ell\nu\nu$ are removed by an upper cut on the invariant mass: $m_{\ell\ell} < 60$ GeV. Moreover it also suppresses additional $t\bar{t}$ and WW.
  As explained in section 2.4.4 the shape of the invariant mass of the two leptons from the $Z^{(\star)}$ decay is bounded at the difference in mass between the $\tilde{\chi}_2^0$ and $\tilde{\chi}_1^0$. For this reason the signal would emerge as a peak in the background, and therefore a shape fit is performed on the $m_{\ell\ell}$ distribution to exploit this characteristic.

- $m_{\mathrm{T}}^{\ell_1}$

The transverse mass is defined as:

$$m_T(\mathbf{p}_{\mathrm{T}}^{\ell}, \mathbf{p}_{\mathrm{T}}^{\mathrm{miss}}) = \sqrt{m_\ell^2 + 2(E_T^\ell E_T^q - \mathbf{p}_T^\ell \cdot \mathbf{p}_{\mathrm{T}}^{\mathrm{miss}})}. \tag{122}$$

This variable reconstructs the decay $W \to \ell\nu$, and so it possible to reduce background coming from this process, where a second lepton is either non prompt or fake. The chosen is $m_{\mathrm{T}}^{\ell_1} < 70$ GeV

- $E_{\mathrm{T}}^{\mathrm{miss}}/H_{\mathrm{T}}^{\mathrm{leptons}}$
  This variable is defined as the ratio between the $E_{\mathrm{T}}^{\mathrm{miss}}$ and the scalar sum of the leptons p_{T}

$$H_{\mathrm{T}}^{\mathrm{leptons}} = \sum_i p_{\mathrm{T}}^{\ell_i}. \tag{123}$$

  For the signal, at high $E_{\mathrm{T}}^{\mathrm{miss}}$, this ratio is usually large due to the soft leptons, instead for backgrounds such as $t\bar{t}$ or diboson, it is much smaller, since with high $E_{\mathrm{T}}^{\mathrm{miss}}$ also comes high p_{T} leptons. In addition, for signal, the smaller the mass difference is between the two $\tilde{\chi}^0$, the larger the ratio is, since small Δm implies softer leptons, and therefore small $H_{\mathrm{T}}^{\mathrm{leptons}}$. For this reason the cut on $E_{\mathrm{T}}^{\mathrm{miss}}/H_{\mathrm{T}}^{\mathrm{leptons}}$ varies dynamically with a function of the reconstructed $m_{\ell\ell}$:

$$E_{\mathrm{T}}^{\mathrm{miss}}/H_{\mathrm{T}}^{\mathrm{leptons}} > \max(3, 15.0 - 2|m_{\ell\ell}|/\ \text{GeV}) \tag{124}$$

  Figure 100 shows a 2D plot of $E_{\mathrm{T}}^{\mathrm{miss}}/H_{\mathrm{T}}^{\mathrm{leptons}}$ and $m_{\ell\ell}$ for signal samples and background. The dashed line represent the cut applied from equation 124. It is possible to see that this cut remove a large portion of the background, while keeping almost all the signal.

- $m_{\tau\tau}$
  An important background that can mimic the signal kinematics is the $Z \to \tau\tau$, in order to remove it, a variable, $m_{\tau\tau}$, is used, that reconstructs the di-tau invariant mass, as a function of the reconstructed p_{T} of the leptons and the missing energy [35, 200, 201]. The aim is to reconstruct the mass of the Z boson as $m(Z)^2 = (\boldsymbol{p}_{\boldsymbol{\tau_1}} + \boldsymbol{p}_{\boldsymbol{\tau_2}})^2$ (where $\boldsymbol{p}_{\boldsymbol{\tau}}$ are 4-vectors), and veto

it. Different definitions exist that try to solve ambiguities due to the non measurable neutrinos. The version used in this analysis is presented in ref [200]. Figure 99 shows the schematics of the fully leptonic ($Z \to \tau\tau$) decays and the naming schemes used for the $m_{\tau\tau}$. In the fully leptonic case, only the p_{T} of the leptons and the $\mathbf{p}_{\mathrm{T}}^{\mathrm{miss}}$is visible. In case of boosted taus decaying from the Z recoiling on a energetic ISR jet, the daughter leptons and the neutrinos are nearly collinear. In this case then the momentum of the neutrinos coming from the i-th tau, defined by $p_{\nu_i} = p_{\nu_{\ell_i}} + p_{\nu_{\tau_i}}$, can be approximated as $p_{\nu_i} \simeq \xi_i p_{\ell_i}$, where ξ is a scalar that must be determined. The tau 4-momentum is defined by $p_{\tau_i} = p_{\ell_i} + p_{\nu_i}$, therefore it is possible to define the tau 4-momentum in the following way:

$$p_{\tau_i} = (1 + \xi_i) p_{\ell_i} \equiv f_i p_{\ell_i} \tag{125}$$

where $(1 + \xi_i) \equiv f_i$. Then it is possible to estimate the momentum of the taus by solving the equation for the scalar, using as additional information:

$$\mathbf{p}_{\mathrm{T}}^{\mathrm{miss}} = \xi_1 \mathbf{p}_{\mathrm{T}}^{\ell_1} + \xi_2 \mathbf{p}_{\mathrm{T}}^{\ell_2}. \tag{126}$$

This equation is solved by inverting the 2×2 matrix in the transverse plane $x - y$:

$$\begin{pmatrix} \xi_1 \\ \xi_2 \end{pmatrix} = \frac{1}{p_x^{\ell_1} p_y^{\ell_2} - p_x^{\ell_2} p_y^{\ell_1}} \begin{pmatrix} p_x^{\mathrm{miss}} p_y^{\ell_2} - p_x^{\ell_2} p_y^{\mathrm{miss}} \\ p_y^{\mathrm{miss}} p_x^{\ell_1} - p_x^{\mathrm{miss}} p_y^{\ell_1} \end{pmatrix}. \tag{127}$$

Since in the scenario considered the taus are assumed boosted, it is fair to put $m_\tau^2 = 0$. In this case it is then possible to write:

$$m_{\tau\tau}^2 = (p_{\tau_1} + p_{\tau_2})^2 \simeq 2 p_{\ell_1} \cdot p_{\ell_2} (1 + \xi_1)(1 + \xi_2). \tag{128}$$

The $m_{\tau\tau}^2$ can be both positive and negative, and not symmetric, so that it is true that:

$$\left(m_{\tau\tau}^2\right)^+ \neq \left| \left(m_{\tau\tau}^2\right)^- \right|. \tag{129}$$

$m_{\tau\tau}$ is indeed positive when the assumption used to compute $m_{\tau\tau}$ are correct. In this case $m_{\tau\tau}$ is around $m(Z)^2$, with a spread that is the resolution of the momenta. However, when one of these

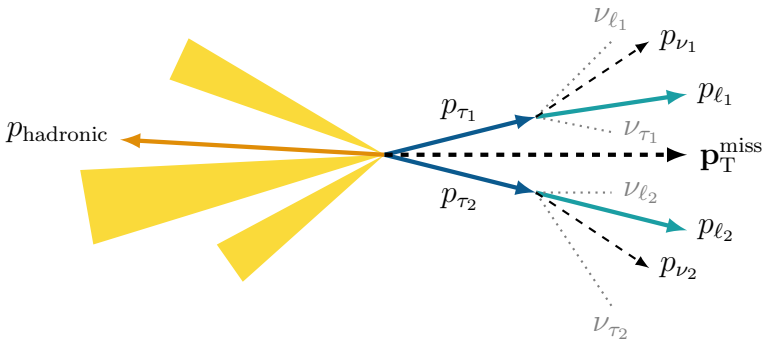

Figure 99: Schematic illustrating the fully leptonic $(Z \to \tau\tau)$ + jets system motivating the construction of $m_{\tau\tau}$.

assumption is not true, $m_{\tau\tau}$ can be negative, as an example when the leptons and the neutrinos are not collinear. This can happen when $E_{\text{T}}^{\text{miss}} > p_{\text{T}}^{\ell_i}$, and the lepton p_{T} points in the other direction with respect to the missing energy. In order then to get the correct invariant mass of the di-tau, the lepton should be inverted in direction, in order to balance the recoil. Therefore the squared root of this value can not describe well the feature of the invariant mass. For highly boosted $Z \to \tau\tau$ this scenario is rare, however this is rather common for lesser boosted scenario and, also, for signal. For this reason $m_{\tau\tau}$ is a very strong discriminant variable. In order to get a variable with the dimension of GeV, it is taken the signed squared root of $m_{\tau\tau}^2$:

$$m_{\tau\tau}\left(p_{\ell_1}, p_{\ell_2}, \mathbf{p}_{\text{T}}^{\text{miss}}\right) = \begin{cases} \sqrt{m_{\tau\tau}^2} & m_{\tau\tau}^2 \geq 0, \\ -\sqrt{|m_{\tau\tau}^2|} & m_{\tau\tau}^2 < 0. \end{cases} \tag{130}$$

This version of the $m_{\tau\tau}$ variable is the one used in the analysis. Figure 101 shows the distribution for MC and two signal samples. It is possible to see a $Z \to \tau\tau$ peak around 100 GeV, while the signal is rather flat. For this reason it is required $m_{\tau\tau} < 0$ GeV or $m_{\tau\tau} > 160$ GeV.

8.2.5 Signal Regions

Signal region are defined starting from the selection reported in table 23, called *preselection*. The signal region is binned in $m_{\ell\ell}$ in

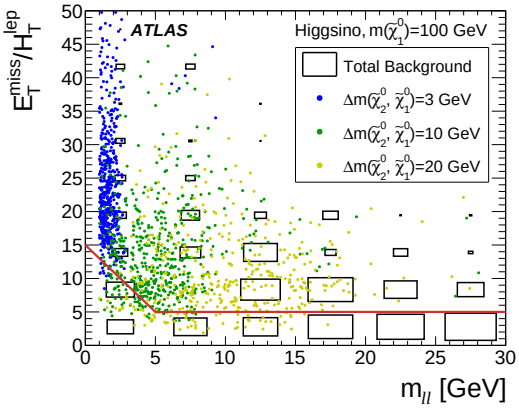

Figure 100: 2D scatter plot of $E_{\mathrm{T}}^{\mathrm{miss}}/H_{\mathrm{T}}^{\mathrm{leptons}}$ and $m_{\ell\ell}$ for different signals samples with the same mass for $\tilde{\chi}_1^0$ (100 GeV) and different mass splitting, in colored points, and the total background (the boxes, the larger the box the larger the background contribution). The dashed line represent the cut of equation 124.

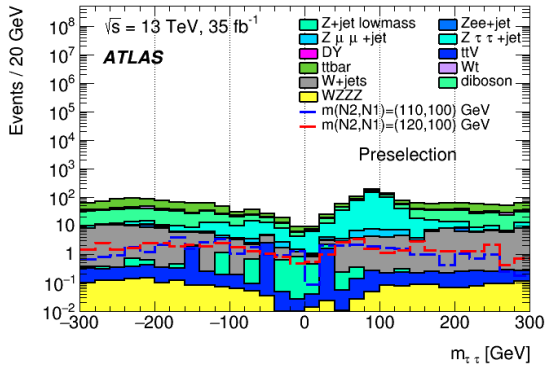

Figure 101: $m_{\tau\tau}$ distribution after applying the cut in preselection (except the one on $m_{\tau\tau}$) for background MC samples and two signal samples. Histograms are stacked.

order to exploit the characteristic signal shape of the invariant mass of the $Z^{(\star)}$ decay. SR are labeled SR-MLL, with exclusive bins have identified by the suffix "e", and inclusive one from the suffix "i". Bins name are suffixed in alphabetical order from the lowest to highest value of $m_{\ell\ell}$: e.g. SR-eMLLb, SR-iMLLg.

- **Exclusive**: Exclusive SR are bin each of different size ortho-

Variable	Requirement
$E_{\mathrm{T}}^{\mathrm{miss}}$	> 200 GeV
Leading jet $p_{\mathrm{T}}(j_1)$	> 100 GeV
$\lvert\Delta\phi(j_1, \mathbf{p}_{\mathrm{T}}^{\mathrm{miss}})\rvert$	> 2.0
$\min\lvert\Delta\phi(\text{all jets}, \mathbf{p}_{\mathrm{T}}^{\mathrm{miss}})\rvert$	> 0.4
$N_{\mathrm{b-jet}}^{20}$, 85% WP	Exactly zero
N_{leptons}	Exactly two baseline and two signal
Lepton charge and flavour	$e^{\pm}e^{\mp}$ or $\mu^{\pm}\mu^{\mp}$
Leading electron (muon) $p_{\mathrm{T}}^{\ell_1}$	$> 5(5)$ GeV
Subleading electron (muon) $p_{\mathrm{T}}^{\ell_2}$	$> 4.5(4)$ GeV
$m_{\tau\tau}$	Veto [0, 160] GeV
$m_{\ell\ell}$	$> 1, < 60$ GeV, veto [3, 3.2] GeV
$\Delta R_{\ell\ell}$	> 0.05

Table 23: Signal region selection common to 2ℓ channel.

gonal with respect of each other. Bin width has been optimized in order to be sensitive to as many different signal as possible. A J/ψ veto is applied between 3.0 GeV and 3.2 GeV. The bins are $[1-3.0]$ GeV, $[3.2-5.]$ GeV, $[5-10]$ GeV, $[10-20]$ GeV, $[20-30]$ GeV, $[30-40]$ GeV, and $[40-60]$ GeV. Bins are further divided in ee and $\mu\mu$ channels, which are then statistically combined. Lower $m_{\ell\ell}$ bins are sensitive to lower Δm signals, and higher $m_{\ell\ell}$ to higher Δm.

- **Inclusive**: Inclusive SR are defined by selecting all the $m_{\ell\ell}$ below the up edge of the exclusive bins: < 3 GeV, < 5 GeV, < 10 GeV, < 20 GeV, < 30 GeV, < 40 GeV, < 60 GeV. These bins were optimized to obtain better sensitivity on the cross section of new physics. The ee and $\mu\mu$ channels are combined together.

Table 24 summarizes all the exclusive and inclusive SRs. Figures from 102 to 104 show key kinematic distributions in SRee-iMLLg (ee) and SRmm-iMLLg ($\mu\mu$), where all the SR cuts are applied except the one on the variable that is shown. These plots are called $N-1$. The uncertainty band contain statistical uncertainty and a flat 20 % systematic

Variable	Selections optimised for Higgsinos						
$E_{\mathrm{T}}^{\mathrm{miss}}/H_{\mathrm{T}}^{\mathrm{leptons}}$	$> \mathrm{Max}\,(5.0, 15 - 2 \cdot m_{\ell\ell}/\ \mathrm{GeV})$						
$\Delta R_{\ell\ell}$	< 2.0						
$m_{\mathrm{T}}^{\ell_1}$	< 70 GeV						
SRee-, SRmm-	eMLLa	eMLLb	eMLLc	eMLLd	eMLLe	eMLLf	eMLLg
$m_{\ell\ell}$ [GeV]	$[1, 3]$	$[3.2, 5]$	$[5, 10]$	$[10, 20]$	$[20, 30]$	$[30, 40]$	$[40, 60]$
SRSF-	iMLLa	iMLLb	iMLLc	iMLLd	iMLLe	iMLLf	iMLLg
$m_{\ell\ell}$ [GeV]	< 3	< 5	< 10	< 20	< 30	< 40	< 60

Table 24: Final signal region selections in addition to those in Table 23 for SR-MLL optimised for Higgsinos. Each exclusive SR is further divided into statistically independent ee and $\mu\mu$ regions. Inclusive SRs only consider $ee + \mu\mu$ events.

on the background.

8.3 Background Estimation

This section will present how all the backgrounds estimates were performed. The main irreducible background comes from top, $t\bar{t}$ and Wt, diboson events, and $Z(\rightarrow \tau\tau)$+jets. For the top processes, events enter the signal region (SR) due to the inefficiency of the b-tagging algorithm, especially with soft b-jets, while diboson and Z events can easily mimic the Higgsino signal events with $E_{\mathrm{T}}^{\mathrm{miss}}$ arising from neutrinos. To constrain the top and $Z(\rightarrow \tau\tau)$ contributions, control regions (CR) are built, enriched in the corresponding background. A simultaneous likelihood fit is then done and many validation regions (VR) are built to check the correctness of the modeling in regions close to the SR.
Diboson events instead are taken directly from MC, due to the difficulty to have a pure enough CR. However their modeling is checked with specially designed VR. Minor backgrounds ($Z(\rightarrow e^+e^-, \mu\mu)$+jets, Higgs, triboson) are instead kept directly from MC. Drell-Yan events at low $m_{\ell\ell}$ are taken also from MC, but their modeling is checked with a data driven method. Fake and non prompt leptons instead are obtained from a data driven method called *Fake Factor*, and their modeling is checked in a VR, with same sign leptons. Table 25 describes all the main backgrounds and how they are treated.

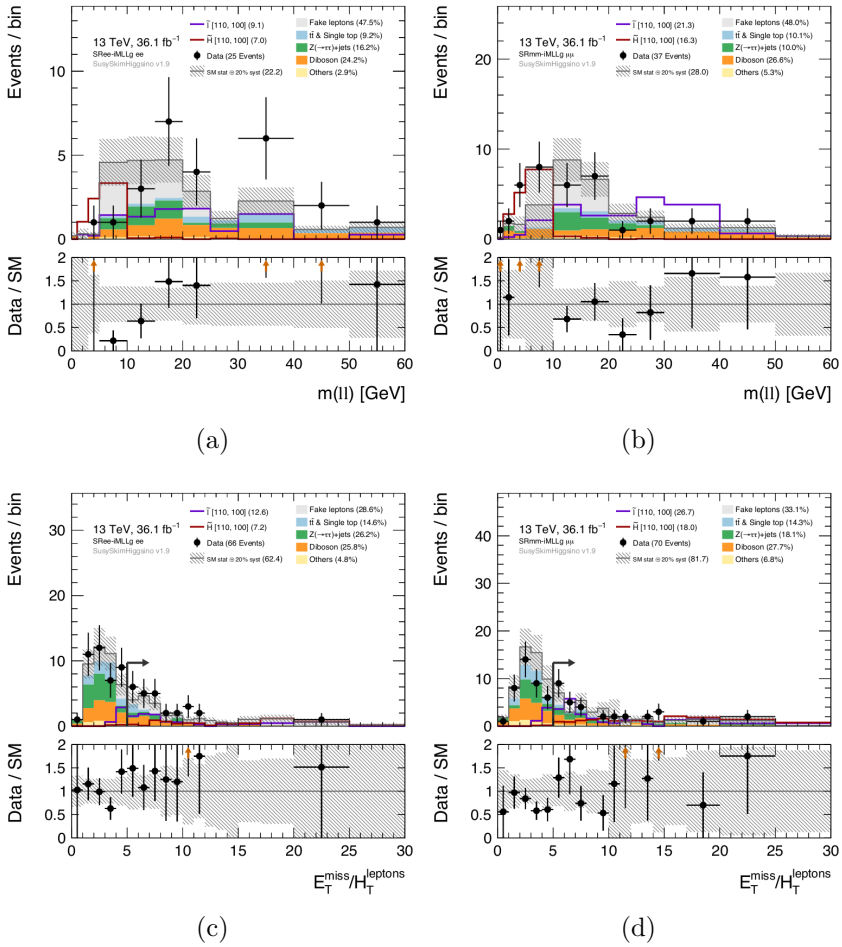

Figure 102: $N-1$ plot in SR-iMLLg (ee and $\mu\mu$) for (a) $m_{\ell\ell}$ (ee), (b) $m_{\ell\ell}$ ($\mu\mu$), (c) $E_{\mathrm{T}}^{\mathrm{miss}}/H_{\mathrm{T}}^{\mathrm{leptons}}$ (ee), and (d) $E_{\mathrm{T}}^{\mathrm{miss}}/H_{\mathrm{T}}^{\mathrm{leptons}}$ ($\mu\mu$).

8.3.1 Control regions

Control regions are designed to be orthogonal to the SR, but still close enough to have a sample representative of the kinematic inside the SR. Additionally the CR must have as low as possible signal events. Two different CR are build, one for top events, called CR-top, and one for $Z \to \tau\tau$, called CR-tau.

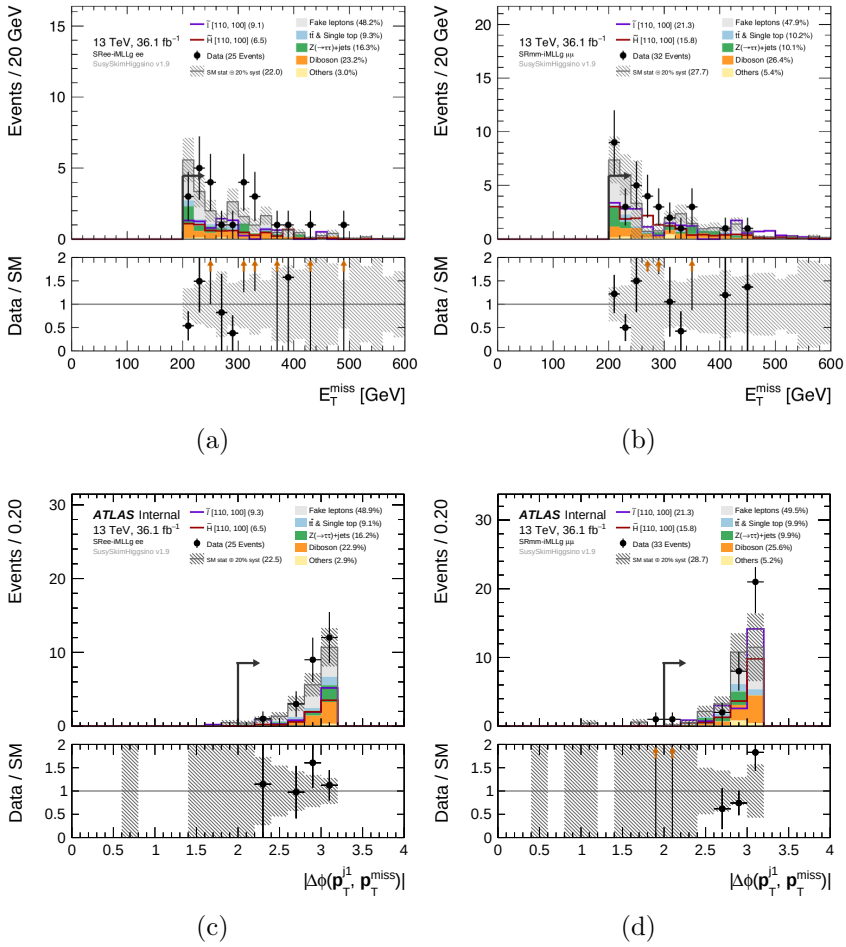

Figure 103: $N-1$ plot in SR-iMLLg (ee and $\mu\mu$) for (a) $E_{\mathrm{T}}^{\mathrm{miss}}$ (ee), (b) $E_{\mathrm{T}}^{\mathrm{miss}}$ ($\mu\mu$), (c) $\left|\Delta\phi(j_1, \mathbf{p}_{\mathrm{T}}^{\mathrm{miss}})\right|$($ee$), and (d) $\left|\Delta\phi(j_1, \mathbf{p}_{\mathrm{T}}^{\mathrm{miss}})\right|$($\mu\mu$).

CR-top The top contribution in SR mainly comes from events where the b-jet from the $t \to Wb$ has not been tagged. CR is then built by asking the same request as for the SR, but with at least one b-jet. This allows having a large contribution of top and almost no signal events, while also being orthogonal to the SR. In order to gain more statistic it is also relaxed the cut on. $E_{\mathrm{T}}^{\mathrm{miss}}/H_{\mathrm{T}}^{\mathrm{leptons}}$, by asking $E_{\mathrm{T}}^{\mathrm{miss}}/H_{\mathrm{T}}^{\mathrm{leptons}} > 5$. Additionally, both Same Flavor and Different Flavor events are considered together, since both $t\bar{t}$ and Wt are flavor

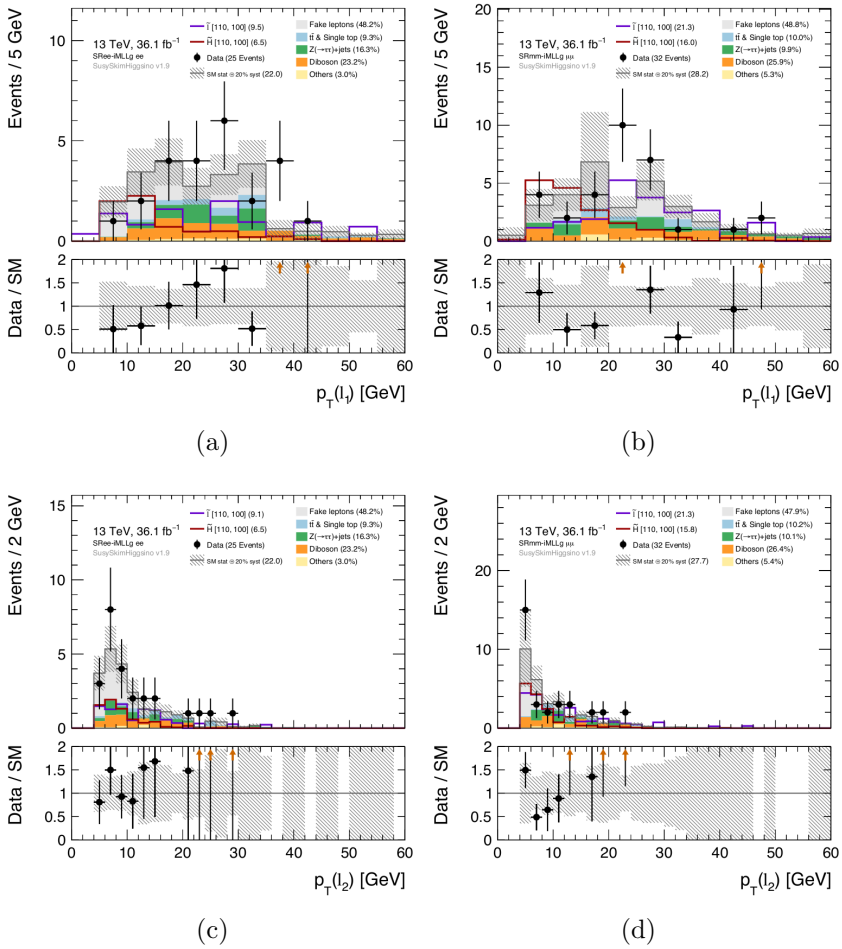

(a) (b)

(c) (d)

Figure 104: $N-1$ plot in SR-iMLLg (ee and $\mu\mu$) for(a) $p_{\mathrm{T}^{\mathrm{lep1}}}(ee)$, (b) $p_{\mathrm{T}^{\mathrm{lep1}}}(\mu\mu)$, (c) $p_{\mathrm{T}^{\mathrm{lep2}}}(ee)$, and (d) $p_{\mathrm{T}^{\mathrm{lep2}}}(\mu\mu)$.

symmetric processes. Figures 105 and 106 show key kinematic variables inside this CR before the fit was performed. The uncertainty band covers statistical uncertainty and a flat 20 % systematic uncertainty. Top contribution amount to $\sim 85\%$, obtaining an high purity of the sample.

CR-tau Contribution from $Z \to \tau\tau$+jets enter the SR due to $E_{\mathrm{T}}^{\mathrm{miss}}$ coming from the neutrinos of the τ decay, that can mimic the signal, and from events that fails the cut on $m_{\tau\tau}$, which happens when

Background process	Origin in signal region	Estimation strategy
$t\bar{t}$, tW (2ℓ)	Irreducible, b-jet fails identification	CR using b-tagging
$Z(\rightarrow \tau\tau)$+jets	Irreducible fully leptonic taus	CR using $m_{\tau\tau}$
$Z(\rightarrow ee, \mu\mu)$+jets	Instrumental $E_{\mathrm{T}}^{\mathrm{miss}}$	Monte Carlo
Low mass Drell-Yan	Instrumental $E_{\mathrm{T}}^{\mathrm{miss}}$	Monte Carlo, data-driven cross check
Fakes (W+jets, $VV(1\ell)$, $t\bar{t}(1\ell)$)	Jet fakes second lepton	Fake factor, same sign VR
VV	Irreducible dileptonic and missed 3rd lepton	Monte Carlo, VR using $E_{\mathrm{T}}^{\mathrm{miss}}/H_{\mathrm{T}}^{\mathrm{leptons}}$
Other rare processes	Irreducible leptonic decays	Monte Carlo

Table 25: Summary of background processes for 2ℓ analysis.

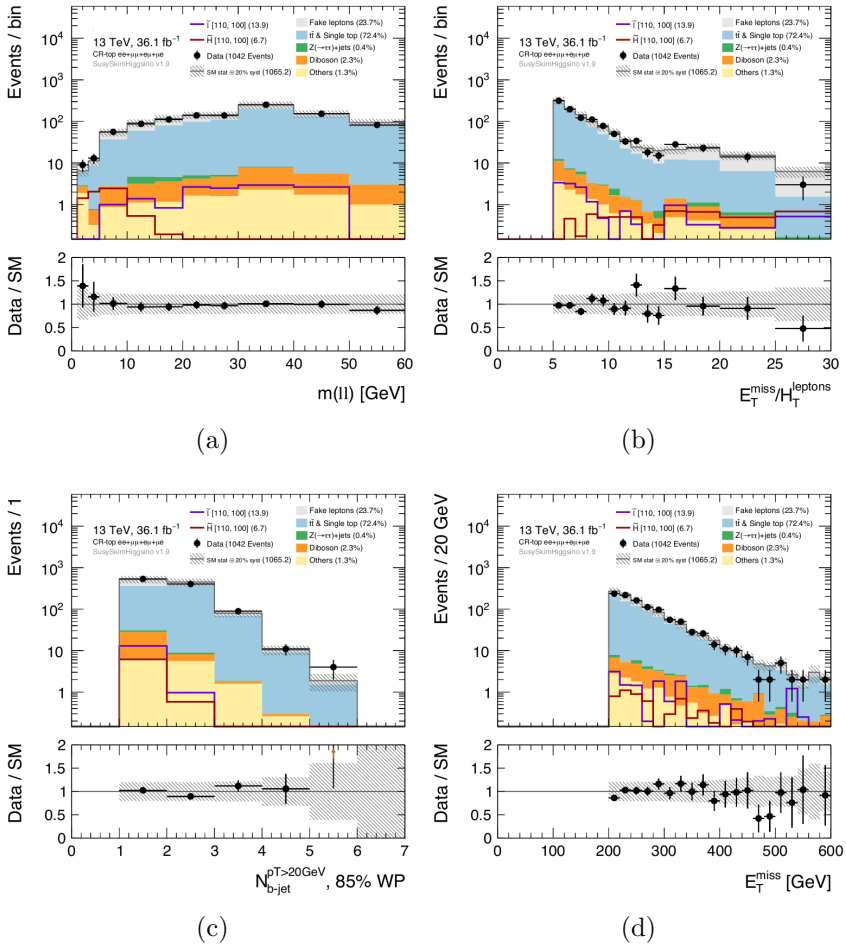

Figure 105: CR-Top plots for all flavor channel, pre-fit.

the neutrinos and the corresponding leptons are not aligned. The dedicated CR is then obtained by inverting the cut on $m_{\tau\tau}$. This

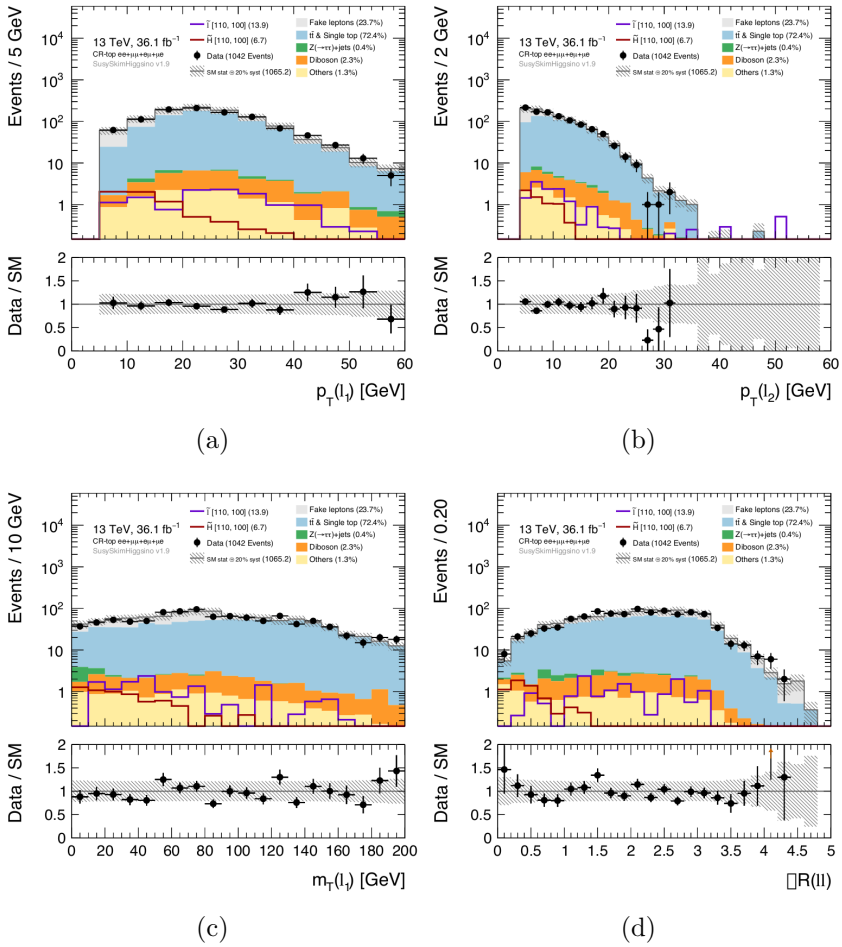

Figure 106: CR-Top plots for all flavor channel, pre-fit.

allows having a very pure sample ($\sim$ 80%) with small contribution from other irreducible background (especially dibosons). This cut also helps to avoid signal events, however in order to further reduce signal contamination, $E_{\mathrm{T}}^{\mathrm{miss}}/H_{\mathrm{T}}^{\mathrm{leptons}}$ is also inverted, with a cut $E_{\mathrm{T}}^{\mathrm{miss}}/H_{\mathrm{T}}^{\mathrm{leptons}} < 8$. In addition, to avoid having a CR too much far away in kinematic composition, a lower cut is also applied to this last variable: $E_{\mathrm{T}}^{\mathrm{miss}}/H_{\mathrm{T}}^{\mathrm{leptons}} > 4$. The statistic of the CR is enhanced by using ee, $\mu\mu$, and $e\mu$ channels. Figures 107 and 108 show key kinematic variables inside this CR before the fit was performed.

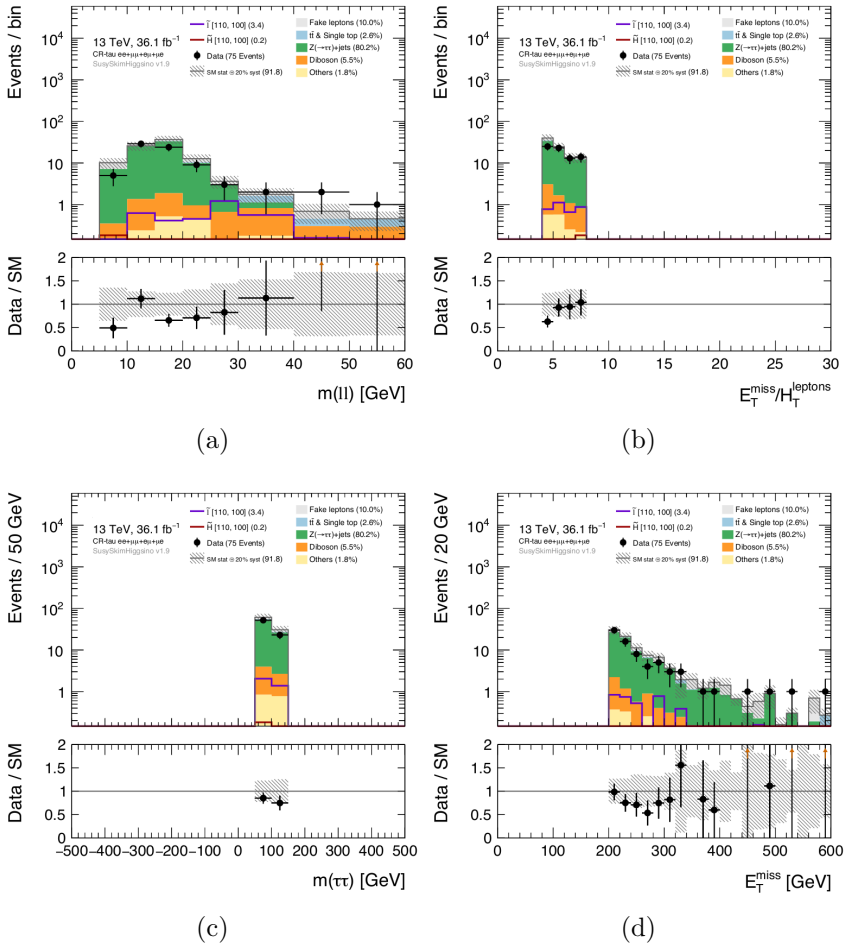

Figure 107: CR-Tau plots for all flavor channel, pre-fit.

8.3.2 Validation Region

Validation Regions are built to ensure the correct extrapolation of the background estimate from the Control Region. VRs are built to be orthogonal to SR and CR, but still closer to SR than CR. Two main VR are built, one targeting specifically the diboson processes, called VR-VV, and one checking the modeling of all the MC in a phase space as close as possible to the SR, using events with Different Flavor leptons, called VRDF.

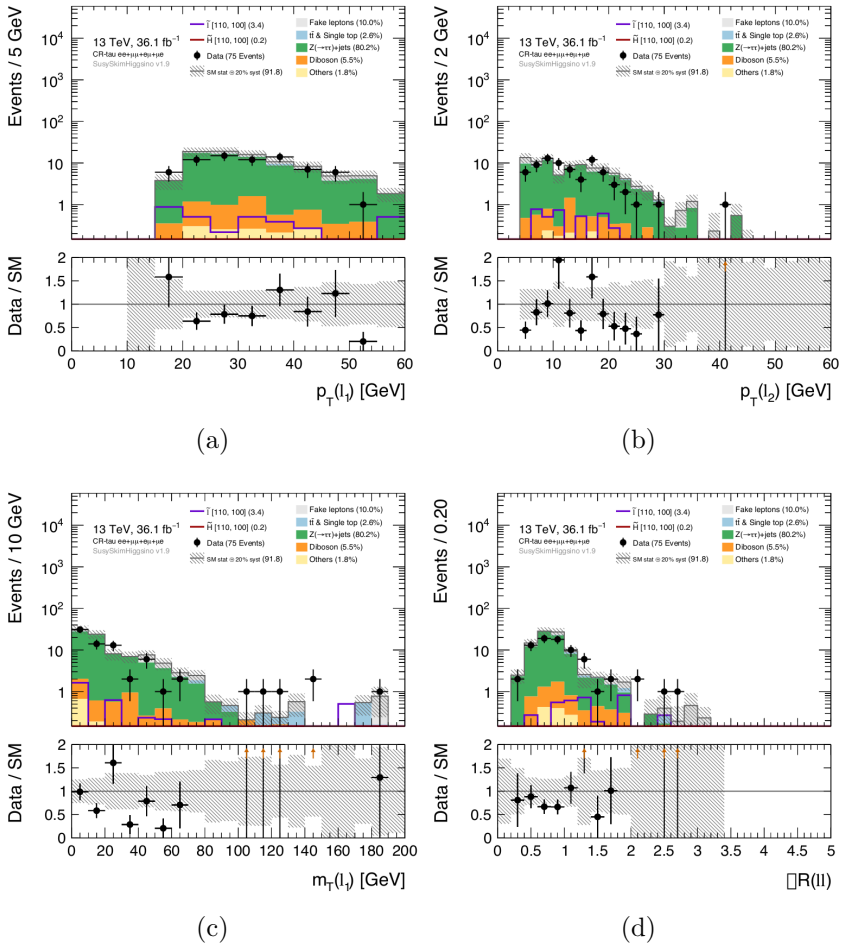

Figure 108: CR-Tau plots for all flavor channel, pre-fit.

VR-VV In order to check the prediction of diboson events it is used a VR. This region is obtained by asking $E_{\mathrm{T}}^{\mathrm{miss}}/H_{\mathrm{T}}^{\mathrm{leptons}} < 3.0$, in order to be orthogonal to the SR and also avoid signal contamination and overlaps with the CR-Tau. In order to have more statistic, all flavor combination are considered: ee, $e\mu$, and $\mu\mu$, since $WW \to \ell\nu\ell\nu$ is dominant over $ZZ \to \ell\ell\nu\nu$. The purity of this region is however rather low: only 50 % of the SM processes in the region are from VV events, and in these, only 30 % comes from 2ℓ events. Most of the remaining processes come from 1ℓ events were the second lepton is non prompt, which however are estimated inside the Fake Factor

method. Due to its low purity this region was only used as a VR instead of a CR. In fact the low purity would have only increased the systematic effect due to the normalization of this process. Figures 109 and 110 show key kinematic variables inside this VR before the fit was performed.

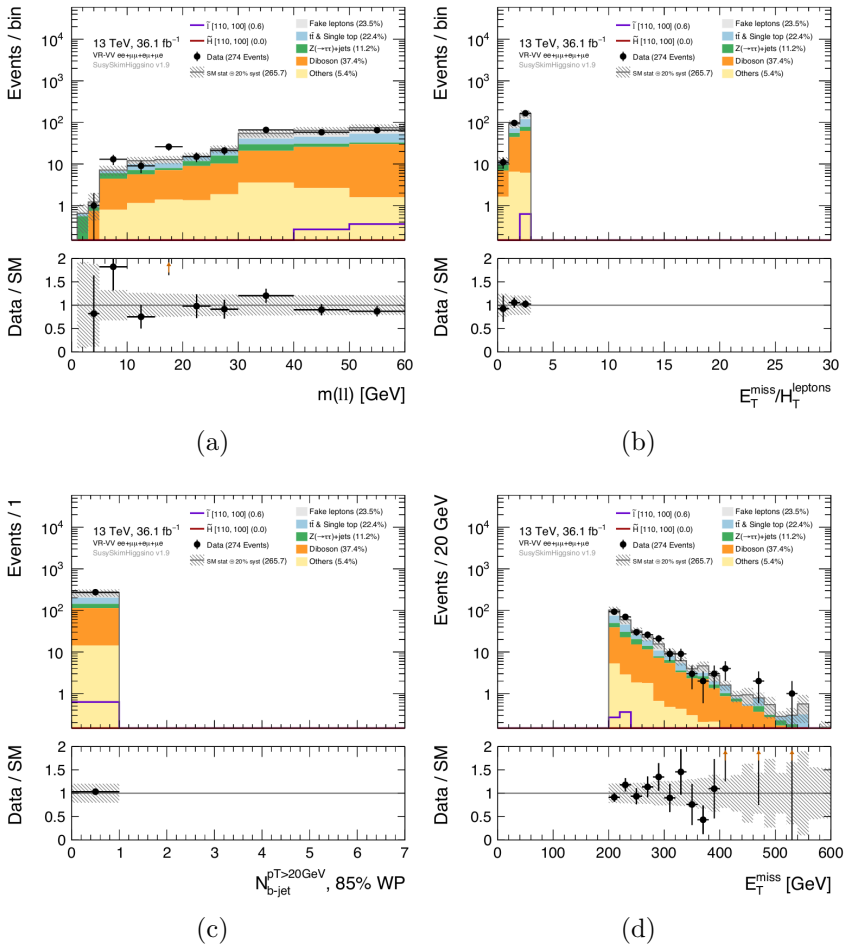

Figure 109: VR-VV plots for all flavor channel, pre-fit.

VRDF In order to check the extrapolation of the fitted MC prediction from the CR to SR a series of VRs are defined. All the backgrounds that enters the SR are symmetric in flavor, therefore $ee + \mu\mu$ rates should be the same as $e\mu + \mu e$, while the signal lives only in

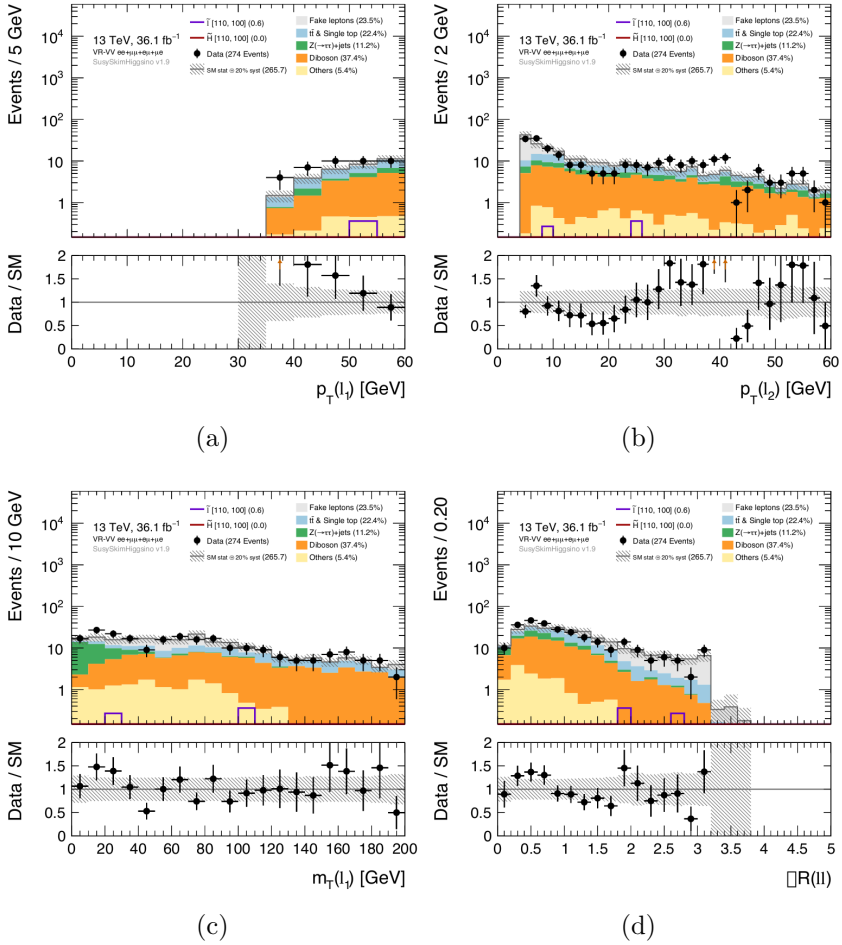

Figure 110: VR-VV plots for all flavor channel, pre-fit.

the $ee + \mu\mu$ channel. For this reason, in order to check as close as possible to the SR's kinematics, the VRDF is build by asking all the requirements of the SR, but looking only to events with different flavor leptons. For each of the exclusive or inclusive SR bins there is a corresponding VR, e.g. for VRDF-iMLLb has the exact same selection as SRSF-iMLLb, but with DF leptons. Figures 111 and 112 show key kinematic variables inside this VR before the fit was performed.

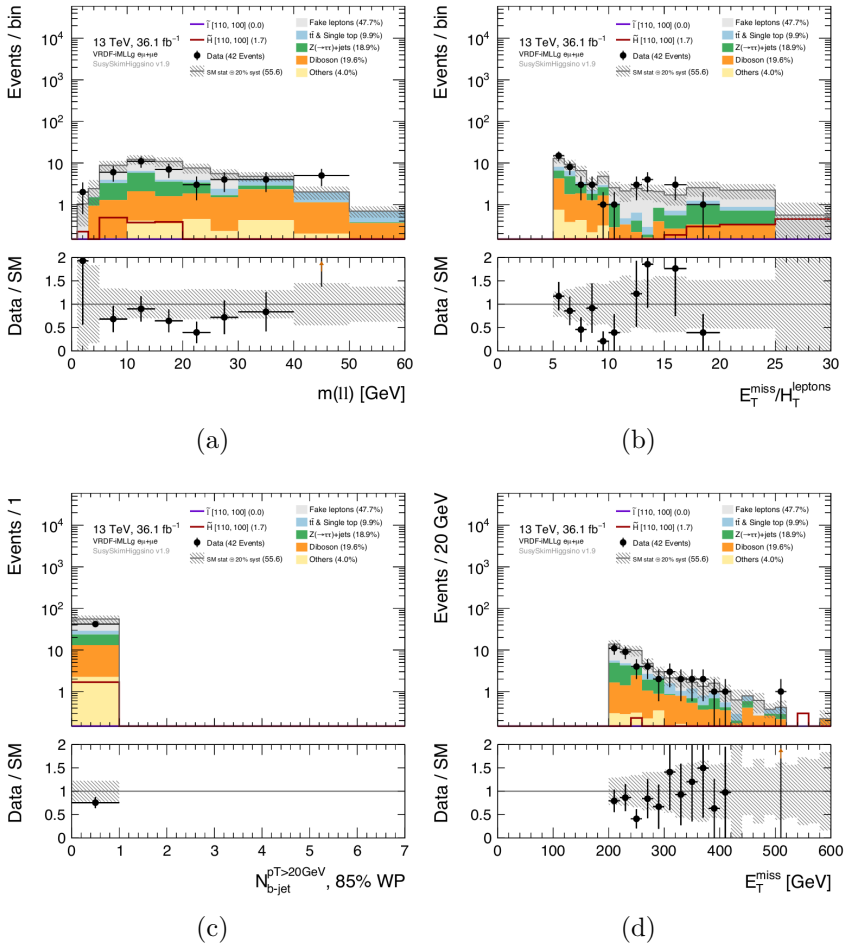

Figure 111: VRDF plots for all flavor channel, pre-fit.

8.3.3 Drell-Yan and instrumental $E_{\mathrm{T}}^{\mathrm{miss}}$ backgrounds

Events from $Z/\gamma^{\star} \rightarrow e^{+}e^{-}/\mu^{+}\mu^{-}$ Drell-Yan, either through resonance (J/ψ, Υ, Z) or off-resonance can enter the signal region due to instrumental $E_{\mathrm{T}}^{\mathrm{miss}}$, being $E_{\mathrm{T}}^{\mathrm{miss}}$ that originates by either "fake" $E_{\mathrm{T}}^{\mathrm{miss}}$, where jets energy are mismeasured in the calorimeter due to finite granularity, or by the fact that $E_{\mathrm{T}}^{\mathrm{miss}}$ triggers are blind to muons. By asking $E_{\mathrm{T}}^{\mathrm{miss}} > 200$ GeV, operating on the trigger plateau, most of these backgrounds are suppressed, however some small contribution can still enter the SR. Since the signal appears in the low $m_{\ell\ell}$ it is then

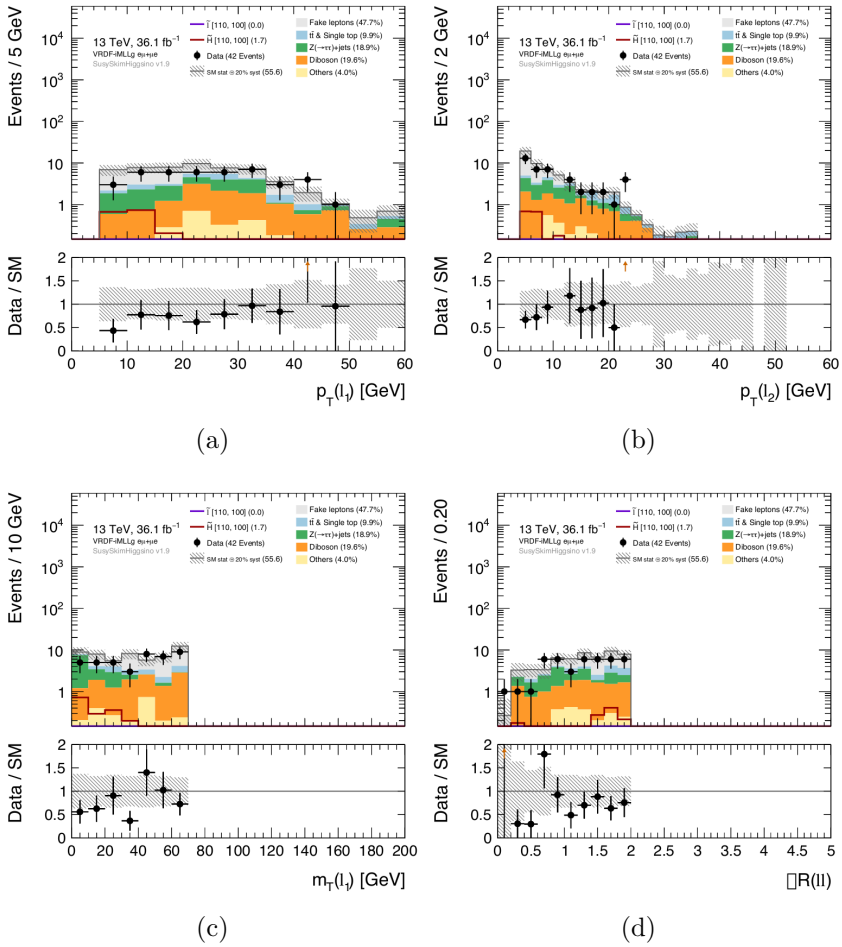

Figure 112: VRDF plots for all flavor channel, pre-fit.

important to check here if any background enter the SR.
Two cuts are applied to reduce this background:

- J/ψ veto: Events around the narrow peak of the J/ψ are removed, so $m_{\ell\ell} < 3.0$ GeV or $m_{\ell\ell} > 3.2$ GeV. The impact on the signal is small, while instead assuring no contribution from this resonance.

- $\min \left|\Delta\phi(\text{all jets}, \mathbf{p}_{\mathrm{T}}^{\mathrm{miss}})\right| > 0.4$: $E_{\mathrm{T}}^{\mathrm{miss}}$ from mismeasured jet energy tends to align with the jet itself, so an angular cut helps to reduce this background.

MC samples in this region are however not entirely reliable due to low statistic and the modeling of QCD. This is because it is difficult to model the tail of the resolution of the $E_{\mathrm{T}}^{\mathrm{miss}}$ that are the main source of this background. It is also complicated because of the combination of a production at high statistic (the Drell-Yann) and a low probability of having high $E_{\mathrm{T}}^{\mathrm{miss}}$. For this same reason the statistic in the MC is limited and the errors are large, as it is possible to see in table 28. It is then important to have a better estimate, since the total background in the SR is of the same order as this background.
Therefore a further check is done with an ABCD method in the $1 < m_{\ell\ell} < 3.$ GeV region, in order to check if this contribution is indeed negligible, and to compare it with the MC prediction, to validate them. The starting point of the ABCD method is a control region (called here CR_Q) constructed starting from the SR definition and making the following modifications:

- requiring $150 < E_{\mathrm{T}}^{\mathrm{miss}} < 200$ GeV, to avoid going too far below the inclusive $E_{\mathrm{T}}^{\mathrm{miss}}$ trigger turn-on while being orthogonal to the SR,
- dropping the requirement on the isolation, to gain statistic in this region,
- selecting the range in $m_{\ell\ell}$ of $1.0 < m_{\ell\ell} < 3.$ GeV.

The definition of CR_Q is reported in table 26. This method can also be used to estimate the number of low $m_{\ell\ell}$ Drell-Yan events in regions other than the SR, by starting from the region of interest (i.e. CR-top, VR-VV or else) and again inverting the $E_{\mathrm{T}}^{\mathrm{miss}}$ cut and isolation.

The estimated number of Drell-Yan events in the SR is then obtained by multiplying the number of events observed in the CR_Q by (different) transfer factors that account for the difference between the two region, namely isolation (TF_{iso}) and $E_{\mathrm{T}}^{\mathrm{miss}}$ ($TF_{E_{\mathrm{T}}^{\mathrm{miss}}}$). The number of events entering the SR can be then estimated using equation 131:

$$N_{\mathrm{SR}} = N_{\mathrm{CR}_Q} \times TF_{E_{\mathrm{T}}^{\mathrm{miss}}} \times TF_{\mathrm{iso}}. \tag{131}$$

$TF_{E_{\mathrm{T}}^{\mathrm{miss}}}$ estimate
For each region where the ABCD method is used, it is necessary to

Variable	$CR^{iso}_{lE_{\mathrm{T}}^{\mathrm{miss}}}$	$CR^{no\,iso}_{lE_{\mathrm{T}}^{\mathrm{miss}}}$	$CR_{hE_{\mathrm{T}}^{\mathrm{miss}}}$	CR_Q	SR
Isolation	applied	removed	removed	removed	applied
$E_{\mathrm{T}}^{\mathrm{miss}}$ [GeV]	$> 150, < 200$	$> 150, < 200$	> 200	$> 150, < 200$	> 200
$\Delta\phi(j_1, E_{\mathrm{T}}^{\mathrm{miss}})$	< 2	< 2	-	> 2	> 2
p_{T}^{jet} [GeV]	> 30	> 30	> 30	> 100	> 100
$m_{\tau\tau}$	removed	removed	removed	removed	removed
$E_{\mathrm{T}}^{\mathrm{miss}}/HT_{lep}$	removed	removed	applied	applied	applied
$m_{\ell\ell}$ [GeV]	> 1 and < 3.0				

Table 26: Definition of the region used in the low $m_{\ell\ell}$ estimate

compute an adequate transfer factor, since all the regions have different $E_{\mathrm{T}}^{\mathrm{miss}}/H_{\mathrm{T}}^{\mathrm{leptons}}$ cut, and therefore it depends on the $E_{\mathrm{T}}^{\mathrm{miss}}$ itself. These TFs are evaluated by computing the ratio between the number of events with $E_{\mathrm{T}}^{\mathrm{miss}} > 200$ GeV and the corresponding $E_{\mathrm{T}}^{\mathrm{miss}}/H_{\mathrm{T}}^{\mathrm{leptons}}$ cut ($CR_{hE_{\mathrm{T}}^{\mathrm{miss}}}$) over the number of events with $150 < E_{\mathrm{T}}^{\mathrm{miss}} < 200$ GeV ($CR_{lE_{\mathrm{T}}^{\mathrm{miss}}}$). Orthogonality with SR is obtained by removing the isolation requirement, and relaxing other cuts, in order to have a small signal contamination. The definition of this region is in table 26.

TF_{iso} estimate

TF_{iso} is evaluated in a specific CR with $150 < E_{\mathrm{T}}^{\mathrm{miss}} < 200$ GeV, computing the ratio between the number of events with and without isolation, respectively called $CR^{\mathrm{iso}}_{lE_{\mathrm{T}}^{\mathrm{miss}}}$ and $CR^{\mathrm{no\,iso}}_{lE_{\mathrm{T}}^{\mathrm{miss}}}$, described in table 26. An additional cut $\left|\Delta\phi(j_1, \mathbf{p}_{\mathrm{T}}^{\mathrm{miss}})\right| < 2$ is applied to reduce signal contamination. However SR is at high $\left|\Delta\phi(j_1, \mathbf{p}_{\mathrm{T}}^{\mathrm{miss}})\right|$, so it must be checked that TF_{iso} doesn't depend on $\left|\Delta\phi(j_1, \mathbf{p}_{\mathrm{T}}^{\mathrm{miss}})\right|$. Figure 113 shows the dependence of TF_{iso} from $\left|\Delta\phi(j_1, \mathbf{p}_{\mathrm{T}}^{\mathrm{miss}})\right|$, $E_{\mathrm{T}}^{\mathrm{miss}}$, and $H_{\mathrm{T}}^{\mathrm{leptons}}$ in the $CR_{lE_{\mathrm{T}}^{\mathrm{miss}}}$ region, with the requirement of $m_{\ell\ell} < 10$ GeV, and it is possible to see that the assumption is, within the uncertainties, correct. The average TF_{iso} is also drawn in the ratio plot as the dashed red line, with the black band representing $\pm 1\sigma$ error.

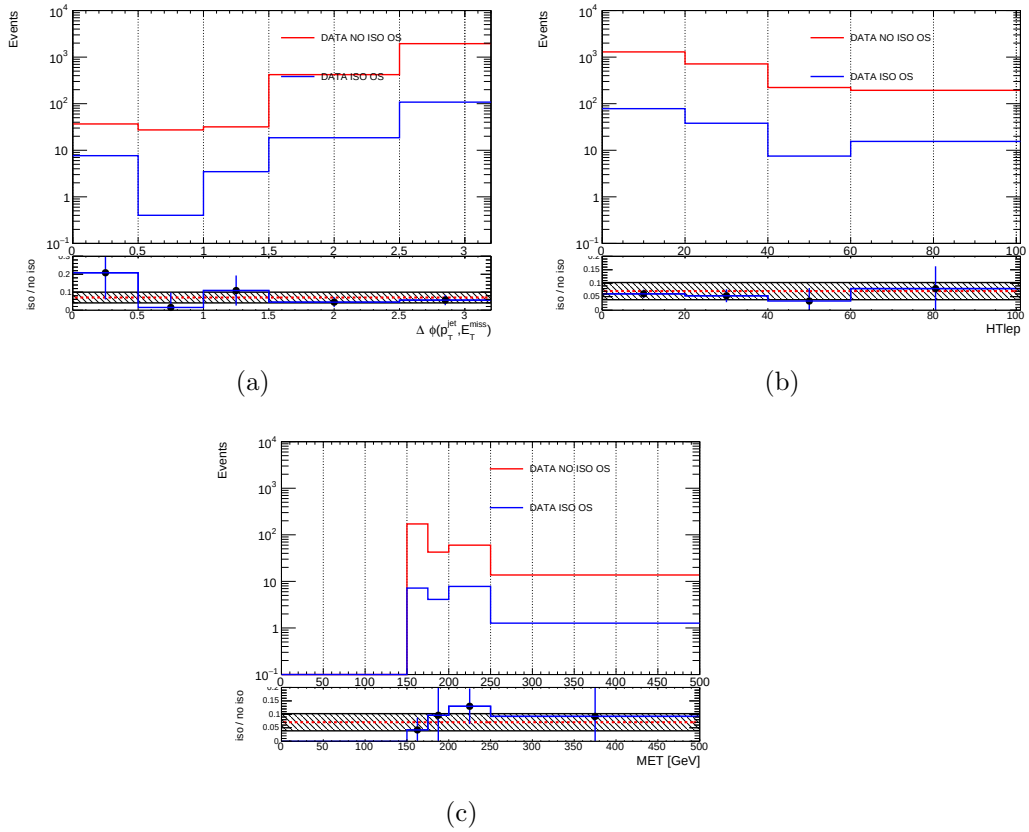

(a) (b)

(c)

Figure 113: Distribution of $\left|\Delta\phi(j_1, \mathbf{p}_{\mathrm{T}}^{\mathrm{miss}})\right|$ (a) $H_{\mathrm{T}}^{\mathrm{leptons}}$ (b) and $E_{\mathrm{T}}^{\mathrm{miss}}$ (c) with and without isolation applied in the $CR_{lE_{\mathrm{T}}^{\mathrm{miss}}}$ region and $m_{\ell\ell} < 10$ GeV

Figure 114 shows the $m_{\ell\ell}$ distribution in the $CR_{lE_{\mathrm{T}}^{\mathrm{miss}}}^{\mathrm{no\,iso}}$ region, without the low $m_{\ell\ell}$ Drell-Yan samples that it is being checked. The large difference in data/MC is due to this missing sample and fakes not included in the $W + jets$ samples, and is exactly what this ABCD method is trying to quantify.

N_{CR_Q} estimate

The number of events in CR_Q, N_{CR_Q}, to be used in equation 131, is obtained by taking the number of events in data in CR_Q and subtracting the MC events without the low $m_{\ell\ell}$ Drell-Yan samples. In

Sample	MC OS	Data OS	MC SS	Data SS
Events	57 ± 85	1331 ± 36	19.10 ± 2.75	409 ± 20

Table 27: The yields in CR_Q in the range $1 < m_{\ell\ell} < 3$ GeV. W+jet are also not considered.

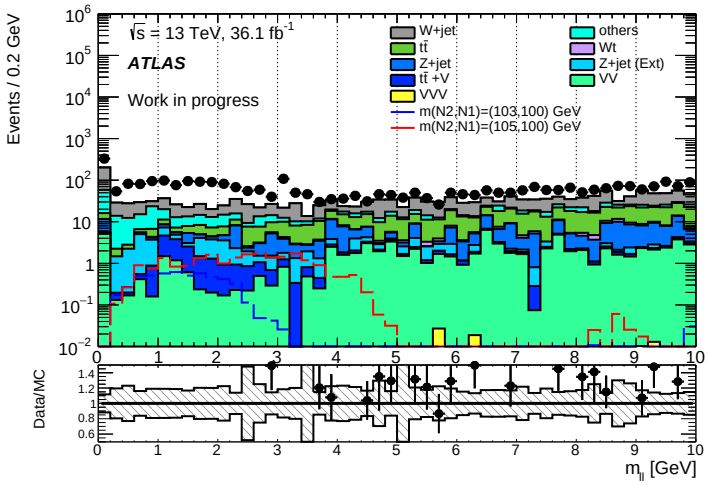

Figure 114: $m_{\ell\ell}$ distribution in $CR_{lE_{\mathrm{T}}^{\mathrm{miss}}}$, with no isolation applied. This figure shows that there is an excess of data with respect of MC outside of the Drell-Yan, and this difference is exactly what is measured by this ABCD method.

order to avoid to double count fake leptons, same sign data ($N_{\mathrm{CR}_Q}^{\mathrm{Data,SS}}$), minus same sign MC ($N_{\mathrm{CR}_Q}^{\mathrm{MC,SS}}$), are also subtracted to opposite sign data. Same sign data are used as proxy for fake leptons, since the probability of having a fake lepton is not correlated to the sign of the prompt lepton. With this correction the number of events in the CR is defined as:

$$N_{\mathrm{CR}_Q} = N_{\mathrm{CR}_Q}^{\mathrm{Data,OS}} - \left[N_{\mathrm{CR}_Q}^{\mathrm{MC,OS}} - \left(N_{\mathrm{CR}_Q}^{\mathrm{Data,SS}} - N_{\mathrm{CR}_Q}^{\mathrm{MC,SS}}\right)\right]. \qquad (132)$$

Table 27 shows the number of OS data, SS data, OS MC, and SS MC in the CR_Q. In the MC the W+jets are not included because fakes are taken from data. The W+jets is however a small correction ($\sim 1\%$).

Range $m_{\ell\ell}$ [GeV]	$TF_{E_{\mathrm{T}}^{\mathrm{miss}}}$	Region	N_{CR_Q}	Estimated Events	Observed MC events
1.0 - 3.0	0.16 ± 0.05	SR-MLL	11.16 ± 9.00	0.13 ± 0.13	0.8 ± 0.6
1.0 - 3.0	0.53 ± 0.13	CRtop	48.03 ± 12.15	1.80 ± 1.03	1.8 ± 0.8
1.0 - 3.0	0.02 ± 0.02	CR-VV	9.44 ± 5.01	0.017 ± 0.018	0.3 ± 0.3

Table 28: Estimated events in region of interest and corresponding $E_{\mathrm{T}}^{\mathrm{miss}}$ TF

SR events estimate It is then possible to estimate the number of events in the SR, and also in the other CRs/VRs. The estimation is shown in table 28 together with the respective $TF_{E_{\mathrm{T}}^{\mathrm{miss}}}$ and the observed events in the CR_Q. In the SR the contribution from this background seems to be rather small and in agreement with the MC predictions. However uncertainties are rather large. These come from the low purity of both CR and the transfer factor (the contribution of the SS subtraction is rather large with respect to the OS). In the end the method correctly validated the prediction of the MC, even if both have large uncertainties, so the latter was used in the analysis.

8.3.4 Fake and non-prompt leptons estimate using Fake Factor

Reducible backgrounds are events that contain at least one non prompt or fake lepton (FNP). These originates from misidentification of light flavor jets or photon conversions, or non prompt leptons from heavy flavor hadrons. Standard Model events that can produce this kind of phenomena are W+jets, multijet, or single top. These kind of background are dealt with a data driven method called Fake Factor Method [202] instead of MC, since MC don't model well enough fake and non prompt leptons.

Fake Factor Method In this data driven method, two sets of leptons are selected with different identification criteria. The first one is the standard definition used for the signal lepton in the analysis, here called *tight* or "ID". The second set is orthogonal to the first, and it is called *loose* or "anti-ID". This set is designed to select events with mainly fake leptons, by reversing or relaxing some of the lepton

identification criteria.
The Fake Factor F is then defined as the ratio of the number of events with the ID identification over the one with the anti-ID identification, measured in a region with fake lepton with a similar composition as in the FNP background in the SR. The Fake Factor can also be binned, usually in p_{T} and can be described as:

$$F(i) = \frac{N_{\mathrm{ID}}(i)}{N_{\text{anti-ID}}(i)} \tag{133}$$

with N the number of events in the i^{th} bin.
The fake contribution in SR can then be obtained from these fake factors, by selecting an anti-ID control region that is identical to the SR, except that one of the ID leptons is replaced with an anti-ID lepton, and multiplying event-by-event, depending on the p_{T} the control region events by the fake factor. The total FNP background is then defined by:

$$N_{\mathrm{FNP}}^{\mathrm{SR}} = \sum_i N_{\text{anti-ID CR}}^{i} \cdot F(i). \tag{134}$$

where i is the content of the i^{th} p_{T} bin. Reducible background is not the only source of anti-ID leptons, so prompt leptons that fails one of the ID criteria, must be removed from the fake factor estimate, and this is done with MC.
This is true in case of just one fake lepton, however in a more general case it is possible to have multiple anti-ID leptons. In the case of two leptons in the final state, it is then possible to have two anti-ID leptons in the signal region. This means that it is also possible to have two fake leptons even in the selection with one ID lepton and one anti-ID leptons, where the Fake Factor is evaluated. These events must then be taken into account. The final estimate is then defined as:

$$N_{TT} - N_{TT}^{RR} = \left[N_{LT} - N_{LT}^{RR}\right] F_1 + \left[N_{TL} - N_{TL}^{RR}\right] F_2 - \left[N_{LL} - N_{LL}^{RR}\right] F_1 F_2 \tag{135}$$

where $F_{1/2}$ is the Fake Factor for the first / second lepton. The superscript RR refers to events with two real leptons, taken from MC. L and T instead refers to "Loose" and "Tight" of either the first or second lepton. The term with both anti-ID leptons is subtracted because in $N_{LT/TL}$ the ID lepton can also be fake, so in order to avoid

Trigger online threshold [GeV]	Prescaled Luminosity [pb^{-1}]	
	2015	2016
5	0.1	0.1
10	0.5	0.8
15	5.5	9
20	10	17
4	0.5	0.5
10	2.3	2.5
14	25	14
18	26	48

Table 29: Prescaled single-lepton triggers from 2015 and 2016 used to compute the lepton fake factors.

double counting N_{LL} must be subtracted.
The main background that is a source of fakes is $W \to \ell\nu$+jets, with one real lepton and one jet faking a lepton. A pure $W \to \ell\nu$+jets region is however difficult to isolate due to similarity with other processes like $t\bar{t}$. For this reason a dijet region is selected. Eventual differences in the composition of the fakes between the fakes in the SR and in the dijet region are assigned as an uncertainty on the Fake Factor method itself.
Events are selected with a prescaled single lepton trigger. Due to the large cross section, most of them are indeed from dijet events. Table 29 summarize all the prescaled single lepton trigger used in the Fake Factor estimate.
Table 30 shows the definition used for the anti-ID leptons. Events must also have a jet with $p_{\mathrm{T}} > 100$ GeV, in order to be closer to the kinematic region of the SR. Fake Factors are evaluated in bin of p_{T}, and for muons also depending on the number of b-jets: with two bin, either 0 or at least 1 b-tagged jet.

8.3.5 Same sign validation region

An additional Validation Region is defined in order to check the results of the Fake Factor Method, called VR-SS. This region selects events with the same kinematics as the SR but, using same sign leptons. This allows having a region enriched in fake leptons. This is possible since the charge of the fake lepton from jets or photon con-

Electrons	Muons
$p_{\mathrm{T}} > 4.5$ GeV $\lvert\eta\rvert < 2.47$ $\lvert z_0 \sin\theta\rvert < 0.5$ mm Pass LooseAndBLayer identification	$p_{\mathrm{T}} > 4$ GeV $\lvert\eta\rvert < 2.5$ $\lvert z_0 \sin\theta\rvert < 0.5$ mm Pass Medium identification
(!Tight identification $\lvert\lvert$ $\lvert d_0/\sigma(d_0)\rvert > 5$ $\lvert\lvert$!GradientLoose isolation)	($\lvert d_0/\sigma(d_0)\rvert > 3$ $\lvert\lvert$!FixedCutTightTrackOnly isolation)

Table 30: Summary of anti-ID lepton definitions.

version is generally uncorrelated with the charge of the lepton from the $W \to \ell\nu$. Signal contamination and prompt background instead are negligible since the leptons from these processes come from the particle-antiparticle production, and therefore their sign is correlated. Figures 115 and 116 show key kinematic variables inside this VR before the fit was performed for events in the channel $\mu\mu + e\mu$, used to check the validation of fake muons, since generally the subleading lepton is the fake one. Instead figure 117 and 118 show key kinematic variables in the same VR but in the channel $ee + \mu e$, that is used to validate the fake electrons. The fake background has a purity of 95%.

8.4 Systematic Uncertainties

Systematic uncertainties must be evaluated in order to get the correct error on the background. There are two different types of systematic uncertainty: experimental and theoretical. The first one comes from the modeling of the reconstruction in the simulation of the detector, luminosity measurement, pileup, and systematic effects in the reconstruction algorithm. Theoretical uncertainty instead come from the modeling of the SM background processes, their cross section, or PDF choice.
The systematic uncertainties, both experimental and theoretical, can be implemented inside the MC samples, as variation of some of the quantities present in the samples, such as p_{T} of some particle or the cross section. Another option is to compare different MC samples produced in a different way. In both cases these variations are then propagated through the whole analysis stream, giving different yields

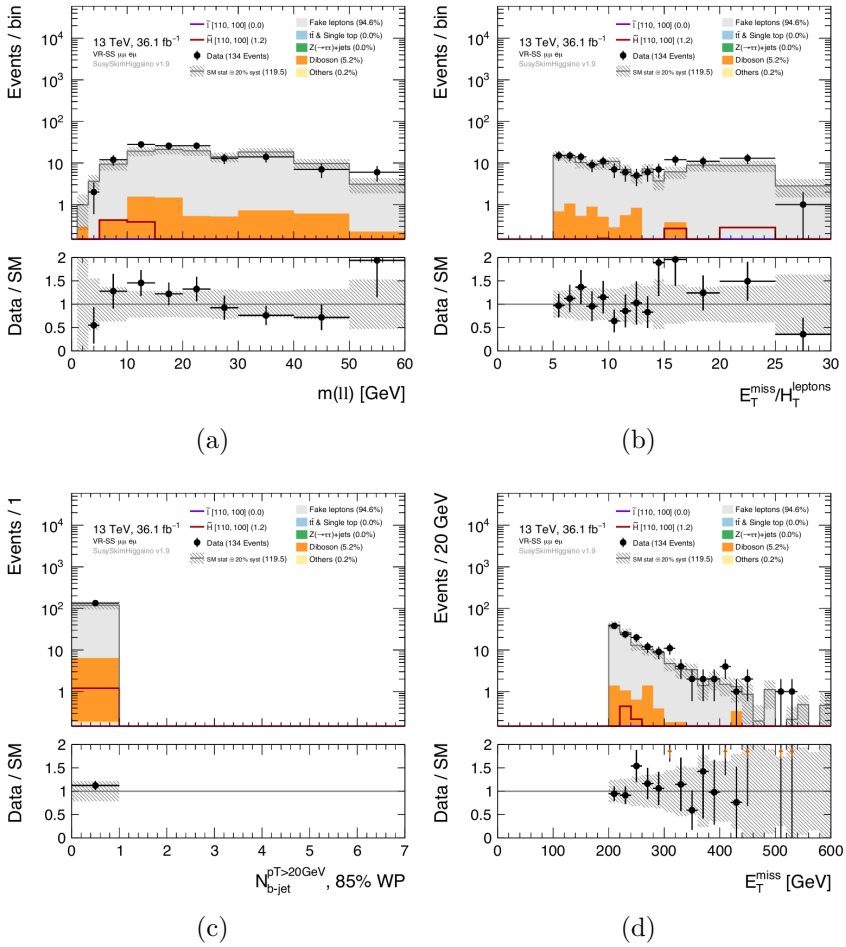

Figure 115: VR-SS plots for all flavor channel, pre-fit.

in CRs, VRs, and SRs. The impact of these variations is then estimated as the difference in yields between the nominal sample and the one with the variation:

$$\text{Uncertainty}[\%] = \frac{N_{\text{nominal}} - N_{\text{variation}}}{N_{\text{nominal}}} \tag{136}$$

where $N_{\text{nominal/variation}}$ is the number of events inside a given region for the nominal/variation sample. When constraining a sample in a CR, the yields in the systematic variations are also normalized, and then the previous formula is changed to:

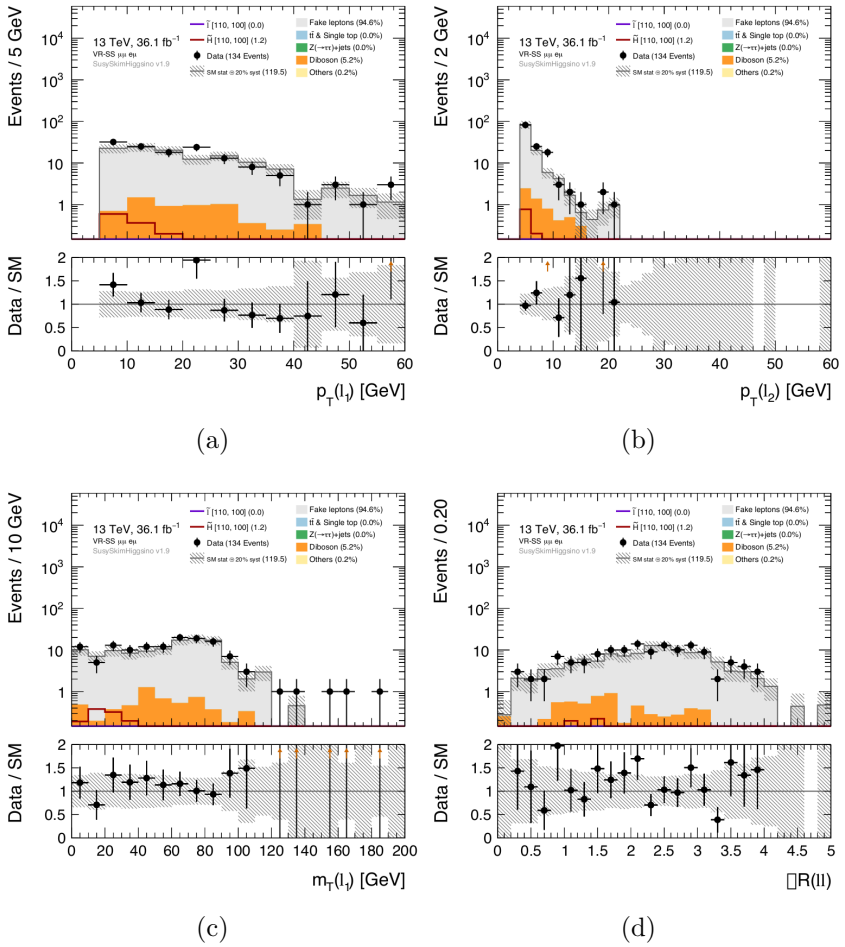

Figure 116: VR-VV plots for all flavor channel, pre-fit.

$$\text{Uncertainty}[\%] = \left(\frac{N_{\text{nominal}}}{N^{CR}_{\text{nominal}}} - \frac{N_{\text{variation}}}{N^{CR}_{\text{variation}}}\right) \cdot \left(\frac{N_{\text{nominal}}}{N^{CR}_{\text{nominal}}}\right)^{-1} \tag{137}$$

These variations are used as input for the systematic uncertainties in the likelihood fit.
The different source of systematic uncertainties are now described.

8.4.1 Experimental Uncertainties

The uncertainty used in the analysis depends on the objects used.

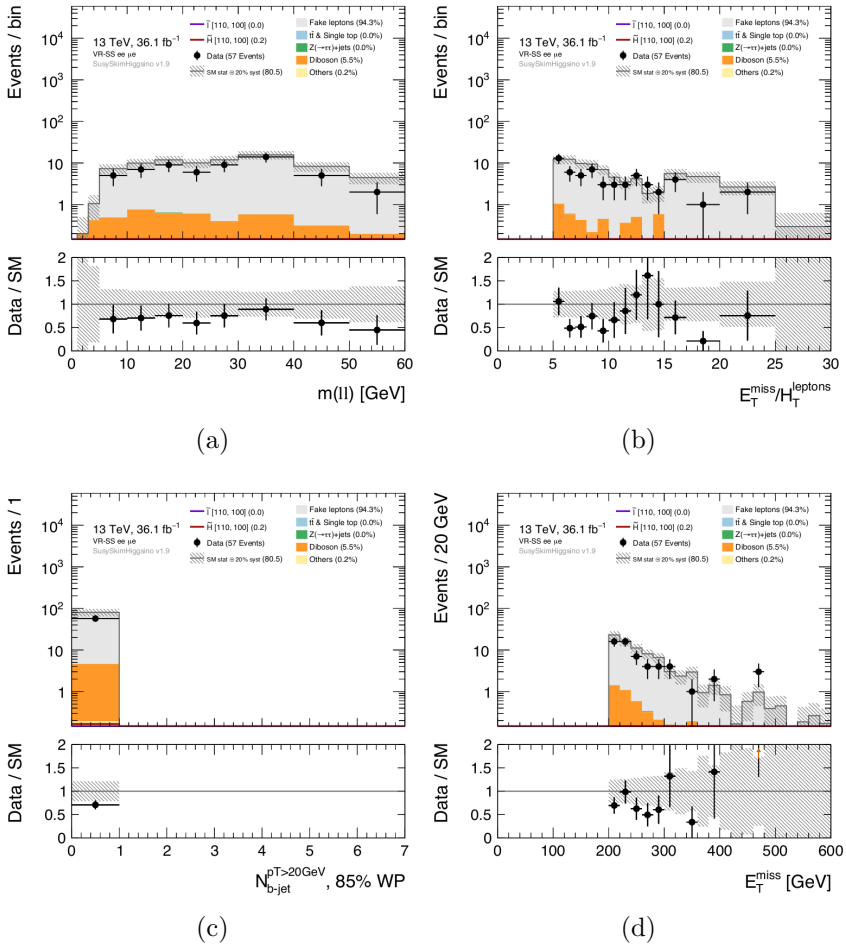

Figure 117: VR-SS plots for all flavor channel, pre-fit.

- Pileup reweighting: MC samples are produced before the data taking they want to describe, for this reason the actual profile of $\langle\mu\rangle$ is not the one in the samples, but with the best guess at the time of production. Therefore it must be reweighted in the simulation to match the one in data. There are uncertainties in the total pp cross section that are reflected as an uncertainty on the conversion between luminosity and $\langle\mu\rangle$. In order to account for this, the $\langle\mu\rangle$ value in data is scaled by 1./1.16, based on studies of data/MC agreement of the number of primary vertices against $\langle\mu\rangle$. An uncertainty is assigned by changing the nominal

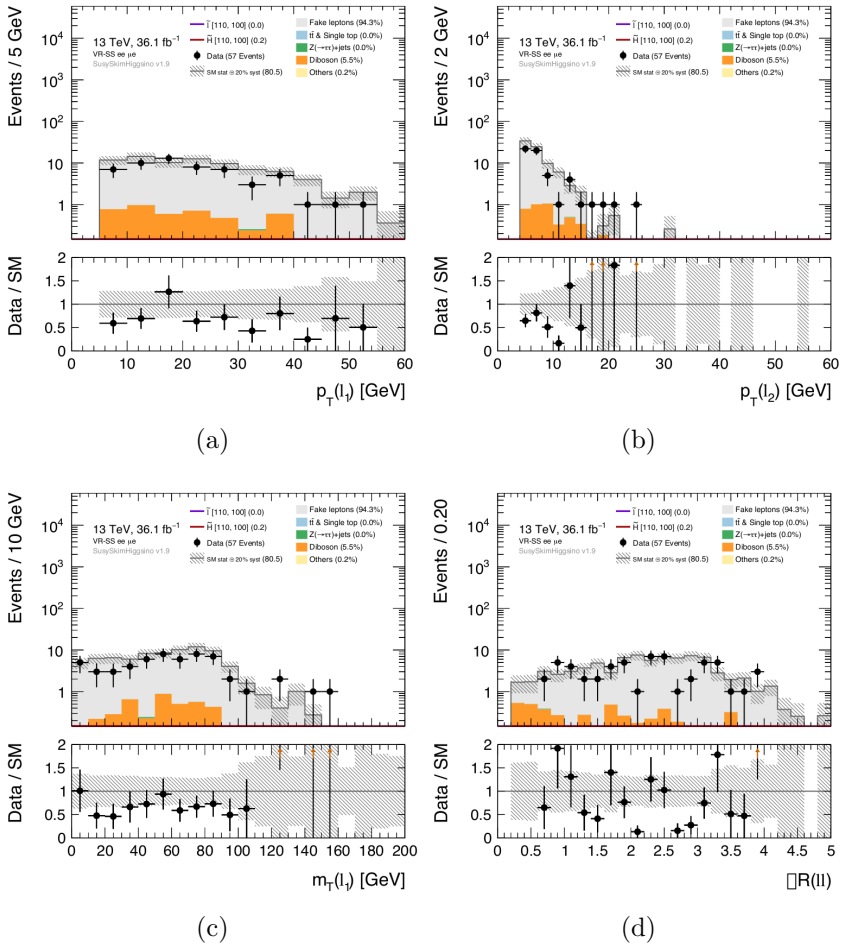

Figure 118: VR-VV plots for all flavor channel, pre-fit.

scaling with a factor (at denominator) 1.00 and 1.23.

- Jets: Uncertainty on the jet accounts for jet energy scale (JES) and resolution (JER). For the JES a reduced set of uncertainty is used, with five NP, for each an up and down variation of 1 σ is performed. For the JER it is used just one up variation. An additional uncertainty is put to take into account the difference between data and MC of the efficiency of the JVT cut. In the same way it is also applied a systematic uncertainty due to the b-tagging algorithm.

- Electrons: Energy scale and resolution uncertainty are considered, with variation up and down of $\pm 1\sigma$. Uncertainty on the identification, reconstruction, and isolation efficiency are also considered, with variations of the Scale Factors of $\pm 1\sigma$.

- Muons: Uncertainty on the muon momentum resolution is considered. This is obtained with a variation of the smearing of the ID and MS track of $\pm 1\sigma$. Energy scale variation of the muon momentum is also considered. Also uncertainty on the identification, reconstruction, and isolation efficiency are considered, as for electrons, with a variation of the Scale Factors.

- Missing Transverse Energy: Uncertainty concerning the $E_{\mathrm{T}}^{\mathrm{miss}}$ arises from propagating the uncertainty on the transverse momentum of the physics objects entering the definition of $E_{\mathrm{T}}^{\mathrm{miss}}$. Additional systematic effects are considered that accounts for the soft term resolution and the scale. These are obtained from variation of $\pm 1\sigma$ of the $E_{\mathrm{T}}^{\mathrm{miss}}$ energy resolution and scale, derived from data/MC comparison.

The impact of the systematic uncertainties on the background is reported in table, 31, 32, and 33 for SR-eMLL (ee and $\mu\mu$) and SR-iMLL. The dominant experimental systematic uncertainty comes from the jet energy scale and resolution (JES and JER).

8.4.2 Fake Factor Uncertainties

The Fake Factor Method is used to estimate the FNP background. This method has different sources of systematic errors, that in the end, enter the estimate of the background.

- Statistical Uncertainty: this uncertainty comes from the limited statistic in the data samples triggered with prescaled single leptons.

- Prompt subtraction: The subtraction of prompt MC in the region for the measurement of the Fake Factor is varied up and down of $\pm 10\%$. This effect is however negligible.

Uncertainty	[1, 3] GeV	[3.2, 5] GeV	[5, 10] GeV	[10, 20] GeV	[20, 30] GeV	[30, 40] GeV	[40, 60] GeV
Total background expectation	0.14	0.25	3.05	7.67	3.99	1.76	1.31
Total statistical ($\sqrt{N_{\text{exp}}}$)	±0.38	±0.50	±1.75	±2.77	±2.00	±1.33	±1.14
Total background systematic [abs]	±0.28	±0.35	±1.56	±1.92	±1.15	±0.57	±0.65
Total background systematic [%]	[197.91%]	[142.22%]	[51.24%]	[25.01%]	[28.93%]	[32.35%]	[49.48%]
Statistical	±0.24	±0.25	±0.30	±0.61	±0.32	±0.29	±0.45
Fake factor	±0.15	±0.10	±1.18	±1.73	±1.02	±0.42	±0.10
Experimental	±0.02	±0.23	±0.28	±0.42	±0.31	±0.18	±0.43
Theory	±0.00	±0.06	±0.93	±0.28	±0.19	±0.11	±0.13
Normalisation	±0.00	±0.00	±0.09	±0.30	±0.07	±0.07	±0.05

Table 31: Breakdown of the dominant systematic uncertainties on background estimates in the various signal regions. Note that the individual uncertainties can be correlated, and do not necessarily add up quadratically to the total background uncertainty. The percentages show the size of the uncertainty relative to the total expected background. Each systematic uncertainty has its colour gradated by its relative contribution to the total background systematic, and only those with magnitude ≥ 1 percent are displayed to reduce clutter.

Uncertainty	[1, 3] GeV	[3.2, 5] GeV	[5, 10] GeV	[10, 20] GeV	[20, 30] GeV	[30, 40] GeV	[40, 60] GeV
Total background expectation	1.61	1.29	3.70	13.01	5.07	1.22	1.59
Total statistical ($\sqrt{N_{\text{exp}}}$)	±1.27	±1.14	±1.92	±3.61	±2.25	±1.11	±1.26
Total background systematic [abs]	±0.84	±0.66	±1.55	±2.88	±1.22	±0.65	±0.40
Total background systematic [%]	[51.97%]	[51.53%]	[41.78%]	[22.11%]	[24.13%]	[53.48%]	[25.15%]
Statistical	±0.55	±0.34	±0.28	±0.83	±0.50	±0.47	±0.27
Fake factor	±0.51	±0.54	±1.28	±2.65	±1.00	±0.16	±0.18
Experimental	±0.35	±0.07	±0.79	±0.36	±0.31	±0.41	±0.15
Theory	±0.10	±0.16	±0.21	±0.23	±0.27	±0.12	±0.16
Normalisation	±0.07	±0.03	±0.02	±0.46	±0.16	±0.03	±0.04

Table 32: Breakdown of the dominant systematic uncertainties on background estimates in the various signal regions. Note that the individual uncertainties can be correlated, and do not necessarily add up quadratically to the total background uncertainty. The percentages show the size of the uncertainty relative to the total expected background. Each systematic uncertainty has its colour gradated by its relative contribution to the total background systematic, and only those with magnitude ≥ 1 percent are displayed to reduce clutter.

Uncertainty	[1, 3] GeV	[1, 5] GeV	[1, 10] GeV	[1, 20] GeV	[1, 30] GeV	[1, 40] GeV	[1, 60] GeV
Total background expectation	1.74	3.14	8.86	28.77	37.84	40.55	43.38
Total statistical ($\sqrt{N_{\text{exp}}}$)	±1.32	±1.77	±2.98	±5.36	±6.15	±6.37	±6.59
Total background systematic [abs]	±0.88	±1.23	±2.49	±5.73	±6.49	±6.63	±6.75
Total background systematic [%]	[50.48%]	[39.10%]	[28.11%]	[19.91%]	[17.16%]	[16.35%]	[15.57%]
Fake factor	±0.57	±0.85	±1.92	±4.19	±4.92	±4.92	±4.94
Statistical	±0.55	±0.64	±0.63	±3.04	±3.10	±3.15	±3.18
Experimental	±0.35	±0.41	±1.27	±2.01	±2.07	±2.17	±2.14
Theory	±0.10	±0.42	±0.67	±1.09	±1.54	±1.74	±2.01
Normalisation	±0.07	±0.10	±0.03	±0.62	±0.85	±0.92	±0.97

Table 33: Breakdown of the dominant systematic uncertainties on background estimates in the various signal regions. Note that the individual uncertainties can be correlated, and do not necessarily add up quadratically to the total background uncertainty. The percentages show the size of the uncertainty relative to the total expected background. Each systematic uncertainty has its colour gradated by its relative contribution to the total background systematic, and only those with magnitude ≥ 1 percent are displayed to reduce clutter.

- Kinematic dependencies: Fake Factors are estimated as a function of p_{T} and the number of b-jets, but there might be other dependency. Different parametrizations are considered with different variables, and the largest deviation from the average muon/electron Fake Factor it is assigned as an uncertainty.

- Non Closure in VR-SS: The difference between data and prediction inside the VR-SS (with the $E_{\text{T}}^{\text{miss}}/H_{\text{T}}^{\text{leptons}}$ removed, to have more statistic) is taken as an uncertainty.

8.4.3 Theoretical Uncertainties

Theoretical uncertainties cover the uncertainties at the generation level of the processes considered. The following uncertainties are considered in the analysis for the VV, $Z \to \tau\tau$ and $t\bar{t}$ backgrounds:

- Factorization and renormalization of the QCD scales: many cross section results depend on the choice of the factorization and renormalization scales, and these can be varied up and down independently. A 7-point scale variation is applied of the renormalization (μ_r) and factorization (μ_f) scale, where the variations are scaled by either a factor 0.5, 1, or 3, leading to the following

setups: $\mu_r, \mu_f \times 0.5, 0.5, 1.0, 0.5, 0.5, 1.0, 1.0, 1.0, 1.0, 2.0, 2.0, 1.0, 1.0, 1.0$. Sometimes is used instead just a 3-point variation, where the two scales are varied together, and therefore having as setups: $\mu_r, \mu_f \times 0.5, 0.5, 1.0, 1.0, 1.0, 1.0$. This in general leads to larger uncertainty. Generally the scale variations will result in a variation of the cross-section and a variation of the differential shape of an observable. The envelope of all this change is taken as an error.

- Choice of α_S: The value of α_S, the strong coupling constant, is varied within its uncertainty and the impact on the acceptance is taken as an uncertainty. This variation is done only on VV and $Z \to \tau\tau$ backgrounds, since it is only available for the Sherpa software. $t\bar{t}$ and VV samples are also compared with MC generated with different software. No $Z \to \tau\tau$ alternative sample with enough statistic was instead available and was then omitted. In any case these variations were compatible with the statistical uncertainties and therefore no additional systematic uncertainty is added.

- Choice of PDF: An additional uncertainty is added in order to take into account the different options for the choice of the parton density function. This is done by symmetrizing the variations with respect to MMHT2014, CT14, and NNPDF PDF sets.

- Choice of specific software: There are many programs that enters the chain of production of the MC prediction of the SM backgrounds. The results obtained with different softwares are compared, and a systematic uncertainty is assigned to cover the differences.

In addition to these uncertainties there are also other specific for the signal samples.

- ISR modeling: An uncertainty on the modeling of the Initial State Radiation jet in the next-to-leading order process is added. This is evaluated by varying a number of generator parameters in MadGraph, and comparing the new samples with the nominal one.

- Choice of PDF: uncertainties are also considered by comparing results with different PDFs according to PDF4LHC15

- Pythia tuning: Different tunes of the parameter in Pythia and the Merging Scale are considered.

- Difference between Fast and Full simulations: The MC for the signal samples use fast simulation for the description of the detector (AFII), so a comparison with the Full simulation is done, and the difference assigned as a systematic uncertainty.

All the variations are evaluated against the nominal sample, and the resulting uncertainties on the signal acceptance are around 20 % for most of the grid points, and a flat 20% is then used in the fit.

8.4.4 Other Uncertainties

Additional sources of systematic uncertainty may affect the results. In particular some of the most important are:

- Monte Carlo statistics: Since the number of generated events in the MC are finite, the statistic might affect the final results. In fact, more MC events are generated than what would be expected from just $\sigma \times \mathcal{L}$, with $\mathcal{L}$ the target luminosity, but in very tight kinematic regions, statistic is still an issue.

- Control Region Statistic: CR are built in order to be close to the SR, but still have a good purity of the targeted background. However this might mean having a CR with reduced statistic, in this case, the normalization factor is affected by the statistical error of the CR. This uncertainty is then propagated to the SR.

Figure 119 shows the percentage of each uncertainty in the different exclusive SRs.
In the exclusive signal regions, uncertainties varies from over 50% to down to 20% depending on the bin. The most important systematic uncertainty comes from the modeling of the Fake Factor, or either the statistic in the very first and last bin in $m_{\ell\ell}$, where there are very few events present. Experimental systematic uncertainties are an important source of error, especially in the last $m_{\ell\ell}$ bin, where they are even more important than the Fake Factor. Theoretical uncertainties instead are always below 10% except in the $m_{\ell\ell}\,[5, 10]$ GeV bin. Errors from the normalization factor instead are below the 5% and not relevant.

In inclusive signal region, the uncertainties decrees down to 15%, mainly due to the reduction of the statistic uncertainty in the last bins.

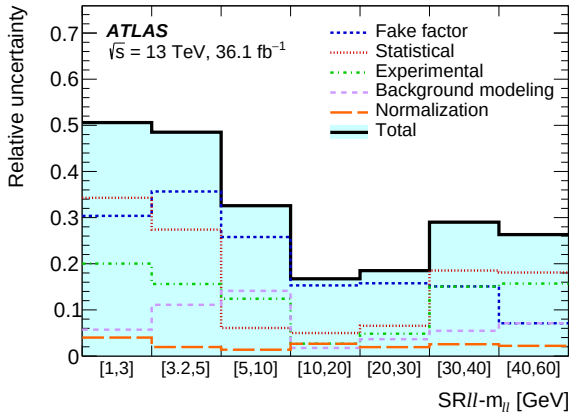

Figure 119: Breakdown of the systematic uncertainties in the exclusive SRs.

8.5 Results

The results obtained in the analysis are reported in this section. Two different normalization factors are obtained for top contributions and $Z \to \tau\tau$: μ_{top} and $\mu_{Z_{tt}}$ respectively. A likelihood is constructed as the product of Poisson distribution with mean values the nominal MC yields in each of the control regions. The values and uncertainties of μ_{top} and $\mu_{Z_{tt}}$ are obtained with the software HistFitter [176] by maximizing the likelihood. The normalization factors are then used to extrapolate the MC in the validation regions, where the modeling is checked against data, and then in the signal regions. Systematic uncertainties are treated as nuisance parameters.

8.5.1 Background only fit

The background only fit assumes that there is no signal. Two different configurations are used:

Control region	Normalisation factor	CR-only bkg-fit fitted value
CR-tau	μ_{Ztt}	0.77 ± 0.14
CR-top	μ_{top}	0.97 ± 0.09

Table 34: Background only CR-only fit normalisation factors.

CRs Only In this fit only the data in the CR are used as constraints in the likelihood, in order to have an SR-independent estimate of the background yields in all regions. Table 34 shows the normalization factors obtained from the background only fit. For the $Z \to \tau\tau$ background is obtained $\mu_{Ztt} = 0.77 \pm 0.14$, while for the top contribution is $\mu_{\text{top}} = 0.97 \pm 0.09$. For the top, the normalization factor is close to 1 within the uncertainty, while for the $Z \to \tau\tau$ it is smaller than one, but within 2σ. No large mismodeling is observed in CR and VR. Table 35 shows the results of the background only fit in the CR and VRs, with values before and after the fit and the observed data, while table 37 and 36 show the same results but inside the SR and VR respectively. Figure 120 shows the $m_{\ell\ell}$ and $E_{\text{T}}^{\text{miss}}/H_{\text{T}}^{\text{leptons}}$ distribution inside the inclusive signal region iMLLg. Figure 121 shows the yields in the SR-eMLL, and in the bottom panel the discrepancy between expected and observed yields. No statistical significant excess is observed, with every SR below a significance of 2 σ except one, whose significance is just above 2 σ.

CRs+SRee-eMLL+SRmm-eMLL In this kind of fit, data in CRs and in all the SR (fourteen) are fitted simultaneously to constrain the background. This fit it is useful to check how well the background fit behave under the assumption of a zero signal hypothesis. Figure 122 shows the results of this kind of fit in the SRs. Again, no significant excess if found, and the previous bin with a small excess is now within 2σ. Results are in general in agreement with the other setup of the fit, meaning that the modeling of the background is good.

8.5.2 Model independent upper limits on new physics

The *model independent limits* at 95 % CL are presented in this section. This are the upper limits on the visible cross section of new

Common	CR-top	CR-tau	VR-VV	VR-SS $ee + \mu e$	VR-SS $\mu\mu + e\mu$
Observed events	1042	75	274	57	134
Fitted SM events	1042 ± 32	75 ± 9	257 ± 28	81 ± 29	119 ± 27
FNP	250 ± 60	9 ± 4	63 ± 15	76 ± 29	113 ± 27
Diboson	24.7 ± 3.3	5.0 ± 1.0	99 ± 17	4.4 ± 1.0	6.2 ± 1.0
$Z(\to \tau\tau)$+jets	2.8 ± 1.8	57 ± 10	23 ± 6	$0.012^{+0.013}_{-0.012}$	$0.01^{+0.23}_{-0.01}$
$t\bar{t}$, Single top	750 ± 70	2.3 ± 0.8	58 ± 13	$0.01^{+0.09}_{-0.01}$	$0.01^{+0.09}_{-0.01}$
Others	14 ± 7	1.6 ± 0.9	14 ± 7	0.19 ± 0.12	$0.19^{+0.28}_{-0.19}$
Pre-fit SM events	1070 ± 60	92 ± 7	266 ± 28	81 ± 29	119 ± 27
FNP	250 ± 60	9 ± 4	63 ± 15	76 ± 29	113 ± 27
Diboson	24.7 ± 3.3	5.0 ± 1.1	99 ± 17	4.4 ± 1.0	6.2 ± 1.0
$Z(\to \tau\tau)$+jets	3.8 ± 2.1	74 ± 5	30 ± 5	$0.016^{+0.016}_{-0.016}$	$0.01^{+0.30}_{-0.01}$
$t\bar{t}$, Single top	771 ± 10	2.4 ± 0.8	59 ± 13	$0.01^{+0.10}_{-0.01}$	$0.01^{+0.10}_{-0.01}$
Others	14 ± 7	1.6 ± 0.9	14 ± 7	0.19 ± 0.12	$0.19^{+0.29}_{-0.19}$

Table 35: Fit results for an integrated luminosity of 36.1 fb^{-1}. The results are obtained from the control regions using the background only fit (CR-only bkg fit). Nominal MC expectations (normalised to MC cross-sections) are given for comparison. The errors shown are the statistical plus systematic uncertainties. Uncertainties on the fitted yields are symmetric by construction, where the negative error is truncated when reaching to zero event yield. The category 'FNP' contains fake and non-prompt leptons. The category 'Others' contains rare backgrounds from triboson, Higgs boson, and the remaining top-quark production processes listed in Table 21. Uncertainties in the fitted background estimates combine statistical and systematic uncertainties.

VRDF-eMLL	[1, 3] GeV	[3.2, 5] GeV	[5, 10] GeV	[10, 20] GeV	[20, 30] GeV	[30, 40] GeV	[40, 60] GeV
Observed events	2	0	6	18	7	4	5
Fitted SM events	1.0 ± 0.8	2.3 ± 1.4	8 ± 4	22 ± 4	12.7 ± 2.6	4.6 ± 1.0	2.7 ± 0.8
FNP	1.0 ± 0.8	0.9 ± 0.8	4.9 ± 1.9	13 ± 4	6.8 ± 2.4	$0.6^{+0.7}_{-0.6}$	$0.01^{+0.13}_{-0.01}$
Diboson	0.033 ± 0.014	$0.9^{+1.0}_{-0.9}$	1.1 ± 0.5	2.9 ± 0.7	2.7 ± 0.5	1.9 ± 0.5	1.29 ± 0.27
$Z(\rightarrow \tau\tau)$+jets	$0.013^{+0.014}_{-0.013}$	$0.4^{+0.5}_{-0.4}$	$1.5^{+3.0}_{-1.5}$	4.4 ± 1.6	1.3 ± 0.6	0.41 ± 0.23	0.021 ± 0.016
$t\bar{t}$, Single top	$0.01^{+0.09}_{-0.01}$	$0.04^{+0.05}_{-0.04}$	0.6 ± 0.4	1.0 ± 0.4	1.2 ± 0.5	1.3 ± 0.5	1.2 ± 0.8
Others	0.0 ± 0.0	$0.025^{+0.032}_{-0.025}$	0.16 ± 0.11	0.8 ± 0.5	0.7 ± 0.4	0.42 ± 0.30	0.20 ± 0.15
Pre-fit SM events	1.0 ± 0.8	2.4 ± 1.4	9 ± 4	23 ± 4	13.1 ± 2.7	4.8 ± 1.0	2.7 ± 0.9
FNP	1.0 ± 0.8	0.9 ± 0.8	4.9 ± 1.9	13 ± 4	6.9 ± 2.4	$0.6^{+0.7}_{-0.6}$	$0.01^{+0.13}_{-0.01}$
Diboson	0.033 ± 0.014	$0.9^{+1.0}_{-0.9}$	1.1 ± 0.5	2.9 ± 0.7	2.7 ± 0.5	1.9 ± 0.5	1.29 ± 0.27
$Z(\rightarrow \tau\tau)$+jets	$0.017^{+0.017}_{-0.017}$	$0.6^{+0.6}_{-0.6}$	2^{+4}_{-2}	5.7 ± 1.8	1.7 ± 0.8	0.53 ± 0.28	0.027 ± 0.020
$t\bar{t}$, Single top	$0.01^{+0.10}_{-0.01}$	$0.04^{+0.05}_{-0.04}$	0.7 ± 0.4	1.0 ± 0.5	1.2 ± 0.5	1.3 ± 0.5	1.2 ± 0.8
Others	0.0 ± 0.0	$0.025^{+0.032}_{-0.025}$	0.15 ± 0.11	0.8 ± 0.5	0.7 ± 0.4	0.42 ± 0.30	0.20 ± 0.15

Table 36: Fit results for an integrated luminosity of 36.1 fb^{-1}. The results are obtained from the control regions using the background only fit (CR-only bkg fit). Nominal MC expectations (normalised to MC cross-sections) are given for comparison. The errors shown are the statistical plus systematic uncertainties. Uncertainties on the fitted yields are symmetric by construction, where the negative error is truncated when reaching to zero event yield. The category 'FNP' contains fake and non-prompt leptons. The category 'Others' contains rare backgrounds from triboson, Higgs boson, and the remaining top-quark production processes listed in Table 21. Uncertainties in the fitted background estimates combine statistical and systematic uncertainties.

Table 37: Observed event yields and exclusion fit results with the signal strength parameter set to zero for the exclusive electroweakino regions. Background processes containing fewer than two prompt leptons are categorized as 'FNP'. The category 'Others' contains rare backgrounds from triboson, Higgs boson, and the remaining top-quark production processes listed in Table **??**. Uncertainties in the fitted background estimates combine statistical and systematic uncertainties.

SRee-$m_{\ell\ell}$	[1, 3] GeV	[3.2, 5] GeV	[5, 10] GeV	[10, 20] GeV	[20, 30] GeV	[30, 40] GeV	[40, 60] GeV
Observed events	0	1	1	10	4	6	2
Fitted SM events	$0.14^{+0.28}_{-0.14}$	$0.25^{+0.35}_{-0.25}$	3.1 ± 1.6	7.7 ± 1.9	4.0 ± 1.2	1.8 ± 0.6	1.3 ± 0.6
FNP	$0.09^{+0.15}_{-0.09}$	$0.01^{+0.10}_{-0.01}$	1.9 ± 1.2	3.7 ± 1.7	1.6 ± 1.0	$0.3^{+0.4}_{-0.3}$	$0.01^{+0.10}_{-0.01}$
Diboson	$0.03^{+0.04}_{-0.03}$	$0.21^{+0.25}_{-0.21}$	0.46 ± 0.27	1.8 ± 0.5	1.29 ± 0.30	0.60 ± 0.19	0.73 ± 0.29
$Z(\to \tau\tau)$+jets	$0.01^{+0.21}_{-0.01}$	$0.01^{+0.21}_{-0.01}$	$0.5^{+1.0}_{-0.5}$	1.6 ± 0.6	0.29 ± 0.25	0.24 ± 0.18	$0.01^{+0.21}_{-0.01}$
$t\bar{t}$, single top	$0.01^{+0.10}_{-0.01}$	$0.01^{+0.10}_{-0.01}$	$0.11^{+0.14}_{-0.11}$	0.33 ± 0.21	0.57 ± 0.32	0.52 ± 0.28	0.6 ± 0.5
Others	$0.001^{+0.007}_{-0.001}$	0.012 ± 0.011	0.11 ± 0.10	0.27 ± 0.17	0.21 ± 0.12	$0.05^{+0.05}_{-0.05}$	$0.003^{+0.004}_{-0.003}$
SR$\mu\mu$-$m_{\ell\ell}$	[1, 3] GeV	[3.2, 5] GeV	[5, 10] GeV	[10, 20] GeV	[20, 30] GeV	[30, 40] GeV	[40, 60] GeV
Observed events	1	2	7	12	2	2	2
Fitted SM events	1.6 ± 0.8	1.3 ± 0.7	3.7 ± 1.5	13.0 ± 2.9	5.1 ± 1.2	1.2 ± 0.7	1.6 ± 0.4
FNP	$0.3^{+0.5}_{-0.3}$	$0.4^{+0.5}_{-0.4}$	2.4 ± 1.3	7.4 ± 2.7	1.3 ± 1.0	$0.01^{+0.16}_{-0.01}$	$0.13^{+0.18}_{-0.13}$
Diboson	0.9 ± 0.5	0.58 ± 0.34	1.0 ± 0.5	1.3 ± 0.5	1.8 ± 0.4	0.8 ± 0.6	0.94 ± 0.28
$Z(\to \tau\tau)$+jets	$0.4^{+0.4}_{-0.4}$	0.16 ± 0.12	$0.0^{+0.4}_{-0.0}$	2.4 ± 0.8	0.8 ± 0.4	$0.003^{+0.023}_{-0.003}$	$0.06^{+0.06}_{-0.06}$
$t\bar{t}$, single top	$0.01^{+0.10}_{-0.01}$	$0.01^{+0.10}_{-0.01}$	0.19 ± 0.11	1.2 ± 0.5	0.7 ± 0.4	0.37 ± 0.21	0.43 ± 0.27
Others	0.048 ± 0.030	$0.10^{+0.10}_{-0.10}$	0.11 ± 0.10	0.7 ± 0.5	0.38 ± 0.22	0.09 ± 0.07	0.024 ± 0.023

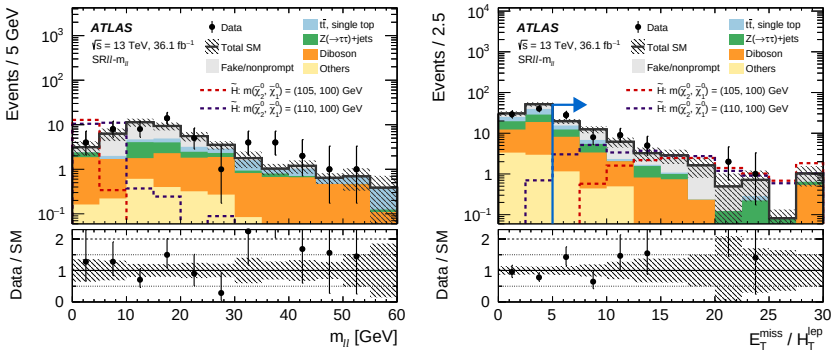

(a) (b)

Figure 120: $m_{\ell\ell}$ (a) and $E_{\mathrm{T}}^{\mathrm{miss}}/H_{\mathrm{T}}^{\mathrm{leptons}}$ (b) distribution inside SR-iMLLg, post-fit. The blue arrow shows the minimum of the cut on $E_{\mathrm{T}}^{\mathrm{miss}}/H_{\mathrm{T}}^{\mathrm{leptons}}$.

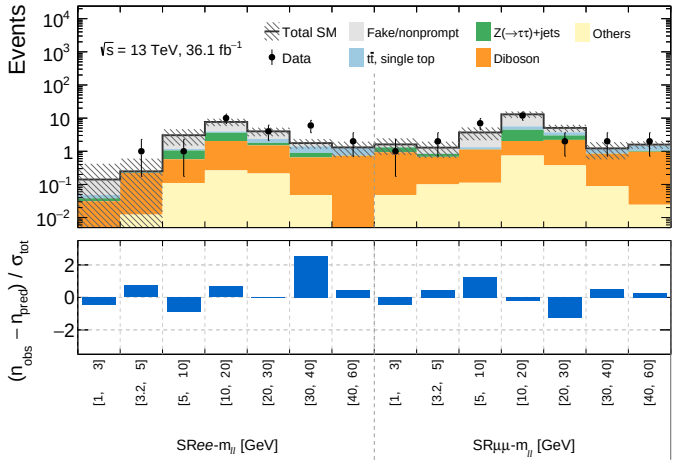

Figure 121: Comparison of observed and expected event yields after the exclusion fit with the signal strength parameter set to zero in the exclusive signal regions. Uncertainties in the background estimates include both the statistical and systematic uncertainties, where σ_{tot} denotes the total uncertainty.

physics ($\langle\epsilon\sigma\rangle_{\mathrm{obs}}^{95}$), assuming same detector efficiency, acceptance and final state. This procedure is called a *discovery fit*. The model dependent fit instead will be presented in the next section. Table 38

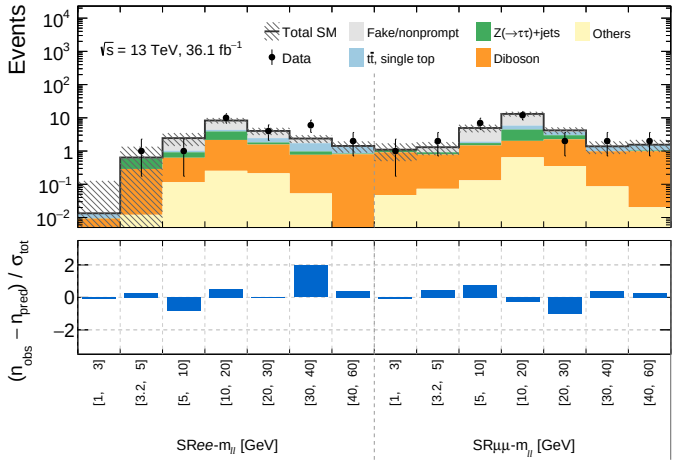

Figure 122: Comparison of observed and expected event yields after the exclusion fit in both the CR and SR with the signal strength parameter set to zero in the exclusive signal regions. Uncertainties in the background estimates include both the statistical and systematic uncertainties, where σ_{tot} denotes the total uncertainty.

shows the results based on the full discovery fit. Electrons and muons are summed together. In table are also presented the $p-$values and are all compatible with the background only hypothesis.

8.6 Interpretation

No statistically relevant excess has been observed, therefore limits have been set on the mass of the supersymmetric particles. Results are interpreted in the context of simplified models. Two different scenarios are considered: the first one is the higgsino LSP, while the second is based on wino production with bino LSP. The differences between this two models has been presented already in 2.4.3. Exclusion fits are performed with hypothesis testing done with the software HistFitter in order to define the confidence of the exclusion using the CLs.

8.6.1 Higgsino

Figure 123 shows the limits at 95 % CL in the higgsino assumption. The limits are projected in a plane with the mass of $\tilde{\chi}_2^0$ on the x axis and the difference in mass between the $\tilde{\chi}_2^0$ and $\tilde{\chi}_1^0$ ($\Delta m(\tilde{\chi}_2^0, \tilde{\chi}_1^0)$) on the

Signal Region	$m_{\ell\ell}$ [GeV]	$\langle\epsilon\sigma\rangle^{95}_{\text{obs}}$ [fb]	S^{95}_{obs}	S^{95}_{exp}	CL_B	$p(s=0)$
SRSF-iMLLa	< 3	0.13	4.8	$4.8^{+2.4}_{-1.4}$	0.51	*nan*
SRSF-iMLLb	< 5	0.20	7.3	$6.3^{+2.9}_{-1.8}$	0.70	0.26
SRSF-iMLLc	< 10	0.35	12.7	$9.8^{+4.0}_{-2.9}$	0.77	0.21
SRSF-iMLLd	< 20	0.56	20.3	$18.8^{+7.8}_{-3.3}$	0.65	0.34
SRSF-iMLLe	< 30	0.60	21.5	$20.5^{+7.4}_{-5.7}$	0.57	0.43
SRSF-iMLLf	< 40	0.71	25.5	$21.9^{+7.9}_{-6.3}$	0.73	0.26
SRSF-iMLLg	< 60	0.80	28.8	$22.7^{+8.2}_{-6.6}$	0.78	0.20

Table 38: Left to right: 95% CL upper limits on the visible cross section ($\langle\epsilon\sigma\rangle^{95}_{\text{obs}}$) and on the number of signal events (S^{95}_{obs}). The third column (S^{95}_{exp}) shows the 95% CL upper limit on the number of signal events, given the expected number (and $\pm1\sigma$ deviations from the expectation) of background events. The last two columns indicate the CL_B value, i.e. the confidence level observed for the background-only hypothesis, and the discovery p-value ($p(s=0)$).

y axis. Here the mass of the $\tilde{\chi}^{\pm}_1$ is assumed in between $\tilde{\chi}^0_2$ and $\tilde{\chi}^0_1$. Blue dashed lined and the solid red line represent the expected and observed contour respectively. The line is obtained by interpolating the results for each simulated point produced. The yellow band represent a $\pm1\sigma$ band from experimental systematic uncertainties, while the dashed red lines represent the theory uncertainty on the cross section of signal samples. The grey area instead are the limits set by the LEP experiment.
$\tilde{\chi}^0_2$ masses were excluded up to 145 GeV for a $\Delta m(\tilde{\chi}^0_2, \tilde{\chi}^0_1)$ in the range of $\sim 5 - 10$ GeV. Signal were also excluded down to $\Delta m(\tilde{\chi}^0_2, \tilde{\chi}^0_1) \sim 2.5$ GeV for masses of $\tilde{\chi}^0_2$ of ~ 100 GeV. This results are important since the analysis was able to set the first limits in this interpretation since the LEP experiment.
Figure 124 shows the results compared also with the disappearing track analysis [203], represented by the orange band in the bottom. It is also worth noticing that in the $y-$axis it is shown the difference in mass between the $\tilde{\chi}^{\pm}_1$ and the $\tilde{\chi}^0_1$, while before it was between the $\tilde{\chi}^0_2$ and the $\tilde{\chi}^0_1$.

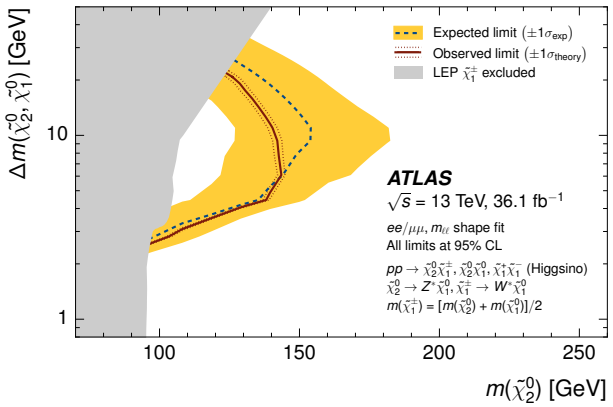

Figure 123: Expected 95% CL exclusion sensitivity (blue dashed line) with $\pm1\sigma$ (yellow band) from experimental systematic uncertainties and observed limits (red solid line) with $\pm1\sigma$ (dotted red line) from signal cross-section uncertainties for simplified models of direct Higgsino. The chargino $\tilde{\chi}_1^{\pm}$ mass is assumed to be halfway between the two lightest neutralino masses. The gray regions denote the lower chargino mass limit from LEP.

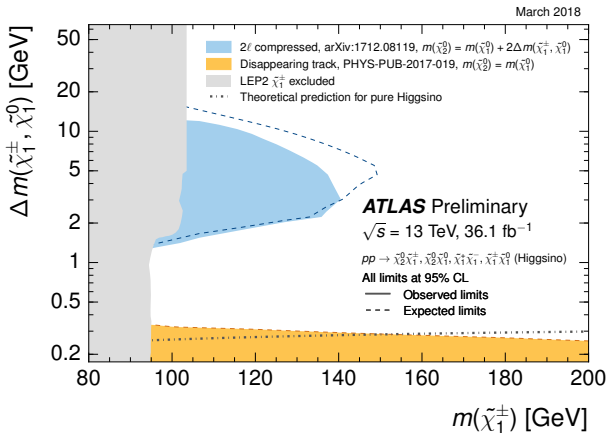

Figure 124: Exclusion limits at 95% CL for higgsino pair production $\tilde{\chi}_1^+\,\tilde{\chi}_1^-$, $\tilde{\chi}_1^{\pm}\,\tilde{\chi}_2^0$, $\tilde{\chi}_1^{\pm}\,\tilde{\chi}_1^0$, and $\tilde{\chi}_2^0\,\tilde{\chi}_1^0$ with off-shell W/Z mediated decay to the $\tilde{\chi}_1^0$, as a function of $\tilde{\chi}_1^{\pm}$ mass and it mass difference with $\tilde{\chi}_1^0$. The results for the disappearing track analysis is also shown in orange.

8.6.2 Wino-Bino

Figure 125 shows the limits at 95 % CL in the wino-bino assumption. The limits are projected in a plane with the mass of $\tilde{\chi}_2^0$ on the x axis and the difference in mass between the $\tilde{\chi}_2^0$ and $\tilde{\chi}_1^0$ ($\Delta m(\tilde{\chi}_2^0, \tilde{\chi}_1^0)$) on the y axis. Here the mass of the $\tilde{\chi}_1^\pm$ is assumed to be degenerate with the mass of the $\tilde{\chi}_2^0$, $m(\tilde{\chi}_1^\pm) = m(\tilde{\chi}_2^0)$. The color code is the same as in the higgsino interpretation. The light blue area instead shows the results of the $2\ell + 3\ell$ analysis combination from Run 1.
Due to the higher cross section, limits were set on the $\tilde{\chi}_2^0$ masses up to 175 GeVfor a $\Delta m(\tilde{\chi}_2^0, \tilde{\chi}_1^0)$ in the range of $sim5 - 10$ GeV, much higher than the higgsino. Signal were also excluded down to $\Delta m(\tilde{\chi}_2^0, \tilde{\chi}_1^0) \sim 2.$ GeV for masses of $\tilde{\chi}_2^0$ of ~ 100 GeV. The assumption on this model are also similar to the ones from CMS.
It is worth noticing hat figure 125 is not just the same plot of figure 123 but with an increased signal cross section in the assumption. The different positions of the $\tilde{\chi}_1^\pm$ with respect to the two neutralinos creates a difference in acceptance, and therefore is not possible to just scale the cross section up. Moreover the shape of the $m_{\ell\ell}$ in the two assumption is different. For all of these reasons this interpretation is done with different signal samples than the higgsino hypothesis.

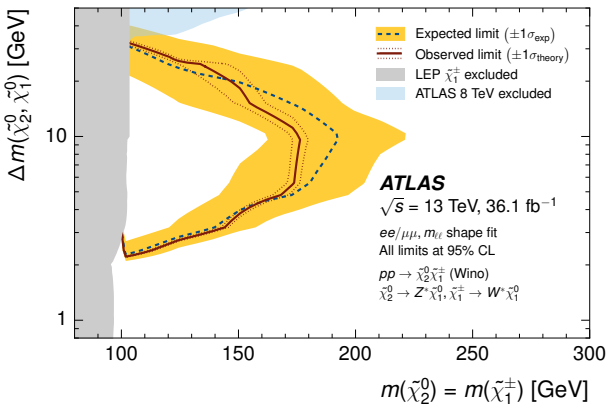

Figure 125: Expected 95% CL exclusion sensitivity (blue dashed line) with $\pm1\sigma$ (yellow band) from experimental systematic uncertainties and observed limits (red solid line) with $\pm1\sigma$ (dotted red line) from signal cross-section uncertainties for simplified models of direct wino production. The chargino $\tilde{\chi}_1^{\pm}$ mass is assumed to be the same as the $\tilde{\chi}_2^0$. The gray regions denote the lower chargino mass limit from LEP. The blue region in the lower plot indicates the limit from the $2\ell + 3\ell$ combination of ATLAS Run 1.

9 Higgsino 1 Lepton 1 Track Analysis

9.1 Full Run 2 Analysis Overview

The analysis done with the partial dataset of 2015 and 2016, with a final state with 2 leptons has been presented in chapter 8. No significant excess was found, and so only limits were set on the mass of the superymmetric particles. There were several limitations to the reach of the search. First of all, the low cross section meant that available luminosity would suffice to exclude only up to around 150 GeV. An increase in Luminosity therefore is already an improvement in the reach, but if combined with a better re-optimization of the cuts it is possible to reach even higher $\tilde{\chi}_1^0$ masses. Additionally, the high $E_{\mathrm{T}}^{\mathrm{miss}}$ cut due to the trigger request reduces the signal acceptance. Being able to recover part of the signal at low $E_{\mathrm{T}}^{\mathrm{miss}}$ would then improve the limits, especially at medium-to-high mass splitting ($\Delta m(\tilde{\chi}_2^0, \tilde{\chi}_1^0) \sim 20 - 40$ GeV). However one of the most important limitations of the analysis was the p_{T} threshold in the leptons. To reach even more compressed scenario it is then needed to reach a lower threshold for lepton p_{T}.
The effort done for the Full Run 2 analysis tried to cover all of these problems [204]. First, the SR-MLL was updated, and re-optimized, relying on the additional statistic. An important change was the addition of new variables that rely on the topology of the production through ISR of the signal to discriminate against the background. Another new aspect was a cut on the p_{T} of the sub-leading lepton that is a function of the invariant mass: $p_{\mathrm{T}}^{\ell_2} > \min(10, 2 + m_{\ell\ell}/3)$.
Two new additional signal regions were built, that relied on lower $E_{\mathrm{T}}^{\mathrm{miss}}$ thresholds. The region used is between 120 GeV and 200 GeV, in the middle of the turn-on of the $E_{\mathrm{T}}^{\mathrm{miss}}$ trigger. For this reason additional Scale Factors were needed to correct for the different response between the data and the MC to the trigger. This low-$E_{\mathrm{T}}^{\mathrm{miss}}$ signal regions were then further divided in two, in order to target two different Δm regimes: high Δm ($\Delta m(\tilde{\chi}_2^0, \tilde{\chi}_1^0) \sim 20 - 40$ GeV) and low Δm ($\Delta m(\tilde{\chi}_2^0, \tilde{\chi}_1^0) \sim 2 - 10$ GeV)). Moreover, a new reconstruction algorithm allowed to have fully reconstructed and calibrated muons down to 3 GeV, allowing to gain in sensitivity to small mass splitting scenarios.

The analysis presented here is aimed at improve in sensitivity by lowering the threshold of the leptons. This is achieved by looking at final state with one lepton and one track, instead of a final state with two leptons. Tracks in the ATLAS detector are reconstructed down to 500 MeV, and therefore can indeed lower the threshold in the lepton p_{T}. In fact scenario with compressed mass spectra produce soft lepton decays, with most of the p_{T} below 3 GeV.
All these different analysis were designed in order to be orthogonal, and therefore in the end they were combined, in order to improve the exclusion power. In this chapter only the channel with one lepton and one track will be described, however the combination with all the other signal regions will also be presented.

9.1.1 1 Lepton 1 Track overall strategy

The production processes which are considered are still the same as those presented in chapter 8, noticeably the production of $\tilde{\chi}_2^0\ \tilde{\chi}_1^0$, $\tilde{\chi}_1^\pm\ \tilde{\chi}_2^0$, $\tilde{\chi}_1^+\ \tilde{\chi}_1^-$, with the $\tilde{\chi}_1^0$ stable and assumed Higgsino LSP . The final state requires a jet from ISR with a $p_{\mathrm{T}} > 100$ GeV, in order to have the SUSY system to recoil against it and boosting it, so that it is possible to trigger on $E_{\mathrm{T}}^{\mathrm{miss}}$, that, for the signal, comes mainly from the $\tilde{\chi}_1^0$.
Most of the variables used in this analysis are similar to the 2ℓ channel, but with most of the variable that handles two leptons substituted with 1 lepton and one track, e.g. instead of $H_{\mathrm{T}}^{\mathrm{leptons}} = p_{\mathrm{T}}^{\mathrm{lep1}} + p_{\mathrm{T}}^{\mathrm{lep2}}$ it is used $H_{\mathrm{T}}^{\mathrm{leptons}} = p_{\mathrm{T}}^{\mathrm{lep1}} + p_{\mathrm{T}}^{\mathrm{track1}}$.
The background of this analysis is rather different than the one of the 2ℓ channel and new techniques were developed to describe it. Since the background of tracks inside the detector is different orders of magnitude larger than the signal tracks, new method for identification of these tracks must be implemented. A loose match between ID tracks and calorimeter deposits (for electron track candidates) and MS tracks (for muon track candidates) is required in order to reduce the background, at the expense of higher threshold on the track. A minimum of 1 GeV threshold is achieved, but with a good efficiency from 2 GeV. Even after this match, most of the background comes from hadron tracks which survive the identification criteria. For this reason the

estimate of the background is done with a full data driven technique, where the events with Same Sign lepton and track pair are used as a proxy of the background of events with opposite sign lepton and track pairs.

9.2 Data and Simulation Samples

9.2.1 Data Samples

The analysis with 1 lepton and 1 track uses the data collected by the ATLAS detector at the LHC from pp collisions at $\sqrt{s} = 13$ TeV, during the Run 2, from 2015 to 2018. The luminosity recorded by ATLAS during Run 2 is 156 fb^{-1}. However, as already explained in the previous chapter, not all of this data are *good for physics*, after removing data used for monitoring, calibration, and special runs (low β runs, low μ, etc), and after the requests of the GRL, the total integrated luminosity is 139 fb^{-1}with an error of $\sim$ 2% [205, 206]. The breakdown per years is as follow:

- 2015 - 3.22. fb^{-1}
- 2016 - 33.0 fb^{-1}
- 2017 - 44.3 fb^{-1}
- 2018 - 60. fb^{-1}

Events were selected using unprescaled $E_{\mathrm{T}}^{\mathrm{miss}}$ triggers, depending on the years. The triggers used are reported in table 39. With increasing years there are increasing online thresholds; this was done in order mitigate the effects of increasing pileup. The data set used in the analysis was specifically designed for this analysis. Events were selected offline only if they passed $E_{\mathrm{T}}^{\mathrm{miss}}$ trigger and had at least one lepton and one isolated track.

9.2.2 Signal samples

Also in this analysis the optimization is done using MC samples for the signal, built in the simplified models framework of the MSSM. The processes simulated are still the same as in figure 94: $\tilde{\chi}_2^0\,\tilde{\chi}_1^0$, $\tilde{\chi}_2^0\,\tilde{\chi}_1^+$, $\tilde{\chi}_2^0\,\tilde{\chi}_1^-$, and $\tilde{\chi}_1^+\,\tilde{\chi}_1^-$, with the $\tilde{\chi}_2^0$ decaying into a virtual Z boson and a $\tilde{\chi}_1^0$

Period	Lowest unprescaled $E_{\mathrm{T}}^{\mathrm{miss}}$ trigger
2015	HLT_xe70_mht
2016	HLT_xe90_mht_L1XE50 HLT_xe100_mht_L1XE50 HLT_xe110_mht_L1XE50
2017	HLT_xe110_pufit_L1XE55 HLT_xe110_pufit_L1XE50
2018	HLT_xe110_pufit_xe70_L1XE50 HLT_xe110_pufit_xe65_L1XE50

Table 39: Lowest unprescaled inclusive $E_{\mathrm{T}}^{\mathrm{miss}}$ trigger chains in 13 TeV pp running.

(with a 100% Branching Ratio). The $Z^{(\star)}$ then decays into 2 ℓ through a: $\tilde{\chi}_2^0 \to \tilde{\chi}_1^0 Z^{(\star)} \to \ell\ell$, while the $\tilde{\chi}_1^{\pm}$ decays through a virtual W into a $\tilde{\chi}_1^0$ and either a $\ell\nu$ or $q\bar{q}$. The samples still uses MadGraph version 5.2.4.2 for the generation and Pythia 8 for the showering. The signals samples are produced in a similar way as the previous analysis, with the main difference being: at least one additional parton emission in the matrix element (ME) with $p_{\mathrm{T}} > 50$ GeV is required in the process, and a second one with at least $p_{\mathrm{T}} > 10$ GeV. Moreover, in the new samples it is required a $E_{\mathrm{T}}^{\mathrm{miss}}$ filter: $E_{\mathrm{T}}^{\mathrm{miss}} > 75$ GeV. These requirements reduce the cross section with respect of the previous version, but the acceptance in the SR should be invariant since it is still required a jet with $p_{\mathrm{T}} > 100$ GeV. This was indeed done in order to have MC samples with more statistic inside the SR, since with the new version of the analysis the integrated luminosity went up from 36fb^{-1}to 139 fb^{-1}, and therefore a factor 4 in statistic was needed. In the previous version the two leptons from the $Z^{\star}$ were both filter in p_{T} in ordered to have them both with $p_{\mathrm{T}} > 2$ GeV. Instead in the new analysis the events are filtered in just one lepton with $p_{\mathrm{T}} > 2$ GeV, while still requiring the $Z^{\star}$ to decay into two leptons. This allows the second lepton to be as low as possible in p_{T}, so that their track can still be saved.

The Branching Ratios from SUSYHIT are unchanged. Decays are also done again with MadSpin, with the merging scheme CKKW-

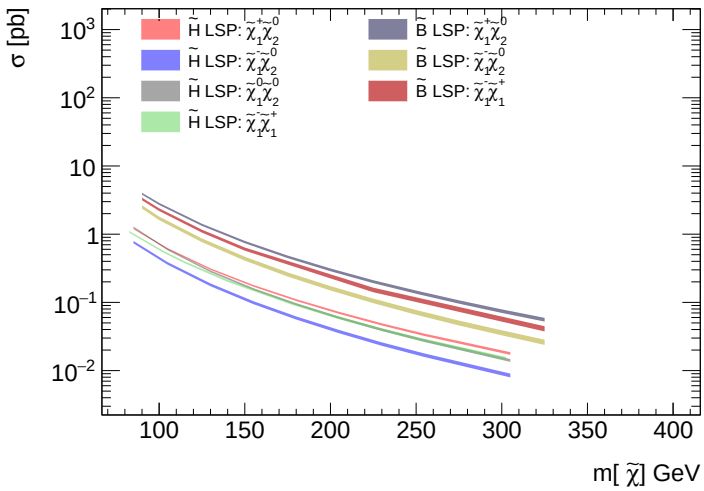

Figure 126: Cross-sections for Higgsino LSP and Wino/Bino LSP for $\tilde{\chi}$ pair-production for proton–proton collisions at $\sqrt{s} = 13$ TeV. Displayed are total cross sections for the processes labelled, as a function of the produced SUSY particle.

L, with a 15 GeV scale. The PDF used in the production is the NNPDF 2.3 LO. Cross sections are recomputed to take into account the additional request on the parton emission. This is done again with Resummino (version 1.0.7) at NLO+NLL. Uncertainties are evaluated by varying the pdf set with CTEQ66 and MSTW, and other pdf sets. An additional interpretation of the results will be done using Wino-Bino samples. These are produced with the exact same setup as the Higgsino samples. The mass scale is set to the Bino-like LSP $\tilde{\chi}^0$, with the Δm representing the $m(\tilde{\chi}^0_2) - m(\tilde{\chi}^0_1)$. The $\tilde{\chi}^0_2$ and the $\tilde{\chi}^\pm_1$ are mass degenerate Winos. The Branching Ratio of the $\tilde{\chi}^0_2 \to \tilde{\chi}^0_1 Z^{(\star)}$ is assumed 100 %, and the BR of $Z^{(\star)} \to \ell\ell$ is set to the SM one on-shell. This last step is done in order to have the same setup as all the other analysis targeting the same model with larger mass differences, which has been one of the standard interpretations of SUSY LHC results for several years.
Figure 126 shows the Higgsino and WinoBino cross section as a function of the mass of the produced SUSY particles.

9.2.3 Background samples

Even if the background estimate is done with a full data driven method, some background samples are used to do preliminary studies and to check the validity of the data driven method used for the estimate of the background. The background whose MC are used are $t\bar{t}$, W/Z+jets, and dibosons (VV). The description of the setup of these samples has been already done in the previous chapter. Here the differences with the previous analysis will be listed and also how the new samples are used.

- **Top Quark** Only the $t\bar{t}$ sample is used in the analysis. This is obtained with POWHEG, and with PYTHIA 8 for the showering. This sample is used to make studies of efficiency on tracks and to study the truth composition of the background.
- **Multiboson** Diboson events are produced to check the presence of prompt events inside the SR.
- **V+Jets** These samples contains either a W or Z boson in association with jet. The W+jets was produced in order to check the correlation between the prompt lepton and the track, and the correlation between the lepton and the jet. Z+jets instead are used for studies of efficiency for track isolation.

9.3 Object Definition and Track Efficiency

9.3.1 Object Definition

The object reconstruction was presented in chapter 6. The working points and the selection used for the objects in the analysis will be presented in this chapter. These WP were chosen in order to reduce the fake component, while keeping an high efficiency, .
As in the 2ℓ analysis, two set of cuts are defined, one a sub set of the other: signal and baseline. Most of the object definitions are the same as in section 8.2, therefore here only the difference with respect to the other analysis will be presented. All the requirements are still reported in table 43.

Electrons Baseline definitions are the same as for the 2ℓ analysis, however the signal Identification WP was changed to *Medium*.

Muons For the muons a new WP for identification was produced, built specifically for low p_{T} objects: *LowPt*, and this was used instead of the Medium WP. With this new WP it is also asked $p_{\mathrm{T}} > 3$ GeV, while the eta coverage is the same, $|\eta| < 2.5$. This improvement is crucial since it allows gaining more signal. The isolation WP is instead changed to *FCTightTrackOnly*.

Jets Jets and b-tagging algorithm are the same as in the previous iteration of the analysis.

$E_{\mathbf{T}}^{\mathbf{miss}}$ The missing transverse momentum is reconstructed using the *Tight* WP.

Overlap Removal The overlap of objects assigned to multiple categories is done with the same procedure as in the previous analysis.

9.3.2 Track Object Definition

The main limitation in probing the low mass splitting region in the previous iteration of this analysis was the threshold on the leptons momenta. The more the mass spectrum of the signals is compressed, the lower the momenta of the leptons are. This means that for $\Delta m = 1/2$ GeV the peak of the p_{T} distribution of the second lepton is well below the current thresholds for identified leptons, with the effect of losing more than 90% of the signal. This can be seen in figure 127 where the truth level p_{T} of the subleading lepton is shown for two signal hypothesis: $\tilde{H} : m(\tilde{\chi}_2^0, \tilde{\chi}_1^0) = (102, 100)$ GeV and $\tilde{H} : m(\tilde{\chi}_2^0, \tilde{\chi}_1^0) = (101, 100)$ GeV. However, even if fully reconstructed leptons are limited in p_{T}, leptons would still leave a track inside the Inner Detector, and here the threshold is as low as 500 MeV, which could recover most of the signal. For this reason an analysis searching a final state for 1 lepton and 1 track is well motivated. However this increases background by many orders of magnitude, since all the backgrounds events have many tracks in the ID. It is then necessary an accurate selection of the tracks in order to recover a good ratio between background and signal.
Track objects to be used in the SR are here defined. As for leptons, two categories of tracks are defined: *signal* and *baseline*.

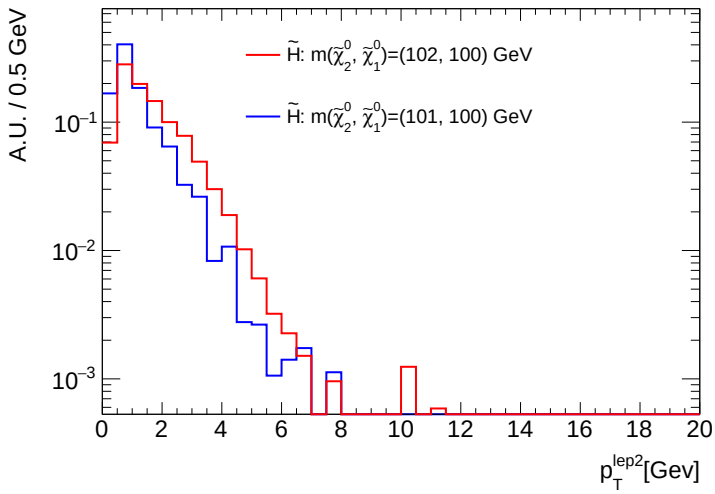

Figure 127: Truth level subleading lepton p_{T} for $\tilde{H}$: $m(\tilde{\chi}_2^0, \tilde{\chi}_1^0) = (102, 100)$ GeV and $\tilde{H} : m(\tilde{\chi}_2^0, \tilde{\chi}_1^0) = (101, 100)$ GeV

Baseline Must satisfy the Tight Primary Working Point selection. In addition to these, the track must be in a $\Delta R < 0.01$ cone within an object inside the list of candidate electrons or muons, called a *container*. In order to have a selection that is orthogonal to the 2ℓ analysis it is required that the object in the container matched to the track does not satisfy the signal lepton requirement. The information of the flavor of the lepton is then added to the track information. For $\sim 2\%$ of tracks both an electron and a muon container match is found. In these cases the track is assigned to the muon. Moreover for the electrons it is required that the track p_{T} satisfies $0.8 < p_{\mathrm{T}}^{\mathrm{track}}/p_{\mathrm{T}}^{\ell} < 1.2$. This is done in order to select the correct track with the calorimeter deposit, since it might happen that more tracks are associated to the same cluster. However, in this case the p_{T} information is different, as shown in figure 128.

The requirement of a match with an electron/muon container is done in order to both reduce the very high background from uncorrelated tracks and also have a loose definition of ID (without this there would only be the information on the charge and not the flavor of the track). However the match implicitly tightens the p_{T} requirement on the track, since container muons (electrons) are only available with p_{T} as low as 2 (1) GeV. This is shown in the plot 129 (left), where we

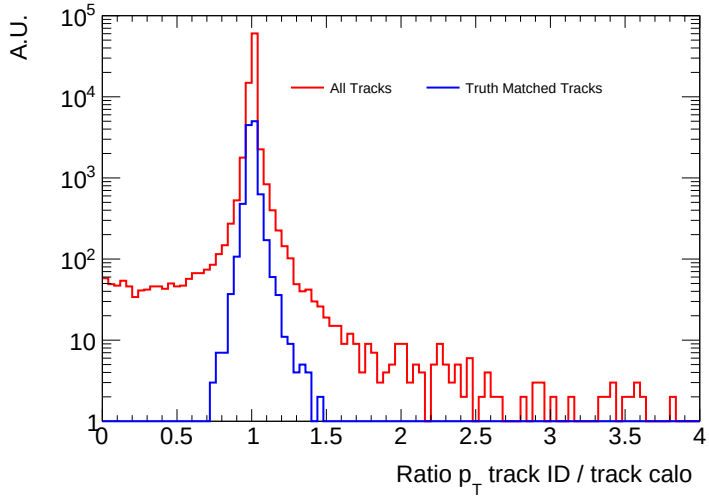

Figure 128: Ratio between the p_{T} from the electron candidate tracks with only the ID information and the calocluster using only the Calorimeter information. In red for all the tracks, while in blue for only tracks with a match with a truth electron. Using $t\bar{t}$ MC.

plot the p_{T} of the objects in the electron container reconstructed with only the calorimetric information, the ID information, or the combination of the two (no cut applied). For muons instead this threshold is at 2 GeV, again this is visible in plot 129 and 130 on the right, where the p_{T} spectrum of the object in the Muon container is shown. Figure 129 is obtained from a $t\bar{t}$ MC sample, while figure 130 from $m(\tilde{\chi}_2^0, \tilde{\chi}_1^0) = 101.5, 100$ GeV MC sample. The different lines correspond to different methods of obtaining the track p_{T}: track information only from the Muon Spectrometer (green), asking for the a combination of ID and Muon Spectrometer (blue), or using tracks only in the ID and none from the muon spectrometer (red). In the analysis, only tracks in the ID are considered. The step in the distribution is due to the lack of CaloTagged muons below 5 GeV, as shown in figure 131. Figure 132 show the difference in p_{T} between the selected track and the selected object in the muon/electron container. Figure 133 shows the distance in ΔR between the selected track and the selected object in the muon/electron container. In both cases the distribution is shown with no selection and with the full SR selection. In the analysis is then used the kinematic of the track.

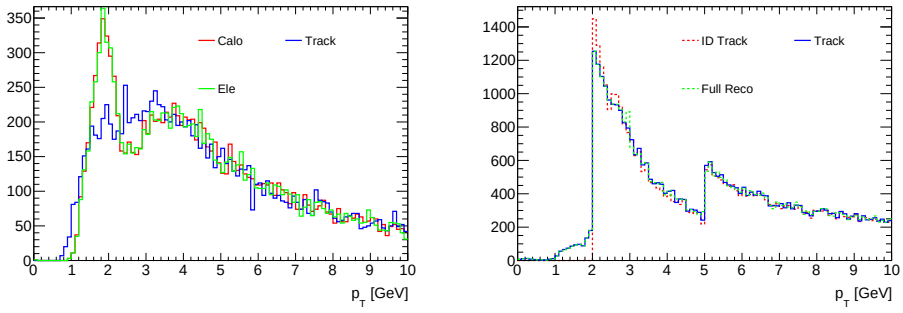

(a) (b)

Figure 129: p_{T} distribution of objects in (a) electron and (b) muon container. Track p_{T} is obtained using, for electrons: xAOD::Electron (green), xAOD::TrackParticle (blue), and, xAOD::CaloCluster (red), while for muons: directly from the Muon container (green), asking for the primaryTrackParticle (blue), or connecting the InDetTrackParticleLink (red). Using $t\bar{t}$ MC samples.

No request is made on the charge of the track, the rate of mismatch is shown in figure 134 for both data and signal: in both cases it is less than $\sim 5\%$ with no selection (except the baseline request on the tracks), while it is always the same charge in the SR. A mismatched track is defined as a track where its charge and the charge of the element in the container don't match.

Signal Tracks are considered signal if:

- $p_{\mathrm{T}} > 1$ GeV
- $|z_0 \sin\theta| < 0.5$ mm and $|d_0/\sigma(d_0)| < 3$
- There is no additional jets within $\Delta R < 0.5$ from the track.
- The sum of the p_{T} of the other tracks (except the signal leptons) in a cone of $\Delta R = 0.3$ is less than 0.5 GeV.

Signal tracks have to satisfy the transverse impact parameter requirement and the longitudinal impact requirement. Isolation for the tracks is evaluated by requiring that the sum of the p_{T} of all the tracks in a cone of $\Delta R = 0.3$ around the track considered should be

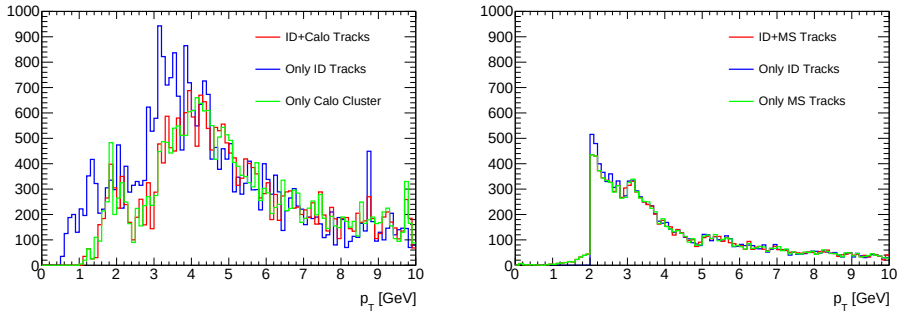

(a) (b)

Figure 130: p_{T} distribution of objects in (a) electron and (b) muon container. Track p_{T} is obtained using, for electrons: only calorimeter information (red), only ID information (blue), ID+Calorimeter information (green), while for muons only ID information (red), only MS information (blue), and ID+MS information (green). Usign signal $m(\tilde{\chi}_2^0, \tilde{\chi}_1^0) = 101.5, 100$ GeV.

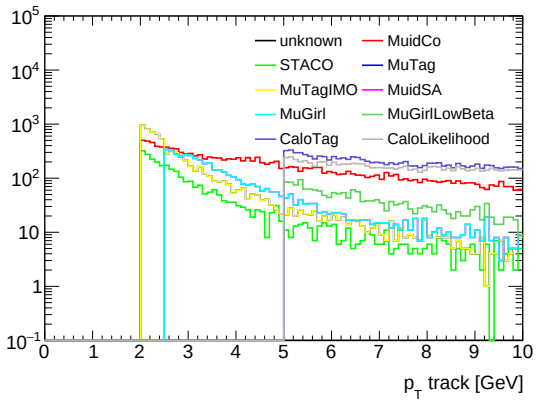

Figure 131: p_{T} distributions of muons container divided by author.

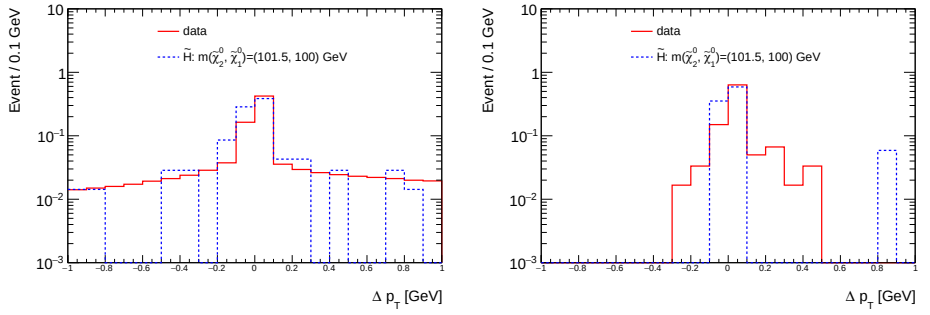

(a) (b)

Figure 132: Distribution of p_{T} difference between objects in electron and muon container and selected track. (a) with no selection, (b) in Signal Region.

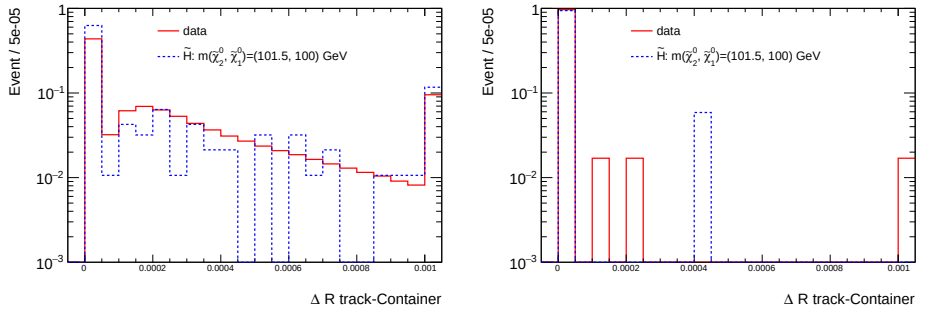

(a) (b)

Figure 133: Distribution of ΔR between objects in electron and muon container and selected track. (a) no selection, (b) in Signal Region.

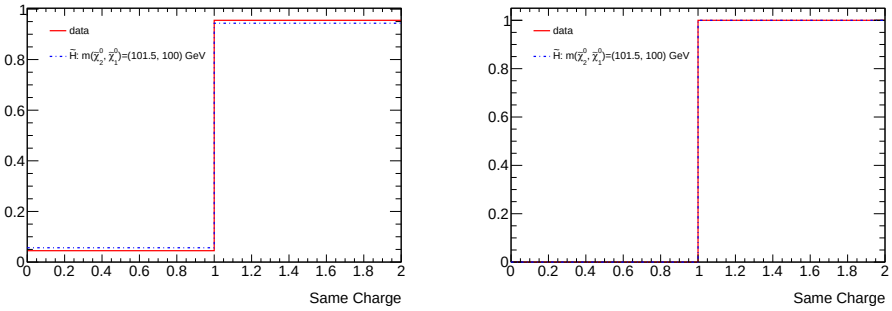

(a) (b)

Figure 134: Fraction of events where the charge of the track and the element in the container don't match for signal and data: 0 means different charge between track and container with match, 1 means same charge. (a) With no selection (b) in SR.

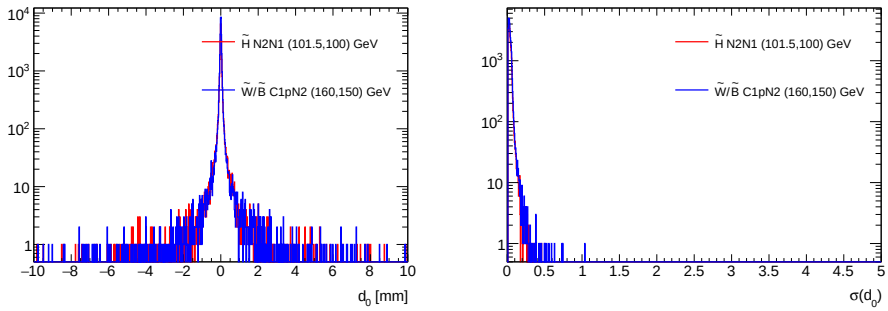

(a) (b)

Figure 135: (a) d_0 and (b) $\sigma(d_0)$ distribution for two signal points for baseline objects of events in the container.

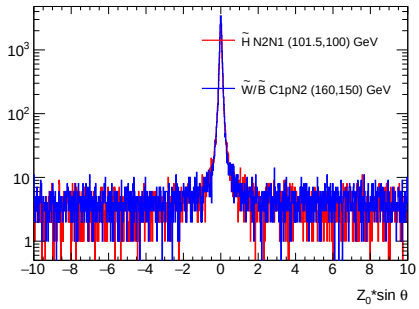

(a)

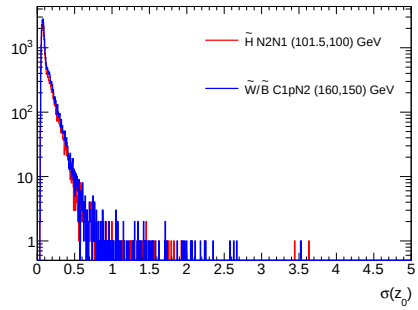

(b)

Figure 136: (a) $z_0 \sin\theta$ and (b) $\sigma(z_0)$ distribution for two signal points for baseline objects of events in the container.

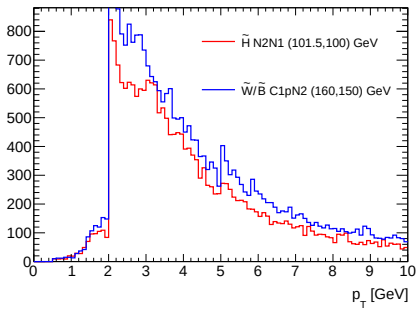

(a)

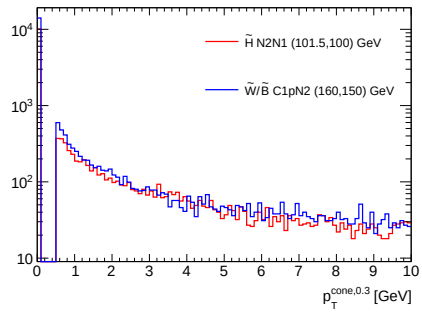

(b)

Figure 137: (a) p_{T} and (b) $p_{\mathrm{T}}^{cone=0.3}$ distribution for two signal points for baseline objects of events in the container.

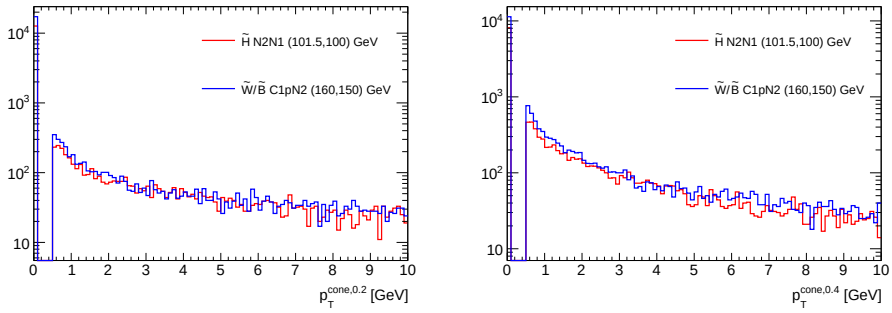

(a) (b)

Figure 138: (a) $p_{\mathrm{T}}^{cone=0.2}$ and (b) $p_{\mathrm{T}}^{cone=0.4}$ distribution for two signal points for baseline objects of events in the container.

less than 0.5 GeV without considering the p_{T} of the signal leptons (this is needed since most of the signal events have very close-by leptons). The ΔR on the nearby tracks was optimized by comparing the results in the SR with three different options: $\Delta R < 0.2$, $\Delta R < 0.3$, and $\Delta R < 0.4$. The best case that balanced significance and statistic was $\Delta R < 0.3$.

Figures 135, 136, 137, and 138 show some of the kinematic variables for baseline tracks for two signal events: $\tilde{H}(\tilde{\chi}_2^0, \tilde{\chi}_1^0) = (101.5, 100)$ GeV and $\tilde{W}/\tilde{B}(\tilde{\chi}_1^{\pm}, \tilde{\chi}_2^0) = (160, 150)$ GeV. These variables are the ones used in the signal selection. It is possible to see how the requirements used select most of the signal, and avoid the tails of the distribution where there are badly reconstructed objects.

Figure 139 shows the efficiency of selecting an object as signal track (red dashed lines) or as a signal lepton (blue solid lines) using $t\bar{t}$ MC sample, while figure 140 it is for signal MC sample $m(\tilde{\chi}_2^0, \tilde{\chi}_1^0) = 82, 80$ GeV. From these plots it is possible to see that there is a recover of the efficiency of around 10-20 % for electron and 20-40 % for the muons a p_{T} below 4.5 GeV for electrons and below 4 GeV for the muons. In addition there is also a bit of recover of events that fail the signal requirement at $p_{\mathrm{T}} > 4$ GeV, however at higher p_{T} the standard identification is more efficient.

The number of baseline and signal tracks per event are shown in figure 141 for both signal and data (using events with same sign lepton and track), after applying all SR selections. The cut on $E_{\mathrm{T}}^{\mathrm{miss}}/H_{\mathrm{T}}^{\mathrm{lep+trk}} >$

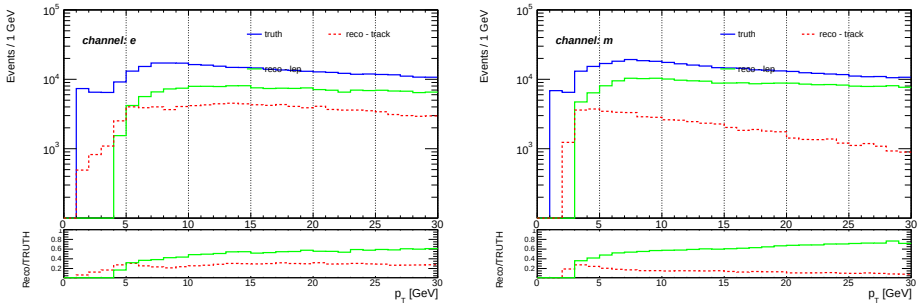

(a) (b)

Figure 139: Identification efficiency as a function of p_{T} for both a signal track and a signal lepton using $t\bar{t}$ MC samples. (a) electrons, (b) muons.

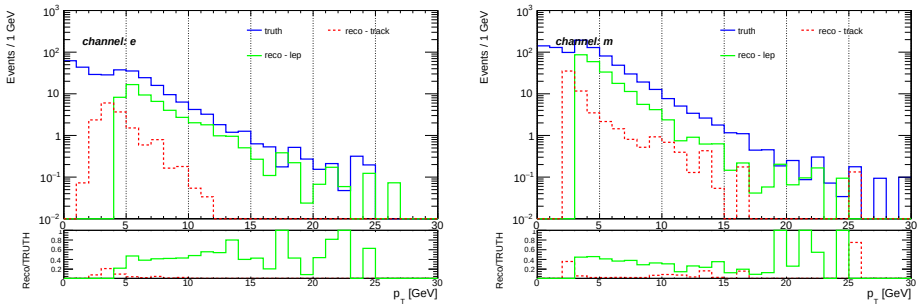

(a) (b)

Figure 140: Identification efficiency as a function of p_{T} for both a signal track and a signal lepton using $m(\tilde{\chi}_2^0, \tilde{\chi}_1^0) = 82, 80$ GeV MC samples. (a) electrons, (b) muons.

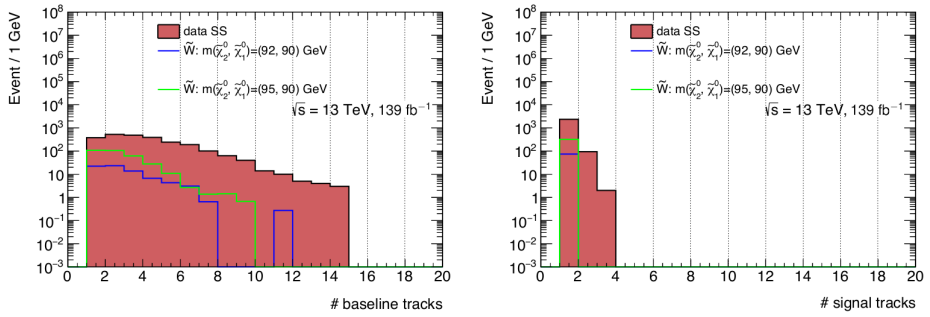

(a) (b)

Figure 141: Number of (a) Baseline and (b) Signal tracks for SS background and Signal.

30 is removed in order to have more statistic. From these plots it is possible to see that for every event there are many baseline tracks, but for the signal selection for most of the signal events there is only one track, reducing the combinatorial ambiguity.

9.3.3 Match efficiency

Even if the backgrounds are data driven, the signal events are taken from MC. This means that the estimate of signal efficiency will depend on how well the MC describes the modeling of the matching between the tracks and the lepton containers. There are then three different components of efficiency that must be taken into account: the efficiency of measuring the track associated to the charged particle, the efficiency of match between the track and the lepton containter, and the isolation efficiency. The first one uses the Scale Factors produced centrally by ATLAS, since they are standard objects used by different analyses. The second and third instead must be evaluated since they are not a standard tool. Here will be presented the *Match* Efficiency, while in the next sub-section it will be presented the *Isolation* Efficiency.
In order to evaluate the efficiency of the lepton-track match a tag-and-probe method was used. The estimate uses events triggered by one lepton and then searches for a second lepton and a near-by track in the mass window of the J/ψ. Selected events must pass a one-lepton trigger and an offline cut of $p_{\mathrm{T}} > 30$ GeV on the triggering

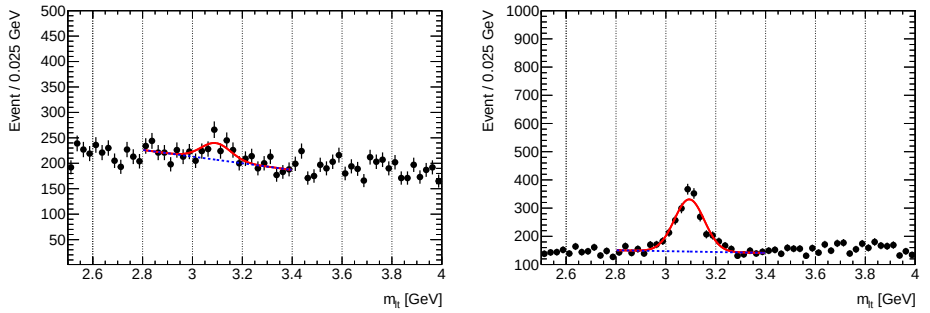

(a) (b)

Figure 142: $m_{\ell t}$ distributions for data events passing 1 lepton trigger and with 1 lepton and 1 track with a match to a (a) electron or (b) muon container.

lepton. The tagging lepton must pass the baseline selection, while the track must pass the signal definition. The track must satisfy the cuts: $p_{\mathrm{T}}^{track} > 2$ GeV and $p_{\mathrm{T}}^{track} < 5$ GeV, and also the second lepton must have $p_{\mathrm{T}}^{\ell} < 10$ GeV, in order to select a kinematic regime closer to the one used in SR. Figure 142 shows, using 80fb^{-1}of data, the $m_{\ell t}$ spectrum for OS events with a track with a match to the electron (a) and muon (b) container. The J/ψ peak is evident in the $\mu\mu$ channel but weaker in the ee channel. Figure 143 instead shows the $m_{\ell t}$ distribution for events with 1 lepton (electron/muon) and 1 track of the opposite sign, where the track doesn't have a match to the electron/muon container.

Figure 144, 145, and 146 shows the p_{T} distribution of the triggering lepton, the second lepton, and track for both data and MC with and without the match between the track and the container with the selection described before. Since the distribution for data and MC are not compatible, the MC samples are reweighted to match the data distributions.
Figure 147 and 148 show the same distribution as 142 and 143, but using $t\bar{t}$ MC. In addition to the selection described above, the tracks in the MC are required to come from mesons with a charmed quark.
For the muons the peak is visible before and after the request of match, for both data and MC. In this case then it is possible to obtain the

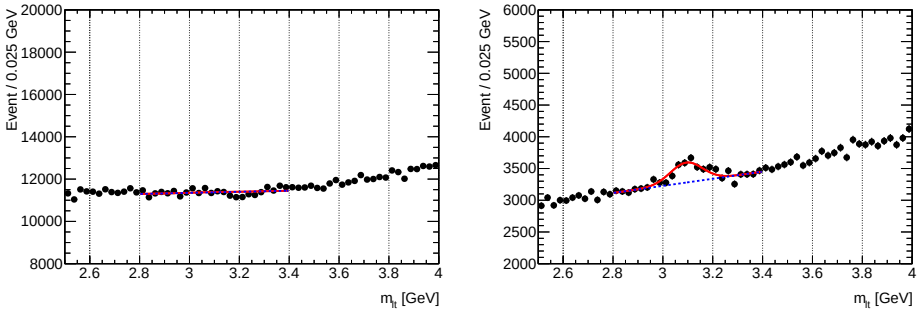

(a) (b)

Figure 143: $m_{\ell \mathrm{t}}$ distributions for data events passing 1 lepton trigger and with 1 lepton and 1 track without a match to a(a) electron or (b) muon container.

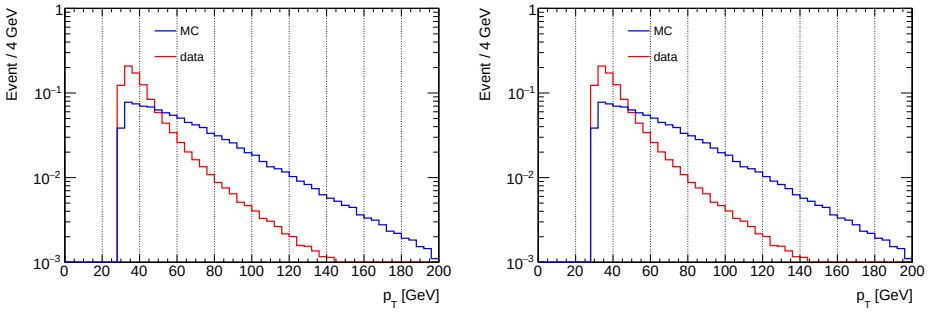

(a) (b)

Figure 144: Triggering Lepton p_{T} distributions for $t\bar{t}$ MC and Data events passing the $J\psi$ selction. (a) With match, (b) without match.

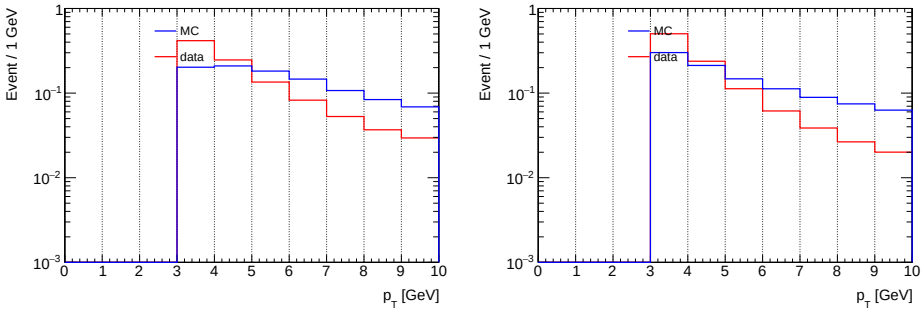

(a) (b)

Figure 145: Triggering Lepton p_{T} distributions for $t\bar{t}$ MC and Data events passing the $J\psi$ selction. (a) With match, (b) without match.

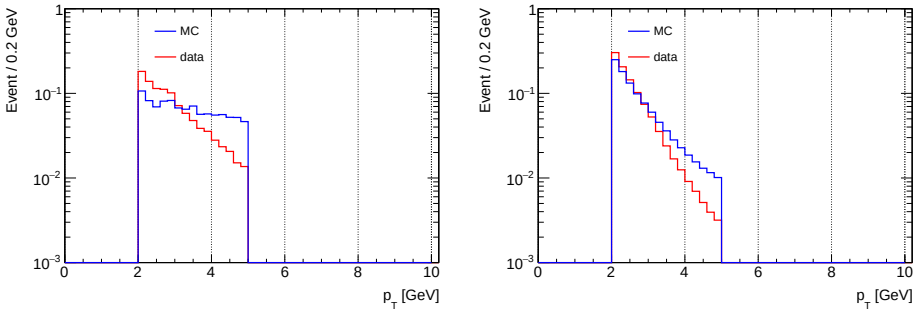

(a) (b)

Figure 146: Track p_{T} distributions for $t\bar{t}$ MC and Data events passing the $J\psi$ selction. (a) With match, (b) without match.

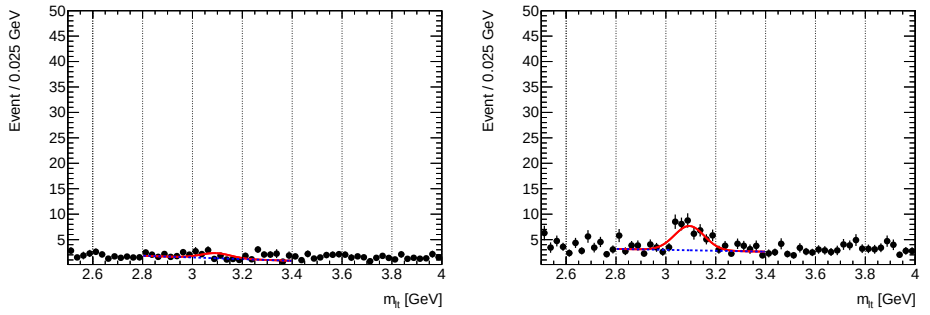

(a) (b)

Figure 147: $m_{\ell \mathrm{t}}$ distributions for $t\bar{t}$ MC events passing 1 lepton trigger and with 1 lepton and 1 track with a match to an (a) electron or (b) muon container.

efficiency as the ratio between the number of signal events with a track with the match and before requiring the match, for data and MC. The scale factors are then evaluated as the ratio between data and MC efficiency.

The number of signal events are evaluated with a fit of a Gaussian function (for the J/ψ signal) plus a straight line (for the background). Table 40 is a summary of the yields in the different scenarios. The yields are obtained subtracting the area under the straight line to the total events between 2.9 GeVand 3.3 GeV. For muons, the ratios match/pre-match are then: 0.53 ± 0.09 for data and 0.39 ± 0.09 for MC. This gives a scale factor of: 1.36 ± 0.39 , which, within the uncertainties, is compatible with 1.

For the electrons instead it is not possible to compute the scale factor in the same way since the J/ψ peak is not visible in the pre-match selection. For this reason the electron scale factor is taken as the muon scale factor times the ratio $ee/\mu\mu$ in data divided by the ratio $ee/\mu\mu$ in MC. Table 41 is a summary of the ratios used for the electron SF. From these results the ratio $ee/\mu\mu$ between data and MC obtained is 0.72 ± 0.43, and therefore the electron scale factor is: $0.97 + /-0.65$. The results is close to 1, but with large uncertainties.

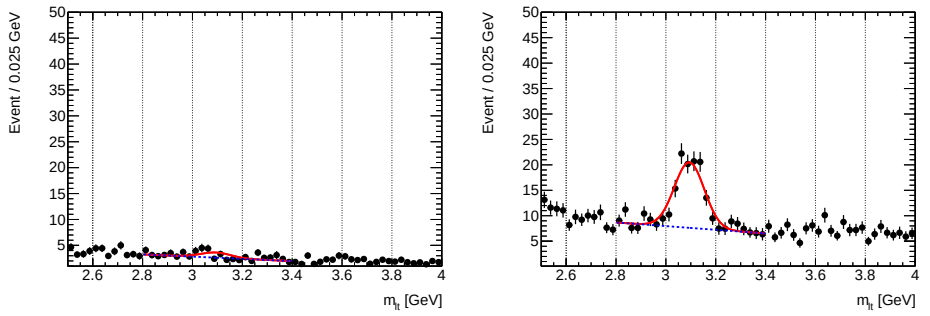

(a) (b)

Figure 148: $m_{\ell \mathrm{t}}$ distributions for $t\bar{t}$ MC events passing 1 lepton trigger and with 1 lepton and 1 track without a match to an (a) electron or (b) muon container.

Sample	Data $\mu\mu$	$t\bar{t}$ $\mu\mu$	Data ee	$t\bar{t}$ ee
Selection				
With L-T Match	1161.75 ± 84.66	$31.5895 + /-6.30347$	213.03 ± 75.24	7.88 ± 3.37
Without L-T Match	2164.46 ± 309.67	$80.8609 + /-9.08059$	-	-
Ratio	0.53 ± 0.09	0.39 ± 0.09	-	-

Table 40: J/ψ fit results for both data and MC, for events with a track with and without a match to a lepton container. The fit function is the sum of a Gaussian function and a straight line. The yields are obtained subtracting the area under the straight line to the total events between 2.9 GeVand 3.3 GeV

Sample	Data	$t\bar{t}$
Ratio $ee/\mu\mu$ with match	$0.17 + /-0.06$	$0.24 + /-0.11$

Table 41: Ratios events $J/\psi \to ee/J/\psi \to \mu\mu$ for both data and MC, for events with a track with a match to a lepton container. The fit function is the sum of a Gaussian function and a straight line. The yields are obtained subtracting the area under the straight line to the total events between 2.9 GeVand 3.3 GeV

9.3.4 Isolation efficiency

In order to evaluate the efficiency of the track isolation a tag-and-probe method was used. Unfortunately it is not possible to use the same strategy with the J/ψ as for the matching efficiency due to the fact that the signal that we are searching for is isolated, while the J/ψ events are not. Therefore a different estimate is used: this uses events triggered by one lepton and then search for a second lepton in the mass window of the Z boson to which it is applied the track isolation. Selected events must pass a one-lepton trigger and an offline cut of $p_{\mathrm{T}} > 30$ GeV on the triggering lepton. The tagging lepton must pass the baseline selection, while the tracks considerd in the isolation must pass the baseline definition.
Figure 149 shows, using 80fb^{-1}of data, the $m_{\ell\ell}$ spectrum for OS events with two electrons (a), and two muons (b), where the second lepton passes the isolation requirement. Figure 151 shows the same plot as figure 149 but using$Z$+jet MC samples. As for the match efficiency, the MC distribution are reweighted to account for the differences in the distribution of the p_{T} of the leptons. Figures 150 and 152 instead show the number of events without the request on the isolation for both data and MC.
The number of signal events are evaluated with a fit of a Crystal Ball function (for the Z boson signal) plus a polynomial function (for the background). Table 42 is a summary of the yields in the different scenarios. The yields are obtained subtracting the area under the polynomial function to the total events between 85 GeVand 95 GeV. Ratios isolaiton/no-isolation are then: 0.991 ± 0.003 for data and 0.965 ± 0.004 for MC. This gives a scale factor of: 1.027 ± 0.005. Instead for electrons we get 0.759 ± 0.003 for data and 0.727 ± 0.003 for MC, giving a scale factor of: 1.044 ± 0.006.
Figure 153 shows the p_{T} dependency of the scale factors from the p_{T} of the probe lepton: the scale factors seems to be consistent within each other. Therefore it is safe to assume that these will be similar in the p_{T} regime of the interest.

9.4 Signal Region Definition

The main strategy of the analysis is to substitute the sub-leading lepton with a track, and then re-evaluate all the variables in the

Sample	Data $\mu\mu$	Z+jet $\mu\mu$	Data ee	Z+jet ee
Selection				
With Isolation	780646 ± 1773	$3.19 \cdot 10^7 \pm 85051$	455669 ± 1356	918589 ± 2885
Without Isolation	765835 ± 1759	$3.31 \cdot 10^7 \pm 86533$	602982 ± 1560	$1.26 \cdot 10^6 \pm 3386$
Ratio	0.991 ± 0.003	0.965 ± 0.004	0.759 ± 0.003	0.727 ± 0.003

Table 42: Z boson fit results for both data and MC. The fit function is the sum of a Crystal Ball function and a polynomial function. The yields are obtained subtracting the area under the polynomial function to the total events between 85 GeVand 95 GeV.

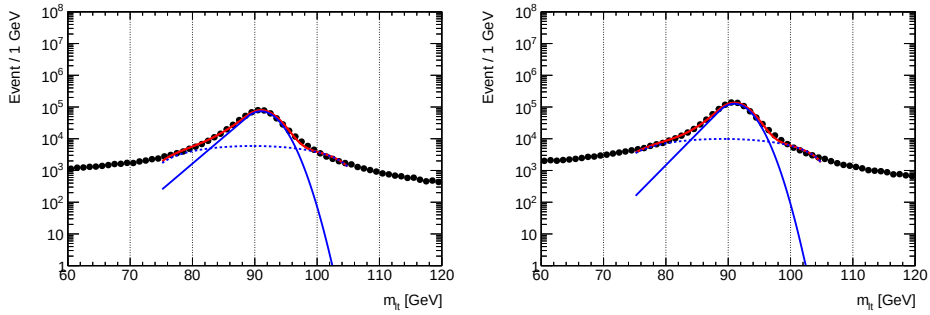

(a) (b)

Figure 149: $m_{\ell\ell}$ distributions for data events passing 1 lepton trigger and with 1 lepton passing track isolation. (a) electrons (b) muons

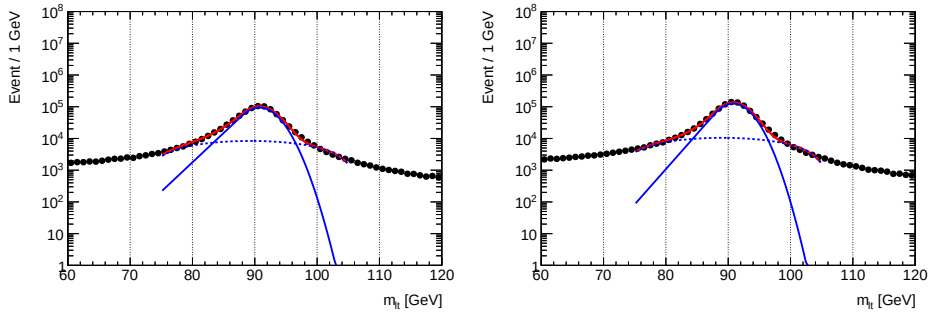

(a) (b)

Figure 150: $m_{\ell\ell}$ distributions for data events passing 1 lepton trigger. (a) electrons (b) muons.

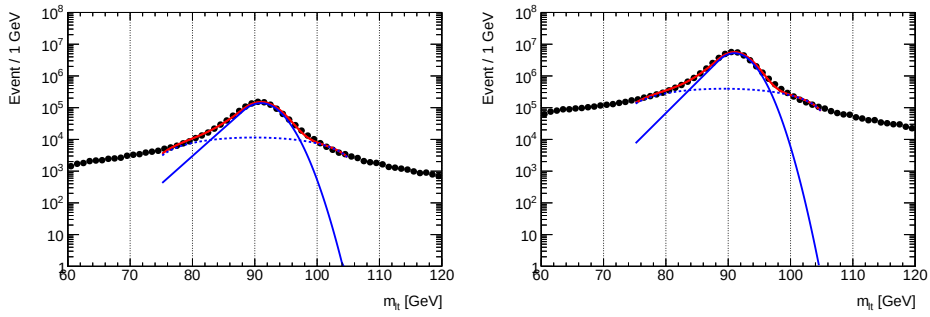

(a) (b)

Figure 151: $m_{\ell\ell}$ distributions for $t\bar{t}$ MC events passing 1 lepton trigger and with 1 lepton passing track isolation. (a) electrons (b) muons

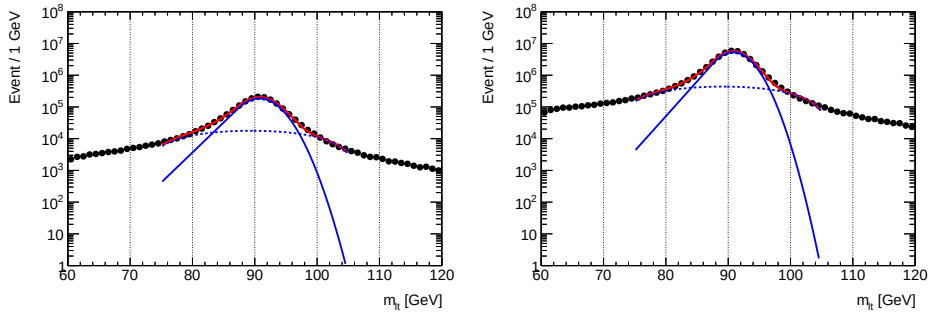

(a) (b)

Figure 152: $m_{\ell\ell}$ distributions for $t\bar{t}$ MC events passing 1 lepton trigger. (a) electrons (b) muons

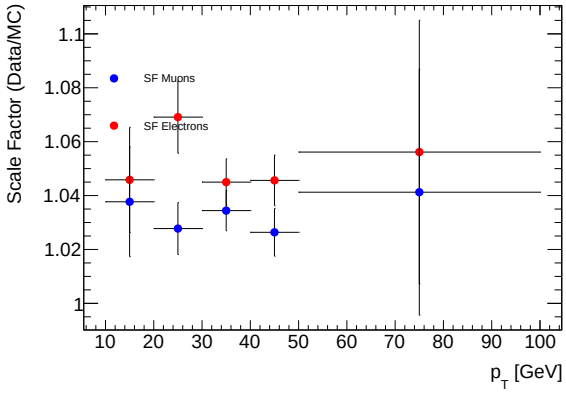

Figure 153: Isolation Scalefactors as a function of p_{T} of the probing lepton

Property	Signal	Baseline
Electrons		
Kinematic	$p_{\mathrm{T}} > 4.5$ GeV, $\|\eta\| < 2.47$ (include crack)	$p_{\mathrm{T}} > 4.5$ GeV
Identification	MediumLLH	VeryLooseLLH
Isolation	Gradient	–
Impact parameter	$\|d_0/\sigma(d_0)\| < 5$, $\|z_0 \sin\theta\| < 0.5$ mm	$\|z_0 \sin\theta\| < 0.5$ mm
Reco algorithm	Veto `author==16`	Veto `author==16`
Muons		
Kinematic	$p_{\mathrm{T}} > 3$ GeV, $\|\eta\| < 2.5$	$p_{\mathrm{T}} > 3$ GeV
Identification	LowPt	LowPt
Isolation	FCTightTrackOnly	–
Impact parameter	$\|d_0/\sigma(d_0)\| < 3$ & $\|z_0 \sin\theta\| < 0.5$ mm	$\|z_0 \sin\theta\| < 0.5$ mm
Jets (Anti-k_t $R = 0.4$ EMTopo)		
Kinematic	$p_{\mathrm{T}} > 30$ GeV, $\|\eta\| < 2.8$	$p_{\mathrm{T}} > 20$ GeV, $\|\eta\| < 4.5$
Pileup mitigation	JVT Medium for $p_{\mathrm{T}} < 120$ GeV, $\|\eta\| < 2.5$	–
b-Jets (Anti-k_t $R = 0.4$ EMTopo)		
Kinematic	$p_{\mathrm{T}} > 20$ GeV, $\|\eta\| < 2.5$	$p_{\mathrm{T}} > 20$ GeV, $\|\eta\| < 4.5$
Pileup mitigation	JVT Medium for $p_{\mathrm{T}} < 120$ GeV, $\|\eta\| < 2.5$	–
b-tagging	MV2c10 FixedCutBeff 85%	–
VBF jets (Anti-k_t $R = 0.4$ EMTopo)		
Kinematic	$p_{\mathrm{T}} > 30$ GeV, $\|\eta\| < 4.5$	$p_{\mathrm{T}} > 20$ GeV, $\|\eta\| < 4.5$
Pileup mitigation	JVT Medium for $p_{\mathrm{T}} < 120$ GeV, $\|\eta\| < 2.5$ fJVT Loose for $p_{\mathrm{T}} < 50$ GeV, $\|\eta\| > 2.5$	–

Table 43: Summary of object definitions.

"standard" analysis with two leptons, e.g. the invariant mass of the lepton and the track ($m_{\ell \mathrm{t}}$) is used instead of the invariant mass of the two leptons ($m_{\ell\ell}$).
The Signal Region (SR) is defined by requiring exactly one signal lepton and at least one signal track with same flavor and opposite sign. $E_{\mathrm{T}}^{\mathrm{miss}}$ is required to be greater than 200 GeV and to have $\left|\Delta\phi(j_1, \mathbf{p}_{\mathrm{T}}^{\mathrm{miss}})\right| > 2.0$, and $\left|\Delta\phi(\ell\ell, \mathbf{p}_{\mathrm{T}}^{\mathrm{miss}})\right| < 1.0$. At least one jet with $p_{\mathrm{T}} > 100$ GeV is also required in the event. The lepton must then have a $p_{\mathrm{T}} < 10$ GeV and the track $p_{\mathrm{T}} < 5$ GeV. Finally the last cut is $E_{\mathrm{T}}^{\mathrm{miss}}/H_{\mathrm{T}}^{\mathrm{lep+trk}} > 30$, in order to enhance the sensitivity at low Δm. The N-1 plot for this signal region are shown in figure 154. The best $E_{\mathrm{T}}^{\mathrm{miss}}/H_{\mathrm{T}}^{\mathrm{lep+trk}}$ cut is chosen in order not only to maximize the significance but take into account the low statistic in the low $m_{\ell \mathrm{t}}$ bins. The background in this selection is evaluated with a fully data driven technique using same sign data as a proxy for the opposite sign contribution. The method is described in details in section 9.5.
Signal Regions are then binned in $m_{\ell \mathrm{t}}$, in order to exploit again the characteristic signal shape of the invariant mass of the particles from the decay of the $Z^{(\star)}$. SR are labelled SR-E-1ℓ1T. As in the previous 2ℓ analysis, exclusive and inclusive signal region are built, with exclusive bins identified by the suffix "e", and inclusive one from the suffix "i".

- **Exclusive**: Exclusive SR are bin each of different size orthogonal with respect of each other. Bin width has been optimized in order to exclude mainly events with $\Delta m(\tilde{\chi}_2^0, \tilde{\chi}_1^0) < 5$ GeV. The bins are $[0.5 - 1.0]$ GeV, $[1.0 - 1.5]$ GeV, $[1.5 - 2.0]$ GeV, $[2 - 3]$ GeV, $[3 - 4]$ GeV, and $[4 - 5]$ GeV. No additional bins at higher $m_{\ell \mathrm{t}}$ are considered, because for signals with a $\Delta m > 5$ GeV most of the leptons are reconstructed and correctly identified and this analysis offers a very reduced gain with respect to the other analysis with 2ℓ. ee and $\mu\mu$ channels are kept together in order to increase the statistics of each bin. In the exclusion fit, only the exclusive bins and not the inclusive SRs. Lower $m_{\ell\ell}$ bins are sensitive to lower Δm signals, and higher $m_{\ell \mathrm{t}}$ to higher Δm.

- **Inclusive**: Inclusive SR are defined by selecting all the $m_{\ell\ell}$ below the up edge of the exclusive bins: < 1 GeV, < 1.5 GeV,

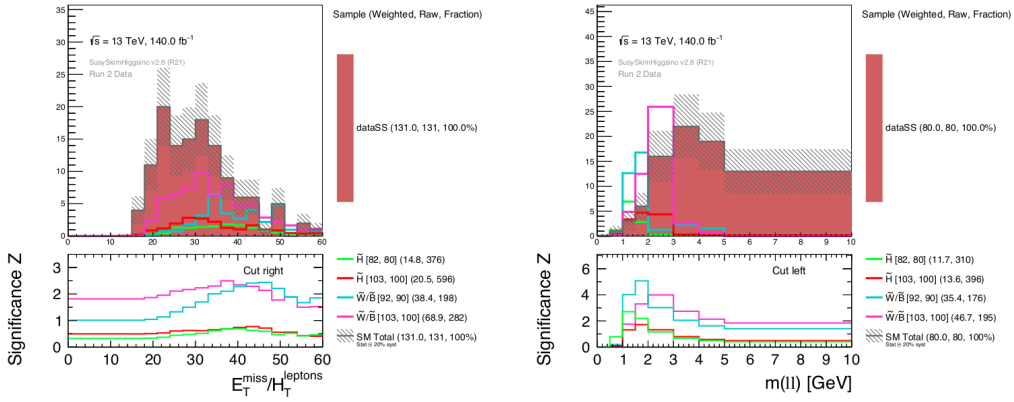

(a) (b)

Figure 154: N-1 plots for $E_{\mathrm{T}}^{\mathrm{miss}}/H_{\mathrm{T}}^{\mathrm{lep+trk}}$ (a), and $m_{\ell\mathrm{t}}$ (b) in the 1ℓ+track SR.

< 2 GeV, < 3 GeV, < 4 GeV, and < 5 GeV. Also here the ee and $\mu\mu$ channels are kept together.

The SR is then divided in bin of $m_{\ell\mathrm{t}}$ (ee and $\mu\mu$ channel together) and fitted. The bins are shown in table 45, while the expected background yields (obtained from SS data) are given in Table 48.

9.5 Background Estimation

The main source of background in the 1ℓ+1T selection is due to combinatory events, where a random track is associated with a real lepton. This fake contribution dominates particularly at very low momentum of the lepton and the track. Since the MC description of the fakes is not perfect, it has been decided to use a completely data driven technique to estimate the background.
The strategy is to use events with the lepton and the track with the same sign of the charge (SS events) as a proxy for the events with opposite charge. For this combinatorial background, the track charge is not correlated with the lepton charge. Thus, there is the same probability that the couple lepton-track could have opposite sign or same sign.

Variable	requirement
Number of leptons (tracks)	= 1 lepton +1 track
$\Delta R_{\ell t}$	$0.05 < \Delta R_{\ell t} < 1.5$
Lepton p_{T} [GeV]	$p_{\mathrm{T}^{\mathrm{lep1}}} > 4.5(e)/3(\mu)$ & $p_{\mathrm{T}^{\mathrm{lep1}}} < 10$
Lepton (track) charge and flavor	$e^{\pm}e^{\mp}$ or $\mu^{\pm}\mu^{\mp}$
$E_{\mathrm{T}}^{\mathrm{miss}}$ [GeV]	> 100
Number of jets	≥ 1
Leading jet p_{T} [GeV]	≥ 100
$\min \lvert\Delta\phi(\text{all jets}, \mathbf{p}_{\mathrm{T}}^{\mathrm{miss}})\rvert$	> 0.4
$\lvert\Delta\phi(j_1, \mathbf{p}_{\mathrm{T}}^{\mathrm{miss}})\rvert$	≥ 2.0
J/ψ invariant mass [GeV]	veto $3 < m_{\ell t} < 3.2$
Lepton-track invariant mass [GeV]	$0.5 < m_{\ell t} < 5$

Table 44: Preselection requirements applied to all events entering into the signal regions.

9.5.1 SS/OS Symmetry

To verify the SS=OS hypothesis it is checked where it is possible to look at the ratio between the SS and OS events in data with no signal contamination. This region is defined by requiring $m_{\ell t} > 5$ GeV and $E_{\mathrm{T}}^{\mathrm{miss}}/(p_{\mathrm{T}}^{lep} + p_{\mathrm{T}}^{track}) < 30$, such that the targeted signals at low Δm are not present. The ratio of OS over SS events as a function of both the lepton and track p_{T} and η is shown in figure 155. As it can be seen at low p_{T}, where the signal region is defined, the ratio is consistent with one, while at increasing p_{T} the ratio is higher that one. Inside the red lines, which show the kinematics relevant in the signal region, the average ratio is: 1.05 ± 0.02.

In figure 156 it is shown a comparison between SS and OS data as a function of $E_{\mathrm{T}}^{\mathrm{miss}}/(p_{\mathrm{T}}^{lep} + p_{\mathrm{T}}^{track})$ for 2015+2016 data, 2017 data, and 2018 data, normalized to 1, after requirements of $m_{\ell t} > 5$ GeV and $p_{\mathrm{T}}^{lep/track} < 10$ GeV. The plot indicates the SS=OS equality does not depend on $E_{\mathrm{T}}^{\mathrm{miss}}/H_{\mathrm{T}}^{\mathrm{leptons}}$ or data-taking year.

Figure 157 shows the dependency of the OS/SS ratio as a function of η. Except at very high η where the statistic is rather low, the ratio is consistent with 1.

Variable	Selection criteria defining the 1ℓ+track SR					
$E_{\mathrm{T}}^{\mathrm{miss}}$	> 200 GeV					
$\left\lvert\Delta\phi(\ell\ell, \mathbf{p}_{\mathrm{T}}^{\mathrm{miss}})\right\rvert$	< 1.0					
$p_{\mathrm{T}}^{\mathrm{track}}$	< 5 GeV					
$E_{\mathrm{T}}^{\mathrm{miss}}/H_{\mathrm{T}}^{\mathrm{lep+trk}}$	> 30					
eSR-E-1ℓ1T	eMLTa	eMLTb	eMLTc	eMLTd	eMLTe	eMLTf
$m_{\ell\ell}$ [GeV]	$[0.5, 1]$	$[1, 1.5]$	$[1.5, 2]$	$[2, 3]$	$[3, 4]$	$[4, 5]$
iSR-E-1ℓ1T	iMLTa	iMLTb	iMLTc	iMLTd	iMLTe	iMLTf
$m_{\ell\ell}$ [GeV]	< 1	< 1.5	< 2	< 3	< 4	< 5

Table 45: Selection criteria defining the 1ℓ+track Electroweakino SRs, in addition to the pre-selection defined in Table 44.

9.5.2 Charge Symmetry

An additional check is done to verify the contribution from events with positively charged and negative charged leptons. Figure 158 shows the ratio between events with SS lepton-track pairs with a positive and negative lepton as a function of both lepton and track p_{T}. The number of events with a positive charge are more than the ones with a negative one by a factor ~ 1.6, which is compatible with the ratio of the cross section of W^+ over W^- [207]. Instead figure 159 (a) shows as a function of the track p_{T} the ratio of events with a positive charged tracks over negative charged one, while the lepton is in both cases positively charged. In figure 159 (b)it is shown the same plot but with negative charged lepton. In both these cases the ratio is close to one in the region of interest for this analysis ($p_{\mathrm{T}}^{track} < 10$ GeV), meaning that again most of the background tracks are not correlated to the lepton, even if there are more positive charged leptons. In all of these plots we require at least one jet with a $p_{\mathrm{T}}^{jet} > 100$ GeV, $E_{\mathrm{T}}^{\mathrm{miss}} > 180$ GeV, and $\left\lvert\Delta\phi(\ell\ell, \mathbf{p}_{\mathrm{T}}^{\mathrm{miss}})\right\rvert > 1.5$, where this last cut allows orthogonality to the SR.

9.5.3 Prompt Contribution and signal contamination

It is also checked that the prompt contribution in the SS region is negligible, meaning that the SS data can be used directly as an

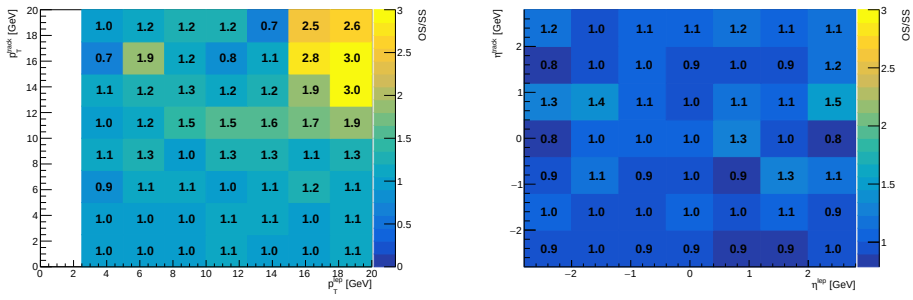

(a) (b)

Figure 155: Ratio of OS over SS events as a function of the lepton and track p_{T} (a) and η (b) in the one lepton + one track channel.η plot has the additional requirement $p_{\mathrm{T}}^{\mathrm{lep}} < 10$ GeV and $p_{\mathrm{T}}^{\mathrm{track}} < 5$ GeV.

estimate of the OS fake background, with no need to subtract processes with two prompt leptons. Sherpa diboson samples of $ll\nu\nu$, $lll\nu$, and $llll$ are used for this check. In figure 160 it is shown the contribution of these backgrounds in the SS region at preselection level, as a function of $E_{\mathrm{T}}^{\mathrm{miss}}/(p_{\mathrm{T}}^{lep} + p_{\mathrm{T}}^{track})$. It is possible to conclude that the prompt contribution can be ignored.

Finally it is checked the contribution to the background from the signal itself. Figure 161 shows the $m_{\ell \mathrm{t}}$ distribution for different signal samples in the SR for both OS and SS contribution, while table 46 shows the integral of these distributions (normalized to 139 fb^{-1}). It is possible to see that the SS contribution is small, especially where the OS signal is dominant.

Sample	OS events	SS events
$\tilde{H}\, m(\tilde{\chi}_2^0\tilde{\chi}_1^0) = (82, 80)$ GeV	11.36 ± 0.72	0.32 ± 0.10
$\tilde{H}\, m(\tilde{\chi}_2^0\tilde{\chi}_1^0) = (103, 100)$ GeV	13.12 ± 0.75	0.53 ± 0.15
$\tilde{W}/\tilde{B}\, m(\tilde{\chi}_2^0\tilde{\chi}_1^0) = (103, 100)$ GeV	43.38 ± 3.50	3.35 ± 0.99

Table 46: Yields for OS and SS signal events in the SR, normalized to 139 fb^{-1}

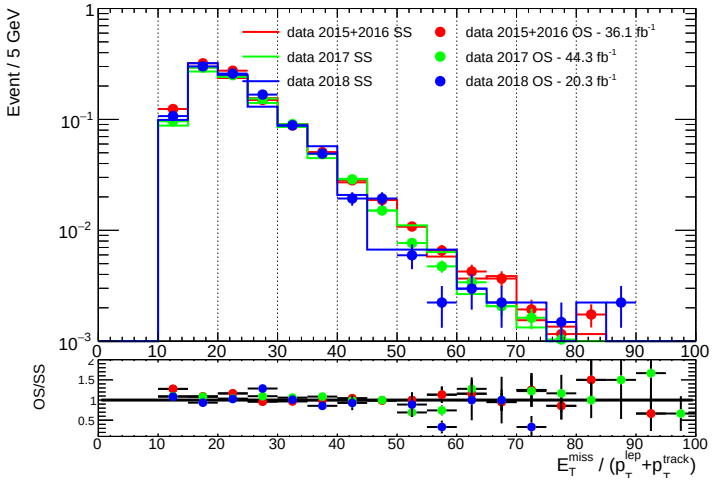

Figure 156: Ratio of OS over SS events as a function of $E_{\mathrm{T}}^{\mathrm{miss}}/(p_{\mathrm{T}}^{lep} + p_{\mathrm{T}}^{track})$ divided by year in the one lepton + one track channel. The distributions are normalized to 1.

9.5.4 Low $m_{\ell \mathrm{t}}$ resonances

Resonances at low $m_{\ell \mathrm{t}}$ are the dominant background, and must be taken into account. The decay into leptons of neutral resonances produces pair of OS leptons, that evades the estimate done before. Moreover they are not visible in most of the previous control plots, since they were done at higher $m_{\ell \mathrm{t}}$.

Figure 162 (a) shows the $m_{\ell \mathrm{t}}$ distribution after preselection and the following requests: $E_{\mathrm{T}}^{\mathrm{miss}} < 180$ GeV, $p_{\mathrm{T}}^{track} < 5$ GeV, and $\left|\Delta\phi(\ell\ell, \mathbf{p}_{\mathrm{T}}^{\mathrm{miss}})\right| > 1.5$. This region is orthogonal to the SR, so that it is possible to look at low $m_{\ell \mathrm{t}}$ events with very low signal contamination. The excess at $m_{\ell \mathrm{t}} < 2$ GeV is expected to decrease as the $E_{\mathrm{T}}^{\mathrm{miss}}$ cut is tightened, since resonance are generally produced with low $E_{\mathrm{T}}^{\mathrm{miss}}$.

In order to check this, the cut on $\left|\Delta\phi(\ell\ell, \mathbf{p}_{\mathrm{T}}^{\mathrm{miss}})\right|$is also inverted, allowing to check the whole $E_{\mathrm{T}}^{\mathrm{miss}}$ distribution at $m_{\ell \mathrm{t}} < 2$ GeV. As shown in figure 162 (b) the ratio OS/SS is flat in this variable, therefore we can reverse this cut and assume that the conclusion obtained for $\left|\Delta\phi(\ell\ell, \mathbf{p}_{\mathrm{T}}^{\mathrm{miss}})\right| > 1.5$ are true also for $\left|\Delta\phi(\ell\ell, \mathbf{p}_{\mathrm{T}}^{\mathrm{miss}})\right| < 1.5$. Figure 163 shows the $m_{\ell \mathrm{t}}$ distribution in the 0 - 4 GeVrange divided in the ee and $\mu\mu$ channel.

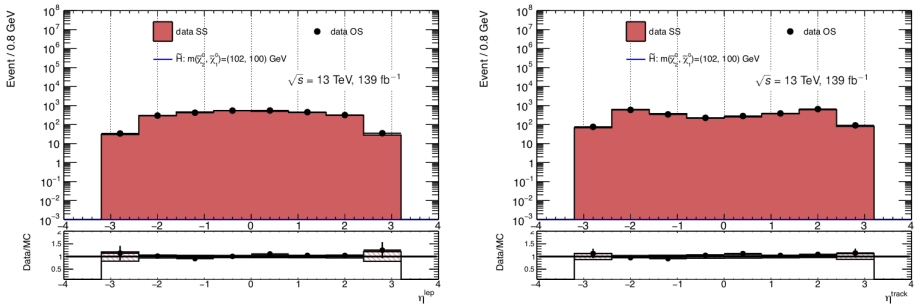

(a) (b)

Figure 157: Ratio of OS over SS events as a function of η for the lepton (a) and the track (b), asking $E_{\mathrm{T}}^{\mathrm{miss}}/(p_{\mathrm{T}}^{lep} + p_{\mathrm{T}}^{track}) < 30$ and $m_{\ell \mathrm{t}} > 5$ GeV, $E_{\mathrm{T}}^{\mathrm{miss}} > 200$ GeV, $p_{\mathrm{T}}^{track} < 5$ GeV, and $p_{\mathrm{T}}^{lep} < 10$ GeV

Figure 164 shows the $E_{\mathrm{T}}^{\mathrm{miss}}$ distribution for $m_{\ell \mathrm{t}} < 2$ GeV, $\left|\Delta\phi(\ell\ell, \mathbf{p}_{\mathrm{T}}^{\mathrm{miss}})\right| > 1.5$. $E_{\mathrm{T}}^{\mathrm{miss}}/H_{\mathrm{T}}^{\mathrm{lep+trk}} > 15$ is also applied in order to be closer to the SR kinematics, but still have good statistics). As shown, the ratio is now close to 1, even if the statistic at high $E_{\mathrm{T}}^{\mathrm{miss}}$ is not optimal. The $m_{\ell \mathrm{t}}$ distribution with $E_{\mathrm{T}}^{\mathrm{miss}}/H_{\mathrm{T}}^{\mathrm{lep+trk}} > 15$ is shown in 165 (a) and it is possible to see that no further excess are observed at low $m_{\ell \mathrm{t}}$.

9.5.5 Validation Region

An additional Validation Region, called VR $-$ 1ℓ1T, is defined to check the SS background in a kinematic region closer to the SR. This region is defined with the same cuts as the SR, except that it is required $\left|\Delta\phi(\ell\ell, \mathbf{p}_{\mathrm{T}}^{\mathrm{miss}})\right| > 1.5$, in order to avoid signal contamination. Also, the requirement on $\Delta R_{\ell \mathrm{t}}$ is removed, and the one on $E_{\mathrm{T}}^{\mathrm{miss}}/H_{\mathrm{T}}^{\mathrm{leptons}}$ is loosened to $E_{\mathrm{T}}^{\mathrm{miss}}/H_{\mathrm{T}}^{\mathrm{leptons}} > 15$, to increase the number of events inside the validation region. Distribution in this region is shown in figure 165 and 166. Good agreement is seen in all the plots.

9.6 Systematic Uncertainties

In this analysis the background is fully obtained from data-driven techniques, therefore no systematic uncertainties on the modeling of

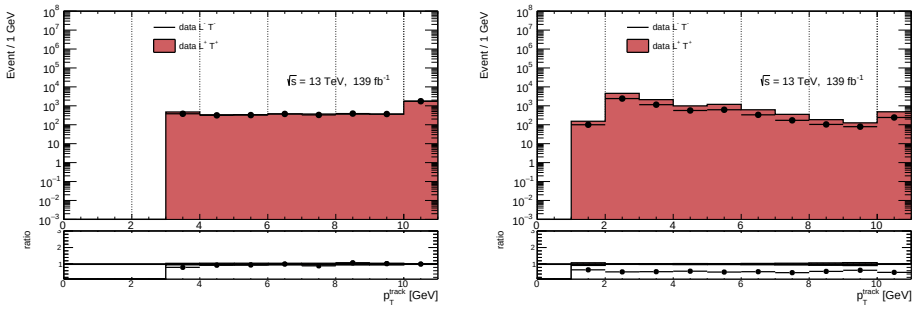

(a) (b)

Figure 158: Ratio of plus charged lepton-track pair over negative charged lepton-track pair as a function of lepton p_{T} (left) and track p_{T} (right) in the one lepton + one track channel. Requiring at least one jet with a $p_{\mathrm{T}}^{jet} > 100$ GeV, $E_{\mathrm{T}}^{\mathrm{miss}} > 180$ GeV, and $\left|\Delta\phi(\ell\ell, \mathbf{p}_{\mathrm{T}}^{\mathrm{miss}})\right| > 1.5$.

the background MC are added. However systematic uncertainties are assigned on the data driven technique itself, and on the modeling of the signal MC. In table 47 it is reported the breakdown of the systematic uncertainties in the 1L+T SRs. The most important uncertainties are statistical, since the background is taken directly from data.

9.6.1 Data Driven Background Uncertainties

The main source of systematic uncertainty on the background comes from the closure of the OS-SS method. As described in 9.5, the background in the SR is taken from the SS data, because we expect the ratio OS/SS to be close to 1, but the difference from 1 must be accounted in the uncertainties.
As it is possible to see in figure 162, two kind of regimes are present: below and above 2 GeV of $m_{\ell \mathrm{t}}$. This limit is chosen because below 2 GeV the main contribution to the background is due to low-mass resonances, while at higher $m_{\ell \mathrm{t}}$ the background is mainly due to the W+jets contribution.

$m_{\ell \mathrm{t}} < 2$ GeV The error on the background for $m_{\ell t} < 2$ GeV is estimated by fitting the OS/SS ratio as a function of $E_{\mathrm{T}}^{\mathrm{miss}}$ in the re-

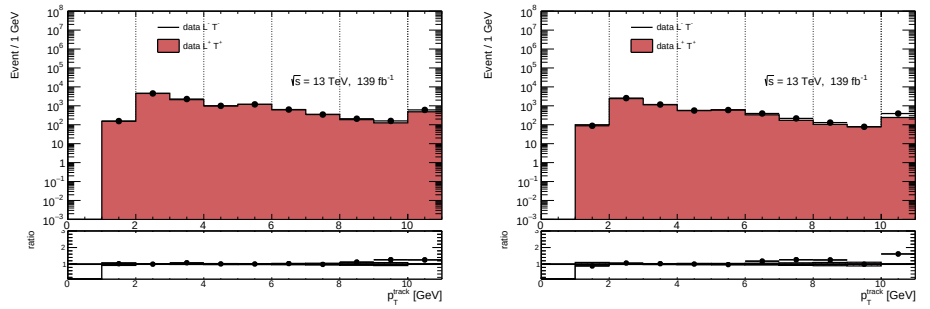

(a) (b)

Figure 159: Ratio of events with plus charged and minus charged tracks with a plus (right) or minus (right) charged lepton, as a function of the track p_{T} in the one lepton + one track channel. Requiring at least one jet with a $p_{\mathrm{T}}^{jet} > 100$ GeV, $E_{\mathrm{T}}^{\mathrm{miss}} > 180$ GeV, and $\left|\Delta\phi(\ell\ell, \mathbf{p}_{\mathrm{T}}^{\mathrm{miss}})\right| > 1.5$.

gion with high $\left|\Delta\phi(\ell\ell, \mathbf{p}_{\mathrm{T}}^{\mathrm{miss}})\right|$and extrapolating the results at $E_{\mathrm{T}}^{\mathrm{miss}} = 200$ GeV. Figure 167 shows the ratio OS/SS as a function of $E_{\mathrm{T}}^{\mathrm{miss}}$ for three sets of selection:

- $\left|\Delta\phi(\ell\ell, \mathbf{p}_{\mathrm{T}}^{\mathrm{miss}})\right| < 1.5$, $E_{\mathrm{T}}^{\mathrm{miss}}/H_{\mathrm{T}}^{\mathrm{lep+trk}} > 15$, $E_{\mathrm{T}}^{\mathrm{miss}} < 180$ GeV (black)
- $\left|\Delta\phi(\ell\ell, \mathbf{p}_{\mathrm{T}}^{\mathrm{miss}})\right| > 1.5$ and $E_{\mathrm{T}}^{\mathrm{miss}}/H_{\mathrm{T}}^{\mathrm{lep+trk}} > 15$ (red)
- $\left|\Delta\phi(\ell\ell, \mathbf{p}_{\mathrm{T}}^{\mathrm{miss}})\right| > 1.5$ and $E_{\mathrm{T}}^{\mathrm{miss}}/H_{\mathrm{T}}^{\mathrm{lep+trk}} > 30$ (blue).

Within the uncertainties all the three results are compatible. The red points are then fitted with both an exponential function and a polynomial function. The results of both fits are compatible results and estimate the following SS/OS ratios: 1.17 ± 0.13 (using the exponential function) and 1.17 ± 0.16 (with the polynomial function). In the end we consider a 30% uncertainty on the background, obtained by adding together the difference from 1 of the fitted ratio and its error.

$m_{\ell t} > 2$ GeV At $m_{\ell t} > 2$ GeV the main source of uncertainties is instead due to the correlation in W+jets between the track and the lepton. The correlation is checked with W+jets MC samples. In figure

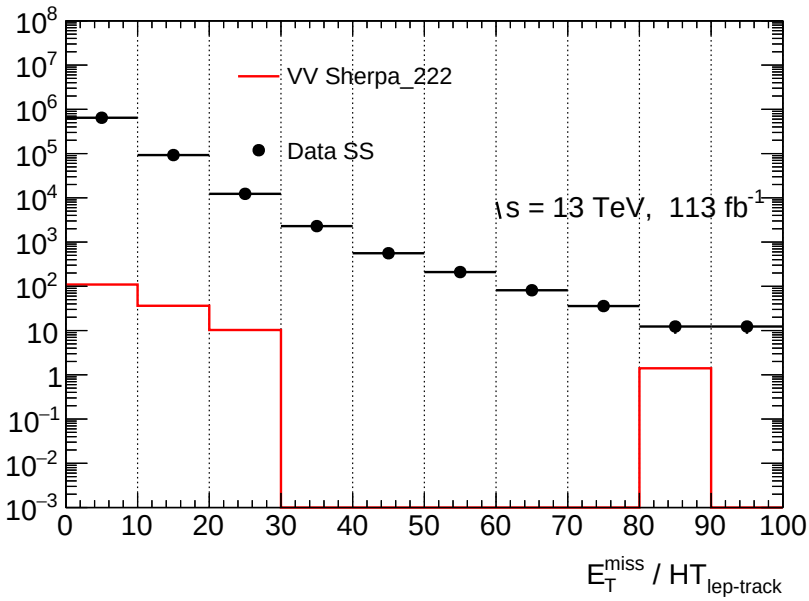

Figure 160: Diboson prompt contribution at preselection level.

168 we show the distribution of $m_{\ell t}$ (left, with $E_{\mathrm{T}}^{\mathrm{miss}} > 180$ GeV) and $E_{\mathrm{T}}^{\mathrm{miss}}$ (right, with $m_{\ell t} < 2$ GeV) for OS and SS events using $W + jets$ MC. The ratio is close to 1 and the uncertainty on the ratio (mainly due to the statistics of the MC sample) is used as uncertainty on the SS data background estimate for $m_{\ell t} > 2$ GeV). This final value of the error is 12% of the yields.

Statistical Uncertainties An additional source of systematic on the background estimate comes from the statistic of the SS data. In fact the estimate is just as precise as the number of SS events in the SR, since it takes directly the SS data in this region. This was also an important factor in the optimization of the SR. In fact the optimization was done before having the full 139 fb^{-1}of Run 2, using only a sub set of the data (2015+2016) scaled to 139 fb^{-1}. This required loose cuts in order to avoid over-optimization in places where the statistic was low. However when the full data set was ready, the cuts were checked and found consistent with what was decided.

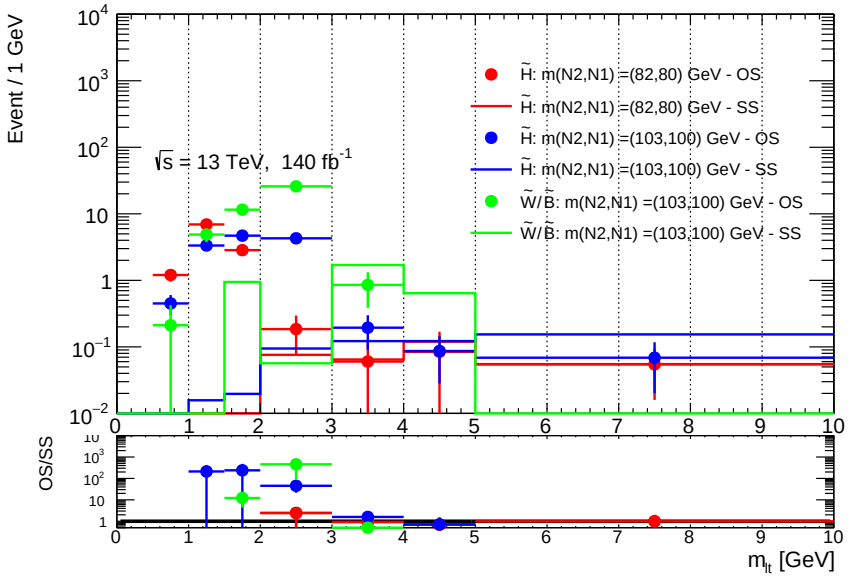

Figure 161: OS and SS events $m_{\ell t}$ distribution for signal samples in the SR The bottom box shows the OS/SS ratio.

9.6.2 Signal Uncertainties

As this analysis selects signal events with energetic initial state radiation, uncertainties arise in modelling these next-to-leading order processes. PDF uncertainties on acceptance are also evaluated for signal samples. Uncertainties on signal cross sections are described in Section 9.2.2 and are typically less than 5%. The implementation is done in the same way as in the 2ℓ analysis. The experimental systematic uncertainties on the signal accounts for:

- Jets: In the same way as in the 2ℓ analysis, uncertainties are considered on the jet energy scale and resolution, with a reduced set of NP: 6 JES components and 8 JER component. The difference in efficiency of the JVT selection is taken into account with an additional systematic uncertainty.

- Electrons and Muons: energy scale and resolution effects are taken into account in the signal uncertainties. Also, uncertainties on the scale factors for identification, isolation, and reconstruction are considered.

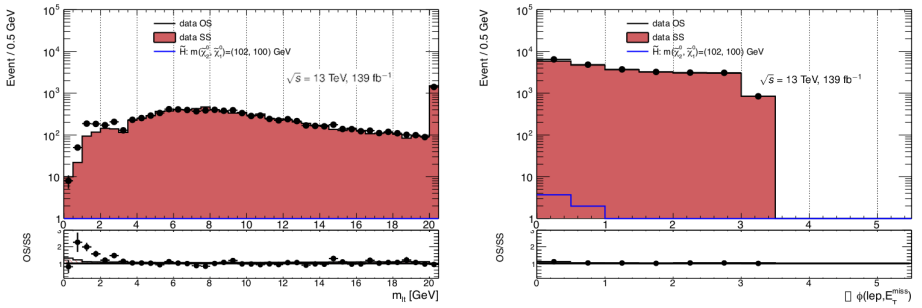

(a) (b)

Figure 162: $m_{\ell t}$ (a) and $\left|\Delta\phi(\ell\ell, \mathbf{p}_{\mathrm{T}}^{\mathrm{miss}})\right|$(b) distributions after preselection and asking $E_{\mathrm{T}}^{\mathrm{miss}} < 180$ GeV, $p_{\mathrm{T}}^{track} < 5$ GeV, and $\left|\Delta\phi(\ell\ell, \mathbf{p}_{\mathrm{T}}^{\mathrm{miss}})\right| > 1.5$.

- Missing transverse energy: The propagation of the uncertainties of the objects entering the $E_{\mathrm{T}}^{\mathrm{miss}}$ definition is taken into account. Also, the uncertainties on the resolution and scale of the soft term are considered.

An addition to the 2ℓ analysis's systematic uncertainties, is the presence of experimental effects coming from the tracks performances. The main sources of uncertainties considered for the tracks are:

- **Inclusive Fake Systematics.** The uncertainty on the Monte Carlo fake rate is the fraction of reconstructed tracks that do not closely match a generated charged particle. This is estimated by comparing the non-linear component of track multiplicity as a function of μ (Pileup) between Monte Carlo and data. This uncertainty depends on p_{T} and η. The impact of this systematic is 100 % on the fake tracks for a Tight Primary selection. However, in Tight Primary tracks the percentage of fake tracks is minimal, therefore the actual error in the final yields is also minimal.

- **Impact Parameter Resolution.** Systematic uncertainties on the transverse (d_0) and longitudinal (z_0) impact parameter (IP) resolution are obtained by studying these parameters in data and MC. A smearing and a biasing is applied to these parameters in order to resemble the data, accordingly with the right data period.

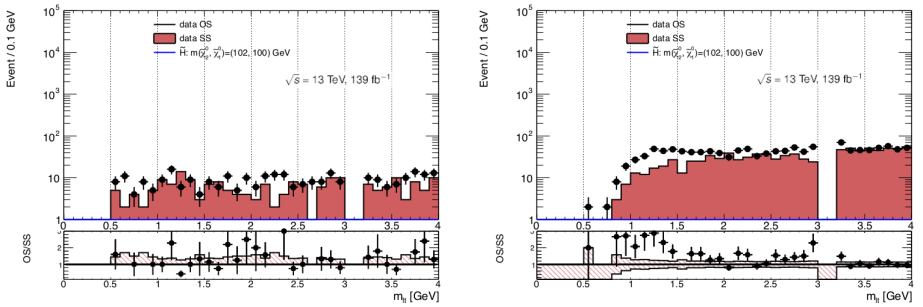

(a) (b)

Figure 163: $m_{\ell t}$ distribution after preselection and asking $E_{\mathrm{T}}^{\mathrm{miss}} <$ 180 GeV, $p_{\mathrm{T}}^{track} < 5$ GeV, and $\left|\Delta\phi(\ell\ell, \mathbf{p}_{\mathrm{T}}^{\mathrm{miss}})\right| > 1.5$ for electrons (a) and muons (b) in the 0-4 GeVrange.

- **Isolation and Match Efficiency Scale Factors** The difference in the efficiency for the lepton-track match and the isolation between data and MC is an additional source of systematic uncertainties. This is obtained by varying the SF obtained in 9.3.3 and 9.3.4 by $\pm 1\sigma$.

9.7 Results

With the background estimate presented in section 9.5 it is then possible to look at the data in the SRs. Contrary to what was done in the previous analysis, the background is not normalized to the data in a CR, and so no background only fit is done. The background is obtained directly from the estimate in 9.5, and assigning the systematic uncertainty presented in 9.6. Table 48 shows the estimated background yields and its uncertainty and the observed events in the 1ℓ+track SR. A small excess is present in the first bins, however it is not statistically significant, since it is within the uncertainty. 8 events are observed against and expected background of 3.0 ± 2.0, that account for $\sim 1.5\sigma$ of significance. Figure 169 shows the $m_{\ell t}$ distribution inside the SRs (the 5-10 GeVbin is not in the SR). In both the table and the figure the uncertainties contains the statistical and the systematic ones. From table 47 it is possible to see that the main uncertainty entering the SR is the statistic on the SS data itself, and in some bins

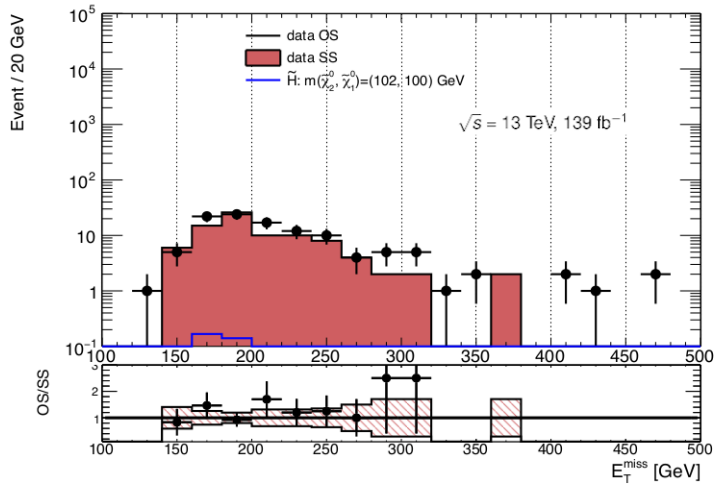

Figure 164: $E_{\mathrm{T}}^{\mathrm{miss}}$ distribution after preselection, $\left|\Delta\phi(\ell\ell, \mathbf{p}_{\mathrm{T}}^{\mathrm{miss}})\right| > 1.5$, $m_{\ell \mathrm{t}} < 2$ GeV, and $p_{\mathrm{T}}^{track} < 5$ GeV.

it can reach over 100 %. This is intrinsic in the method, since the background statistic is taken from data itself.

9.8 Interpretation

The results are interpreted in the context of simplified models of supersymmetry. Signal regions are used to set limits on two simplified models - one with Higgsino LSPs and another based on wino production decaying to a bino LSP. Exclusion fits are performed and hypothesis testing using HistFitter to determine the confidence of exclusion using the CLs prescription [208]. This procedure is used to sets limits at 95 % confidence level (CL) on the observed and expected number of signal events. The asymptotic approximation is used throughout rather than pseudoexperiments 'toys' to improve performance.

9.8.1 Compressed Higgsinos

Figure 170 shows the obtained exclusion limit for the higgsino signals using only the 1ℓ+track signal region. Due to some excess in the

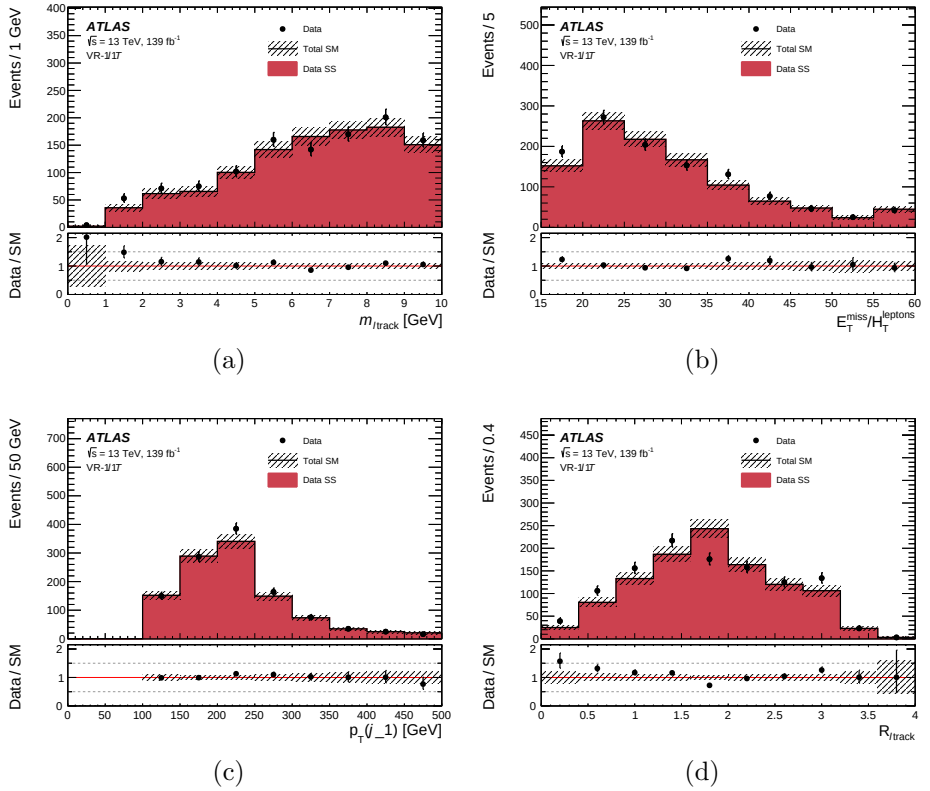

Figure 165: VR $-$ 1ℓ1T plots for all flavor channel.

first bins there is no excluded point. The loss in sensitivity, even if the excesses are small, is due to the fact that these excesses are in nearby bins, like the signal. The limits even if rather weak can be combined with the other 2ℓ selections and could help reach over the 2 σ for the exclusion of the points with a $\Delta m = 2$ GeV. The points at $\Delta m = 1$ GeV are rather difficult to be reached mainly due to the intrinsic lepton p_{T} threshold.

9.8.2 Compressed Wino-Bino

Figure 171 shows the obtained exclusion limit for Wino/Bino interpretation using the 1ℓ+track signal region. Two different assumptions are made on the relative sign of the mass parameter of the $\tilde{\chi}_2^0$ and $\tilde{\chi}_1^0$. In figure 171 (a) it is assumed $m(\tilde{\chi}_2^0) \times m(\tilde{\chi}_1^0) > 0$, as in the wino-bino

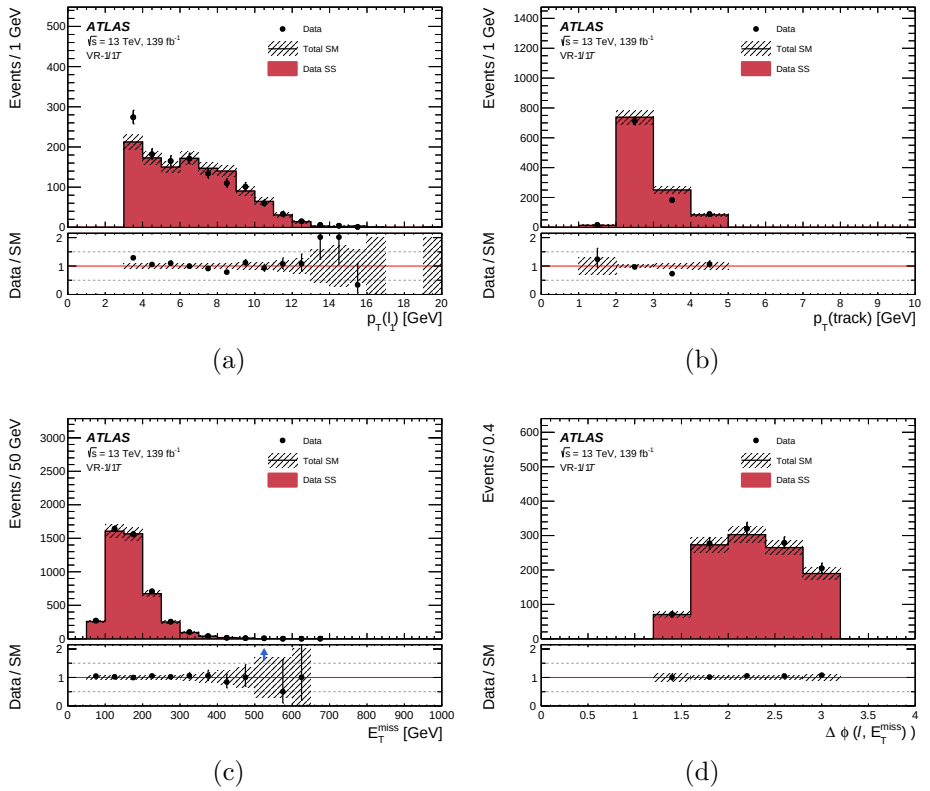

Figure 166: VR $-$ 1ℓ1T plots for all flavor channel.

interpretation used in the 2015+2016 2ℓ analysis (presented in section 8), while in figure 171 (b) it is assumed $m(\tilde{\chi}_2^0) \times m(\tilde{\chi}_1^0) < 0$. Note that here the physical masses are still positive. It is just the mass parameters that are can be negative. In the second scenario the $m_{\ell t}$ shape is the same as for the Higgsino case, but with an higher cross section. The case shown in (c) is obtained by reweighting each signal events in scenario (b) by the ratio of the $m_{\ell t}$ distribution shown in figure 10.

For the Wino / Bino interpretation the contour excludes only a part of the grid, again this is due to the mild excess of events in the first bins.

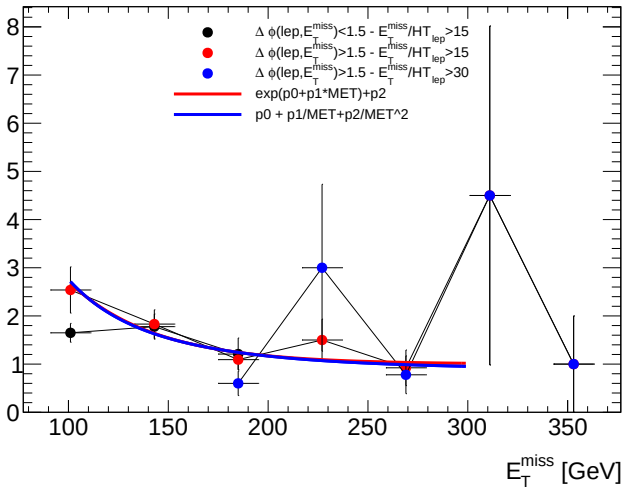

Figure 167: OS/SS ratio as a function of $E_{\mathrm{T}}^{\mathrm{miss}}$ for $m_{\ell \mathrm{t}} < 2$ GeV, with the following selections: $\left|\Delta\phi(\ell\ell, \mathbf{p}_{\mathrm{T}}^{\mathrm{miss}})\right| < 1.5$, $E_{\mathrm{T}}^{\mathrm{miss}}/H_{\mathrm{T}}^{\mathrm{lep+trk}} > 15$, $E_{\mathrm{T}}^{\mathrm{miss}} < 180$ GeV (black), $\left|\Delta\phi(\ell\ell, \mathbf{p}_{\mathrm{T}}^{\mathrm{miss}})\right| > 1.5$ and $E_{\mathrm{T}}^{\mathrm{miss}}/H_{\mathrm{T}}^{\mathrm{lep+trk}} > 15$ (red), and $\left|\Delta\phi(\ell\ell, \mathbf{p}_{\mathrm{T}}^{\mathrm{miss}})\right| > 1.5$ and $E_{\mathrm{T}}^{\mathrm{miss}}/H_{\mathrm{T}}^{\mathrm{lep+trk}} > 30$ (blue). The red and blue lines are, respectively, an exponential and a polynomial fit of the red data points.

9.9 Combination

As said in the introduction of this chapter, this analysis was inside a larger effort for the search of supersymmetry with compressed spectra. All the different signal regions were designed to be orthogonal, so that they could be combined. The channel considered in the combination are the following:

- SR-E-low: SR using the low $E_{\mathrm{T}}^{\mathrm{miss}}$ region, on the turn on of the trigger, targeting signals with a mass splitting larger than $\Delta m(\tilde{\chi}_2^0, \tilde{\chi}_1^0) \sim 10$ GeV
- SR-E-med: SR using the low $E_{\mathrm{T}}^{\mathrm{miss}}$ region, on the turn on of the trigger, targeting signals with a mass splitting $\Delta m(\tilde{\chi}_2^0, \tilde{\chi}_1^0) < 10$ GeV
- SR-E-high: requires $E_{\mathrm{T}}^{\mathrm{miss}} > 200$ GeV, on the plateau of the

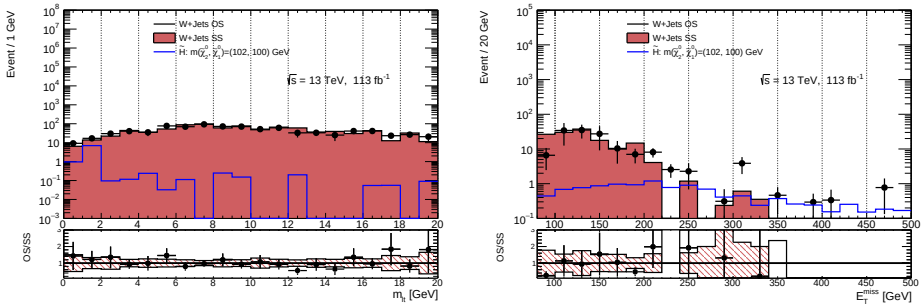

(a) (b)

Figure 168: OS/SS ratio as a function of $m_{\ell t}$ (left, $E_{\mathrm{T}}^{\mathrm{miss}} > 180$ GeV) and $E_{\mathrm{T}}^{\mathrm{miss}}$ (right, for $m_{\ell t} < 2$ GeV)

efficiency of the $E_{\mathrm{T}}^{\mathrm{miss}}$ triggers.

- SR-E-1ℓ1T: SR with 1 lepton and 1 track, presented in this chapter.

Figure 172 shows the expected yields in all the SR with 2ℓ and the $1\ell + 1$track together with the observed events. In the bottom panel it is shown the statistical significance of all the signal regions. No statistically significant excess is observed in any SR, with all bins being below 2σ. However some adjacent bins show excess, as would the signal, causing a reduction of the observed limits with respect of the expected limits.

9.9.1 Model Independent Limits

The combination of all the SRs is also used to place upper limits at 95% of confidence level (CL) on the observed and expected number of signal events $S^{95}_{\mathrm{obs\ (exp)}}$ in each SR, and on the visible cross section of $\langle \epsilon\sigma \rangle^{95}_{\mathrm{obs}}$ of new physics. Results are shown in Table 49, together with the $p-$value for each bin, so that it is possible to quantify the probability of producing yields equal or greater than the observed one, under the hypothesis of background-only. Some regions have low p-values due to excesses, with the lowest in $m_{\ell\ell} < 20$ GeV, corresponding to a local significance of 2.7σ.

Uncertainty of Signal Regions	SR_eMLLa	SR_eMLLb	SR_eMLLc	SR_eMLLd	SR_eMLLe	SR_eMLLf
Total background expectation	1.00	3.00	6.00	16.00	22.00	19.00
Total statistical ($\sqrt{N_{\text{exp}}}$)	±1.00	±1.73	±2.45	±4.00	±4.69	±4.36
Total background systematic [abs]	±1.04	±1.95	±3.04	±4.4	±5.38	±4.9
Total background systematic [%]	[104.40%]	[65.06%]	[50.66%]	[27.73%]	[24.47%]	[25.89%]
stat bin eMLLa	±1.00	±0.00	±0.00	±0.00	±0.00	±0.00
OSSS Closure	±0.30	±0.90	±1.80	±1.92	±2.64	±2.28
stat bin eMLLc	±0.00	±0.00	±2.45	±0.00	±0.00	±0.00
stat bin eMLLb	±0.00	±1.73	±0.00	±0.00	±0.00	±0.00
stat bin eMLLd	±0.00	±0.00	±0.00	±4.00	±0.00	±0.00
stat bin eMLLe	±0.00	±0.00	±0.00	±0.00	±4.69	±0.00
stat bin eMLLf	±0.00	±0.00	±0.00	±0.00	±0.00	±4.36

Table 47: SignalRegions. Breakdown of the dominant systematic uncertainties on background estimates in the various signal regions. Note that the individual uncertainties can be correlated, and do not necessarily add up quadratically to the total background uncertainty. The percentages show the size of the uncertainty relative to the total expected background. Each systematic uncertainty has its colour gradated by its relative contribution to the total background systematic, and only those with magnitude ≥ 1 percent are displayed to reduce clutter.

9.9.2 Model Dependent Limits

The combined model dependent limits are shown in figure 173, for the three models presented before: Higgsino (a), Wino/Bino with (b) $m(\tilde{\chi}_2^0) \times m(\tilde{\chi}_1^0) > 0$ and (c) $m(\tilde{\chi}_2^0) \times m(\tilde{\chi}_1^0) < 0$.

Figure 174 instead shows the expected and observed limits for both combination of all the results, and each channel by itself. These results are presented only for the Wino/Bino results, since in the Higgsino case there is no observed limits for the 1ℓ+track channel.
These plots shows how the 1ℓ+track channel can improve the sensitivity and the exclusion limits at low Δm, and at very low Δm, this analysis has the best expected limits. Instead it is also possible to see how the low $E_{\text{T}}^{\text{miss}}$ regions helps to recover sensitivity at high Δm.
The difference in behavior of the two Wino / Bino hypothesis at $\Delta m \sim 30 - 40$ GeV is due to the different shape of the $m_{\ell\ell}$ in these two cases. In fact in the case with $m(\tilde{\chi}_2^0) \times m(\tilde{\chi}_1^0) > 0$ the $m_{\ell\ell}$ for a signal with $\Delta m \sim 30 - 40$ GeV peaks at around $m_{\ell\ell} \sim 30 - 40$ GeV, where there is an excess. Instead in the case with $m(\tilde{\chi}_2^0) \times m(\tilde{\chi}_1^0) < 0$ the $m_{\ell\ell}$ distribution for the same signals peaks at $m_{\ell\ell} \sim 15 - 20$ GeV,

Region	SR_eMLTa	SR_eMLTb	SR_eMLTc	SR_eMLTd	SR_eMLTe	SR_eMLTf
Observed events	0	8	8	24	24	16
SS events	$1.000^{+1.044}_{-1.000}$	3.000 ± 1.952	6.000 ± 3.040	16.000 ± 4.437	22.000 ± 5.382	19.000 ± 4.919

Table 48: Expected yields from SS data for an integrated luminosity of 139 fb^{-1}. The errors shown are the statistical plus systematic uncertainties. Uncertainties on the yields are symmetric by construction, where the negative error is truncated when reaching to zero event yield.

and therefore the excess is more relevant for the first case.
The analysis was able to exclude different signal models. Considering the Higgsino production scenario, signal with a mass of the $\tilde{\chi}_1^0$ up to $\sim$ 175 GeV were excluded for a $\Delta m \sim 9$ GeV, while signals down to $\sim$ 2.4 GeV were excluded for $m(\tilde{\chi}_1^0) \sim 100$ GeV. Instead, for the Wino / Bino production scenario, with the assumption $m(\tilde{\chi}_2^0) \times m(\tilde{\chi}_1^0) < 0$, the exclusion power reached signal with a mass of the $\tilde{\chi}_1^0$ up to $\sim$ 225 GeV for a $\Delta m \sim 8.5$ GeV, while signals were also excluded from $\sim$ 1.5 GeV to $\sim$ 30 GeV for $m(\tilde{\chi}_1^0) \sim 100$ GeV. Instead, still for Wino / Bino production, but with the assumption $m(\tilde{\chi}_2^0) \times m(\tilde{\chi}_1^0) > 0$, signals were excluded at $\Delta m \sim 6$ GeV up until $\sim$ 230 GeV, while at $m(\tilde{\chi}_1^0) \sim 100$ GeV signals were excluded from $\sim$ 1.5 GeV to $\sim$ 40 GeV, and at $\Delta m \sim 40$ GeV up to a mass of the $\tilde{\chi}_1^0$ of 160 GeV.

Signal Region	N_{obs}	N_{exp}	$\langle\epsilon\sigma\rangle^{95}_{\text{obs}}$ [fb]	S^{95}_{obs}	S^{95}_{exp}	$p(s=0)$
$m_{\ell\ell} < 1$	0	1.1 ± 1.0	0.02322	3.227	$3.006^{+0.016}_{-0.012}$	0.50
$m_{\ell\ell} < 2$	46	44 ± 6.8	0.15	21	19^{+7}_{-5}	0.38
$m_{\ell\ell} < 3$	90	77 ± 12	0.29	41	30^{+12}_{-8}	0.18
$m_{\ell\ell} < 5$	151	138 ± 18	0.38	52	43^{+16}_{-11}	0.24
$m_{\ell\ell} < 10$	244	200 ± 19	0.62	90	50^{+40}_{-13}	0.034
$m_{\ell\ell} < 20$	383	301 ± 23	1.0	140	80^{+50}_{-34}	0.0035
$m_{\ell\ell} < 30$	453	366 ± 27	1.04	144	69^{+27}_{-19}	0.0061
$m_{\ell\ell} < 40$	492	420 ± 30	0.97	130	70^{+40}_{-20}	0.026
$m_{\ell\ell} < 60$	583	520 ± 35	0.97	135	83^{+33}_{-23}	0.061

Table 49: Left to right: The first column indicates the inclusive signal region under study, considering both events in the 2ℓ and 1ℓ+track channels. The next two columns present observed (N_{obs}) and expected (N_{exp}) event yields in the inclusive signal regions. The latter are obtained by the background-only fit of the control regions, and the errors include both statistical and systematic uncertainties. The next two columns show the observed 95% CL upper limits on the visible cross section ($\langle\epsilon\sigma\rangle^{95}_{\text{obs}}$) and on the number of signal events (S^{95}_{obs}). The next column $\left(S^{95}_{\text{exp}}\right)$ shows the 95% CL upper limit on the number of signal events, given the expected number (and $\pm 1\sigma$ deviations from the expectation) of background events. The last column indicates the discovery p-value ($p(s=0)$).

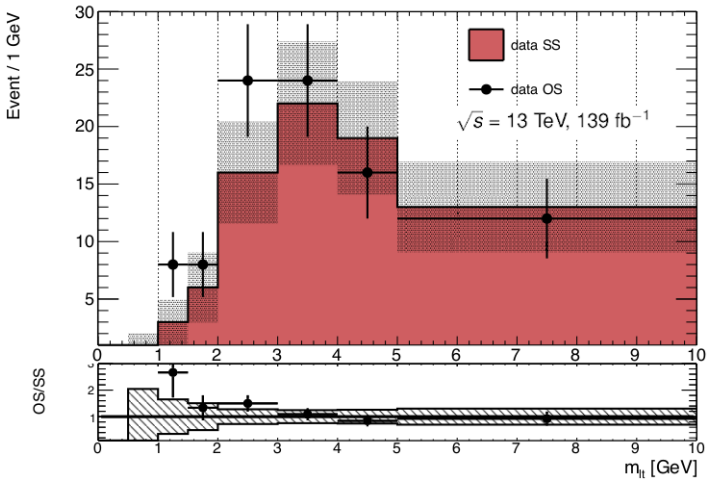

Figure 169: $m_{\ell t}$ distribution in the SR. Uncertainties band contain statistical and systematic error. The 5-10 GeVis not in the SR

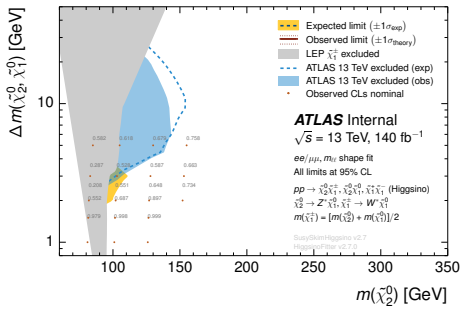

Figure 170: Expected and observed exclusion contours for the Higgsino grid using the 1ℓ+track selection

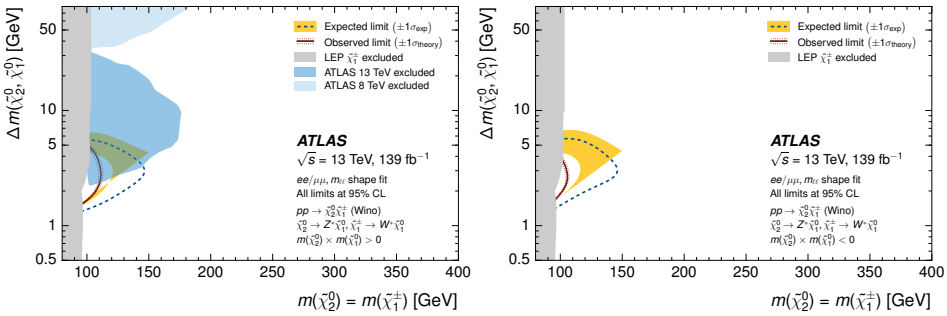

(a) (b)

Figure 171: Expected and observed exclusion contours for the Wino / Bino grid using the 1ℓ+track selection, with assumption (a) $m(\tilde{\chi}_2^0) \times m(\tilde{\chi}_1^0) > 0$ and (b) $m(\tilde{\chi}_2^0) \times m(\tilde{\chi}_1^0) < 0$

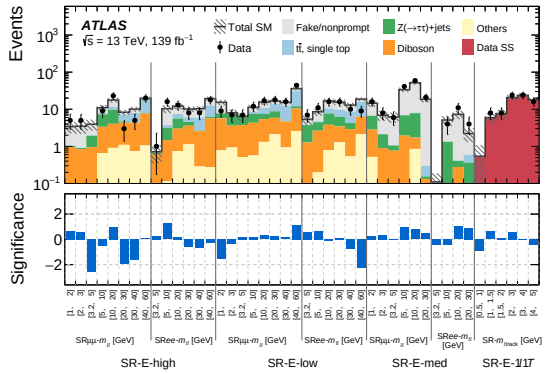

Figure 172: Expected and observed yields in all the 2ℓ channels and in the one lepton + one track selection

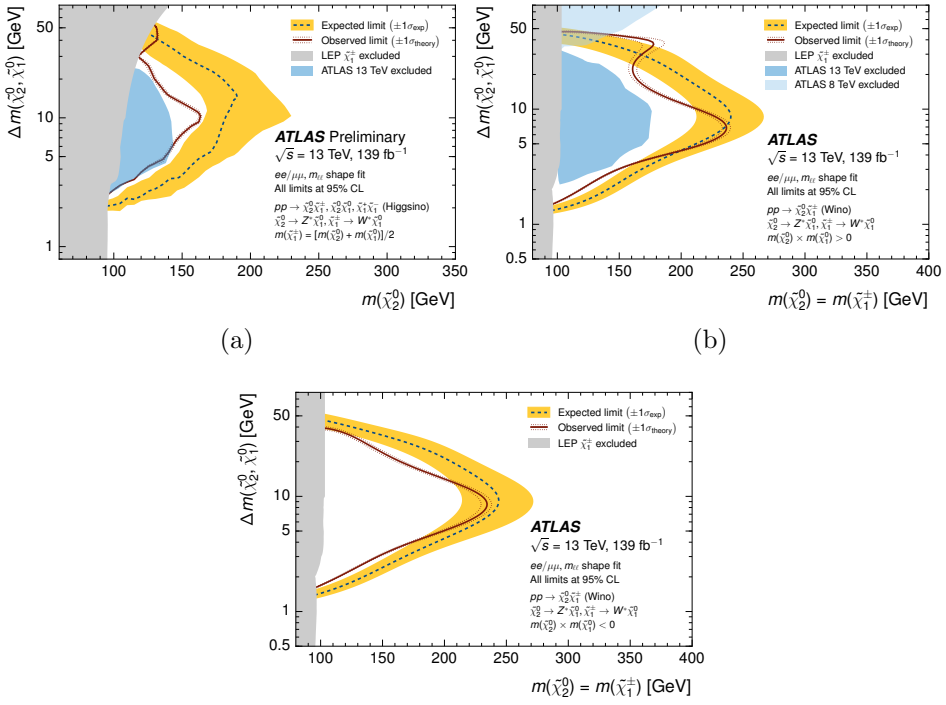

Figure 173: Expected and observed exclusion contours combining all the 2ℓ channels and the 1ℓ+track selection for the model with (a) Higgsino and Wino / Bino with (b) $m(\tilde{\chi}_2^0) \times m(\tilde{\chi}_1^0) > 0$ and (c) $m(\tilde{\chi}_2^0) \times m(\tilde{\chi}_1^0) < 0$.

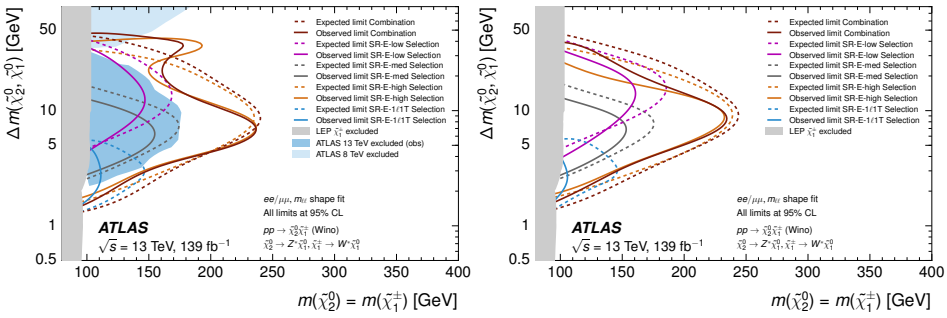

(a) (b)

Figure 174: Expected and observed exclusion contours combining all the 2ℓ channels and the 1ℓ+track selection, and for each channel separately for the Wino /Bino model with (a) $m(\tilde{\chi}_2^0) \times m(\tilde{\chi}_1^0) > 0$ and (b) $m(\tilde{\chi}_2^0) \times m(\tilde{\chi}_1^0) < 0$.

10 Conclusions

This thesis presented the analyses for electroweak production of supersymmetric particles with a compressed mass spectrum. The analyses were performed using the data collected by the ATLAS detector at the LHC during the so called Run 2, between 2015 and 2018. Two analyses were presented, one targeting a final state with 2 leptons, $E_{\mathrm{T}}^{\mathrm{miss}}$, and an energetic initial state radiation jet, that used data from 2015 and 2016, for a total of 36.1 fb^{-1}. The second analysis instead searched for events with 1 lepton and 1 track in the final state, still in association with $E_{\mathrm{T}}^{\mathrm{miss}}$ and ISR jet; the analysis used data from the whole Run 2, with a total integrated luminosity of 139 fb^{-1}.
The analysis strategies are the same in both the analyses: different signal regions are defined, by optimizing the statistical significance. Two kind of SR are defined: exclusive and inclusive. The first try to maximize the exclusion power with a set of orthogonal SRs, while the second one maximize the discovery power, with non-orthogonal SR. The SR are binned in $m_{\ell\ell}$ (for the 2 lepton analysis) or in $m_{\ell \mathrm{t}}$ (for the 1 lepton 1 track analysis).
In the first analysis the main background comes from non prompt and fake leptons (jets or conversion photon that are misidentified as leptons), diboson events (WW, WZ, ZZ), top events ($t\bar{t}, Wt$), and $Z \to \tau\tau$+jets. The fakes are dealt with a data driven method, called Fake Factor, while for top and $Z \to \tau\tau$+jets specific control regions are defined to constrain the MC to the observed data, transfer factors are obtained and applied to these backgrounds in the SR.
No statistically significant excess was found, and the results were used to set limits on superparticles masses. Two different interpretations were considered: one with the electroweakino produced were mainly higgsino, with the mass of the $\tilde{\chi}_1^{\pm}$ in between the $\tilde{\chi}_2^0$ and the $\tilde{\chi}_1^0$. In the other scenario considered, the electroweakinos are a mix of Wino / Bino, in this case the mass of the $\tilde{\chi}_1^{\pm}$ is the same as the $\tilde{\chi}_2^0$. In the first interpretation limits were set up to a mass of 145 GeV of the $\tilde{\chi}_2^0$, for a mass splitting ($\Delta m(\tilde{\chi}_2^0, \tilde{\chi}_1^0)$) of $\sim 5 - 10$ GeV, and going down to $\Delta m(\tilde{\chi}_2^0, \tilde{\chi}_1^0) \sim 2.5$ GeV for masses of $\tilde{\chi}_2^0$ of ~ 100 GeV. These results are important since they are the first in this interpretation since the LEP experiment. In the Wino / Bino interpretation instead limits were set on the $\tilde{\chi}_1^0$ mass up to 175 GeVfor a $\Delta m(\tilde{\chi}_2^0, \tilde{\chi}_1^0)$ in

the range of $\sim 5 - 10$ GeV, much higher than the higgsino. Signal were also excluded down to $\Delta m(\tilde{\chi}_2^0, \tilde{\chi}_1^0) \sim 2.$ GeV for masses of $\tilde{\chi}_2^0$ of ~ 100 GeV.

In the 1 lepton + 1 track analysis the background is instead completely data driven, using data with pair of lepton and track with the same sign as a proxy for the data with lepton-track pair with opposite sign. This is done since the main source of background comes from events with one lepton and an uncorrelated track. The probability of these events is then the same for lepton-track couple with opposite sign or same sign. The difference from unity of the ratio Opposite Sign and Same Sign is taken as an uncertainty. Tracks were required also to have a match with an object in the list of reconstructed (but not necessarily identified) electrons or muons (this list called container). This was done in order to reduce the background due to hadrons.

No significant excess was found, even if some mild excess (below 2σ) was found in some adjacent bins, causing the observed limits to be weaker than the expected.

In the 1 lepton + 1 track analysis instead were used three different interpretation to set limits, the first one is still the Higgsino interpretation, while the other two are Wino / Bino, but with two different assumption on the sign of the mass parameter. The first has $m(\tilde{\chi}_2^0) \times m(\tilde{\chi}_1^0) < 0$ while the second $m(\tilde{\chi}_2^0) \times m(\tilde{\chi}_1^0) > 0$. The positive signed case is the same Wino / Bino scenario as for the 2 lepton analysis, while the negative signed one is a new one.

In the Higgsino case, limits were set on the $\tilde{\chi}_2^0$ mass up to ~ 175 GeV for a $\Delta m \sim 9$ GeV, while signals down to ~ 2.4 GeV were excluded for $m(\tilde{\chi}_1^0) \sim 100$ GeV. For the Wino / Bino with $m(\tilde{\chi}_2^0) \times m(\tilde{\chi}_1^0) < 0$ limits on the signal were set up to a mass of the $\tilde{\chi}_2^0 \sim 225$ GeV for a $\Delta m \sim 8.5$ GeV, while signals were also excluded from ~ 1.5 GeV to ~ 30 GeV for $m(\tilde{\chi}_2^0) \sim 100$ GeV. Instead, still for Wino / Bino production, but with the assumption $m(\tilde{\chi}_2^0) \times m(\tilde{\chi}_1^0) > 0$, signals were excluded at $\Delta m \sim 6$ GeV up until ~ 230 GeV, while at $m(\tilde{\chi}_2^0) \sim 100$ GeV signals were excluded from ~ 1.5 GeV to ~ 40 GeV, and at $\Delta m \sim 40$ GeV up to a mass of the $\tilde{\chi}_1^0$ of 160 GeV.

The results of both analyses are an important results for the SUSY community, setting limits on models that were not yet tested by experiments in the last 20 years. Results are also interesting because they

prove how well the ATLAS detector is able to reconstruct and correctly identify leptons with very soft momentum, even below 5 GeV. At the moment no significant deviation from the Standard Model has been found, and now the LHC is undergoing a 2 year period of shut down, were many improvement will be done on the detectors. During this shut down period additional studies will be done in order to combine together all the SUSY results, in order to have a more complete view of the field. After this period, in 2021, in the so called Run 3, additional data are expected, for a total integrated luminosity of 300 $\text{fb}^{-1}$by the end of 2023. Discussions on the strategy on how to use all of these new data are already undergoing. Moreover the energy of the center of mass of the pp collision will be increased to $\sqrt{s} = 14$ TeV. The new data, combined with the increased energy, will provide a fascinating opportunity to keep investigating the nature of the Standard Model, and to look into corners not yet probed, to search for hint of new physics.

11 Bibliography

References

[1] *The ATLAS Experiment at the CERN Large Hadron Collider*, JINST **3** (2008) S08003.

[2] The CMS Collaboration, *The CMS experiment at the CERN LHC*, Journal of Instrumentation **3** (2008) S08004, URL: https://doi.org/10.1088%2F1748-0221%2F3%2F08%2Fs08004.

[3] L. Evans and P. Bryant, *LHC Machine*, JINST **3** (2008) S08001.

[4] ATLAS Collaboration, *Observation of a new particle in the search for the standard model Higgs boson with the ATLAS detector at the LHC*, Phys. Lett. **B 716** (2012) 1, arXiv: 1207.7214 [hep-ex].

[5] CMS Collaboration, *Observation of a new boson at a mass of 125 GeV with the CMS experiment at the LHC*, Phys. Lett. **B 716** (2012) 30, arXiv: 1207.7235 [hep-ex].

[6] S. L. Glashow, *Partial symmetries of weak interactions*, Nucl. Phys. **22** (1961) 579.

[7] S. Weinberg, *A model of leptons*, Phys. Rev. Lett. **19** (1967) 1264.

[8] A. Salam, *In elementary particle theory, p. 367*, ed. by N. Svartholm, Stockholm: Almqvist and Wiksell, 1968.

[9] G. Bertone, D. Hooper and J. Silk, *Particle dark matter: Evidence, candidates and constraints*, Phys. Rept. **405** (2005) 279, arXiv: hep-ph/0404175.

[10] Plank Collaboration, *Planck 2013 results. XVI. Cosmological parameters*, 2013, arXiv: 1303.5076 [astro-ph.CO].

[11] V. C. Rubin and W. K. Ford Jr., *Rotation of the Andromeda Nebula from a Spectroscopic Survey of Emission Regions*, apj **159** (Feb. 1970) 379.

[12] Y. e. a. Fukuda,
Evidence for Oscillation of Atmospheric Neutrinos,
Phys. Rev. Lett. **81** (8 Aug. 1998) 1562, URL: https://link.aps.org/doi/10.1103/PhysRevLett.81.1562.

[13] Z.-Z. Xing and S. Zhou,
'Cosmological Matter-antimatter Asymmetry',
Neutrinos in Particle Physics, Astronomy and Cosmology,
Berlin, Heidelberg: Springer Berlin Heidelberg, 2011 375,
ISBN: 978-3-642-17560-2,
URL: https://doi.org/10.1007/978-3-642-17560-2_11.

[14] H. Georgi and S. L. Glashow,
Unity of All Elementary-Particle Forces,
Phys. Rev. Lett. **32** (8 Feb. 1974) 438, URL:
https://link.aps.org/doi/10.1103/PhysRevLett.32.438.

[15] G. F. Giudice, *Naturalness after LHC8*,
PoS **EPS-HEP2013** (2013) 163,
arXiv: 1307.7879 [hep-ph].

[16] G. F. Giudice, *Naturally Speaking: The Naturalness Criterion and Physics at the LHC*, (2008) 155,
arXiv: 0801.2562 [hep-ph].

[17] J. L. Feng, *Naturalness and the Status of Supersymmetry*,
Ann. Rev. Nucl. Part. Sci. **63** (2013) 351,
arXiv: 1302.6587 [hep-ph].

[18] WMAP Collaboration,
Seven-Year Wilkinson Microwave Anisotropy Probe (WMAP) Observations: Cosmological Interpretation,
Astrophys. J. Suppl. **192** (2011) 18,
arXiv: 1001.4538 [astro-ph.CO].

[19] F. Zwicky,
On the Masses of Nebulae and of Clusters of Nebulae,
apj **86** (Oct. 1937) 217.

[20] G. Steigman and M. S. Turner, *Cosmological Constraints on the Properties of Weakly Interacting Massive Particles*,
Nucl. Phys. B **253** (1985) 375.

[21] K. Griest and D. Seckel,
Three exceptions in the calculation of relic abundances,
Phys. Rev. D **43** (10 May 1991) 3191, URL:
https://link.aps.org/doi/10.1103/PhysRevD.43.3191.

[22] J. Edsjö and P. Gondolo,
Neutralino relic density including coannihilations,
Phys. Rev. D **56** (4 Aug. 1997) 1879, URL:
https://link.aps.org/doi/10.1103/PhysRevD.56.1879.

[23] P. Mobius,
Green, M. B.; Schwarz, J. H.; Witten, E., Superstring Theory. Vol. 1: Introduction. Cambridge etc., Cambridge University Press 1987. X, 469 pp., £ 32.50 B/C H/c. ISBN 0 521 32384 3 (Cambridge Monographs on Mathematical Physics), ZAMM - Journal of Applied Mathematics and Mechanics / Zeitschrift für Angewandte Mathematik und Mechanik **68** (1988) 258,
eprint: https://onlinelibrary.wiley.com/doi/pdf/10.1002/zamm.19880680630, URL: https://onlinelibrary.wiley.com/doi/abs/10.1002/zamm.19880680630.

[24] C. Rovelli, *Quantum Gravity*,
Cambridge Monographs on Mathematical Physics,
Cambridge University Press, 2004.

[25] Y. Golfand and E. Likhtman, *Extension of the Algebra of Poincare Group Generators and Violation of p Invariance*,
JETP Lett. **13** (1971) 323.

[26] D. Volkov and V. Akulov,
Is the Neutrino a Goldstone Particle?,
Phys. Lett. B **46** (1973) 109.

[27] J. Wess and B. Zumino,
Supergauge Transformations in Four-Dimensions,
Nucl. Phys. B **70** (1974) 39.

[28] J. Wess and B. Zumino, *A Lagrangian Model Invariant Under Supergauge Transformations*, Phys. Lett. B **49** (1974) 52.

[29] R. Barbieri, S. Ferrara and C. Savoy,
Gauge models with spontaneously broken local supersymmetry,
Physics Letters B **119** (1982) 343 , ISSN: 0370-2693,
URL: http://www.sciencedirect.com/science/article/pii/0370269382906852.

[30] S. Ferrara and B. Zumino,
Supergauge invariant Yang-Mills theories,
Nuclear Physics B **79** (1974) 413 , ISSN: 0550-3213,
URL: http://www.sciencedirect.com/science/article/pii/0550321374905598.

[31] A. Salam and J. Strathdee,
Super-symmetry and non-Abelian gauges,
Physics Letters B **51** (1974) 353 , ISSN: 0370-2693,
URL: http://www.sciencedirect.com/science/article/pii/0370269374902263.

[32] S. P. Martin, *A Supersymmetry primer*,
(1997) 1, [Adv. Ser. Direct. High Energy Phys.18,1(1998)],
arXiv: hep-ph/9709356 [hep-ph].

[33] U. Ellwanger, C. Hugonie and A. M. Teixeira,
The Next-to-Minimal Supersymmetric Standard Model,
Phys. Rept. **496** (2010) 1, arXiv: 0910.1785 [hep-ph].

[34] N. Craig,
'The State of Supersymmetry after Run I of the LHC',
Beyond the Standard Model after the first run of the LHC Arcetri, Florence, Italy, May 20-July 12, 2013, 2013,
arXiv: 1309.0528 [hep-ph].

[35] Z. Han et al., *Hunting quasidegenerate Higgsinos*,
Phys. Rev. **D89** (2014) 075007, arXiv: 1401.1235 [hep-ph].

[36] H. Baer et al.,
Radiatively-driven natural supersymmetry at the LHC,
JHEP **12** (2013) 013, [Erratum: JHEP06,053(2015)],
arXiv: 1310.4858 [hep-ph].

[37] H. Fukuda et al., *Higgsino Dark Matter or Not: Role of Disappearing Track Searches at the LHC and Future Colliders*,
Phys. Lett. **B781** (2018) 306, arXiv: 1703.09675 [hep-ph].

[38] S. D. Thomas and J. D. Wells,
Phenomenology of Massive Vectorlike Doublet Leptons,
Phys. Rev. Lett. **81** (1998) 34,
arXiv: hep-ph/9804359 [hep-ph].

[39] M. M. Nojiri and Y. Yamada,
Neutralino decays at the CERN LHC,
Phys. Rev. **D60** (1999) 015006,
arXiv: hep-ph/9902201 [hep-ph].

[40] U. De Sanctis et al., *Perspectives for the detection and measurement of supersymmetry in the focus point region of mSUGRA models with the ATLAS detector at LHC*,
Eur. Phys. J. **C52** (2007) 743, arXiv: 0704.2515 [hep-ex].

[41] D. Collaboration, *DarkSide search for dark matter*,
Journal of Instrumentation **8** (2013) C11021, URL: https://doi.org/10.1088%2F1748-0221%2F8%2F11%2Fc11021.

[42] J. A. Casas et al., *What is a Natural SUSY scenario?*,
JHEP **06** (2015) 070, arXiv: 1407.6966 [hep-ph].

[43] ATLAS Collaboration, *Search for a scalar partner of the top quark in the jets plus missing transverse momentum final state at $\sqrt{s}$=13 TeV with the ATLAS detector*,
JHEP **12** (2017) 085, arXiv: 1709.04183 [hep-ex].

[44] ATLAS Collaboration,
Search for direct top squark pair production in events with a Higgs or Z boson, and missing transverse momentum in $\sqrt{s} = 13$ TeV pp collisions with the ATLAS detector,
JHEP **08** (2017) 006, arXiv: 1706.03986 [hep-ex].

[45] ATLAS Collaboration,
Search for top squarks in final states with one isolated lepton, jets, and missing transverse momentum in $\sqrt{s} = 13$ TeV pp collisions with the ATLAS detector, (2016),
arXiv: 1606.03903 [hep-ex].

[46] ATLAS Collaboration,
Search for chargino and neutralino production in final states with a Higgs boson and missing transverse momentum at $\sqrt{s} = 13$ TeV with the ATLAS detector,
Phys. Rev. **D100** (2019) 012006,
arXiv: 1812.09432 [hep-ex].

[47] ATLAS Collaboration, *Search for pair production of higgsinos in final states with at least three b-tagged jets in $\sqrt{s} = 13$ TeV pp collisions using the ATLAS detector*,
Phys. Rev. **D98** (2018) 092002, arXiv: 1806.04030 [hep-ex].

[48] ATLAS Collaboration, *Search for electroweak production of supersymmetric particles in final states with two or three leptons at $\sqrt{s} = 13$ TeV with the ATLAS detector*, Eur. Phys. J. **C78** (2018) 995, arXiv: 1803.02762 [hep-ex].

[49] ATLAS Collaboration, *Search for B-L R -parity-violating top squarks in $\sqrt{s}$ =13 TeV pp collisions with the ATLAS experiment*, Phys. Rev. **D97** (2018) 032003, arXiv: 1710.05544 [hep-ex].

[50] ATLAS Collaboration, *Search for heavy charged long-lived particles in the ATLAS detector in 36.1 fb^{-1} of proton-proton collision data at $\sqrt{s} = 13$ TeV*, Phys. Rev. **D99** (2019) 092007, arXiv: 1902.01636 [hep-ex].

[51] D. Alves, *Simplified Models for LHC New Physics Searches*, J. Phys. **G39** (2012) 105005, ed. by N. Arkani-Hamed et al., arXiv: 1105.2838 [hep-ph].

[52] ATLAS Collaboration, *SUSY July 2019 Summary Plot Update*, (), URL: https://atlas.web.cern.ch/Atlas/GROUPS/PHYSICS/PUBNOTES/ATL-PHYS-PUB-2019-022/.

[53] ATLAS Collaboration, *SUSY Summary Plot*, (), URL: http://atlas.web.cern.ch/Atlas/GROUPS/PHYSICS/CombinedSummaryPlots/SUSY/.

[54] ALEPH, DELPHI, L3, OPAL Experiments, *Combined LEP Chargino Results, up to 208 GeV for low DM*, (2002), URL: http://lepsusy.web.cern.ch/lepsusy/www/inoslowdmsummer02/charginolowdm_pub.html.

[55] ALEPH, DELPHI, L3, OPAL Experiments, *Combined LEP Selectron/Smuon/Stau Results, 183-208 GeV*, (2004), URL: http://lepsusy.web.cern.ch/lepsusy/www/sleptons_summer04/slep_final.html.

[56] ALEPH Collaboration, *Search for scalar leptons in e^+e^- collisions at center-of-mass energies up to 209 GeV*, Phys. Lett. B **526** (2002) 206, arXiv: hep-ex/0112011.

[57] ALEPH Collaboration, *Search for charginos nearly mass degenerate with the lightest neutralino in e^+e^- collisions at center-of-mass energies up to 209 GeV*, Phys. Lett. B **533** (2002) 223, arXiv: hep-ex/0203020.

[58] ALEPH Collaboration, *Absolute lower limits on the masses of selectrons and sneutrinos in the MSSM*, Phys. Lett. B **544** (2002) 73, arXiv: hep-ex/0207056.

[59] ALEPH Collaboration, *Absolute mass lower limit for the lightest neutralino of the MSSM from e^+e^- data at $\sqrt{s}$ up to 209 GeV*, Phys. Lett. B **583** (2004) 247.

[60] DELPHI Collaboration, *Searches for supersymmetric particles in e^+e^- collisions up to 208 GeV and interpretation of the results within the MSSM*, Eur. Phys. J. C **31** (2003) 421, arXiv: hep-ex/0311019.

[61] L3 Collaboration, *Search for charginos with a small mass difference with the lightest supersymmetric particle at $\sqrt{s} = 189$ GeV*, Phys. Lett. B **482** (2000) 31, arXiv: hep-ex/0002043.

[62] L3 Collaboration, *Search for scalar leptons and scalar quarks at LEP*, Phys. Lett. B **580** (2004) 37, arXiv: hep-ex/0310007.

[63] OPAL Collaboration, *Search for anomalous production of dilepton events with missing transverse momentum in e^+e^- collisions at $\sqrt{s} = 183$ GeV to 209 GeV*, Eur. Phys. J. C **32** (2004) 453, arXiv: hep-ex/0309014.

[64] OPAL Collaboration, *Search for nearly mass degenerate charginos and neutralinos at LEP*, Eur. Phys. J. C **29** (2003) 479, arXiv: hep-ex/0210043.

[65] A. Anandakrishnan and C. S. Hill, *Connecting Simplified Models: Constraining Supersymmetry on Triangles*, Phys. Lett. **B735** (2014) 412, arXiv: 1403.4294 [hep-ex].

[66] The CEPC Study Group, *CEPC-SPPC Preliminary Conceptual Design Report. 1. Physics and Detector*, (2015).

[67] The CEPC Study Group, *CEPC Conceptual Design Report: Volume 2 - Physics & Detector*, (2018), ed. by J. B. Guimaraes da Costa et al., arXiv: 1811.10545 [hep-ex].

[68] FCC Collaboration, *FCC-ee: The Lepton Collider*, Eur. Phys. J. ST **228** (2019) 261.

[69] CLIC Collaboration, *Detector Technologies for CLIC*, (2019), ed. by D. Dannheim et al., arXiv: 1905.02520 [physics.ins-det].

[70] ILC Collaboration, *ILC Reference Design Report Volume 1 - Executive Summary*, (2007), ed. by J. Brau, Y. Okada and N. Walker, arXiv: 0712.1950 [physics.acc-ph].

[71] ILC Collaboration, *International Linear Collider Reference Design Report Volume 2: Physics at the ILC*, (2007), ed. by A. Djouadi et al., arXiv: 0709.1893 [hep-ph].

[72] ILC Collaboration, *ILC Reference Design Report Volume 3 - Accelerator*, (2007), ed. by N. Phinney, N. Toge and N. J. Walker, arXiv: 0712.2361 [physics.acc-ph].

[73] ILC Collaboration, *ILC Reference Design Report Volume 4 - Detectors*, (2007), ed. by T. Behnke et al., arXiv: 0712.2356 [physics.ins-det].

[74] The ALICE Collaboration, *The ALICE experiment at the CERN LHC*, Journal of Instrumentation **3** (2008) S08002, URL: https://doi.org/10.1088%2F1748-0221%2F3%2F08%2Fs08002.

[75] The LHCb Collaboration, *The LHCb Detector at the LHC*, Journal of Instrumentation **3** (2008) S08005, URL: https://doi.org/10.1088%2F1748-0221%2F3%2F08%2Fs08005.

[76] The TOTEM Collaboration, *The TOTEM Experiment at the CERN Large Hadron Collider*, Journal of Instrumentation **3** (2008) S08007, URL: https://doi.org/10.1088%2F1748-0221%2F3%2F08%2Fs08007.

[77] The LHCf Collaboration,
The LHCf detector at the CERN Large Hadron Collider,
Journal of Instrumentation **3** (2008) S08006, URL: https://doi.org/10.1088%2F1748-0221%2F3%2F08%2Fs08006.

[78] Pinfold, James L, *The MoEDAL Experiment at the LHC*,
EPJ Web of Conferences **71** (2014) 00111,
URL: https://doi.org/10.1051/epjconf/20147100111.

[79] ATLAS Collaboration,
The ATLAS inner detector commissioning and calibration,
Eur. Phys. J. **C 70** (2010) 787,
arXiv: 1004.5293 [physics.ins-det].

[80] G. Aad et al., *ATLAS pixel detector electronics and sensors*,
JINST **3** (2008) P07007.

[81] ATLAS Collaboration,
ATLAS Insertable B-Layer Technical Design Report, (2010).

[82] ATLAS SCT Collaboration,
The ATLAS semiconductor tracker (SCT),
Nucl. Instrum. Meth. **A541** (2005) 89, [,89(2005)].

[83] ATLAS TRT Collaboration, *The ATLAS TRT barrel detector*,
JINST **3** (2008) P02014.

[84] ATLAS Collaboration,
ATLAS liquid argon calorimeter: Technical design report,
(1996).

[85] ATLAS Collaboration,
ATLAS tile calorimeter: Technical Design Report,
Technical Design Report ATLAS, Geneva: CERN, 1996,
URL: https://cds.cern.ch/record/331062.

[86] ATLAS Collaboration,
ATLAS muon spectrometer: Technical Design Report,
Technical Design Report ATLAS, Geneva: CERN, 1997,
URL: https://cds.cern.ch/record/331068.

[87] ATLAS Collaboration, *Commissioning of the ATLAS muon spectrometer with cosmic rays*, Eur. Phys. J. **C 70** (2010) 875,
arXiv: 1006.4384 [physics.ins-det].

[88] J. P. Badiou et al.,
ATLAS barrel toroid: Technical design report, (1997).

[89] ATLAS Collaboration,
ATLAS endcap toroids: Technical design report, (1997).

[90] A. Yamamoto et al., *The ATLAS central solenoid*,
Nucl. Instrum. Meth. **A584** (2008) 53.

[91] ATLAS Collaboration,
Performance of the ATLAS Trigger System in 2015,
Eur. Phys. J. **C77** (2017) 317, arXiv: 1611.09661 [hep-ex].

[92] P. Jenni et al., *ATLAS high-level trigger, data-acquisition and controls: Technical Design Report*,
Technical Design Report ATLAS, Geneva: CERN, 2003,
URL: https://cds.cern.ch/record/616089.

[93] G. A. et al, *ATLAS pixel detector electronics and sensors*,
Journal of Instrumentation **3** (2008) P07007, URL: https://doi.org/10.1088%2F1748-0221%2F3%2F07%2Fp07007.

[94] B. Abbott et al.,
Production and Integration of the ATLAS Insertable B-Layer,
JINST **13** (2018) T05008,
arXiv: 1803.00844 [physics.ins-det].

[95] M. Garcia-Sciveres et al.,
The FE-I4 pixel readout integrated circuit,
Nuclear Instruments and Methods in Physics Research Section A: Accelerators, Spectrometers, Detectors and Associated Equipment **636** (2011) S155 , 7th International Hiroshima Symposium on the Development and Application of Semiconductor Tracking Detectors, ISSN: 0168-9002,
URL: http://www.sciencedirect.com/science/article/pii/S0168900210009551.

[96] I. Peri et al.,
The FEI3 readout chip for the ATLAS pixel detector,
Nuclear Instruments and Methods in Physics Research Section A: Accelerators, Spectrometers, Detectors and Associated Equipment **565** (2006) 178 , Proceedings of the International Workshop on Semiconductor Pixel Detectors for Particles and Imaging, ISSN: 0168-9002,
URL: http://www.sciencedirect.com/science/article/pii/S0168900206007649.

[97] S. Parker, C. Kenney and J. Segal, *3D A proposed new architecture for solid-state radiation detectors*, Nuclear Instruments and Methods in Physics Research Section A: Accelerators, Spectrometers, Detectors and Associated Equipment **395** (1997) 328 , Proceedings of the Third International Workshop on Semiconductor Pixel Detectors for Particles and X-rays, ISSN: 0168-9002, URL: http://www.sciencedirect.com/science/article/pii/S0168900297006943.

[98] ATLAS Collaboration, *Modelling radiation damage to pixel sensors in the ATLAS detector*, JINST **14** (2019) P06012, arXiv: 1905.03739 [physics.ins-det].

[99] ATLAS Collaboration, *IBL Calibration Plots and Drift of Calibration with Luminosity in 2016*, (), URL: https://atlas.web.cern.ch/Atlas/GROUPS/PHYSICS/PLOTS/PIX-2017-002/.

[100] A. Rosenfeld and J. L. Pfaltz, *Sequential Operations in Digital Picture Processing*, J. ACM **13** (Oct. 1966) 471, ISSN: 0004-5411, URL: http://doi.acm.org/10.1145/321356.321357.

[101] ATLAS Collaboration, *A neural network clustering algorithm for the ATLAS silicon pixel detector. A neural network clustering algorithm for the ATLAS silicon pixel detector*, JINST **9** (2014) P09009. 38 p, Comments: 6 pages plus author list + cover pages (38 pages total), 10 figures, 0 tables, submitted
to JINST, All figures including auxiliary figures are available at http://atlas.web.cern.ch/Atlas/GROUPS/PHYSICS/PAPERS/PERF-2012-05,
URL: https://cds.cern.ch/record/1712337.

[102] G. Aad et al., *A neural network clustering algorithm for the ATLAS silicon pixel detector*, JINST **9** (2014) P09009, arXiv: 1406.7690 [hep-ex].

[103] N. Wermes et al., *Pixel Detectors, From Fundamentals to Applications*, Springer-Verlag, 2006, ISBN: 3-540-28332-3.

[104] M. Moll, 'Radiation damage in silicon particle detectors: Microscopic defects and macroscopic properties', PhD thesis: Hamburg U., 1999, URL: http://www-library.desy.de/cgi-bin/showprep.pl?desy-thesis99-040.

[105] RD48 Collaboration, *Radiation hard silicon detectors developments by the RD48 (ROSE) collaboration*, Nuclear Instruments and Methods in Physics Research Section A: Accelerators, Spectrometers, Detectors and Associated Equipment **466** (2001) 308 , 4th Int. Symp. on Development and Application of Semiconductor Tracking Detectors, ISSN: 0168-9002, URL: http://www.sciencedirect.com/science/article/pii/S0168900201005605.

[106] A. Vasilescu, 'The NIEL scaling hypothesis applied to neutron spectra of irradiation facilities and in the ATLAS and CMS SCT', tech. rep. ROSE/TN/97-2, CERN, 1997.

[107] A Chilingarov, *Temperature dependence of the current generated in Si bulk*, Journal of Instrumentation **8** (2013) P10003, URL: https://doi.org/10.1088%2F1748-0221%2F8%2F10%2Fp10003.

[108] G. Lutz, *Semiconductor radiation detectors: device physics*, Berlin: Springer, 1999, URL: https://cds.cern.ch/record/411172.

[109] V. Eremin et al., *The origin of double peak electric field distribution in heavily irradiated silicon detectors*, Nucl. Instr. and Meth. A **476** (2002) 556.

[110] G. Kramberger et al., *Effective trapping time of electrons and holes in different silicon materials irradiated with neutrons, protons and pions*, Nucl. Instrum. Meth. **A481** (2002) 297.

[111] T. Sjostrand et al., *An Introduction to PYTHIA 8.2*, Comput. Phys. Commun. **191** (2015) 159, arXiv: 1410.3012 [hep-ph].

[112] T. Sjostrand, S. Mrenna and P. Z. Skands, *PYTHIA 6.4 Physics and Manual*, JHEP **05** (2006) 026, arXiv: hep-ph/0603175 [hep-ph].

[113] 'A study of the Pythia 8 description of ATLAS minimum bias measurements with the Donnachie-Landshoff diffractive model', tech. rep. ATL-PHYS-PUB-2016-017, CERN, 2016, URL: https://cds.cern.ch/record/2206965.

[114] G. Battistoni et al., *The FLUKA code: description and benchmarking*, AIP Conference Proceedings **896** (2007) 31, eprint: https://aip.scitation.org/doi/pdf/10.1063/1.2720455, URL: https://aip.scitation.org/doi/abs/10.1063/1.2720455.

[115] A Ferrari et al., *FLUKA: A multi-particle transport code (program version 2005)*, CERN Yellow Reports: Monographs, Geneva: CERN, 2005, URL: https://cds.cern.ch/record/898301.

[116] ATLAS Collaboration, *Radiation Simulation Public Results*, (), URL: https://twiki.cern.ch/twiki/bin/view/AtlasPublic/RadiationSimulationPublicResults.

[117] ATLAS Collaboration, *Radiation damage in 2015-2017*, (), URL: https://atlas.web.cern.ch/Atlas/GROUPS/PHYSICS/PLOTS/PIX-2018-005/.

[118] S. Agostinelli et al., *GEANT4: A Simulation toolkit*, Nucl. Instrum. Meth. **A506** (2003) 250.

[119] J. Idarraga and M. Benoit, *Generic Geant4 implementation for pixel detectors*, The AllPix Simulation Framework (2006) [twiki.cern.ch:AllPix].

[120] Silvaco, http://www.silvaco.com, Santa Clara, California (USA).

[121] Silvaco, 'Atlas User's Manual: Device Simulation Software'.

[122] Synopsys, http://synopsys.com, Mountain View, California (USA).

[123] Synopsys, 'Sentaurus Device User Guide'.

[124] V. Chiochia et al., *Simulation of heavily irradiated silicon pixel sensors and comparison with test beam measurements*, IEEE Trans. Nucl. Sci. **52** (2005) 1067, arXiv: physics/0411143 [physics].

[125] M. Petasecca et al., *Numerical Simulation of Radiation Damage Effects in p-Type and n-Type FZ Silicon Detectors*, IEEE Transactions on Nuclear Science **53** (2006) 2971.

[126] F. Moscatelli et al., *Combined Bulk and Surface Radiation Damage Effects at Very High Fluences in Silicon Detectors: Measurements and TCAD Simulations*, IEEE Transactions on Nuclear Science **63** (2016) 2716.

[127] G. Lutz, *Effects of deep level defects in semiconductor detectors*, Nuclear Instruments and Methods in Physics Research Section A: Accelerators, Spectrometers, Detectors and Associated Equipment **377** (1996) 234 .

[128] C. Jacoboni et al., *A review of some charge transport properties of silicon*, Solid-State Electronics **20** (1977) 77 , URL: http://www.sciencedirect.com/science/article/pii/0038110177900545.

[129] O. Krasel et al., *Measurement of trapping time constants in proton-irradiated silicon pad detectors*, IEEE Trans. Nucl. Sci. **51** (2004) 3055.

[130] G. Alimonti et al., *A study of charge trapping in irradiated silicon with test beam data*, (2003).

[131] S. Ramo, *Currents Induced by Electron Motion*, Proceedings of the IRE **27** (1939) 584.

[132] L. Landau, *On the energy loss of fast particles by ionization*, J. Phys.(USSR) **8** (1944) 201.

[133] ATLAS Collaboration, *Charge Collection Efficiency as a function of integrated luminosity*, (), URL: https://atlas.web.cern.ch/Atlas/GROUPS/PHYSICS/PLOTS/PIX-2017-004/.

[134] 'Modeling the Mobility and Lorentz angle for the ATLAS Pixel Detector', tech. rep. ATL-INDET-PUB-2018-001, CERN, 2018, URL: https://cds.cern.ch/record/2629889.

[135] ATLAS Collaboration, *Radiation damage to the ATLAS pixel*, (), URL: https://atlas.web.cern.ch/Atlas/GROUPS/PHYSICS/PLOTS/PIX-2017-005/.

[136] ATLAS Collaboration, *dE/dx simulation plots for Run 2*, (), URL: https://atlas.web.cern.ch/Atlas/GROUPS/PHYSICS/PLOTS/PIX-2018-004/.

[137] T. Cornelissen et al., *The new ATLAS track reconstruction (NEWT)*, J. Phys. Conf. Ser. **119** (2008) 032014.

[138] R. Fruhwirth, *Application of Kalman filtering to track and vertex fitting*, Nucl. Instrum. Meth. **A262** (1987) 444.

[139] 'Early Inner Detector Tracking Performance in the 2015 data at $\sqrt{s} = 13$ TeV', tech. rep. ATL-PHYS-PUB-2015-051, CERN, 2015, URL: http://cds.cern.ch/record/2110140.

[140] ATLAS Collaboration, *Average Number of Tracks against μ for Data 2017*, (), URL: https://atlas.web.cern.ch/Atlas/GROUPS/PHYSICS/PLOTS/IDTR-2017-007/.

[141] ATLAS Collaboration, *Reconstruction of primary vertices at the ATLAS experiment in Run 1 proton–proton collisions at the LHC*, Eur. Phys. J. **C77** (2017) 332, arXiv: 1611.10235 [physics.ins-det].

[142] R. Fruhwirth, W. Waltenberger and P. Vanlaer, *Adaptive vertex fitting*, J. Phys. **G34** (2007) N343.

[143] 'Vertex Reconstruction Performance of the ATLAS Detector at $\sqrt{s} = 13$ TeV ', tech. rep. ATL-PHYS-PUB-2015-026, CERN, 2015, URL: http://cds.cern.ch/record/2037717.

[144] ATLAS Collaboration, *Vertex performance in 2018 data*, (), URL: https://atlas.web.cern.ch/Atlas/GROUPS/PHYSICS/PLOTS/IDTR-2018-006/.

[145] J. R. Forshaw and D. A. Ross,
Quantum chromodynamics and the pomeron,
Cambridge Lect. Notes Phys. **9** (1997) 1.

[146] W Lampl et al., 'Calorimeter Clustering Algorithms: Description and Performance', tech. rep. ATL-LARG-PUB-2008-002. ATL-COM-LARG-2008-003, CERN, 2008, URL: https://cds.cern.ch/record/1099735.

[147] ATLAS Collaboration, *Topological cell clustering in the ATLAS calorimeters and its performance in LHC Run 1*, Eur. Phys. J. **C77** (2017) 490, arXiv: 1603.02934 [hep-ex].

[148] M. Cacciari, G. P. Salam and G. Soyez,
The anti-k_t jet clustering algorithm, JHEP **04** (2008) 063,
arXiv: 0802.1189 [hep-ph].

[149] ATLAS Collaboration, *Jet energy scale measurements and their systematic uncertainties in proton-proton collisions at $\sqrt{s} = 13$ TeV with the ATLAS detector*,
Phys. Rev. **D96** (2017) 072002, arXiv: 1703.09665 [hep-ex].

[150] M. Cacciari and G. P. Salam,
Pileup subtraction using jet areas,
Phys. Lett. **B659** (2008) 119, arXiv: 0707.1378 [hep-ph].

[151] 'Pile-up subtraction and suppression for jets in ATLAS', tech. rep. ATLAS-CONF-2013-083, CERN, 2013, URL: https://cds.cern.ch/record/1570994.

[152] ATLAS Collaboration, *Jet energy scale and uncertainties in 2015-2017 data and simulation*, (), URL: https://atlas.web.cern.ch/Atlas/GROUPS/PHYSICS/PLOTS/JETM-2018-006/.

[153] ATLAS Collaboration,
Jet energy resolution in 2017 data and simulation, (),
URL: https://atlas.web.cern.ch/Atlas/GROUPS/PHYSICS/PLOTS/JETM-2018-005/.

[154] 'Tagging and suppression of pileup jets with the ATLAS detector', tech. rep. ATLAS-CONF-2014-018, CERN, 2014, URL: https://cds.cern.ch/record/1700870.

[155] ATLAS Collaboration,
Performance of pile-up mitigation techniques for jets in pp collisions at $\sqrt{s} = 8$ TeV using the ATLAS detector,
Eur. Phys. J. **C76** (2016) 581, arXiv: 1510.03823 [hep-ex].

[156] 'Commissioning of the ATLAS high-performance b-tagging algorithms in the 7 TeV collision data',
tech. rep. ATLAS-CONF-2011-102, CERN, 2011,
URL: https://cds.cern.ch/record/1369219.

[157] 'Tagging and suppression of pileup jets',
tech. rep. ATL-PHYS-PUB-2014-001, CERN, 2014,
URL: https://cds.cern.ch/record/1643929.

[158] ATLAS Collaboration, *JVT Public Plots for ICHEP 2016*, (),
URL: https://atlas.web.cern.ch/Atlas/GROUPS/PHYSICS/PLOTS/JETM-2016-011/.

[159] 'Commissioning of the ATLAS b-tagging algorithms using $t\bar{t}$ events in early Run-2 data',
tech. rep. ATL-PHYS-PUB-2015-039, CERN, 2015,
URL: http://cds.cern.ch/record/2047871.

[160] G. Aad et al.,
ATLAS b-jet identification performance and efficiency measurement with $t\bar{t}$ events in pp collisions at $\sqrt{s} = 13$ TeV,
(2019), arXiv: 1907.05120 [hep-ex].

[161] 'Optimisation of the ATLAS b-tagging performance for the 2016 LHC Run', tech. rep. ATL-PHYS-PUB-2016-012,
CERN, 2016, URL: http://cds.cern.ch/record/2160731.

[162] ATLAS Collaboration,
Measurements of b-jet tagging efficiency with the ATLAS detector using $t\bar{t}$ events at $\sqrt{s} = 13$ TeV,
JHEP **08** (2018) 089, arXiv: 1805.01845 [hep-ex].

[163] ATLAS Collaboration, *Electron reconstruction and identification in the ATLAS experiment using the 2015 and 2016 LHC proton-proton collision data at $\sqrt{s} = 13$ TeV*,
Submitted to: Eur. Phys. J. (2019),
arXiv: 1902.04655 [physics.ins-det].

[164] ATLAS Collaboration, *Electron and photon performance measurements with the ATLAS detector using the 2015-2017 LHC proton-proton collision data*, (2019), arXiv: 1908.00005 [hep-ex].

[165] ATLAS Collaboration, *Electron and photon energy calibration with the ATLAS detector using 2015–2016 LHC proton-proton collision data*, JINST **14** (2019) P03017, arXiv: 1812.03848 [hep-ex].

[166] 'Electron shower shapes, tracking, isolation and invariant mass distributions from $Z \to ee$ and $J/\psi \to ee$ events', https://atlas.web.cern.ch/Atlas/GROUPS/PHYSICS/PLOTS/EGAM-2015-003/index.html.

[167] 'Electron isolation efficiency measurements in 2017 data : evolution versus p_T,η, and pileup', https://atlas.web.cern.ch/Atlas/GROUPS/PHYSICS/PLOTS/EGAM-2018-006/index.html.

[168] ATLAS Collaboration, *Muon reconstruction performance of the ATLAS detector in proton–proton collision data at $\sqrt{s}$ =13 TeV*, Eur. Phys. J. **C76** (2016) 292, arXiv: 1603.05598 [hep-ex].

[169] ATLAS Collaboration, *JVT Public Plots for ICHEP 2016*, (), URL: https://atlas.web.cern.ch/Atlas/GROUPS/PHYSICS/PLOTS/MUON-2018-005/index.html.

[170] ATLAS Collaboration, *ATLAS Muon Combined Performance in 2016*, (), URL: https://atlas.web.cern.ch/Atlas/GROUPS/PHYSICS/PLOTS/MUON-2016-004/index.html.

[171] ATLAS Collaboration, *Performance of missing transverse momentum reconstruction with the ATLAS detector using proton-proton collisions at $\sqrt{s}$ = 13 TeV*, Eur. Phys. J. **C78** (2018) 903, arXiv: 1802.08168 [hep-ex].

[172] '$E_{\mathrm{T}}^{\mathrm{miss}}$ performance in the ATLAS detector using 2015-2016 LHC p-p collisions', tech. rep. ATLAS-CONF-2018-023, CERN, 2018, URL: https://cds.cern.ch/record/2625233.

[173] G Cowan et al.,
Asymptotic formulae for likelihood-based tests of new physics,
Eur. Phys. J. **C 71** (2011) 1554,
arXiv: 1007.1727 [physics.data-an].

[174] W. Buttinger and M. Lefebvre,
'Formulae for Estimating Significance',
tech. rep. ATL-COM-GEN-2018-026, CERN, 2018,
URL: https://cds.cern.ch/record/2643488.

[175] L. Moneta et al., *The RooStats project*,
PoS **ACAT2010** (2010) 057,
arXiv: 1009.1003 [physics.data-an].

[176] M. Baak et al.,
HistFitter software framework for statistical data analysis,
Eur. Phys. J. C **75** (2015) 153, arXiv: 1410.1280 [hep-ex].

[177] J. Neyman and E. S. Pearson, 'On the Problem of the Most Efficient Tests of Statistical Hypotheses',
Breakthroughs in Statistics: Foundations and Basic Theory,
ed. by S. Kotz and N. L. Johnson,
New York, NY: Springer New York, 1992 73,
ISBN: 978-1-4612-0919-5,
URL: https://doi.org/10.1007/978-1-4612-0919-5_6.

[178] A. L. Read, *Presentation of search results: theCLstechnique*,
Journal of Physics G: Nuclear and Particle Physics **28** (2002) 2693, URL:
https://doi.org/10.1088%2F0954-3899%2F28%2F10%2F313.

[179] G Zech, *Upper limits in experiments with background or measurement errors*,
Nucl. Instrum. Methods Phys. Res., A **277** (1988) 608. 6 p,
URL: https://cds.cern.ch/record/193135.

[180] T. Junk, *Confidence Level Computation for Combining Searches with Small Statistics*,
Nucl. Instrum. Meth. **A 434** (1999) 435,
arXiv: hep-ex/9902006.

[181] ATLAS Collaboration, *Search for electroweak production of supersymmetric states in scenarios with compressed mass spectra at* $\sqrt{s} = 13$ *TeV with the ATLAS detector*,
Phys. Rev. **D97** (2018) 052010, arXiv: 1712.08119 [hep-ex].

[182] J. Alwall et al., *MadGraph 5 : Going Beyond*, JHEP **1106** (2011) 128, arXiv: 1106.0522 [hep-ph].

[183] T. Sjostrand, S. Mrenna and P. Z. Skands, *A brief introduction to PYTHIA 8.1*, Comput. Phys. Commun. **178** (2008) 852, arXiv: 0710.3820 [hep-ph].

[184] A. Djouadi, M. M. Muhlleitner and M. Spira, *Decays of supersymmetric particles: The Program SUSY-HIT (SUspect-SdecaY-Hdecay-InTerface)*, Acta Phys. Polon. **B38** (2007) 635, arXiv: hep-ph/0609292 [hep-ph].

[185] P. Artoisenet et al., *Automatic spin-entangled decays of heavy resonances in Monte Carlo simulations*, JHEP **03** (2013) 015, arXiv: 1212.3460 [hep-ph].

[186] L. Lonnblad and S. Prestel, *Matching Tree-Level Matrix Elements with Interleaved Showers*, JHEP **03** (2012) 019, arXiv: 1109.4829 [hep-ph].

[187] R. D. Ball et al., *Parton distributions with LHC data*, Nucl. Phys. B **867** (2013) 244, arXiv: 1207.1303 [hep-ph].

[188] B. Fuks et al., *Precision predictions for electroweak superpartner production at hadron colliders with Resummino*, Eur. Phys. J. **C73** (2013) 2480, arXiv: 1304.0790 [hep-ph].

[189] B. Fuks et al., *Revisiting slepton pair production at the Large Hadron Collider*, JHEP **01** (2014) 168, arXiv: 1310.2621.

[190] C. Borschensky et al., *Squark and gluino production cross sections in pp collisions at* $\sqrt{s} = 13, 14, 33$ *and 100 TeV*, Eur.Phys.J. **C74** (2014) 3174, arXiv: 1407.5066 [hep-ph].

[191] B. Fuks et al., *Gaugino production in proton-proton collisions at a center-of-mass energy of 8 TeV*, JHEP **10** (2012) 081, arXiv: 1207.2159 [hep-ph].

[192] S. Frixione, P. Nason and C. Oleari, *Matching NLO QCD computations with Parton Shower simulations: the POWHEG method*, JHEP **11** (2007) 070, arXiv: 0709.2092 [hep-ph].

[193] T. Gleisberg et al., *Event generation with SHERPA 1.1*, JHEP **02** (2009) 007, arXiv: 0811.4622 [hep-ph].

[194] S. Catani et al., *Vector boson production at hadron colliders: a fully exclusive QCD calculation at NNLO*, Phys.Rev.Lett. **103** (2009) 082001, arXiv: 0903.2120 [hep-ph].

[195] F. Cascioli, P. Maierhofer and S. Pozzorini, *Scattering Amplitudes with Open Loops*, Phys. Rev. Lett. **108** (2012) 111601, arXiv: 1111.5206 [hep-ph].

[196] T. Gleisberg and S. Höche, *Comix, a new matrix element generator*, JHEP **12** (2008) 039, arXiv: 0808.3674 [hep-ph].

[197] H.-L. Lai et al., *New parton distributions for collider physics*, **82** (2010) 074024, arXiv: 1007.2241 [hep-ph].

[198] S. Hoeche et al., *QCD matrix elements + parton showers: The NLO case*, JHEP **04** (2013) 027, arXiv: 1207.5030 [hep-ph].

[199] ATLAS Collaboration, *Search for supersymmetry in events with four or more leptons in $\sqrt{s} = 13$ TeV pp collisions with ATLAS*, Phys. Rev. **D98** (2018) 032009, arXiv: 1804.03602 [hep-ex].

[200] A. Barr and J. Scoville, *A boost for the EW SUSY hunt: monojet-like search for compressed sleptons at LHC14 with 100 fb^{-1}*, JHEP **04** (2015) 147, arXiv: 1501.02511 [hep-ph].

[201] H. Baer, A. Mustafayev and X. Tata, *Monojet plus soft dilepton signal from light higgsino pair production at LHC14*, Phys. Rev. **D90** (2014) 115007, arXiv: 1409.7058 [hep-ph].

[202] G. Aad et al., *Observation and measurement of Higgs boson decays to WW* with the ATLAS detector*, Phys. Rev. **D92** (2015) 012006, arXiv: 1412.2641 [hep-ex].

[203] 'Search for direct pair production of higgsinos by the reinterpretation of the disappearing track analysis with 36.1 fb^{-1} of $\sqrt{s} = 13$ TeV data collected with the ATLAS experiment', tech. rep. ATL-PHYS-PUB-2017-019, CERN, 2017, URL: https://cds.cern.ch/record/2297480.

[204] 'Searches for electroweak production of supersymmetric particles with compressed mass spectra in $\sqrt{s} = 13$ TeV pp collisions with the ATLAS detector',
tech. rep. ATLAS-CONF-2019-014, CERN, 2019,
URL: https://cds.cern.ch/record/2675954.

[205] ATLAS Collaboration, *Luminosity determination in pp collisions at $\sqrt{s} = 8$ TeV using the ATLAS detector at the LHC*,
to be submitted to Eur. Phys. J. C.

[206] G. Avoni et al., *The new LUCID-2 detector for luminosity measurement and monitoring in ATLAS*,
Journal of Instrumentation **13** (2018) P07017, URL: https://doi.org/10.1088%2F1748-0221%2F13%2F07%2Fp07017.

[207] G. Aad et al.,
Measurement of $W^{\pm}$ and Z-boson production cross sections in pp collisions at $\sqrt{s} = 13$ TeV with the ATLAS detector,
Phys. Lett. **B759** (2016) 601, arXiv: 1603.09222 [hep-ex].

[208] A. L. Read,
Presentation of search results: The CL(s) technique,
J. Phys. G **28** (2002) 2693.